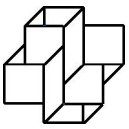

Laboratório Nacional de Computação Científica

Programa de Pós Graduação em Modelagem Computacional

An effective numerical technique for pipe-like domains and its application in computational hemodynamics

Por

Luis Alonso Mansilla Alvarez

PETRÓPOLIS, RJ - BRASIL

MARCH, 2018.

AN EFFECTIVE NUMERICAL TECHNIQUE FOR PIPE-LIKE DOMAINS AND ITS APPLICATION IN COMPUTATIONAL HEMODYNAMICS

Luis Alonso Mansilla Alvarez

TESE SUBMETIDA AO CORPO DOCENTE DO LABORATÓRIO NACIONAL DE COMPUTAÇÃO CIENTÍFICA COMO PARTE DOS REQUISITOS NECESSÁRIOS PARA A OBTENÇÃO DO GRAU DE DOUTOR EM CIÊNCIAS EM MODELAGEM COMPUTACIONAL

Aprovada por:

Prof. Pablo Javier Blanco, D.Sc (Presidente)

Prof. Abimael Fernando Dourado Loula, D.Sc.

Prof. Regina Célia Cerqueira de Almeida, D.Sc.

Prof. Alessandro Veneziani, Ph.D.

Prof. Alvaro Luiz Gayoso de Azeredo Coutinho, D.Sc.

PETRÓPOLIS, RJ - BRASIL
MARCH, 2018

Mansilla Alvarez, Luis Alonso

XXXX An effective numerical technique for pipe-like domains and its application in computational hemodynamics / Luis Alonso Mansilla Alvarez. Petropólis, RJ. : Laboratório Nacional de Computação Científica, 2018.

xix, 194 p. : il.; 29 cm

Orientadore(s): Pablo Javier Blanco e Raúl Antonino Feijóo

Tese (D.Sc.) – Laboratório Nacional de Computação Científica, 2018.

1. ASSUNTO. 2. Computational hemodynamics. 3. Finite Element Method. 4. Fluid mechanics. 5. Patient-specific simulations. I. Blanco, Pablo Javier. II. LNCC/MCT. III. Título.

CDD XXX.XXX

”Toute réussite déguise une abdication“.
— **Simone de Beauvoir.**

A todos aqueles que oferecem um sorriso aberto, um café quente e uma conversa boa.

Acknowledgement

O presente trabalho representa, entre outras coisas, o final de uma jornada única e a realização de um sonho. Nessa aventura, no programa de doutorado do Laboratório Nacional de Computação Científica - LNCC, tive a sorte de conhecer pessoas excelentes que mudaram minha visão da vida, tanto no pessoal quanto no acadêmico, e sem as quais teria sido impossível ter atingido esse objetivo na minha vida.

Não tenho como começar sem agradecer o apoio, confiança, exigência e paciência daqueles que me guiaram nesses anos. Sem a orientação deles, Pablo J. Blanco e Raúl A. Feijóo, esse trabalho não existiria e, com certeza, minha forma de ver o mundo acadêmico seria totalmente contraria á que tenho hoje. Só tenho a agradecer pela oportunidade de trilhar esse caminho juntos e pelos diversos ensinamentos transmitidos durante esse tempo. Agradecer também aos meus amigos Carlitos, Gonzalo Ares, Gonzalo Maso e Felipe, que formam parte do HeMoLab e que sempre estiveram dispostos a ajudar e compartilhar conhecimento e risadas.

A versão final desse texto foi obtida graças às críticas e comentários altamente relevantes dos membros da banca avaliadora. Muito obrigado a cada um deles, Abimael, Regina, Alessandro e Álvaro, por dedicar seu tempo e experiência para poder aprimorar os resultados aqui apresentados.

Ao longo desse tempo no LNCC, quase seis anos em um pais que me recebeu de braços abertos, tive a sorte de conhecer muitas pessoas que com um sorriso, um café, uma conversa ou simplesmente com a própria presenạ fizeram que nunca me sentisse como um estrangeiro. A vocês Su, Bruno, Thaís, Maguinho, Fernandinho, Diony, Fortià, Caio, Aline, Tchê, Lucão e muitas outras pessoas que dia após dia deram uma palavra de apoio, souberam lidar com as minhas neuras e tiveram a força para entender meu portunhol. Esse trabalho também é seu.

Para finalizar, no tenho palavras para agradecer à minha mãe e minha avó, sem vocês eu não seria nada do que sou agora. Obrigado pelo seu apoio incondicional, por se sacrificar por mim e pelas forças brindadas para seguir meus sonhos.

Luis Alonso Mansilla Alvarez
Petrópolis - RJ, 2018.

Resumo da Tese submetida à Coordenação de Pós-Graduação do Laboratório Nacional de Computação Científica - LNCC/MCTIC como parte dos requisitos necessários para a obtenção do grau de Doutor em Ciências (D.Sc.)

AN EFFECTIVE NUMERICAL TECHNIQUE FOR PIPE-LIKE DOMAINS AND ITS APPLICATION IN COMPUTATIONAL HEMODYNAMICS

Luis Alonso Mansilla Alvarez
March, 2018

Orientador: Pablo Javier Blanco, D.Sc
Co-orientador: Raúl Antonino Feijóo, D.Sc.

Nas últimas décadas, o papel desenvolvido pela hemodinâmica computacional no campo das doenças cardiovasculares tem sido fundamental devido à demonstrada correlação entre quantidades próprias do escoamento (tais como velocidade, pressão, tensões cisalhantes, entre outras) e a localização e evolução de alterações na mecanobiologia da parede arterial.

Embora altamente promissoras, o uso de uma abordagem computacional na prática médica tem sido altamente limitado devido ao balanço entre a qualidade (e quantidade) de informação que metodologias atuais podem prover e o custo computacional que tais estratégias demandam (em termos de tempo e recursos físicos). Exemplos clássicos desse balanço são os modelos unidimensionais que, embora não sendo computacionalmente custosos, são incapazes de prover informação sobre as tensões cisalhantes exercidas pelo sangue sobre o endotélio, e os modelos 3D os quais, mesmo sendo capazes de dar informação detalhada da dinâmica sanguínea, tem seu uso restrito a pequenas regiões do sistema cardiovascular devido ao enorme custo computacional envolvido. Tal contexto tem motivado a procura por novas metodologias capazes de prover informação relevante para o uso clínico mas com uma redução significativa no custo computacional.

Nesse trabalho, um novo esquema numérico é proposto para a discretização das equações de Navier-Stokes. Essa abordagem, denominada *Transversally Enriched Pipe Element Method* (TEPEM), tem se demonstrado capaz de fornecer informação relevante do escoamento sanguíneo empregando uma fração do tempo utilizado em simulações 3D baseadas no FEM. As capacidades desta abordagem são exploradas e os resultados demonstram sua eficácia em termos de manter uma precisão aceitável, reduzir os recursos computacionais necessários e o tempo de simulação.

Abstract of a Thesis submitted to de Postgraduate Department of the National Laboratory of Scientific Computing - LNCC/MCTIC as a partial fulfillment of the requirements for the degree of Doctor in Sciencies (D.Sc.)

AN EFFECTIVE NUMERICAL TECHNIQUE FOR PIPE-LIKE DOMAINS AND ITS APPLICATION IN COMPUTATIONAL HEMODYNAMICS

Luis Alonso Mansilla Alvarez
March, 2018

Advisor: Pablo Javier Blanco, D.Sc
Co-advisor: Raúl Antonino Feijóo, D.Sc.

In the last decades, the role of the computational hemodynamics in the domain of cardiovascular diseases has become fundamental due the large evidence of the correlation between flow-related quantities (such as velocity, pressure, wall shear stresses among others) and the localization and onset of alterations in the mechanobiology of the arterial wall.

These promising capabilities are still strongly limited for massive usage in the daily medical practice due to the trade-off between the quantity/quality of information provided by the current methodologies and their computational costs (in terms of time and physical resources). Classical examples are the cheap one-dimensional models, unable to provide insight about wall shear stresses, and the full 3D models with extensive predictive capabilities but highly prohibitive for massive use due to the large computational cost.

In this work, a novel numerical technique is proposed for the discretization of the Navier-Stokes equations. This approach, coined as Transversally Enriched Pipe Element Method (TEPEM), is able to provide hemodinamically relevant information at a fraction of the time of full 3D simulations with standard finite element methods. The capabilities of this methodology are studied and the results confirm the effectiveness in terms of maintaining satisfactory accuracy and of reducing the computational resources and execution time.

Contents

Figures

Figure

Tables

Table

Chapter 1

Introduction

Since early in the seventies, numerical methodologies such as the Finite Element Method (FEM) started to be employed in the field of computational fluid dynamics. These days, in the hemodynamics realm, the FEM has been established as a standard strategy to simulate patient-specific blood flow, ensuring low risk (zero physical risk if compared with invasive studies) and at the same time provides fundamental information that can be employed in the medical practice. Accurate description of blood velocity, pressure distribution, wall shear stress, fractional flow reserve among others flow-related indexes is of utmost importance in the clinical practice.The accuracy of model predictions is fundamental for the correct assessment of some related vascular problems. In fact, the medical literature has systematically reported a strong positive correlation between the preferred sites for the genesis and development of cardiovascular diseases and regions featuring disturbances in some flow-related quantities [Caro et al. 1975, Nerem and Cornhill 1980, Yoshida et al. 1988, Glagov et al. 1988]. Some relevants biomechanical factors that may be responsible for the localization/progression of atherosclerosis are:

- Velocity flow profiles: Several authors have pointed out the departure from axially aligned, unidirectional laminar flow, in regions where an increase in the internal arterial wall thickening and atherosclerosis development occurs. See, for example, the works of [Giddens et al. 1993, Karino and Goldsmith 1983, Karino 1985, Zarins et al. 1983, Morbiducci et al. 2007, Cebral et al. 2011].

- Pressure spatial distribution: The hypothesis that pressure-induced high stress areas are related to the sites of atherosclerotic plaques was introduced in [Thubrikar and Robicsek 1995]. Several other works ([Salzar et al. 1995, Giannoglou et al. 2002]) provided further evidence to confirm this correlation.

- Wall shear stress (WSS): The role of the wall shear stress in atherosclerosis progression and wall thickening has been extensively studied in different works, for example [Caro et al. 1971, Zarins et al. 1983, Friedman et al. 1986, Gibson et al. 1993]. It is well known that both low WSS and high oscillatory patterns of WSS are related to intimal wall thickening.

- Oscillatory shear index (OSI): As reported in [Ku et al. 1985], there is a positive correlation between the plaque localization and regions wherein the OSI achieves lower values. At this point, it is important to highlight that, for medical practical applications, it is much more important to accurately identify the regions with high/low values in OSI and WSS rather than the exact value of these indexes.

The correlation between the onset of several cardiovascular diseases and the flow dynamics becomes more relevant if we recall that diseases such as atherosclerosis are the leading cause of death worldwide (around 31% of total deaths on 2017, according the World Health Organization) in front of diseases such as neoplasms, neurological diseases, among others (see Figure 1.1).

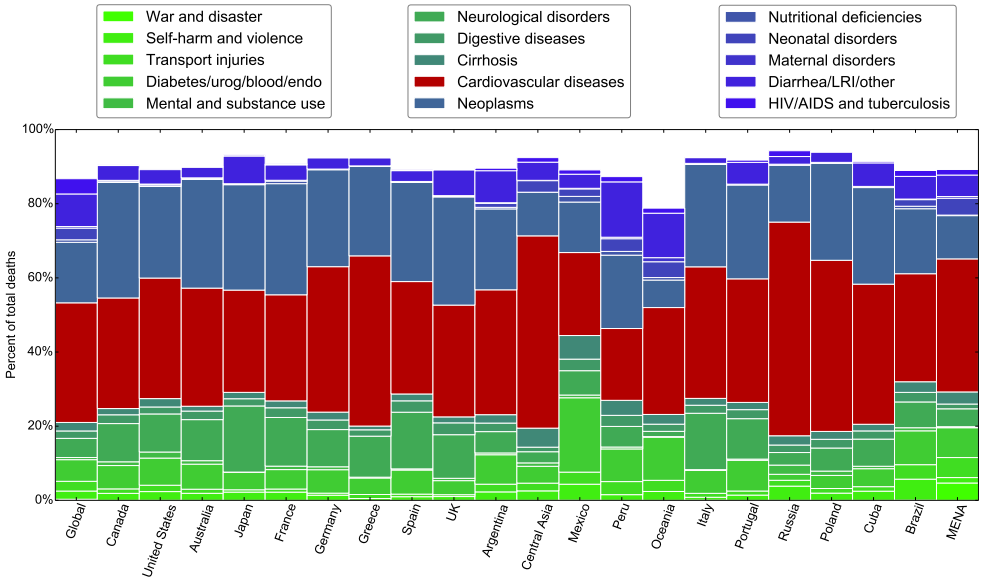

Figure 1.1: Cardiovascular diseases (highlighted in red) represent the leading cause of death in most countries. Data from Global burden of disease study 2016 (GBD 2016). Available from *http://vizhub.healthdata.org/gbd-compare/*.

Aiming to deal with the pressing need for improving diagnosis strategies, several successful proofs of concept have been appears in the literature demonstrating that numerical simulations can provided a terrific insight into physiopathological dynamics, with a potential impact on diagnosis, prognosis, and ultimately in the clinical universe (see, for example, [Taylor et al. 1998b, Coşkun et al. 2006, Botnar et al. 2000, Maurits et al. 2007, Olufsen et al. 2000]).

Unfortunately, the massive penetration of scientific computing techniques in the medical practice is not yet a reality due to the insufficient capability of numerical methodologies to effectively deal with large-scale problems of the size of whole cardiovascular network in a reasonably and timely manner. This restriction imposed by the current methods/resources has been clearly stated in [Grinberg et al. 2009] where the authors point out that the simulation of one single cardiac cycle in the whole cardiovascular system demands a total of 27 hours and 40 000 processors, a computational burden that certainly makes prohibitive their use in daily medical practice.

Within the context exposed in the previous paragraph, the main goal of this work is to develop a new numerical methodology to efficiently accommodate the trade-off between computational burden and accuracy, and which is tailored specifically for its use within the scope of hemodynamic simulations. The numerical approach, coined as Transversally Enriched Pipe Element Method (TEPEM), closely follows the classical structure of FEM strategies (domain partition into small pieces, or elements, geometrical mapping to a reference element, field approximation in finite-dimensional spaces, etc.) but providing a goal-oriented selection for geometry/field interpolants by exploiting the available *a priori* information for the problems in which we are interested in.

Coming up next, in this chapter, a brief revision on the most common alternatives to model the blood flow. Also is addressed a state-of-art review of the numerical methodologies available in the literature. This revision is focused in highlight the predictive capabilities and provide an idea on the computational burden associated to each approach. Finally, a detailed description of the specific goals of this thesis is outlined and the structure of the document and contributions are commented.

1.1 Blood flow modeling

Considering the blood as a Newtonian fluid, the blood flow can be effectively modeled by the Navier-Stokes (NS) equations. Let us consider $\Omega \subset \mathbb{R}^3$ a domain representing the internal region of the vessel (or system of vessels) in which the blood flow is studied.

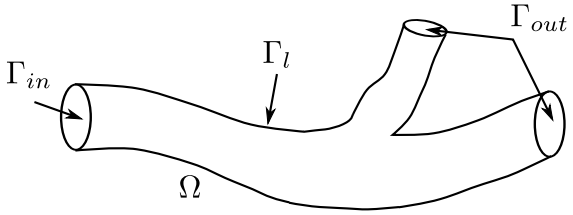

Figure 1.2: Model geometry for the blood flow.

In this domain, like the one presented in Figure 1.2, the blood flow is described through the velocity $\mathbf{u}$ and pressure p fields, solution of the problem:

$$\begin{aligned} &\rho\left(\frac{\partial \mathbf{u}}{\partial t} + (\mathbf{u}\cdot\nabla)\mathbf{u}\right) + \nabla p - 2\mu\nabla\cdot(\nabla\mathbf{u})^s = \mathbf{f} && \text{in}\,\Omega, t \in (0,T) \\ &\nabla\cdot\mathbf{u} = 0 && \text{in}\,\Omega, t \in (0,T) \end{aligned} \tag{1.1}$$

where ρ and μ stand for the blood density and viscosity, respectively, T a positive and fixed real value and the vector field $\mathbf{f} : \Omega \times (0,T) \to \mathbb{R}^3$ indicates the body forces. To complete the problem description, suitable initial and boundary conditions must be described. The initial condition of the fluid velocity, provided by the function $\mathbf{u}_0$ reads $\mathbf{u}(\mathbf{x}, t=0) = \mathbf{u}_0(\mathbf{x})$ for each $\mathbf{x} \in \Omega$ while several options are available for the boundary conditions that can be imposed over the inlet boundaries Γ_{in} and outlet boundaries Γ_{out}. Over the lateral boundary Γ_l, for a rigid wall model, no-slip condition is imposed ($\mathbf{u} = 0$).

From a theoretical point of view, it is not possible to analytically solve the Equation 1.1, and therefore we must resort to numerical strategies to find approximate solutions. The Newtonian assumption in the blood constitutive model is suitable for larger and middle size vessels, wherein it is reasonable neglect the shear thinning and viscoelastic effects [Quarteroni et al. 2000]. For smaller vessels and capillaries it is necessary to abandon the Newtonian assumption because the continuum hypothesis becomes questionable and in certain cases absolutely invalid. Medical literature, see for example the work of [LaBarbera 1990], report that the average radius for middle size vessels is nearly 0.2 cm while the larger artery in the human body, the aorta, has a radius of 1.5 cm. For a detailed description of the geometrical characteristics of the most representative arteries in the cardiovascular system, the reader is referred to [Avolio 1980, Watanabe 2013].

In practice, the high potentialities of modeling the blood flow through the 3D Navier-Stokes model, which have been demonstrated in the accurate prediction of several flow-related quantities, are in contrast with the high computational cost in real life problems.

Numerical methods aimed to solve the NS equations, which will be addressed in the next section, struggle to deal with the high computational effort that represent the numerical simulation of the whole, or at least large portions of the cardiovascular system when considered as a three-dimensional structure.

Hence, in order to reduce the computational cost, in detriment of the accuracy of the model, several alternatives to model the blood flow appeared as a way of reducing both the complexity and the computational cost but also trying to keep as close as possible the predictive capabilities compared to those delivered by the three-dimensional model. Perhaps some of the most popular numerical schemes developed to reduce the computational burden are grouped under the label of *dimensionally-reduced models*, in which the high complexity associated to the NS model is tackled by reducing the 3D dynamics to lower-dimensional models by introducing suitable kinematic and geometric assumptions, such as the cylindrical morphology of the vessels or the one-directional nature of the blood flow.

Even under the imposition of several hypotheses on the dynamics and their apparent deviation from the real problem, when compared with the original full 3D model, these reduced models are capable of providing reliable numerical results at a low computational cost. Unfortunately, these models are not able to provide some three-dimensional details which are crucial for decision-making in the clinic, such as recirculation patterns, spatial heterogeneity of the pressure, detailed spatial description for the wall shear stress, among others, essentially, three-dimensional features.

Two-dimensional models Under hypothesis of geometrical symmetry (with respect to a straight axis), the computational domain can be reduced to a two-dimensional one and, neglecting the angular component of the external loads, also the velocity of the fluid can be reduced to axial and radial components. This process directly reduces the size of the problem without losing three-dimensional features (owing to the symmetry hypothesis) and without any assumption on the velocity profile.

Theoretical and practical results available in the literature, see for example [Bernardi et al. 1999, Deparis 2004, Belhachmi et al. 2006], highlight the advantages of these models and the effective reduction of complexity of 3D NS equations maintaining model capabilities proper to be employed in the study of blood flow simulations. However, such symmetry assumptions are extremely restrictive when considering the simulation of blood flow in real patient-specific arterial vessels.

One-dimensional models Initially studied by [Euler 1844] and rationally introduced in [Hughes and Lubliner 1973], these models are a simplification of the 3D NS equations by imposing assumptions on the geometry, considering the axis of the vessel as a straight segment, and considering that the axial flow velocity along the elastic vessels is much greater than the flow velocity perpendicular to the longitudinal axis. The resulting model is a nonlinear coupled system of equations, comprising mass and momentum conservation laws

$$\begin{aligned} &\partial_t A + \partial_x q = 0 \\ &\partial_t q + \partial_x \left(\frac{q^2}{A} \right) + \frac{A}{\rho} \partial_x p = -f \end{aligned} \tag{1.2}$$

where x is the axial coordinate and t the temporal variable. These equations involve the cross-sectional area of the vessel $A(x,t)$, the flow rate $q(x,t)$ and the average

internal pressure over a cross-section $p(x,t)$. To close the system, a constitutive law is needed to relate the internal pressure $p(x,t)$ with the cross-sectional area $A(x,t)$. Although their simplicity, this type of model can easily provide useful information about the global dynamics of the system, with an excellent compromise between descriptive capabilities concerning wave propagation phenomena in the cardiovascular network and low computational cost in comparison with full 3D models [Hughes 1974, Avolio 1980, Stergiopulos et al. 1992, Formaggia et al. 2003, Xiao et al. 2014].

Regarding the geometry of this type of 1D model, a popular representation of the whole cardiovascular system is the arterial network proposed by Avolio in [Avolio 1980], constructed based on the anatomical branching structure of the arterial tree and composed by 128 segments. A high improvement in the anatomical modeling appeared with the ADAN model ([Watanabe et al. 2013, Watanabe 2013, Blanco et al. 2014a,b]), currently the most detailed description of the arterial circulation and composed by more than 2 000 arteries. A comparison of these both representative schemes for this type of model is shown in Figure 1.3.

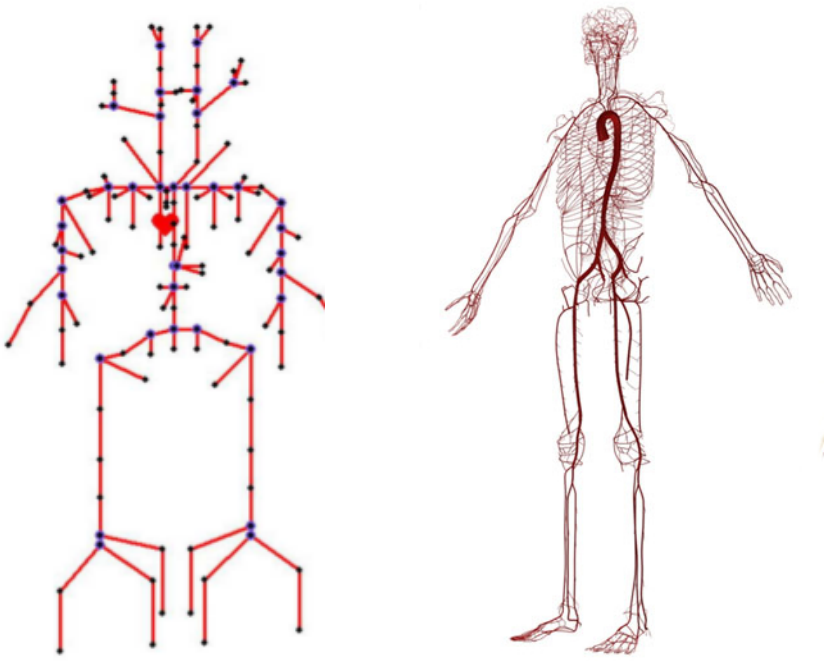

Figure 1.3: Representative schemes of one-dimensional models. Left: Arterial network proposed in [Avolio 1980]. Right: ADAN model proposed in [Blanco et al. 2014b]. Figures inspired in the ones proposed in the corresponding references.

The search for enriched one-dimensional models, aiming to increase the descriptive capabilities in the direction of 3D models, has experimented little advancement. For example, in [Reymond et al. 2009] a Womersley approximation is considered to improve the modeling of viscous dissipation and convective acceleration (the latter only valid in the case of unidirectional flow), and in [Carapau and Sequeira 2006, Green and Naghdi 1993, Green et al. 1993, Robertson and Sequeira 2005] the so-called Cosserat models are considered. However, we have not been aware, until very recently (as explained before) of the existence of a systematic and, more importantly, hierarchical strategy to go from 1D models to 3D models.

Zero-dimensional models Also known as lumped models, they can be derived directly by introducing further simplifications into the 1D models, thus establishing an analogy between the cardiovascular system and electrical circuits [Lee et al. 2004, Huberts et al. 2009, Liang and Liu 2005]. In this type of model, each segment of the system is modeled by the concept of *compartment* yielding a set of ordinary differential equations in the time domain.

The complex network that comprises the human circulatory system can be simulated even more efficiently in this way. The main disadvantage of these 0D models is that they are unable to take into account some important features of cardiovascular function, such as accurate wave propagation and reflection phenomena along vessels. Evidently, as happens with 1D models, 0D models are completely unable to provide spatial information about the fields.

Dimensionally-heterogeneous models The use of dimensionally-heterogeneous models is being seen with increasing frequency in the specialized literature due to the natural ability to couple the best of both worlds. This type of models are capable of coupling the advantages of 3D models ,concerning the predictive capabilities to accurately simulate a region of interest, and reduced 1D/0D/2D models to deal with the surrounding vascular domains or even the whole cardiovascular system where simplistic hypotheses are reasonable ([Formaggia et al. 2001, Lagana et al. 2002, Urquiza et al. 2006, Blanco et al. 2009, 2010]).

The main attractive of this class of models is the coupling between reduction of complexity and high predictive capabilities provided by 3D models focused only on some selected regions of interest, see Figure 1.4, dealing at the same time with the complex problem of imposing boundary conditions when such 3D portion of the arterial system has been isolated from the rest of the system to carry out numerical simulations. Nevertheless, in this approach the 3D regions of interest are limited to small regions of the cardiovascular system, being that, as explained above, large 3D simulations are still prohibitive in real life problems.

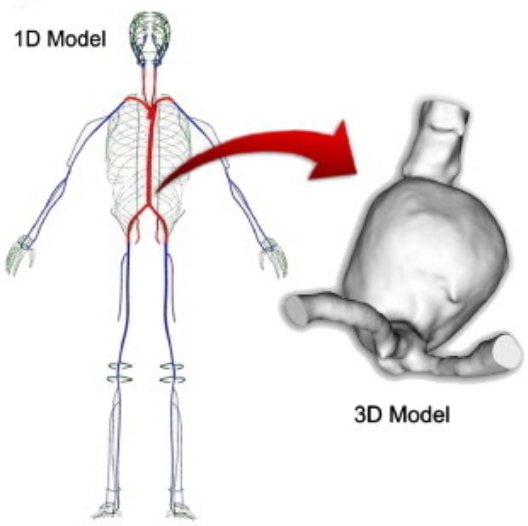

Figure 1.4: Coupling of dimensionally-heterogeneous models. A three-dimensional region is coupled to a 1D model. Figure extracted from [Blanco et al. 2009].

1.2 Numerical techniques for the 3D fluid flow

The predictive capabilities of the dimensionally reduced models are, at some level, restricted by the kinematic assumptions considered for their formulation, if compared with the full three-dimensional Navier-Stokes equations. As said, these reduced models are able to provide excellent insight about the hemodynamics at different scales but completely fail to describe in detail the spatial behavior or heterogeneities in velocity/pressure fields.

The valuable information inherent to the three-dimensional Navier-Stokes equations, and particularly in the hemodynamics realm, together with the almost impossible task to analytically solve the problem in real patient-specific geometries, makes it mandatory to develop numerical strategies able to provide approximate solutions with significant information about flow-related entities which can be useful in medical practice.

From the practical point of view, two major characteristics concerning the choice of a numerical method for hemodynamics applications are the accuracy in the approximate solution and the computational burden associated to the numerical simulation. This dichotomy between accuracy and efficiency has inspired the development of several strategies aiming to improve the quality in one or both of these aspects. In this section we present a brief classification of the most representative numerical strategies in computational hemodynamics based on the counterbalance between accuracy and efficiency:

(i) Methods based in the concept of elements. General enough to be applied in several areas of scientific computing and to which the accuracy and computational cost are strongly correlated. And

(ii) Goal-oriented strategies. Here the sophistication of the numerical approximation is substantially higher by employing efficient techniques for the approximation spaces, but that at the same time reduce the range of applicability.

We will present the following strategies focusing solving the spatial description of the physical fields we are interested in, leaving the time dependence treated by a general time-advancing scheme, constructing the solution at the time $t^{n+1} = t^n + \Delta t$ based on the approximation of the field obtained at previous time steps.

1.2.1 General purpose element-based methods

The most traditional alternatives to numerically solve the Navier-Stokes equations are based on a subdivision of the computational domain Ω into a grid. The solution is approximated by the field u_h which depends on a finite number of parameters as, for example, the values of the approximation at the nodes of the grid. The index h in the approximation stands for an indicator of the grid refinement and drives the accuracy of u_h and also the computational burden associated to the computing of the approximation. Further details of these approaches can be found in [Morton and Mayers 2005, Quarteroni and Valli 2008, Thomas 2013].

Four general approximating strategies (Finite difference method, finite element method, finite volume method and spectral element method) are briefly described here, exposing the main characteristics of each method and highlighting the existing dependence between the accuracy and the size of the problem at the discrete level.

Finite difference method Possibly, the first technique adopted for spatial discretization, the finite difference method (FDM), approximates the solution u_h in the nodes of the computational grid as the solution of the system of equations generated by replacing the differential operators, in the strong formulation of the problem, by finite differences. This discrete equivalence between a differential operator $\mathcal{L}$ and finite differences, is performed through the concept of *stencils*, approximations of the type

$$\mathcal{L}u(\mathbf{x}_i) \approx \sum_{j=1}^{N} \alpha_i u(\mathbf{x}_j) \tag{1.3}$$

where the value of $\mathcal{L}u(\mathbf{x}_i)$, with $\mathbf{x}_i$ a selected node in the grid, is approximate based on the value of the field u at selected neighbor nodes.

Different stencils can be proposed by each differential operator, modifying the structure of the resulting linear system as well as the convergence properties, but generally the accuracy is strongly correlated with the grid spacing h, that is, the finest the mesh the better the quality of the approximation.

Currently, these techniques are little employed mainly due to the difficulty to construct stencils for non uniform and unstructured meshes. Even so, some applications of the FDM in computational hemodynamics can be found in the literature ([Tang et al. 2001, Peyret and Taylor 2012]).

Finite volume method Proposed for problems that can be recast in a conservation form, i.e. problems of the form

$$\operatorname{div} \mathbf{F}(u) = f \tag{1.4}$$

where $\mathbf{F}$ is the flux vector, the finite volume method (FVM) is based on a domain division into the so-called *control volumes* where the physical field u is approximated by the solution of a system of linear (or non-linear) equations obtained by integrating within each control volume C the conservation equation and by employing the relation

$$\int_C \operatorname{div} \mathbf{F}(u)\, d\mathbf{x} = \int_{\partial C} \mathbf{F}(u) \cdot \mathbf{n}\, d\gamma \approx \sum_j \mathbf{F}_j(u_h) \cdot \mathbf{n}_j \tag{1.5}$$

where $\mathbf{F}_j$ is an approximation of the flux vector on the j-th side of C, and $\mathbf{n}_j$ is the corresponding normal vector. Naturally, the size of the discrete system depends on the number of control volumes considered.

Establishing a parallel with the FDM, explained before, if we introduce the parameter h as being the maximum size of the control volumes we can relate the accuracy in the FVM with the value of this parameter: The smaller h the more accurate the approximation and the greater the computational cost. A detailed description of the FVM in computational fluid dynamics can be found in [LeVeque 2002, Versteeg and Malalasekera 2007].

Finite element method The most widely used spatial discretization technique in the computational mechanics domain, the Finite Element Method (FEM), is based on the discretization of the geometrical domain into subregions called *finite elements* and on the variational formulation of the physical problem stated in general form as follows: Find $u \in \mathcal{U}$ such that

$$a(u, v) = F(v) \qquad \forall\, v \in \mathcal{V} \tag{1.6}$$

with suitable spaces for the field and where $\mathcal{V}$ is the generator of the linear manifold $\mathcal{U}$. Lets assume, without loss of generality, that $\mathcal{U} = \mathcal{V}$.

The discrete counterpart to this problem is obtained by replacing the space $\mathcal{V}$ with a finite-dimensional space $\mathcal{V}_h = \text{span}\{\varphi_i, i = 1, \ldots, N_h\}$. Hence, assuming the linearity of the form $a(\cdot, \cdot)$, the continuous problem can be written in the form of a linear system of equations $\mathbf{Au} = \mathbf{b}$, where

$$\mathbf{A}_{ji} = a(\varphi_i, \varphi_j) \qquad \mathbf{b}_j = F(\varphi_j) \tag{1.7}$$

For the FEM, the finite-dimensional spaces $\mathcal{V}_h$ are constructed taking into account the discretization of the computational domain into a grid, defining the space as generated by piecewise polynomials with compact support and a given degree within each element. Numerical and mathematical properties, different types of meshes and variants of the finite-dimensional spaces are largely studied at literature, exposing their high potentialities in the fluid mechanics domain, including the field of hemodynamics ([Zienkiewicz and Taylor 1977, Girault and Raviart 1986, Perktold et al. 1991, Taylor et al. 1998a, Cebral et al. 2002]).

In FEM, the computational cost is directly dependent on how fine the discrete mesh is. Denoting by h the characteristic size of the finite elements employed to construct the mesh, the accuracy (and also the computational burden) is also correlated with this value. As happens with the FVM and FDM, the smaller the value of h the better the approximation but at the same time the higher the computational cost and, for real large-scale hemodynamics simulations, this may become an insurmountable difficulty.

Spectral approaches The last approach briefly described here is known as Spectral element method (SEM). Similarly to the FEM, the SEM is based on a discretization of the domain into finite subdomains and the construction of finite-dimensional spaces where the approximated solution is sought. The main difference between these two approaches is the way in which the basis functions for $\mathcal{V}_h$ are constructed.

The approximate solution in the SEM is commonly defined as a truncated Fourier series defined in the whole domain or with piecewise polynomials of high order. For a fixed mesh, the quality in the approximation is here defined by the chosen polynomial order `p`. High theoretical convergence rates can be obtained for the SEM, achieving exponential convergence in some cases, in situations where the solution is regular enough, which is a condition often unreachable for most real problems. Further details for SEM can be found in [Canuto et al. 1988, Maday and Patera 1989, Bernardi and Maday 1997, Karniadakis and Sherwin 2013].

1.2.2 Goal-oriented strategies

Although the excellent capabilities of the general purpose methods described before, the accuracy in the solution directly depends on the problem size, sometimes achieving unpractical requirements in terms of physical resources and computational effort to solve the problem [Grinberg et al. 2009, 2011].

In this regard, the development of computationally cheap flow models (cost of the order of solving reduced-order approaches as the 1D model) capable of predicting flow-related quantities accurately (accuracy of the order of 3D models solved with high-fidelity methods) is of the utmost relevance for academic studies and for their translation into clinical practice [Quarteroni et al. 2001, Formaggia et al. 2009, Peiró and Veneziani 2009].

Order-reduction techniques A popular way to deal with the high computational cost involved in the approximation of the three-dimensional fluid flow problem is to express the approximate solution as a function of only a few well selected modes. Among the strategies within this class, there are two popular choices: *Proper Orthogonal Decomposition* (POD) and *Reduced Basis* (RB) methods. POD techniques, introduced in [Lucia et al. 2004] in the context of fluid dynamics, reduce the dimensionality of a system by transforming the original unknowns into a new set of N_r variables such that the first few modes retain most of the physical phenomena in the problem. Basically, the method relies on the approximation of the solution by a linear combination of some spatial modes computed after offline simulations. On the other hand, the goal of the Reduced Basis technique is to compute a low-dimensional approximation by seeking a linear combination of well-chosen solutions corresponding to specific choices of certain parameters of the problem [Patera and Rozza 2007].

Both of them (POD and RB techniques) are based on a strong offline-online paradigm, share several features and have an extensive theory behind them that allow their application in several fields (see for example, [Quarteroni and Rozza 2014]), but the linear nature of these methods together with the high computational cost of the offline step make them unpractical for the current goal of simulating the blood flow in patient-specific 3D geometries in a cheap and accurate way.

Hierarchical modeling techniques Another very useful way to obtain reduced models is based on an *a priori* definition of the behavior of the physical model across certain physical spatial direction. The main idea behind these techniques is that the physics in the problem is dominantly determined across a certain dimension of the domain where the physics unfolds. By adopting different approximation strategies for the different spatial dimensions one can reduce the dimension of the problem, just as a 3D solid can become a 2D plate/shell or a 1D beam/bar under certain hypotheses [Kraus 1967].

In recent years, a methodology called Hierarchical Modeling (HiMod) has refloated this idea in the general context of elliptic problems [Ern et al. 2008]. In such cases, based on the presence of a spatial dimension that predominates over the others, the authors propose a hybrid numerical approximation to the problem by combining finite element functions for the dominant direction with spectral approximants for the transversal directions. Since its appearance, many theoretical contributions of the HiMod method have been reported. For example, in [Perotto et al. 2010], the HiMod method was combined with domain decomposition strategies to allow for different degrees of spectral approximation in different regions of the domain of analysis. In turn, in [Perotto and Zilio

2013], different numerical approaches are presented towards performing the reduction of the problem using modal functions. More recently, in [Perotto 2012, 2014, Perotto and Veneziani 2014] several procedures to select the number of modal functions in an automatic manner are discussed.

In 2014, Guzzetti [Guzzetti 2014] showed the first application of the HiMod method to approximate the Navier-Stokes equations but still restricted to academic cases, thus highlighting the potentialities of HiMod in the domain of computational hemodynamics and also pointing the difficulties to be circumvented in order to accomplish this task for real life problems.

1.3 Objectives

Current limitations of the numerical techniques together with academical and medical needs point out the need for the development of efficient numerical schemes to be employed in computational hemodynamics. The main goal of this thesis work is to contribute towards the translation of scientific computing into the clinic through the development of a new numerical approximation for the three-dimensional Navier-Stokes equations, especially tailored for computational hemodynamics.

This new methodology, coined as Transversally Enriched Pipe Element Method (TEPEM) is aimed at filling the gap between (cheap) 1D models and (computationally expensive) full 3D models. Furthermore, is provided solid evidence of the numerical capabilities while offering a substantial reduction in the computational burden when addressing patient-specific blood flow simulations.

Accomplishing this major goal, implies in several specific goals also addressed along this work and which are listed below.

- **TEPEM definition**

  (1) Regarding the geometry, a novel geometrical meshing strategy is proposed in order to exploit the pipe-like structure of the domains of interest. Also, suitable geometric mapping is described which features enough accuracy for the problems under consideration.

  (2) High order field interpolants are constructed, and accurate numerical integration recipes are proposed and employed.

  (3) As for the computational implementation of TEPEM, this is carried out into the same distributed computing framework in which FEM is also implemented in order to report consistent comparisons between these methodologies utilizing the same computational paradigm.

- **Scalar transport problems**

  (1) The study of the TEPEM approach in the approximation of elliptic problems is first addressed. Here we focus on situations which follow the main hypotheses: pipe-like domain of definition and presence of mainstream direction.

  (2) Numerical verification of TEPEM capabilities is reported using controlled geometries and compared to standard FEM solutions.

- **Fluid-flow problems**

  (1) Study of combinations for the approximation spaces for velocity and pressure is performed, as well as the investigation into the inf-sup stability condition.

  (2) Numerical verification for velocity, pressure and also derived indexes such as wall shear stress in stationary and transient cases is presented by using analytical and reference FEM solutions.

- **Patient-specific hemodynamics**

  (1) A study of pipe meshing strategies to guarantee a similar TEPEM topology in comparison with real vascular domains is performed.

  (2) The establishment of a computational pipeline to perform a semi-automatic discretization of patient-specific geometries and deliver a pipeline discrete mesh is described.

  (3) Implementation of boundary conditions, classical boundary conditions as dictated by hemodynamic problems, within the TEPEM scope is also developed.

  (4) The verification of the approach in several patient-specific hemodynamic situations and for increasing large-scale arterial structures is performed.

The computational implementation of this novel formulation to solve elliptic problems (Section 3), Navier-Stokes equations (Section 4) as well as the corresponding boundary conditions for hemodynamic simulations (Section 5.2) was executed in the context of an in-house general purpose parallel solver called *SolverGP* ([Urquiza and Vénere 2002]), and which is under continuous development by the HeMoLab research group [HeMoLab 2015].

1.4 Thesis structure

Aiming at a comprehensive presentation of the TEPEM, their potentialities in large-scale hemodynamic simulations and looking into the list of specific goals appointed in the previous section, this document is outlined in the following way:

- **Chapter 2**. This chapter is focused in the introduction of the basic ingredients for the definition of the proposed methodology. The geometric setting, reference element, physical interpolants as well numerical details that are relevant for the computational implementation are described for the two- and three-dimensional versions of the TEPEM. The algebraic structure rendered by the proposed method is here detailed in a general scope without further restrictions than that established by a pipe-like domain of analysis and a dynamics with a clear dominant direction.

- **Chapter 3**. Although the motivation behind the TEPEM is its application in computational hemodynamics, it is actually a general methodology that can be applied for the simulation of several problems whenever assumptions in the geometry and the presence of a dominant direction hold. In this sense, this chapter is devoted to studying the performance of the TEPEM when applied to advection-diffusion-reaction problems. The discrete structure of the resulting

algebraic system is presented and the numerical advantages in certain situations over classical finite element approaches are studied and discussed in relation to the accuracy of the solution as well as to the problem size.

- **Chapter 4**. In this chapter, the application of the TEPEM to the numerical approximation of the Navier-Stokes equations is studied. The definition of feasible finite-dimensional spaces for velocity-pressure fields as well as a numerical approach for the inf-sup condition are presented. Finally, several numerical examples that demonstrate the model predictive capabilities in two and three dimensional problems are documented. The numerical examples reported in this chapter are defined in synthetic domains in order to develop a controlled convergence study.

- **Chapter 5**. As said before, utilizing the TEPEM in complex patient-specific geometries requires the development of new, although simple, meshing algorithms for a precise approximation of the topology based in pipe-type elements. In this chapter we present: (i) a geometrical pipeline able to discretize patient-specific structures from the image segmentation step to a final pipe-based mesh and (ii) a discussion of different boundary conditions suitable for hemodynamic simulations and their implementation in the scope of the TEPEM. The chapter is finalized with several numerical simulations with increasing complexity.

- **Chapter 6**. The contributions, open problems and future works related with the context brought by the TEPEM are summarized in this final chapter.

1.5 Scientific contributions

Relevant results obtained from this work were presented in the form of manuscripts published in indexed journals as well as articles in conference proceedings.

Articles in peer-reviewed journal. Three papers were submitted to indexed journals. These works, listed as references [Blanco et al. 2015, Mansilla Alvarez et al. 2017a, 2018-submitted] at the bibliography chapter, cover in detail the development of TEPEM from 2D to 3D cases, the application on patient-specific geometries (including domains with several bifurcations) as well as an extensive comparison between TEPEM and FEM in terms of accuracy and computational burden. These works are listed below.

- P.J. Blanco, L.A. Mansilla Alvarez, R.A. Feijóo. *Hybrid element-based approximation for the Navier-Stokes equations in pipe-like domains*. Computer Methods in Applied Mechanics and Engineering, v. 283, p. 971-993. 2015.

- L.A. Mansilla Alvarez, P.J. Blanco, C.A. Bulant, E.A. Dari, A. Veneziani, R.A. Feijóo. *Transversally Enriched Pipe Element Method (TEPEM). An effective numerical approach for blood flow modeling*. International Journal for Numerical Methods in Biomedical Engineering, v. 33, n. 4. 2017.

- L.A. Mansilla Alvarez, P.J. Blanco, C.A. Bulant, R.A. Feijóo. *Towards fast hemodynamics simulations in large-scale circulatory networks*. Submitted to Computer Methods in Applied Mechanics and Engineering.

Articles in conference proceedings. Some preliminary results reporting the consolidation of the TEPEM as an efficient numerical methodology were presented in national and international conferences. These works, referenced as [Aletti et al. 2014, Mansilla Alvarez et al. 2015, Aletti et al. 2016, Mansilla Alvarez et al. 2017d,c,b, 2018], also reflect the collaboration with other strong research groups in the same field.

- M. Aletti, L.A. Mansilla Alvarez, P.J. Blanco, S. Perotto, A. Veneziani. *Hierarchical model (HiMod) reduction for incompressible fluid dynamics in rigid and deformable pipes*. In: WCCM 2014, World Congress on Computational Mechanics, 2014, Barcelona.
- L.A. Mansilla Alvarez, P.J. Blanco, R.A. Feijóo. *Pipe-oriented finite elements for the three-dimensional blood flow simulation*; In: USNCCM13, US National Congress on Computational Mechanics, 2015, San Diego.
- M. Aletti, L.A. Mansilla Alvarez, P.J. Blanco, S. Guzzetti, S. Perotto, A. Reali, P. Rusconi, A. Veneziani. *Hierarchical Model Reduction Methods for Incompressible Fluids: Basics, IsoGeometric formulation, Applications*. In: HOFEIM 2016. High Order Finite Element and Isogeometric Methods, 2016, Jerusalem.
- L.A. Mansilla Alvarez, P.J. Blanco, R.A. Feijóo. *Fast patient-specific blood flow simulations: The transversally enriched pipe element method (TEPEM)*. In: EMI 2017. 3rd Engineering Mechanics Institute International Conference, 2017, Rio de Janeiro.
- L.A. Mansilla Alvarez, P.J. Blanco, R.A. Feijóo. *An efficient method for the numerical solution of blood flow in 3D bifurcated regions*. In: CNMAC 2017. XXXVII Congresso nacional de matemática aplicada e computacional, 2017, São José dos Campos.
- L.A. Mansilla Alvarez, P.J. Blanco, C.A. Bulant, R.A. Feijóo. *Fast blood flow simulation in three-dimensional arterial trees*. In: CILAMCE 2017. XXXVIII Ibero-Latin American Congress on Computational Methods in Engineering, 2017, Florianópolis.
- L.A. Mansilla Alvarez, P.J. Blanco, R.A. Feijóo. *On enhanced reduced models for advection-diffusion problems*. In: EAMC 2018. XI Encontro Acadêmico de Modelagem Computacoinal, 2018, Petrópolis.

Chapter 2

The Transversally Enriched Pipe Element Method

One of the major challenges in modern scientific computing is the controlled reduction of the computational cost without sacrificing accuracy. The improvement of computing strategies, architectures and massive use of high performance computing (HPC) facilities is only a partial answer to this need [Grinberg et al. 2009], turning mandatory the coupling between HPC strategies with novel customized models that can effectively provide the trade off between efficiency and accuracy. As discussed in the introduction, most of the numerical methodologies aimed at reducing the computational cost, achieve this in detriment of substantial loss in the spatial description of the physical fields or even reducing its versatility, not being applicable to complex patient-specific geometries. It is evident the need to work in the development of new methodologies capable to deal with the following three aspects:

(i) Reduction of the computational burden. Understanding this as computational time and physical resources needed to perform numerical simulations.

(ii) Capacity to provide spatially detailed information of hemodynamics fields: Focusing in an proper description of the spatial heterogeneities of flow-related quantities such as wall shear stress (WSS).

(iii) Versatility so that they can be applied to complex domains as those appearing in the cardiovascular network, specially, in the case of patient-specific vascular regions.

In this scenario, the Transversally Enriched Pipe Element Method (TEPEM) emerges as an attempt to find a practical trade-off between the accuracy of 3D modeling and the efficiency, in terms of diminished computational burden, of reduced-order models. This methodology is specially designed for problems in computational hemodynamics and deals with the three key aspects commented in previous paragraph by making use of *a priori* knowledge in its conception. This *a priori* knowledge consists of two natural assumptions for our field of study: (i) As for the geometrical domains we are interested in, the blood flow mainly occurs (except within the heart) in a large network of pipes and (ii) In these inter-connected tubular regions, the flow is basically one-dimensional, that is, it flows dominantly across the axial direction of each pipe. However, the transversal dynamics is in many cases important to be retained, and this will naturally be accounted for through the field interpolants constructed in the pipe elements.

In this chapter, we present the basic ideas and key ingredients behind the proposed approach in the two- and three-dimensional cases. As a novel methodology, aspects related to the geometrical description of the computational domains, the field interpolation strategy and finite-dimensional spaces defined for the discrete approximation are described in detail in this chapter. The TEPEM fundamentals closely follow the ones observed in classical FEM: starting from the variational formulation of the physical problem, and based on a partition of the domain of analysis, each physical field is approximated by a function living in a finite-dimensional space and computed as the solution of a problem defined by the collection of local contributions. Because of this similarity, and for ease of clarity in this chapter, each component in the TEPEM will be introduced while performing a comparison between the proposed approach and the analogous component in the context of the FEM. Some comments on mesh generation, numerical details in the TEPEM implementation and relation with some other methodologies are also addressed.

2.1 An interpolation problem

To expose the idea of *dominant direction* and the way in which the TEPEM proposal tackles problems with this characteristic, let us focus first in an interpolation problem on a two-dimensional domain. Let $\Omega = [-2, 2] \times [-0.25, 0.25] \subset \mathbb{R}^2$ denote the domain of analysis, then the function to be interpolated is defined as:

$$\begin{array}{rl} u: & \Omega \to \mathbb{R} \\ & (x, y) \mapsto u(x, y) = f(x)g(y) \end{array} \tag{2.1}$$

where

$$\begin{aligned} f(x) &= (1 - 0.25x^2)\cos(6\pi x)\exp\left(-\pi x^2\right) \\ g(y) &= 1 - 16y^2 \end{aligned}$$

This function, displayed in Figure 2.1 together with each component $f(x)$ and $g(y)$, has a more complex dynamic over the $x-$axis when compared with the dynamics over the $y-$axis: While, for a fixed value $x = x_0$, the solution is simply a quadratic function, the opposite case (the behavior for $y = y_0$) is more complicated to be expressed as a simple polynomial function. This quality of one direction being more "interesting" than other (or others, in the 3D case) is directly related with what we call as *dominant direction*: The direction, not necessarily aligned with a coordinate axis, which presents more information of the dynamics than the others. Hereafter, this main direction will be referred to as *axial direction* in contrast to *transversal direction* for the other directions. However, we note here that we do not want to completely miss the important information contained in the transversal component of the function. Going back to the interpolation problem, let us focus on the following two approaches: (i) an interpolation on an uniform triangular mesh, considering linear piecewise basis functions with the exact value at each mesh node; and (ii) a spectral interpolation with Ω as a single domain and Fourier basis with coefficients that ensure a best approximation in a finite dimensional space. The intention is to know how difficult is, for each case, to obtain a visually precise approximation and the number of parameters required in each case.

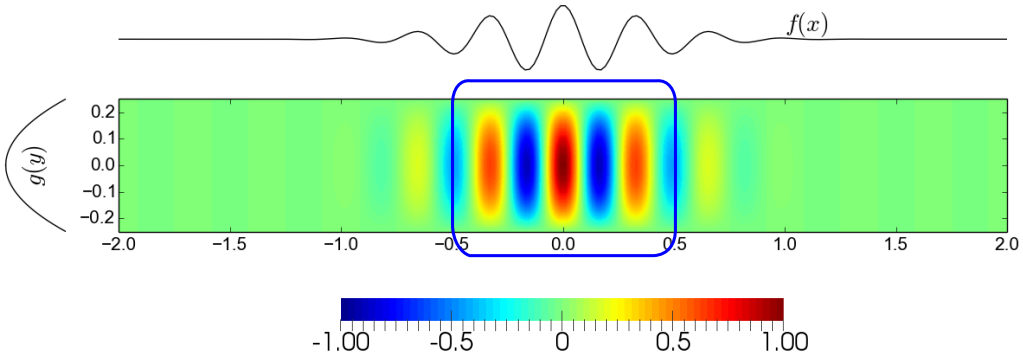

Figure 2.1: Function to be interpolated and their horizontal and vertical components. The region $[-0.5, 0.5]\times[-0.25, 0.25]$ (delimited in blue) is employed for a detailed examination of the interpolation strategies.

The first approach consists in piecewise interpolating the function in an analogous way using a classical finite-dimensional space utilized in a typical finite element methodology: For a fixed triangular partition $\mathcal{T}_h$ of Ω we will compute the values of $u(x, y)$ at each mesh node (vertices of every triangle on the partition) and the interpolant function will be constructed as a linear piecewise function in each triangle and with these values. In other words, the interpolant function (u_h) will be defined as the only function coincident with the function $u(x, y)$ on each vertex of each partition element and belonging to the finite-dimensional space:

$$\mathcal{U}_h = \{u \in C^0(\Omega) : u|_\tau \in \mathbb{P}_1,\ \forall \tau \in \mathcal{T}_h(\Omega)\}. \tag{2.2}$$

The parameter h, which characterizes the partition, stands for a characteristic size of the elements composing the partition of Ω into the triangular elements. Reducing the element size, the approximation (interpolant function in this case) becomes naturally more accurate but, at the same time, the problem size and computational cost increase. Let us start considering a coarse mesh, composed by 922 nodes and 1 662 triangular elements, and let us successively refine this mesh until we obtain a satisfactory result. In Figure 2.2 we show the interpolant function, focused on the central region of Ω, obtained with four different meshes. As expected, it is clear the improvement in the interpolant obtained with each mesh refinement. It was necessary approximately 34 000 nodes (vertices) to obtain a (visually) accurate interpolant function, this quantity increases considerably when thinking of 3D problems. It is important to note that we are using uniform meshes without taking advantage of any a priori knowledge of the original function. Different mesh types (composed by quadrilateral or hexagonal elements, among others) can equally be employed but with the same qualitative result: A better interpolation is linked with an increase on the number of elements (therefore, number of vertices or nodes), needing a large quantity of these for a satisfactory result.

On the other hand, opposedly to the use of not-so-regular piecewise polynomial functionals, we have the idea of using regular functions to devise a spectral interpolation. Instead of a partition, for the single domain case of the spectral method, we consider the whole domain as a unique element where a finite-dimensional space is defined and which is spanned by, typically, a family of continuous functions such as polynomials, trigonometric functions, etc.

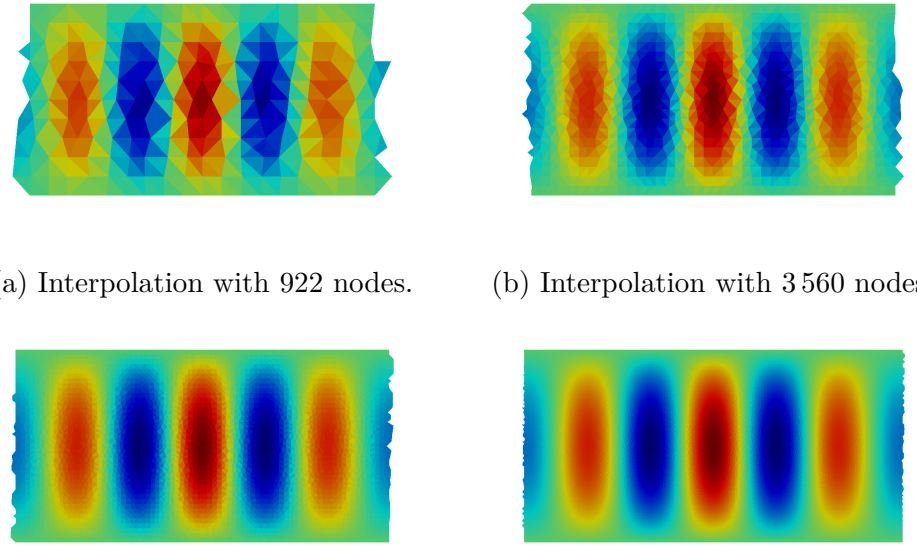

(a) Interpolation with 922 nodes. (b) Interpolation with 3 560 nodes.

(c) Interpolation with 14 214 nodes. (d) Interpolation with 34 264 nodes.

Figure 2.2: Linear interpolation, using FEM, over different triangular meshes with increasing number of nodes (vertices). The comparison is focused in the center region of the original domain (blue region in Figure 2.1).

The cost in the spectral case is given by the quantity of elements utilized to form the basis to get a good interpolation, the more elements spanning the discrete space the more accurate will be the interpolant function but, at the same time, more computationally expensive will be the calculation of the parameters needed by the interpolant. These parameters are the coefficients, in the linear combination of the elements on the space basis, which define each function in the space. Without loss of generality, a basis related to the Fourier series will be chosen to generate the finite-dimensional space. Indexed by the parameter $m \in \mathbb{N}$, we define the discrete space where the interpolant lives as $\mathcal{U}^m \times \mathcal{U}^m \subset C^0(\Omega)$, where

$$\mathcal{U}^m = span\{\sin(i\pi x), \cos(i\pi x) : i = 0, \ldots, m\}. \tag{2.3}$$

As happened in the previous piecewise polynomial approach, it is important to emphasize that no special consideration is taken into account to choose the basis functions. For each $m \in \mathbb{N}$, the interpolant function u_m has a form

$$u_m(x, y) = \left(\sum_{i=0}^{m} a_i^s \sin(i\pi x) + a_i^c \cos(i\pi x) \right) \left(\sum_{j=0}^{m} b_j^s \sin(j\pi y) + b_j^c \cos(j\pi y) \right) \tag{2.4}$$

That is, a total of $(2m + 1)^2$ parameters obtained via solving a linear system yielded from by inner product of $u(x, y)$ with each element of the basis. In Figure 2.3 we show the interpolating function for increasing values of m, this is, each time a larger space. As expected, a better interpolation is obtained when increasing m but with a number of unknowns around 1 100 and without considering the needed of assembling and solving the system of equations associated to the coefficients.

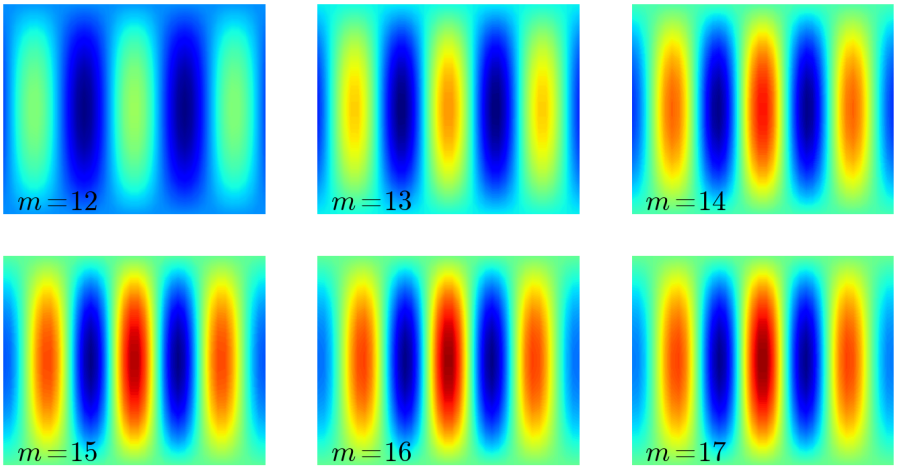

Figure 2.3: Interpolation using the spectral method and the same number of modes for each direction (axial and transversal). The total number of degrees of freedom is equal to $(2m+1)^2$. The comparison is focused in the center region of the original domain (blue region in Figure 2.1).

The interpolation problem is closely related to solving problems such as the Laplace equation via classical finite element method or spectral-type strategies. In both approaches the solution is sought in a finite-dimensional space, and the discrete problem becomes the problem of solving a linear algebraic system. This approximate solution shares similar properties shown above:

(i) For the classical finite element method, the solution is as accurate as the mesh size allows, sometimes needing several refinements to get the desired precision.

(ii) For spectral methods, the approximate solution improves in accuracy when increasing the number of elements in the basis; generally a large quantity of elements are needed to correctly approximate a complexly behaved function, as seen above.

In both cases, a good approximation demands a large number of unknowns and an elevated computational cost.

Back to the inteprolation problem, a possible way to reduce the computational cost, number of unknowns and, therefore, the size of the linear system, but keeping accurate results is to take into account the presence of a dominant direction in the function to be interpolated. As the behavior on the axial direction ($x-$axis) is more complex than the other it seems reasonable to treat independently the space on where interpolate the axial component and the space where the transversal component lives. For example in the spectral approach case, we can interpolate the function in the discrete space $\mathcal{U}^m \times \mathcal{U}^3 \subset C^0(\Omega)$ keeping accurate results (as shown in Figure 2.4) and reducing considerably the computational cost. Although the transversal behavior is satisfactorily interpolated in $\mathcal{U}^3$ (with a reduction up to five times than the original interpolation on $\mathcal{U}^m$), the axial component still requires a large number of basis functions to get an accurate result.

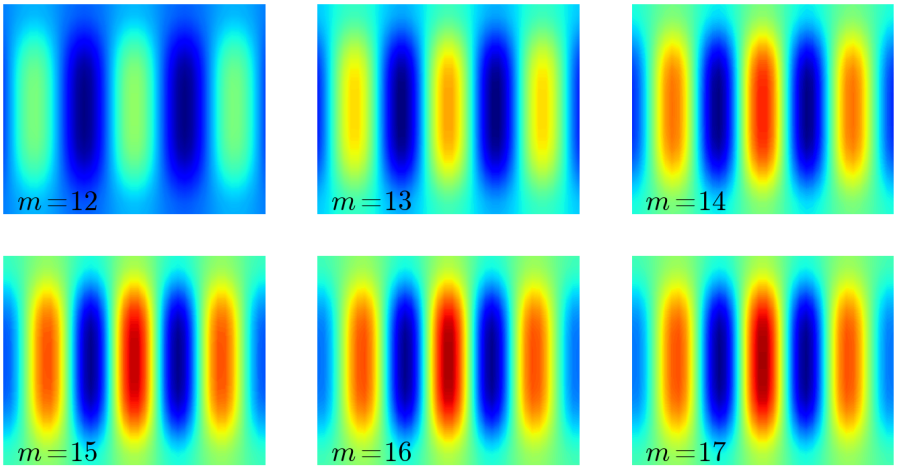

Figure 2.4: Interpolation with different number of modes for each direction: three for the transversal direction and m for the axial direction. The total number of degrees of freedom is equal to $7(2m+1)$. The comparison is focused in the center region of the original domain (blue region in Figure 2.1).

The TEPEM approach is based on the idea of diversifying the choice for the axial and transversal interpolating functions. Using the *a priori* knowledge of the presence of a dominant direction, we approach each component (axial and transversal) through different ways as dictated by physical and also practical issues.

The transversal component is hypothesized to be less complex because the physics is confined to unfold in the cross-section of the domain of analysis which, in general, precludes large variations of the fields from occurring. Therefore, we postulate that the approximation can be effectively achieved by using a few number of high-order interpolants. To be more general, we choose high-order Lagrange polynomials for this component instead of trigonometric functions, which are more difficult to be dealt with at the implementation level. Concerning the axial component, a low-order polynomial interpolation is employed due to its versatility and capacity of correctly approximating complex patterns.

It is clear than neither a classical triangular partition nor considering the whole domain as a single element correspond to the proposed interpolation splitting. That is, the partition must be adapted in order to accommodate aligned finite elements necessary to interpolate the axial direction with crossing mono-elements to account for the spectral interpolation in the transversal direction. This special partition strategy, fundamental to the TEPEM scope, will be denominated as *pipe-type partition*, or equivalently *slab-type partition*, and can be understood as a first step to severely reduce the number of elements when compared with classical finite element meshes (as can be observed in the example in Figure 2.5). This type of partitioning, naturally allows a differentiation between the axial and the transversal directions which is fundamental to exploit the idea exposed above for tackling in an independent way the interpolation of each component (axial and transversal) of the physical field.

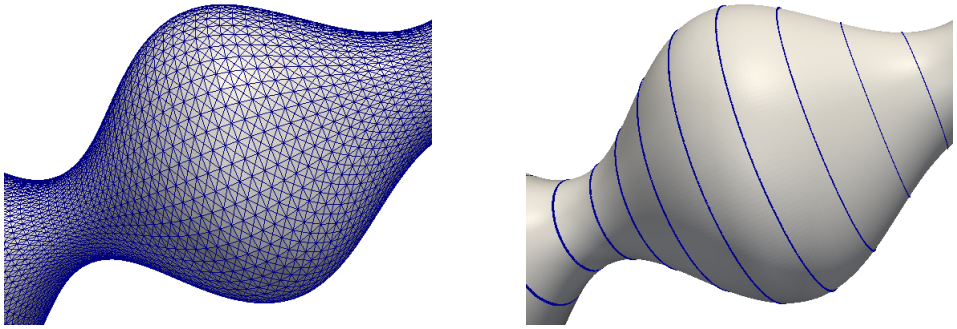

Figure 2.5: Comparison between FEM and TEPEM meshes. The FEM mesh (left) is composed by tetrahedral elements and TEPEM mesh (right) by slab-type elements.

The formalization of these ideas into an element-based methodology has been coined as Transversally Enriched Pipe Element Method, for being constructed based on a pipe-type domain discretization and for having the characteristic of effectively controlling the transversal predictive capabilities according to the problem needs.

Coming up next, we present the TEPEM ingredients in the context of a generic variational problem defined in a domain $\Omega \subset \mathbb{R}^d$ $(d = 2, 3)$. The variational equation reads as follows: Find $u \in \mathcal{U}$ such that

$$(\mathcal{R}u, \hat{u})_{\mathcal{Q}' \times \mathcal{Q}} = f(\hat{u}) \qquad \forall\, \hat{u} \in \mathcal{V}, \tag{2.5}$$

with the set of admissible solutions defined by

$$\mathcal{U} = \{u \in \mathcal{Q} : \mathcal{B}u = g\}. \tag{2.6}$$

Here the boundary operator $\mathcal{B}$ is related with the essential boundary conditions and $\mathcal{V}$ is the space of admissible variations. In this problem, $\mathcal{Q}$ is a functional space defined in Ω with its algebraic dual space $\mathcal{Q}'$, $(\cdot, \cdot)_{\mathcal{Q}' \times \mathcal{Q}}$ is a duality product defining the equilibrium and involving the (generic) operator $\mathcal{R}(\cdot) : \mathcal{Q} \to \mathcal{Q}'$. Moreover, assuming the case in which the case is linear and the essential boundary conditions are homogeneous, i.e. $g = 0$, the problem can be rewritten as: Find $u \in \mathcal{V}$ such that

$$a(u, \hat{u}) = f(\hat{u}) \qquad \forall\, \hat{u} \in \mathcal{V}, \tag{2.7}$$

where $a : \mathcal{V} \times \mathcal{V} \to \mathbb{R}$ is a bilinear form related to the (now linear) differential operator $\mathcal{R}$ and $f : \mathcal{V} \to \mathbb{R}$ is a linear functional. We also assume that the well posedness of the problem is guaranteed.

As it is usual in the literature [Ciarlet 1978, Atkinson and Han 2005, Brenner and Scott 2007], a $d-$dimensional finite element is defined as a triple $(\mathcal{K}_0, \mathcal{P}_0, \mathcal{N}_0)$, where

(i) $\mathcal{K}_0$ is a closed bounded subset of $\mathbb{R}^d$ with nonempty interior and a piecewise smooth boundary.

(ii) $\mathcal{P}_0$ is a finite-dimensional vector space of functions defined on $\mathcal{K}_0$.

(iii) $\mathcal{N}_0 = \{\phi_i, i = 1, \cdots, N\}$ is a basis of the dual space $\mathcal{P}_0'$.

The function space $\mathcal{P}_0$ is the space of the shape functions and the elements of $\mathcal{N}_0$ are the nodal variables (degrees of freedom). One of the most common choice for the degrees of freedom is the form $\phi \mapsto \phi(a_i)$ for each $\phi \in \mathcal{P}_0$ and where the points a_i belong to the finite element and are denominated as *nodes of the finite element*.

In the next section, the components of the finite element proposed in the TEPEM framework are detailed for the two-dimensional case while the three-dimensional case is addressed in Section 2.3. As previously commented, in the development of this methodology we consider two assumptions: A pipe-like structure is featured by the geometrical domain, and there is the presence of a mainstream direction where the physical phenomena is developed.

2.2 Basis functions in 2D

For the description of the approach in the two-dimensional case, we consider a pipe-like geometrical domain Ω, with boundary $\Gamma = \Gamma_i \cup \Gamma_o \cup \Gamma_L$, where Γ_i and Γ_o stand for the inlet and outlet boundaries, respectively, while Γ_L is the lateral boundary. Example of this type of geometry is outlined in the Figure 2.6

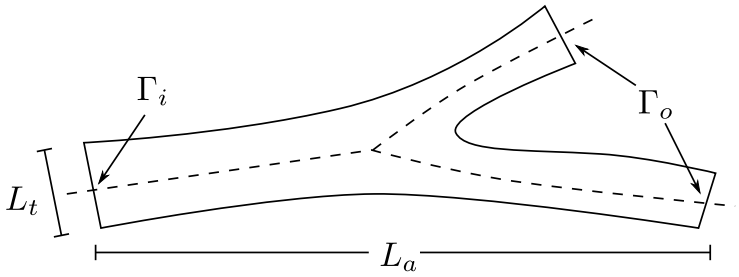

Figure 2.6: Geometrical setting for the TEPEM in 2D. The dotted line stand by the centerline while the lateral boundary Γ_L is defined as $\Gamma_L = \Gamma - \{\Gamma_i \cup \Gamma_o\}$.

We also assume that axial boundaries Γ_i and Γ_o are planar surfaces, while Γ_L is a piecewise smooth boundary. This geometric structure is inspired in the geometries of application we are interested in: domains representing isolated arterial segments where the characteristic axial length (L_a) is much larger than the transversal length (L_t) and where the centerline (dotted line) defines the mainstream direction in each tubular region. Domains with multiples inlet/outlet boundaries are also allowed.

2.2.1 Geometrical setting: Parallelogram elements

In the context of classical finite element approach, domains are partitioned by using triangular or quadrilateral elements due their flexibility in representing arbitrary geometries. Commonly, focusing on the case of triangular meshes, the computational domain is divided through a structured or unstructured mesh composed by several small elements forming the triangulation.

In the TEPEM approach, we make use of the pipe-like structure of the geometry to propose a sort of clever, problem-oriented, discretization, capable of reducing the number of elements and exploiting the *a priori* knowledge about the existence of a dominant geometrical and phenomenological direction.

Let us first suppose $\Omega \subset \mathbb{R}^2$ as being a single tubular domain, i.e. a tubular region without branches nor inner holes. For this domain we perform a partition where each element K_i ($i = 1, \ldots, \mathrm{n_{el}}$) is a quadrilateral and the distribution of these elements is aligned with the dominant direction in the geometry, as outlined in Figure 2.7. In each element it is easy to differentiate both geometrical/phenomenological directions: dominant (axial) and secondary (transversal). This partitioned domain, which is denoted as $\mathcal{T}_h(\Omega)$, where the parameter h stands for the characteristic axial length of the elements, closely resembles a one-dimensional discretization and allows us to lump the transversal dynamic within a single (or, as can be seen next, a few) pipe element and turn the mesh refinement task into a very natural and direct process.

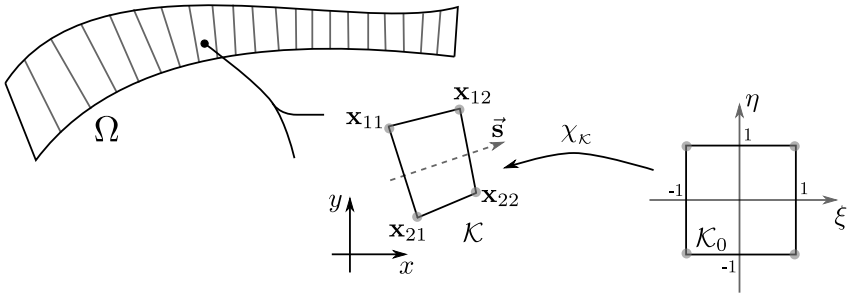

Figure 2.7: Geometrical discretization of domain Ω through pipe-type elements. Also, the geometrical mapping between an arbitrary element $\mathcal{K}$ and the reference element $\mathcal{K}_0$ is outlined. Vector $\vec{\mathbf{s}}$ correspond to the axial direction in the actual configuration.

Each pipe element $\mathcal{K}$ (in the xy-plane) is mapped to the reference element, $\mathcal{K}_0 = [-1, 1]^2$ in the $\xi\eta$-plane, through the following transformation

$$\chi_{\mathcal{K}}(\xi, \eta) = \sum_{i=1}^{2}\sum_{j=1}^{2} \mathbf{x}_{ij} L_i(\xi) L_j(\eta) = \sum_{i=1}^{2}\sum_{j=1}^{2} \mathbf{x}_{ij} G_{ij}(\xi, \eta) \tag{2.8}$$

where $\{\mathbf{x}_{ij}, i, j = 1, 2\}$ are the geometrical nodes in the element $\mathcal{K}$ and the set $\{L_1, L_2\}$ is the set of basis functions for the space of polynomials up to degree one (i.e. linear polynomials) defined in $[-1, 1]$ (space hereafter denoted as $\mathbb{P}_1$), this is

$$L_1(t) = \frac{1}{2}(1 - t), \quad L_2(t) = \frac{1}{2}(1 + t) \qquad t \in [-1, 1] \tag{2.9}$$

For such tubular domains, this meshing strategy is good enough to perform an accurate discretization while maintaining bounded the total number of elements when compared with classical triangulations.

Moving a step forward, it is also natural to think into the nesting of more than one pipe-element in the transversal direction either for the whole domain or for restricted areas of interest, a sort of local h-refinement of the mesh in the TEPEM scope. This process of transversal refinement is performed through the introduction of a *transition element*, which is capable of naturally densify (or condensate) pipe-type elements. Introduced in the two-dimensional case in [Gupta 1978] and largely explored in later works as for example [McDill et al. 1987, Morton et al. 1995], this element splits into two parts one axial boundary of the actual element configuration to achieve conformity in the mesh, as outlined in Figure 2.8.

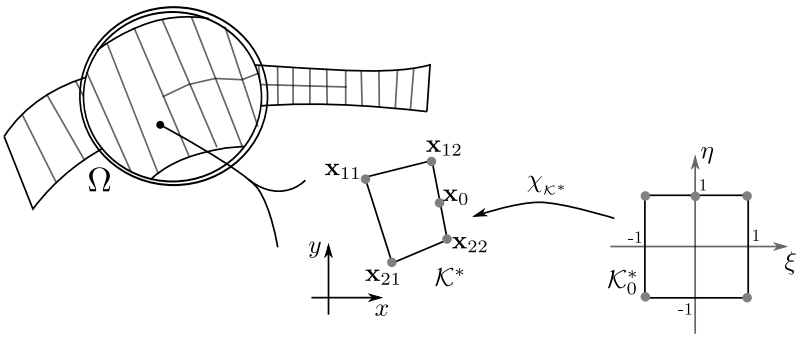

Figure 2.8: Detail of transversal refinement through the inclusion of a transition element. Also is outlined the geometrical mapping between a transition element $\mathcal{K}^*$ and the reference element $\mathcal{K}_0^*$.

The transition element is characterized by five geometrical nodes instead of the four nodes that characterize the *simple* pipe-element (here we use *simple* pipe-element to refer to the pipe element introduced in Figure 2.7). The mapping between the actual configuration of the transition element and the reference transition element $\mathcal{K}_0^* = [-1,1]^2$ is constructed to ensure that, by following the notation from Figure 2.8, the segment $[\mathbf{x}_{11}, \mathbf{x}_{21}]$ is mapped to the line $\{\eta = -1, -1 \leq \xi \leq 1\}$, the segment $[\mathbf{x}_{12}, \mathbf{x}_0]$ to $\{\eta = 1, -1 \leq \xi \leq 0\}$ and the segment $[\mathbf{x}_0, \mathbf{x}_{22}]$ into $\{\eta = 1, 0 \leq \xi \leq 1\}$. In other words, the geometrical mapping $\chi_{\mathcal{K}^*} : \mathcal{K}_0^* \to \mathcal{K}^*$ is defined as follows

$$\begin{aligned}\chi_{\mathcal{K}^*}(\xi,\eta) = {} & \mathbf{x}_{11} L_1(\xi) L_1(\eta) + \mathbf{x}_{21} L_2(\xi) L_1(\eta) \\ & + \mathbf{x}_{12} L_1(2\xi+1) \mathbb{1}_{\xi\leq 0}(\xi) L_2(\eta) + \mathbf{x}_0 L_2(2\xi+1) \mathbb{1}_{\xi\leq 0}(\xi) L_2(\eta) \\ & + \mathbf{x}_0 L_1(2\xi-1) \mathbb{1}_{\xi>0}(\xi) L_2(\eta) + \mathbf{x}_{22} L_2(2\xi-1) \mathbb{1}_{\xi>0}(\xi) L_2(\eta)\end{aligned} \tag{2.10}$$

where the function $\mathbb{1}_{\mathcal{I}}(t)$ stands for the characteristic function of the set $\mathcal{I}$, i.e. $\mathbb{1}_{\mathcal{I}}(t) = 1$ if $t \in \mathcal{I}$ and zero otherwise. This map can be expressed in a more compact way, similar with the simple pipe-element mapping, as:

$$\chi_{\mathcal{K}^*}(\xi,\eta) = \sum_{i=1}^{2}\sum_{j=1}^{2} \mathbf{x}_{ij} \tilde{G}_{ij}(\xi,\eta) + \mathbf{x}_0 \tilde{G}_0(\xi,\eta) \tag{2.11}$$

where

$$\begin{aligned}&\tilde{G}_{11}(\xi,\eta) = L_1(\xi) L_1(\eta) \qquad \tilde{G}_{12}(\xi,\eta) = L_1(2\xi+1) \mathbb{1}_{\xi\leq 0}(\xi) L_2(\eta) \\ &\tilde{G}_{21}(\xi,\eta) = L_2(\xi) L_1(\eta) \qquad \tilde{G}_{22}(\xi,\eta) = L_2(2\xi-1) \mathbb{1}_{\xi>0}(\xi) L_2(\eta) \\ &\tilde{G}_0(\xi,\eta) = (1-|\xi|)\, L_2(\eta)\end{aligned} \tag{2.12}$$

The use of transition elements within a pipe-like meshing procedure introduces several advantages not only as a strategy to provide local transversal refinement for the mesh but, primarily, to make possible the discretization of more complex geometrical domains such as, for example, branched or perforated domains.

For a domain Ω, being a junction of tubular regions, the meshing strategy is based on the identification of simple tubular regions which can be discretized in a straightforward way (as explained at the beginning of this section) and on the discretization of junction regions by employing a combination of transition and simple pipe elements. In Figure 2.9, two examples of the use of transition elements to perform a pipe-like discretization for complex domains are outlined.

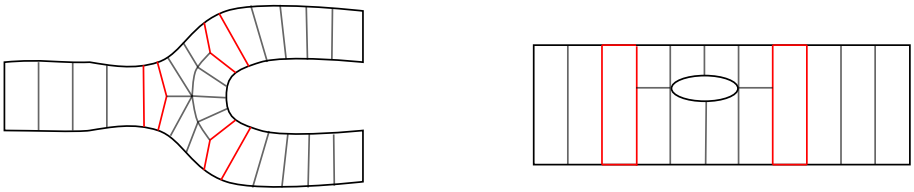

Figure 2.9: Examples of pipe-type meshes and the use of transition elements (highlighted in red) to discretize branched (left) and perforate (right) domains.

The geometrical mapping, for both simple and transition elements, consists in a pair of linear transformations for the axial direction and for the transversal direction. These transformations could be straightforwardly improved by, for example, considering higher order mapping functions for the axial/transversal directions.

2.2.2 Field interpolation: Transversal enrichment

Once a pipe-type partition $\mathcal{T}_h(\Omega)$ is established, composed by both simple and transition elements, we need to approximate the solution of the model (Equation (2.7)). Typically in the finite element method, the approximate solution is obtained through the definition of a finite-dimensional space $\mathcal{V}_h \subset \mathcal{V}$ spanned by functions with compact support. Hence, the approximate solution, say u_{F}, is computed as a linear combination of the basis functions chosen for $\mathcal{V}_h$, that is

$$u_{\mathrm{F}} = \sum_{n=1}^{n_{\mathrm{F}}} d_n \phi_n(\mathbf{x}), \tag{2.13}$$

where $\{d_n, n = 1, \ldots, n_{\mathrm{F}}\}$ is the set of unknown or degrees of freedom (DoFs) and $\{\phi_n, n = 1, \ldots, n_{\mathrm{F}}\}$ is the basis chosen for the space $\mathcal{V}_h$.

The main characteristic of this basis is the locality of the support. For example, in the case of piecewise linear finite elements, each element in the basis is defined as the unique piecewise linear function with value one in the corresponding node of the triangulation and zero at all the other nodes.

For the TEPEM, the interpolation strategy follows the same structure than that of the FEM, just with the proper modification in the field interpolants to deal with the geometric mesh constructed as described in the previous section, and with the differentiation between the axial and transversal dynamics. Let us see this in detail next.

Interpolants in simple pipe-elements Each pipe-element $\mathcal{K} \in \mathcal{T}_h(\Omega)$ is mapped to the reference element $\mathcal{K}_0$ in such way that the axial direction in the dynamics is aligned with the η-axis (in the reference configuration) while the transversal direction is aligned with the ξ-axis. In the reference element, the interpolants are constructed by the product of polynomials defined for each axis, splitting in this way the dependence and allowing for an independent enrichment in each direction according to the problem needs.

Formally, considering integer values s and p and for an arbitrary simple pipe-element in the partition $\mathcal{T}_h(\Omega)$, we approximate any scalar field u by the function u_{T} defined by

$$u_{\mathrm{T}} \circ \chi_{\mathcal{K}}(\xi, \eta) = \sum_{j=1}^{\mathsf{s}+1} \sum_{i=1}^{\mathsf{p}+1} u_{ij}^h \phi_i(\xi) \varphi_j(\eta), \qquad \mathcal{K} \in \mathcal{T}_h(\Omega) \tag{2.14}$$

where $\{\phi_i : i = 1, \ldots, \mathsf{p}+1\}$ is a basis for the space $\mathbb{P}_{\mathsf{p}}$ of polynomials up to degree p in $[-1, 1]$ and $\{\varphi_j : j = 1, \ldots, \mathsf{s}+1\}$ is a basis for the space $\mathbb{P}_{\mathsf{s}}$. We identify the basis $\phi_i(\xi)$ as *transversal interpolants* and the basis $\varphi_j(\eta)$ as *axial interpolants*. The integers, s (axial order) and p (transversal order), command the enrichment capabilities of our numerical model, being possible a natural and independent enrichment.

For practical purposes, and since we are interested in problems where the axial dynamics is dominant in relation to the transversal one, we combine a small axial order s ($\mathsf{s} = \{1, 2\}$) with a moderate high transversal order p. In this manner, the axial dynamics is easily accounted for through a large number of versatile low order interpolants, while the transversal dynamics is captured by the unique (except for transition elements) high order transversal polynomial defined in the pipe element.

Even when, in principle, there are no restrictions in the way in which the basis functions for $\mathbb{P}_{\mathsf{p}}$ and for $\mathbb{P}_{\mathsf{s}}$ are defined, we employ a special polynomial set as basis. For axial and transversal interpolants, Lagrange polynomials defined in the Chebyshev-Gauss-Lobatto (CGL) nodes are considered. This is, for an arbitrary integer r, as a basis of $\mathbb{P}_{\mathsf{r}}$ we consider the set $\{\psi_j(t) : j = 1, \ldots, \mathsf{r}+1\}$ where each element in the basis has the form

$$\psi_j(t) = \prod_{\substack{i=1 \\ i \neq j}}^{\mathsf{r}+1} \frac{t - x_j}{x_i - x_j} \qquad j = 1, \ldots, \mathsf{r}+1, \qquad t \in [-1, 1] \tag{2.15}$$

where each node of the CGL set $\{x_i, i = 1, \ldots, \mathsf{r}+1\}$ is defined as

$$x_i = -\cos\left(\frac{(i-1)\pi}{\mathsf{r}}\right). \tag{2.16}$$

Note that the CGL set for $\mathsf{s} = \{1, 2\}$ coincides with the classical set of equidistant nodes. Then, the axial interpolants are, for $\mathsf{s} = 1$

$$\varphi_1(t) = \frac{1}{2}(1 - t), \quad \varphi_2(t) = \frac{1}{2}(1 + t), \tag{2.17}$$

and for $\mathsf{s} = 2$

$$\varphi_1(t) = \frac{1}{2}(t^2 - t), \quad \varphi_2(t) = (1 - t^2), \quad \varphi_3(t) = \frac{1}{2}(t^2 + t). \tag{2.18}$$

This particular choice of nodes to define the polynomial interpolants is considered because this set mitigates the appearance of spurious oscillations when using high order polynomials. This unacceptable behavior, known as *Runge phenomenom*, and the impact of the use of CGL points to define the Lagrange polynomials can be appreciated in Figure 2.10 where the interpolation of the function $f(x) = \dfrac{1}{1+25x^2}$ is displayed.

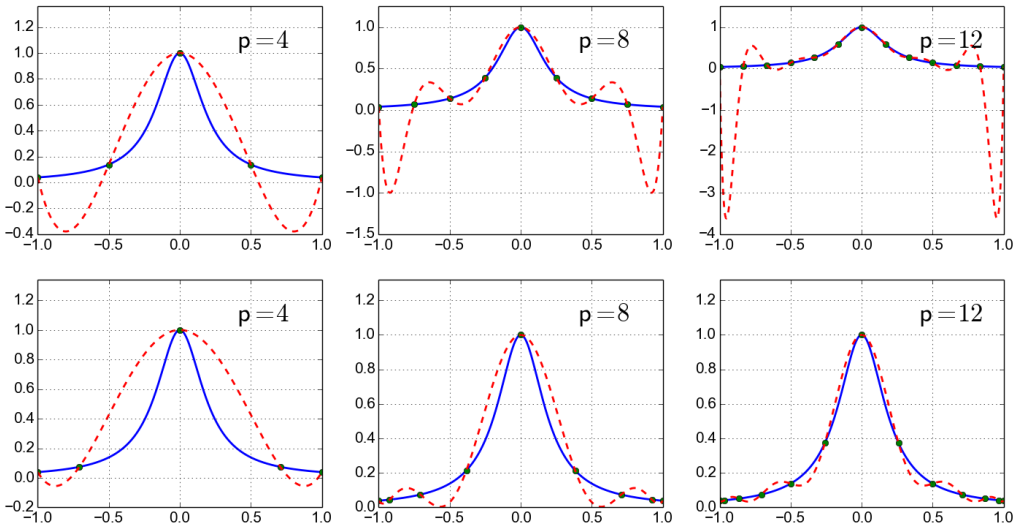

Figure 2.10: Comparison of Runge function (blue) and its polynomial interpolantion (red) of order p with Lagrange polynomials defined in equidistant points (top row) and in the CGL points (bottom row).

The oscillating behavior in the interpolation of certain type of functions through high order polynomials (defined in an equidistant set of points) can also affect in a hybrid order approximation strategy like the TEPEM. In [Blanco et al. 2015], an initial version of this technique was explored and its applications in a three-dimensional fluid flow modeling problem reveals oscillations in the velocity profiles for high order polynomials of order between 8 and 14.

An example of field interpolants for the particular combination $\mathsf{p} = 2$ and $\mathsf{s} = 1$ is featured in Figure 2.11. The choice of Lagrange polynomials as interpolant functions permits to relate the degrees of freedom (unknown coefficients) in Equation (2.14) with the nodal values of the approximate solution. In fact we have

$$u^h_{ij} = u_{\mathrm{T}} \circ \chi_{\mathcal{K}}(\xi_i, \eta_j) \qquad 1 \leq i \leq \mathsf{p}+1, \quad 1 \leq j \leq \mathsf{s}+1, \tag{2.19}$$

where

$$\xi_i = -\cos\left(\frac{(i-1)\pi}{\mathsf{p}}\right) \qquad \eta_j = -\cos\left(\frac{(j-1)\pi}{\mathsf{s}}\right). \tag{2.20}$$

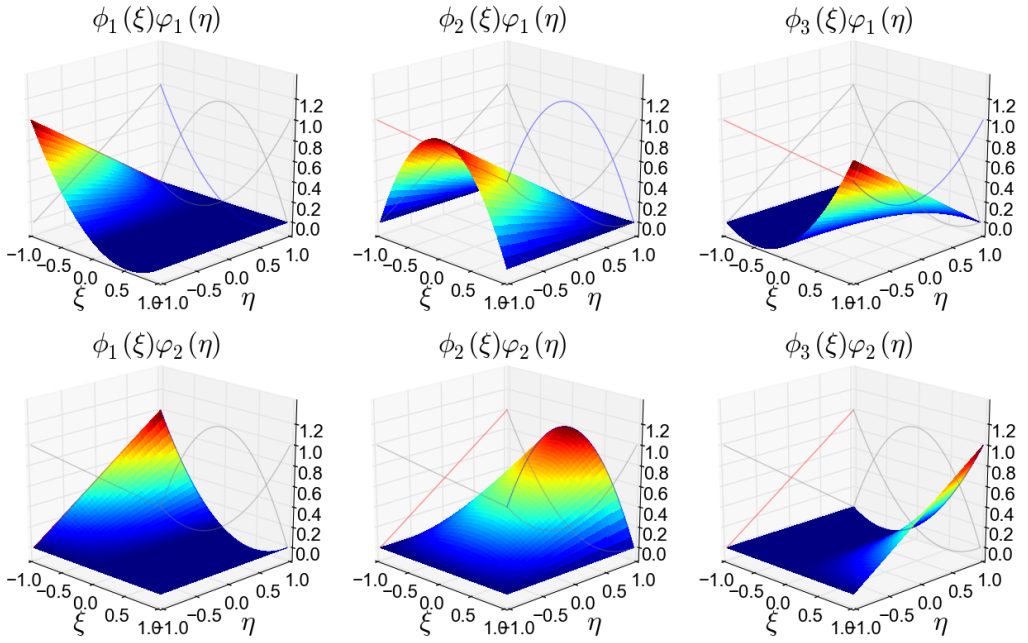

Figure 2.11: Field interpolants for the pipe-element and for the particular combination for axial/transversal order $\mathsf{s} = 1$ (along η) and $\mathsf{p} = 2$ (along ξ).

Regarding the geometrical distribution of the degrees of freedom in the reference element, we can rewrite Equation (2.14) in a compact form by

$$u_{\mathrm{T}} \circ \chi_{\mathcal{K}}(\xi, \eta) = \sum_{n=1}^{N} u_n^h \psi_n(\xi, \eta), \tag{2.21}$$

where $N = (\mathsf{s}+1)(\mathsf{p}+1)$, and the interpolant functions in this form are defined as

$$\psi_n(\xi, \eta) = \phi_i(\xi)\varphi_j(\eta), \tag{2.22}$$

with $n = (j-1)(\mathsf{p}+1) + i$. By using this notation, the degrees of freedom for the field interpolation are distributed as depicted in Figure 2.12.

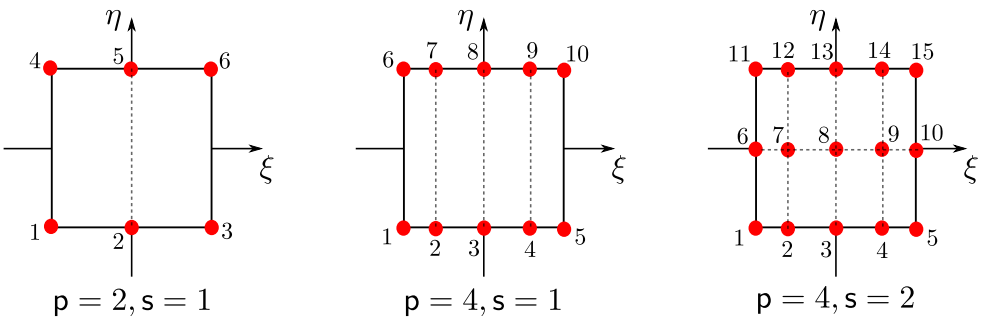

Figure 2.12: Geometrical distribution of the degrees of freedom for three types of pipe elements.

With the Lagrangian interpolation as defined before, we define the two-dimensional *pipe-element* for the TEPEM approach as composed by the tuple $(\mathcal{K}_0, \mathcal{P}_0, \mathcal{N}_0)$ where

(i) $\mathcal{K}_0 = [-1, 1]^2$ is the reference element defined in the $\xi\eta-$plane.

(ii) $\mathcal{P}_0 = \{\phi_i(\xi)\varphi_j(\eta) : i = 1, \ldots, \mathsf{p}+1; j = 1, \ldots, \mathsf{s}+1\}$ is the function space composed by interpolants of different orders for each direction as defined in the reference element.

(iii) The degrees of freedom defined through the relation $\psi \mapsto \psi(\xi_i, \eta_j)$, $\psi \in \mathcal{P}_0$, where the nodes (ξ_i, η_j), are those defined in Equation (2.20).

Next, we define the TEPEM interpolation employed for the *transition pipe-element*.

Interpolants in transition pipe-elements The geometric structure of the transition element allows to conformally refine a pipe mesh in the transversal region in a very straightforward way, which requires slightly modified geometrical interpolants.

We extend the idea of transversal enrichment in the interpolation of physical fields by adapting the interpolants employed in the pipe-element to enable the continuity in the field at the axial boundaries of the element. This is, we define the field interpolants for the transition element by ensuring that the approximation u_{T} is continuous at the boundaries Γ_1 (related with the segment $\eta = -1$ in the reference configuration), Γ_2 (corresponding with $\{\eta = 1, -1 \leq \xi \leq 0\}$) and Γ_3 (related with $\{\eta = 1, 0 \leq \xi \leq 1\}$). The geometrical structure of the transition element, as well as the axial boundaries in which we are interested into ensure the continuity, are outlined in Figure 2.13.

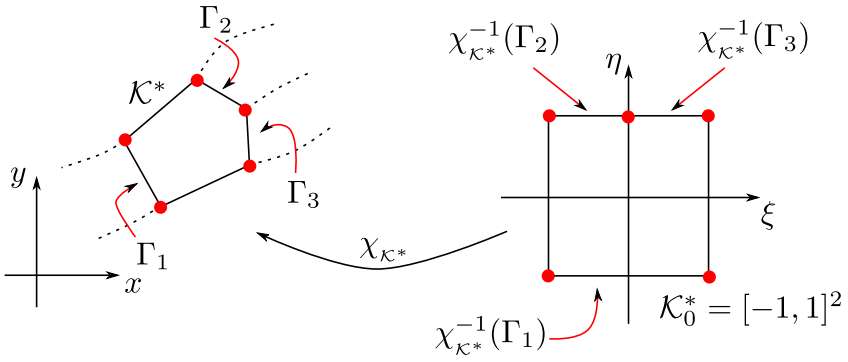

Figure 2.13: Geometrical structure of the transition element. Axial boundaries in the actual transition element are denoted as Γ_1, Γ_2 and Γ_3.

As seen in previous section, the transition element acts as a link between one simple element (corresponding to $\eta = -1$) and two pipe elements, corresponding to $\eta = 1$ in the reference element. Denoting by s and p the axial and transversal order employed for the definition of interpolants in the pipe-element, we define the field interpolants on the transition element by ensuring the following conditions

$$u_{\mathrm{T}} \circ \chi_{\mathcal{K}^*}(\boldsymbol{\xi})|_{\Gamma_1} \in \mathbb{P}_{\mathsf{p}}, \qquad u_{\mathrm{T}} \circ \chi_{\mathcal{K}^*}(\boldsymbol{\xi})|_{\Gamma_2} \in \mathbb{P}_{\mathsf{p}}, \qquad u_{\mathrm{T}} \circ \chi_{\mathcal{K}^*}(\boldsymbol{\xi})|_{\Gamma_3} \in \mathbb{P}_{\mathsf{p}}. \tag{2.23}$$

This means that, the restriction at each axial boundary must be a polynomial up to degree p, and the approximate solution at these boundaries must be expressed as a linear combination of the basis functions ϕ_i chosen for $\mathbb{P}_{\mathsf{p}}$. This ensures a unique representation for the field u_{T} in the elements sharing the boundary Γ_i $(i = 1, 2, 3)$.

For an arbitrary transition-pipe element in the partition $\mathcal{T}_h(\Omega)$, we approximate any scalar field u by the function u_{T} defined by

$$u_{\mathrm{T}} \circ \chi_{\mathcal{K}^*}(\xi,\eta) = \sum_{j=1}^{\mathsf{s}} \sum_{i=1}^{\mathsf{p}+1} u_{ij}^h \phi_i(\xi)\varphi_j(\eta) + \sum_{i=1}^{\mathsf{p}+1} \left(\check{u}_{i,\mathsf{s}+1}^h \check{\phi}_i(\xi) + \hat{u}_{i,\mathsf{s}+1}^h \hat{\phi}_i(\xi) \right) \varphi_{\mathsf{s}+1}(\eta), \tag{2.24}$$

where $\{\phi_i : i = 1, \ldots, \mathsf{p}+1\}$ is the set of Lagrange polynomials basis, defined in the CGL nodes, for the space $\mathbb{P}_{\mathsf{p}}$, $\{\varphi_j : j = 1, \ldots, \mathsf{s}+1\}$ is the set of Lagrange polynomials for $\mathbb{P}_{\mathsf{s}}$ and the functions $\hat{\phi}_i$ and $\check{\phi}_i$ are defined as follows

$$\check{\phi}_i(\xi) = \phi_i(2\xi + 1)\mathbb{1}_{\xi \leq 0}, \qquad \hat{\phi}_i(\xi) = \phi_i(2\xi - 1)\mathbb{1}_{\xi > 0} \tag{2.25}$$

An example of the interpolant functions defined in the transition element $\mathcal{K}^*$ is presented in Figure 2.14.

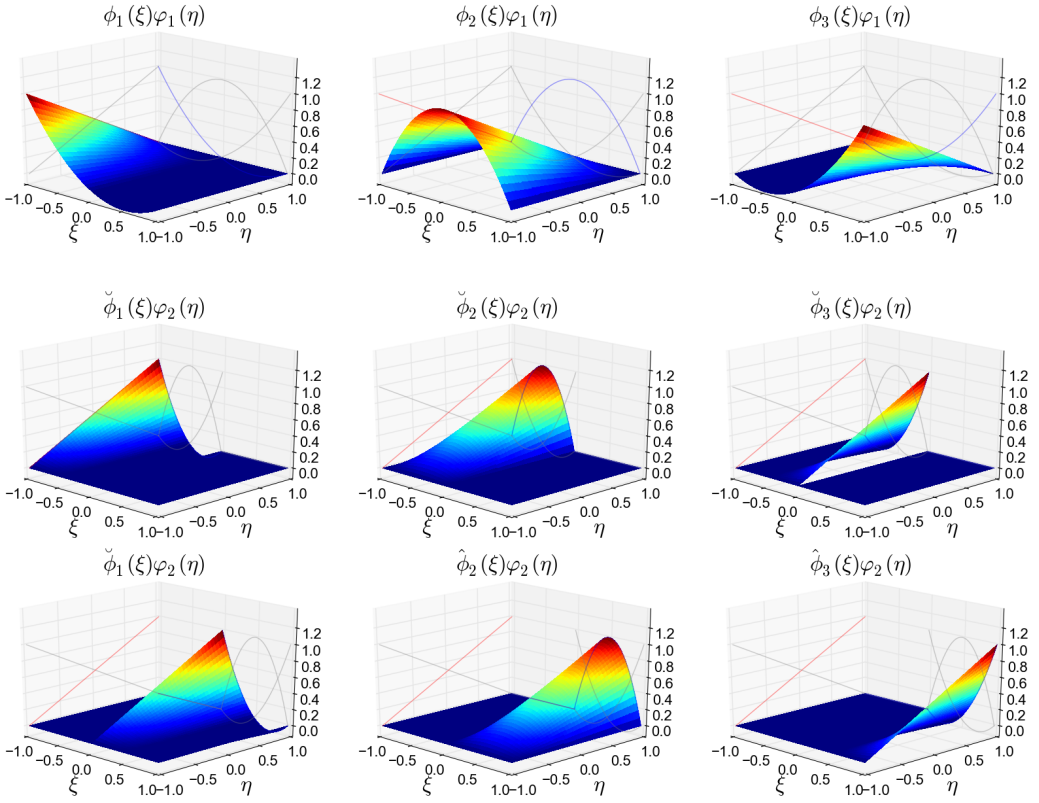

Figure 2.14: Field interpolants for the transition element and the particular combination for axial/transversal orders $\mathsf{s} = 1$ and $\mathsf{p} = 2$.

The choice of interpolant functions in the transition element as variations of the interpolants employed in the pipe element allows us to impose the continuity in the approximation u_{T} in a very straightforward way. In fact, let us focus in the boundary Γ_2: Let us denote by $\mathcal{K}_2$ the pipe element sharing the boundary Γ_2 with the actual transition element $\mathcal{K}^*$ and also let us assume that, for $\mathcal{K}_2$, the boundary Γ_2 is in correspondence with the segment $\{\eta = -1\}$ at the pipe reference element $\mathcal{K}_0$. Then for an arbitrary

point $\mathbf{x} \in \Gamma_2$ there is $\xi_0 \in [-1, 1]$ such that

$$\mathbf{x} = \chi_{\mathcal{K}_2}(\xi_0, -1) = \chi_{\mathcal{K}^*}\left(\frac{\xi_0 - 1}{2}, 1\right) \tag{2.26}$$

where the last part follows from the definition of the geometrical mapping in the transition element $\mathcal{K}^*$. Then, the approximate solution u_{T} satisfies

$$\begin{aligned} u_{\mathrm{T}}(\mathbf{x})|_{\mathcal{K}_2} &= u_{\mathrm{T}} \circ \chi_{\mathcal{K}_2}(\xi_0, -1) = \sum_{i=1}^{\mathsf{p}+1} u^h_{i1}|_{\mathcal{K}_2}\phi_i(\xi_0) \\ u_{\mathrm{T}}(\mathbf{x})|_{\mathcal{K}^*} &= u_{\mathrm{T}} \circ \chi_{\mathcal{K}^*}\left(\frac{\xi_0 - 1}{2}, 1\right) = \sum_{i=1}^{\mathsf{p}+1} \check{u}^h_{i,\mathsf{s}+1}\check{\phi}_i\left(\frac{\xi_0 - 1}{2}\right) = \sum_{i=1}^{\mathsf{p}+1} \check{u}^h_{i,\mathsf{s}+1}|_{\mathcal{K}^*}\phi_i(\xi_0) \end{aligned} \tag{2.27}$$

and the continuity at Γ_2 follows from the fact that $u^h_{i1}|_{\mathcal{K}_2} = \check{u}^h_{i,\mathsf{s}+1}|_{\mathcal{K}^*}$, for each $i = 1, \ldots, \mathsf{p}+1$. Similar conditions can be obtained for the boundaries Γ_1 and Γ_3.

The imposition of the continuity can be better understood when explored the relation between the degrees of freedom in the transition element and the nodal values of the approximate field u_{T}. Notably, the use of Lagrange polynomials implies

$$\begin{aligned} u^h_{ij} &= u_{\mathrm{T}} \circ \chi_{\mathcal{K}^*}(\xi_i, \eta_j) && 1 \le i \le \mathsf{p}+1, 1 \le j \le \mathsf{s} \\ \check{u}^h_{i,\mathsf{s}+1} &= u_{\mathrm{T}} \circ \chi_{\mathcal{K}^*}(0.5(\xi_i - 1), 1) && 1 \le i \le \mathsf{p}+1 \\ \hat{u}^h_{i,\mathsf{s}+1} &= u_{\mathrm{T}} \circ \chi_{\mathcal{K}^*}(0.5(\xi_i + 1), 1) && 1 \le i \le \mathsf{p}+1 \end{aligned} \tag{2.28}$$

where

$$\xi_i = -\cos\left(\frac{(i-1)\pi}{\mathsf{p}}\right) \qquad \eta_j = -\cos\left(\frac{(j-1)\pi}{\mathsf{s}}\right). \tag{2.29}$$

Then, the continuity through the whole boundary Γ_2 (and also the other axial boundaries) depends upon the imposition of continuity at the nodes $\mathbf{x}_i = \chi_{\mathcal{K}_2}(\xi_i, -1)$ once

$$u^h_{i1}|_{\mathcal{K}_2} = u_{\mathrm{T}}(\mathbf{x}_i)|_{\mathcal{K}_2} \qquad \text{and} \qquad \check{u}^h_{i,\mathsf{s}+1}|_{\mathcal{K}^*} = u_{\mathrm{T}}(\mathbf{x}_i)|_{\mathcal{K}^*}. \tag{2.30}$$

The geometrical distribution of the degrees of freedom, for three transition elements, is displayed in Figure 2.15.

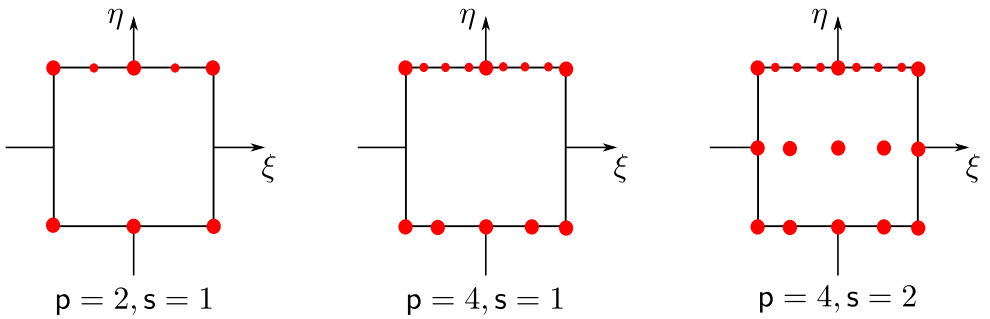

Figure 2.15: Geometrical distribution of the degrees of freedom for the transition element and three combinations of transversal and axial interpolation orders.

Thus, the two-dimensional *transition element* for the TEPEM approach is defined by the triple $(\mathcal{K}_0^*, \mathcal{P}_0^*, \mathcal{N}_0^*)$ where

(i) $\mathcal{K}_0^* = [-1,1]^2$ is the reference element defined in the $\xi\eta-$plane.

(ii) $\mathcal{P}_0^* = \{\phi_i(\xi)\varphi_j(\eta), \hat{\phi}_i(\xi)\varphi_{\mathsf{s}+1}(\eta), \check{\phi}_i(\xi)\varphi_{\mathsf{s}+1}(\eta) : i = 1,\dots,\mathsf{p}+1; j = 1,\dots,\mathsf{s}\}$ is the function space composed by interpolants of different order for each direction as defined in the reference element.

(iii) The degrees of freedom defined through the relations in Equation (2.28).

It is important to highlight that the field interpolation is independent from the mesh structure. Once defined a pipe-type partition, it is possible to obtain a family of interpolation strategies to the desired problem without the modification of the approximated geometry.

2.3 Basis functions in 3D

The description of the TEPEM approach in the three-dimensional case follows the same structure exposed for the two-dimensional case, in the sense of performing a pipe-type discretization of the geometrical domain and building an approximation for the physical fields through interpolants of different order according to each direction, but with proper modifications to deal with the additional transversal dimension in the problem.

Let us consider the three-dimensional domain Ω, with boundary $\Gamma = \Gamma_i \cup \Gamma_o \cup \Gamma_L$, as presented in Figure 2.16. Here Γ_i and Γ_o stand for the inlet and outlet boundaries, respectively, while Γ_L is the lateral boundary which is considered smooth enough and represents the arterial wall in the case of hemodynamics applications.

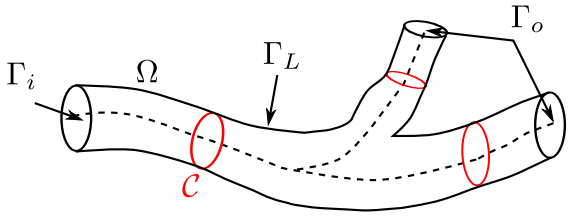

Figure 2.16: Schematic setting for the model problem in 3D. Here the dotted line represents the axial direction for the geometry and phenomenology.

Both Γ_i and Γ_o are surfaces in the space, which are considered planar and with regular boundary. Moreover, we can assume that these surfaces as well as any transversal section, denoted by $\mathcal{C}$, obtained from slicing the domain Ω (see the curves highlighted in red in Figure 2.16) have a regular boundary that can be geometrically well approximated by the mapping $\chi_{\mathcal{C}} : [-1,1]^2 \to \mathbb{R}^3$ defined as

$$\chi_{\mathcal{C}}(\xi,\eta) = \sum_{n=1}^{12} \mathbf{x}_n \mathcal{S}_n(\xi,\eta) \tag{2.31}$$

where $\{\mathbf{x}_n, n = 1,\dots,12\}$ are selected nodes over the boundary of the planar section $\mathcal{C}$ and functions $\{\mathcal{S}_i\}$ are the cubic Serendipity functions ([Arnold and Awanou 2011]),

defined by

$$\begin{aligned}
\mathcal{S}_1(\xi,\eta) &= \frac{1}{32}(1+\xi)(1-\eta)(9(\xi^2+\eta^2)-10) & \mathcal{S}_2(\xi,\eta) &= \frac{1}{32}(1+\xi)(1+\eta)(9(\xi^2+\eta^2)-10)\\
\mathcal{S}_3(\xi,\eta) &= \frac{1}{32}(1-\xi)(1+\eta)(9(\xi^2+\eta^2)-10) & \mathcal{S}_4(\xi,\eta) &= \frac{1}{32}(1-\xi)(1-\eta)(9(\xi^2+\eta^2)-10)\\
\mathcal{S}_5(\xi,\eta) &= \frac{9}{32}(1+\xi)(1-\eta^2)(1-3\eta) & \mathcal{S}_6(\xi,\eta) &= \frac{9}{32}(1+\xi)(1-\eta^2)(1+3\eta)\\
\mathcal{S}_7(\xi,\eta) &= \frac{9}{32}(1-\xi^2)(1+3\xi)(1+\eta) & \mathcal{S}_8(\xi,\eta) &= \frac{9}{32}(1-\xi^2)(1-3\xi)(1+\eta)\\
\mathcal{S}_9(\xi,\eta) &= \frac{9}{32}(1-\xi)(1-\eta^2)(1+3\eta) & \mathcal{S}_{10}(\xi,\eta) &= \frac{9}{32}(1-\xi)(1-\eta^2)(1-3\eta)\\
\mathcal{S}_{11}(\xi,\eta) &= \frac{9}{32}(1-\xi^2)(1-3\xi)(1-\eta) & \mathcal{S}_{12}(\xi,\eta) &= \frac{9}{32}(1-\xi^2)(1+3\xi)(1-\eta)
\end{aligned} \tag{2.32}$$

In other words, we are supposing that transversal sections can be approximated by piecewise cubic polynomials. This assumption seems plausible for hemodynamics simulations, where the domain represents a vascular region and transversal sections $\mathcal{C}$ (of tubular non-branching regions) are smooth and with nearly circular shape.

In what follows we will define the 3D counterparts for the pipe and transition elements defined for the 2D case. These elements are defined following the same idea to differentiate the way in which different dynamics are approximated. Always, we employ the Serendipity functions defined above for the geometrical approximation.

2.3.1 Simple pipe element

To introduce the three-dimensional pipe-element let us consider the computational domain Ω as being a tubular non-branched domain as shown in Figure 2.17. In this domain, the elemental discretization can be performed by slicing the geometry along the centerline (dotted curve in the mentioned figure).

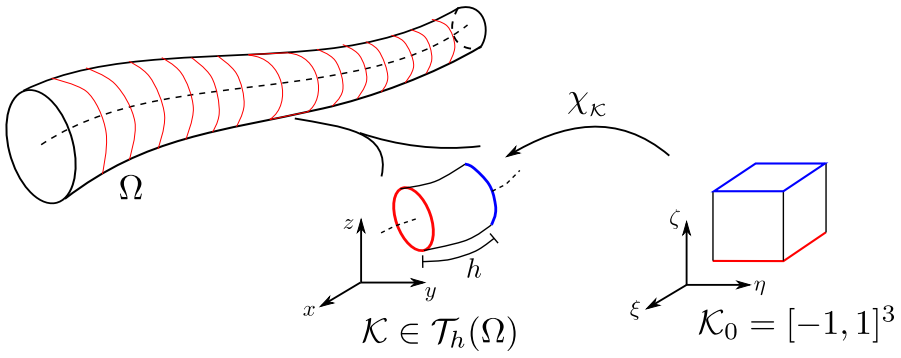

Figure 2.17: Tubular domain and pipe-element discretization in 3D.

The sequential slicing of the domain defines a partition $\mathcal{T}_h(\Omega) = \{\mathcal{K}_i, i = 1, \ldots, \mathrm{n_{el}}\}$ of pipe-like elements, where the index h is associated to the axial length of the elements. Note that each resulting slab $\mathcal{K} \in \mathcal{T}_h(\Omega)$ is constructed such that it is axially bounded by two closed planar surfaces and can be mapped to the reference element $\mathcal{K}_0 = [-1, 1]^3$, in the $\xi\eta\zeta$-space, through the transformation

$$\chi_{\mathcal{K}}(\xi, \eta, \zeta) = \sum_{k=1}^{2} \sum_{n=1}^{12} \mathbf{x}_n^k \mathcal{S}_n(\xi, \eta) L_k(\zeta) \tag{2.33}$$

where $\{L_k : k = 1, 2\}$ is the classical Lagrangian basis for $\mathbb{P}_1$, the set $\{\mathcal{S}_n : n = 1, \ldots, 12\}$ the Serendipity cubic basis and $\{\mathbf{x}_n^k : n = 1, \ldots, 12\ k = 1, 2\}$ is a set of points picked over the transversal section mapped from the section $\zeta = 2k - 3$ $(k = 1, 2)$ in the reference element. That is, each cross-section in the pipe element is geometrically approximated as piecewise cubic element while a linear mapping is considered for the axial direction.

As commented in the 2D case, quadratic polynomials can be considered for the axial direction in the pipe-element, for which a middle transversal section must be added in both the actual and reference elements and the linear basis $\{L_k\}$ must be replaced by the quadratic basis $\{Q_k, k = 1, 2, 3\}$ of $\mathbb{P}_2$.

The geometrical mapping is constructed such that the axial dynamics, in the pipe element $\mathcal{K}$, corresponds with the ζ-axis in the reference element $\mathcal{K}_0$. Conversely, the transversal dynamics is now placed, over the reference element, in the $\xi\eta$-plane.

The field interpolants are defined in $\mathcal{K}_0$ seeking to differentiate between axial and transversal dynamics. For integer values s (axial order) and p (transversal order), we approximate any scalar field u by the function u_{T} defined by

$$u_{\mathrm{T}} \circ \chi_{\mathcal{K}}(\xi, \eta, \zeta) = \sum_{k=1}^{\mathsf{s}+1} \left(\sum_{i=1}^{\mathsf{p}+1} \sum_{j=1}^{\mathsf{p}+1} u_{ijk}^h \phi_i(\xi) \phi_j(\eta) \right) \varphi_k(\zeta) \qquad \mathcal{K} \in \mathcal{T}_h(\Omega) \tag{2.34}$$

where the sets $\{\phi_i : i = 1, \ldots, \mathsf{p} + 1\}$ and $\{\varphi_i : i = 1, \ldots, \mathsf{s} + 1\}$ are basis of $\mathbb{P}_{\mathsf{p}}$ and $\mathbb{P}_{\mathsf{s}}$, respectively, constructed such that each element is a Lagrange polynomial defined in the CGL set of nodes. In this manner, we split the axial and transversal predictive capabilities of the model, allowing for an independent enrichment over each direction according the problem needs. The functions $\phi_{ij}(\xi, \eta) = \phi_i(\xi)\phi_j(\eta)$ are denominated as transversal interpolants and an example of these, for a particular value of p, are shown in Figure 2.18. In turn, the functions $\varphi_k(\zeta)$ are called axial interpolants.

The degrees of freedom in Equation (2.34) are the nodal values of the function u_{T} by virtue of the Lagrangian nature of the interpolants, that means

$$u_{ijk}^h = u_{\mathrm{T}} \circ \chi_{\mathcal{K}}(\xi_i, \eta_j, \zeta_k) \qquad 1 \leq i, j \leq \mathsf{p} + 1, \quad 1 \leq k \leq \mathsf{s} + 1 \tag{2.35}$$

where the point $(\xi_i, \eta_j, \zeta_k) \in \mathcal{K}_0$ is defined as

$$\xi_i = -\cos\left(\frac{(i-1)\pi}{\mathsf{p}}\right), \quad \eta_j = -\cos\left(\frac{(j-1)\pi}{\mathsf{p}}\right), \quad \zeta_k = -\cos\left(\frac{(k-1)\pi}{\mathsf{s}}\right) \tag{2.36}$$

The spatial distribution of these degrees of freedom, in the 3D pipe-element, is shown in Figure 2.19.

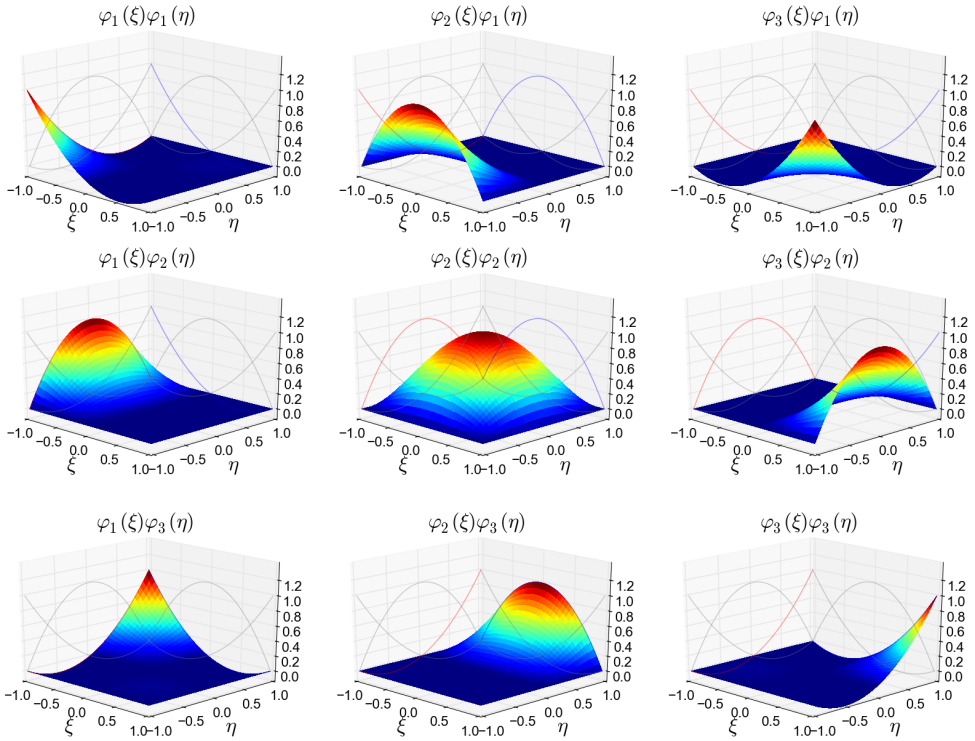

Figure 2.18: Transversal interpolants in the three-dimensional pipe-element for the particular case $\mathsf{p} = 2$.

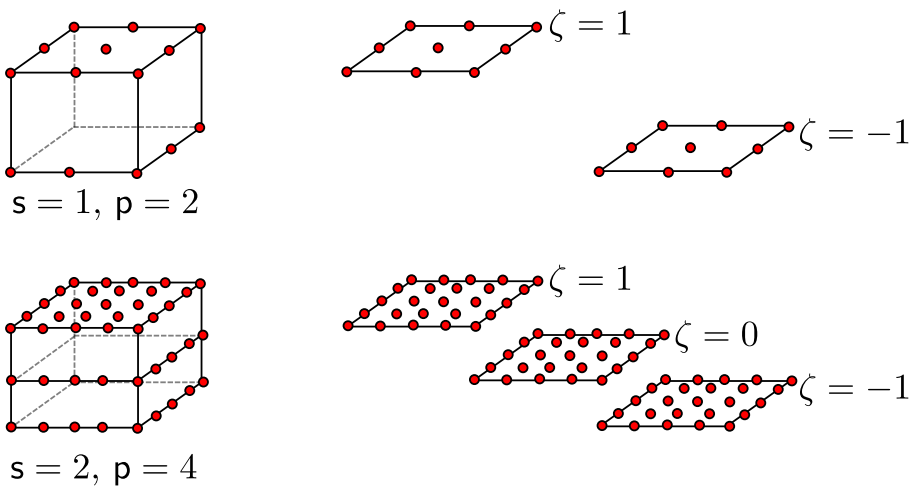

Figure 2.19: Geometrical distribution of the degrees of freedom for the three-dimensional pipe element and two combinations of axial and transversal order.

Hence, the three-dimensional pipe element is defined as the triple $(\mathcal{K}_0, \mathcal{P}_0, \mathcal{N}_0)$ where each component is defined as

(i) $\mathcal{K}_0 = [-1,1]^3$ is the reference element defined in the $\xi\eta\zeta-$space.

(ii) $\mathcal{P}_0 = \{\phi_i(\xi)\phi_j(\eta)\varphi_k(\zeta) : i,j = 1,\dots,\mathsf{p}+1; k = 1,\dots,\mathsf{s}+1\}$ is the function space composed by interpolants of different order for each direction as defined in the reference element.

(iii) The degrees of freedom defined through the relations given in Equation (2.35).

Notice that, similarly to the 2D case, the increase of model capabilities is achieved through the modification of parameters p and s (for the transversal and axial directions, respectively) without the need of modifying the geometrical partition of Ω in pipe-elements.

2.3.2 Transition pipe element

The pipe element introduced before meets the requirement to perform an accurate geometrical discretization of tubular regions. Nevertheless, the element is unable to deal with the topological changes occurring at a bifurcation. To extend the abilities of TEPEM to be employed in 3D hemodynamics simulations, where the presence of bifurcated regions is commonplace, we introduce a variation of the transition pipe element introduced in Section 2.2.1 in the context of a pipe discretization in 3D space.

Let us consider a simple branching domain Ω, as presented in Figure 2.20, which can be initially subdivided into tubular regions and the bifurcation area as

$$\Omega = \omega \cup \left(\bigcup_{i=A,B,C} \Omega_i \right) \tag{2.37}$$

where the notation follows the introduced in the aforementioned figure.

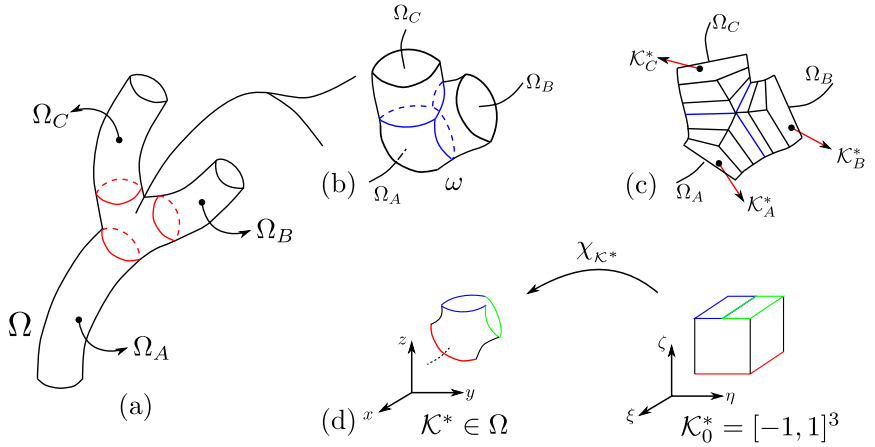

Figure 2.20: Geometric approximation for a branching pipe. (a)-(b) Division into tubular subdomains and bifurcation region ω. (c) Lateral view of the partition of ω and the inclusion of transition elements $\mathcal{K}_i^*$. (d) Geometrical mapping between actual and reference transition element.

This initial subdivision allows to deal with the geometrical discretization and the field interpolation in each tubular region Ω_i $(i = A, B, C)$ directly with the use of standard pipe-elements. For each region Ω_i a geometrical discretization is performed in a partition $\mathcal{T}_h(\Omega_i)$ such that each element $\mathcal{K} \in \mathcal{T}_h(\Omega_i)$ is a pipe-element, related to the reference element $\mathcal{K}_0 = [-1, 1]^3$ and where each physical field is approximated with a combination of p-order polynomials for the transversal in-plane directions and s-order polynomials for the axial direction.

For the junction region denoted by ω, a pipe partition is performed as illustrated in panel (c) from Figure 2.20 for which the inclusion of transition elements $\mathcal{K}_i^*$ $(i = A, B, C)$ is fundamental to connect the inner pipe-discrete structure with the tubular regions Ω_i. Each of these transition elements is composed by three planar sections, colored in red, blue and green in the panel (d) in Figure 2.20, and related to $\zeta = -1$ (red region), $\{\zeta = 1, -1 \leq \eta \leq 0\}$ (blue region) and $\{\zeta = 1, 0 \leq \eta \leq 1\}$ (green region) in the reference element $\mathcal{K}_0^* = [-1, 1]^3$.

Each transition element is related to the reference element $\mathcal{K}_0^*$ through a mapping $\chi_{\mathcal{K}^*}$ constructed such that the conformity in the mesh is satisfied. This mapping is defined as

$$\chi_{\mathcal{K}^*}(\xi, \eta, \zeta) = \sum_{k=1}^{3} \sum_{n=1}^{12} \mathbf{x}_n^k \hat{\mathcal{S}}_{n,k}(\xi, \eta, \zeta) \tag{2.38}$$

where $\{\mathbf{x}_n^k, n = 1, \ldots, 12; k = 1, 2, 3\}$ is a set of points on the transversal sections mapped from the section $\zeta = -1$ $(k = 1)$, $\{\zeta = 1, -1 \leq \eta < 0\}$ $(k = 2)$ and $\{\zeta = 1, 0 \leq \eta \leq 1\}$ $(k = 3)$ in the reference element, and the functions $\hat{\mathcal{S}}_{n,k}$ are modifications of the cubic Serendipity basis and are defined as

$$\begin{aligned}
\hat{\mathcal{S}}_{n,1}(\xi, \eta, \zeta) &= \mathcal{S}_n(\xi, \eta) L_1(\zeta) && n = 1, \ldots, 12. \\
\hat{\mathcal{S}}_{n,2}(\xi, \eta, \zeta) &= \mathcal{S}_n(\xi, 2\eta + 1) L_2(\zeta) \mathbb{1}_{\eta<0} && n = 1, \ldots, 12. \\
\hat{\mathcal{S}}_{n,3}(\xi, \eta, \zeta) &= \mathcal{S}_n(\xi, 2\eta - 1) L_2(\zeta) \mathbb{1}_{\eta\geq 0} && n = 1, \ldots, 12.
\end{aligned} \tag{2.39}$$

where $\mathbb{1}_{\eta<0}$ $(\mathbb{1}_{\eta\geq 0})$ is the characteristic function in the set defined by $\eta < 0$ $(\eta \geq 0)$.

From the definition of the geometric map, and postulating the following relations between the geometric nodes lying at the intersection $\mathsf{S}_2 \cap \mathsf{S}_3$ (surfaces described in Figure 2.21)

$$\mathbf{x}_2^2 = \mathbf{x}_1^3, \quad \mathbf{x}_3^2 = \mathbf{x}_4^3, \quad \mathbf{x}_7^2 = \mathbf{x}_{12}^3, \quad \mathbf{x}_8^2 = \mathbf{x}_{11}^3 \tag{2.40}$$

we ensure that the mapping in Equation (2.38) is totally continuous inside the transition element. Moreover, the way in which the geometric mapping is defined guarantees the total conformity of the mesh due the use of the same set of geometrical nodes for the approximation of interfacial curves (curves S_1, S_2 and S_3 in Figure 2.21) for both the adjacent pipe-elements and the transition element. Geometric degrees of freedom associated to the transition pipe-element are outlined in Figure 2.21.

For the complete definition of the transition element, it is required the proper modification of the interpolant functions in the reference element such that ensures the continuity of physical fields of interest. As said, the reference element acts as a link between one simple pipe element (corresponding with $\zeta = -1$ in $\mathcal{K}_0^*$) and two simple pipe elements (corresponding with two planar interfacial boundaries at $\zeta = 1$), thus in the reference element $\mathcal{K}_0^*$ any scalar field u is approximated through the function u_{T} defined

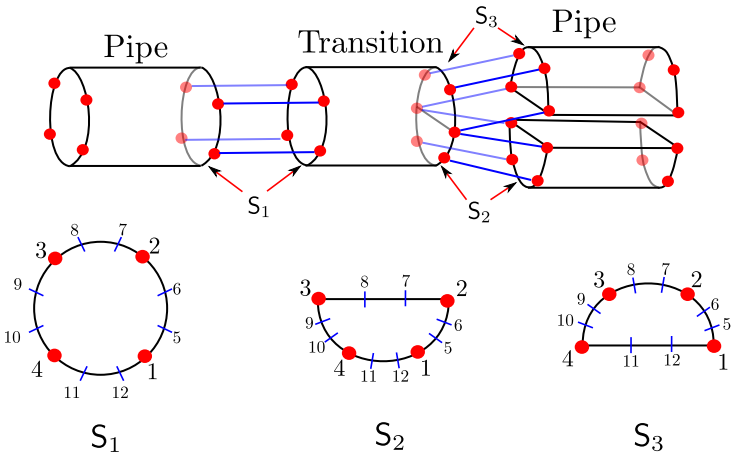

Figure 2.21: Outline of the transversal mesh refinement process through the inclusion of a transition element. Also, the geometric nodes for the approximation of each transversal section are shown.

by

$$
\begin{aligned}
u_{\mathrm{T}} \circ \chi_{\mathcal{K}^*}(\xi,\eta,\zeta) = &\sum_{k=1}^{\mathsf{s}} \left(\sum_{i=1}^{\mathsf{p}+1} \sum_{j=1}^{\mathsf{p}+1} u_{ijk}^h \phi_i(\xi)\phi_j(\eta) \right) \varphi_k(\zeta) \\
&+ \left(\sum_{i=1}^{\mathsf{p}+1} \sum_{j=1}^{\mathsf{p}+1} \hat{u}_{ij}^h \phi_i(\xi)\phi_j(2\eta+1)\mathbb{1}_{\eta<0} \right) \varphi_{\mathsf{s}+1}(\zeta) \\
&+ \left(\sum_{i=1}^{\mathsf{p}+1} \sum_{j=1}^{\mathsf{p}+1} \check{u}_{ij}^h \phi_i(\xi)\phi_j(2\eta-1)\mathbb{1}_{\eta\geq 0} \right) \varphi_{\mathsf{s}+1}(\zeta),
\end{aligned}
\tag{2.41}
$$

where the sets $\{\phi_i : i = 1, \ldots, \mathsf{p}+1\}$ and $\{\varphi_i : i = 1, \ldots, \mathsf{s}+1\}$ are basis for $\mathbb{P}_{\mathsf{p}}$ and $\mathbb{P}_{\mathsf{s}}$, respectively, constructed such that each element is a Lagrange polynomial defined in the CGL set of nodes.

Moreover, denoting by

$$\phi_{ij}(\xi,\eta) = \phi_i(\xi)\phi_j(\eta), \tag{2.42.1}$$

$$\hat{\phi}_{ij}(\xi,\eta) = \phi_i(\xi)\phi_j(2\eta+1)\mathbb{1}_{\eta<0}, \tag{2.42.2}$$

$$\check{\phi}_{ij}(\xi,\eta) = \phi_i(\xi)\phi_j(2\eta-1)\mathbb{1}_{\eta\geq 0}, \tag{2.42.3}$$

for $1 \leq i,j \leq \mathsf{p}+1$, we can identify the functions ϕ_{ij} as the same transversal interpolants in the pipe-element and the functions $\hat{\phi}_{ij}$ and $\check{\phi}_{ij}$ as variations of these same interpolants. In fact, for the functions $\hat{\phi}_{ij}$ in (2.42.2) the polynomial interpolants in direction η are obtained by properly changing the domain of definition from $[-1,1]$ to $[-1,0]$ and extended by zero to the complementary half.

In a similar way, interpolants in the direction η for the functions $\check{\phi}_{ij}$ in (2.42.3) are redefined to $[0,1]$ and extended by zero in the interval $[-1,0)$. Panel (a) in Figure 2.22 shows the interpolants in direction η, as well as their variants where the domain of definition is modified, for the particular case $\mathsf{p} = 3$. Also in the panel (b) of the same figure, the transversal interpolants $\hat{\phi}_{ij}$ and $\check{\phi}_{ij}$ are outlined.

Following the notation in Figure 2.21, it is easy to see that the proposed modification in the interpolants guarantees the continuity of the function u_{T} through the interfacial boundaries S_2 and S_3. Furthermore, notice that for each $i = 1, \ldots, \mathsf{p}+1$ it holds

$$\lim_{\eta \to 0^-} \hat{\phi}_{i,\mathsf{p}+1}(\xi, \eta) = \check{\phi}_{i,1}(\xi, 0) \qquad \text{for all } \xi \in [-1, 1] \tag{2.43}$$

which, together with the relations

$$\hat{u}^h_{i,\mathsf{p}+1} = \check{u}^h_{i,1} \qquad i = 1, \ldots, \mathsf{p}+1 \tag{2.44}$$

ensures a continuous interpolation, with discontinuous normal derivatives, over the surface $\mathsf{S}_2 \cap \mathsf{S}_3$.

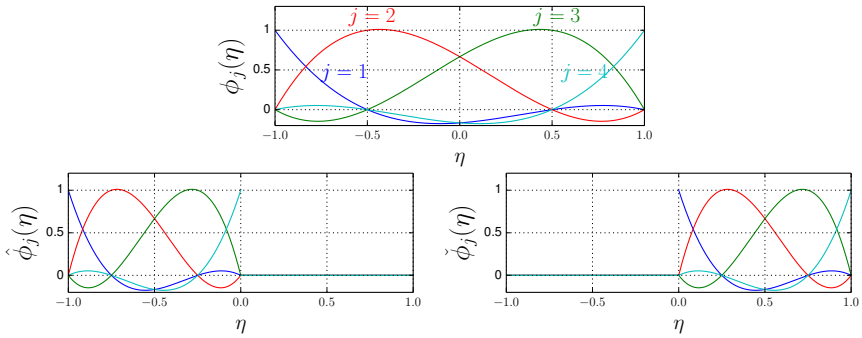

(a) Transversal interpolants ϕ_j defined in η (top row) and their variants $\hat{\phi}_j(\eta) = \phi_j(2\eta + 1)\mathbb{1}_{\eta<0}$ (bottom left) and $\check{\phi}_j(\eta) = \phi_j(2\eta - 1)\mathbb{1}_{\eta\geq 0}$ (bottom right).

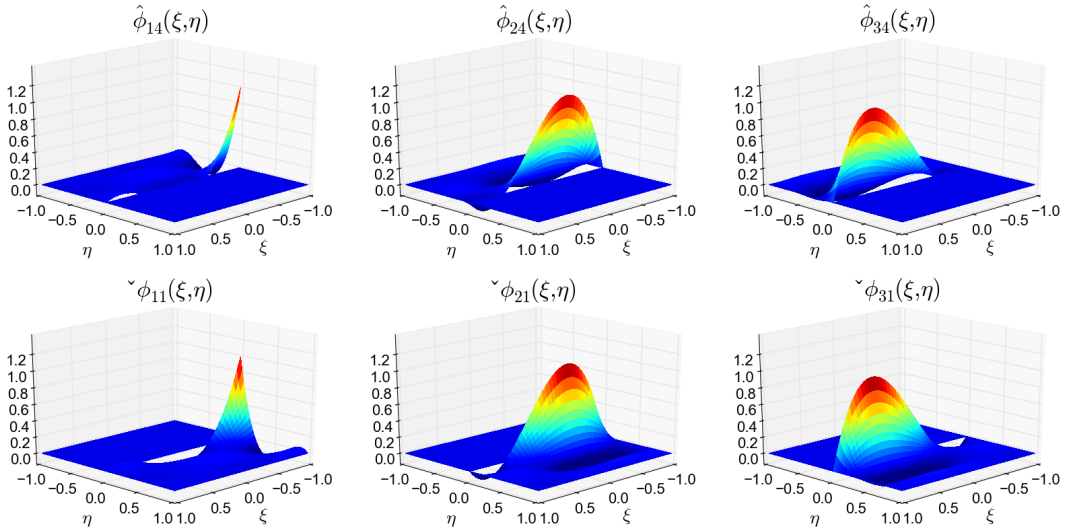

(b) Detail of the transversal interpolants associated to nodes over the line $\eta = 0$.

Figure 2.22: Transversal interpolants for the transition element and for $\mathsf{p} = 3$.

Finally, regarding the degrees of freedom in the transition element, they are the nodal values of the approximation u_{T} through the relations

$$\begin{aligned} u^h_{ijk} &= u_{\mathrm{T}} \circ \chi_{\mathcal{K}^*}\left(\xi_i, \eta_j, \zeta_k\right) && 1 \le i,j \le \mathsf{p}+1, \qquad 1 \le k \le \mathsf{s}, \\ \hat{u}^h_{ij} &= u_{\mathrm{T}} \circ \chi_{\mathcal{K}^*}\left(\xi_i, \frac{\eta_j - 1}{2}, 1\right) && 1 \le i,j \le \mathsf{p}+1, \\ \check{u}^h_{ij} &= u_{\mathrm{T}} \circ \chi_{\mathcal{K}^*}\left(\xi_i, \frac{\eta_j + 1}{2}, 1\right) && 1 \le i,j \le \mathsf{p}+1, \end{aligned} \tag{2.45}$$

with

$$\xi_i = -\cos\left(\frac{(i-1)\pi}{\mathsf{p}}\right), \quad \eta_j = -\cos\left(\frac{(j-1)\pi}{\mathsf{p}}\right), \quad \zeta_k = -\cos\left(\frac{(k-1)\pi}{\mathsf{s}}\right). \tag{2.46}$$

2.3.3 The transversally enriched space

For a pipe type partition $\mathcal{T}_h(\Omega)$ of the geometrical domain (here recall that h stands for the characteristical axial length of the partition) and fixed parameters $\mathsf{s}, \mathsf{p} \in \mathbb{N}$, which control the axial and transversal enrichment of the fields, respectively, we introduce the finite-dimensional space

$$\mathbb{T}_h^{\mathsf{p},\mathsf{s}} = \left\{ w^h \in L^2(\Omega) : w^h \circ \chi_{\mathcal{K}}(\xi,\eta,\zeta) = \sum_{k=1}^{\mathsf{s}+1} w_k^{\mathsf{p}}(\xi,\eta)\varphi_k(\zeta), \;\; \mathcal{K} \in \mathcal{T}_h(\Omega) \right\} \tag{2.47}$$

where $\{\varphi_k : k = 1, \ldots, \mathsf{s}+1\}$ is the classical Lagrangian basis for $\mathbb{P}_{\mathsf{s}}$ ($\mathsf{s} \in \{1,2\}$) and the functions $\{w_k^{\mathsf{p}} : k = 1, \ldots, \mathsf{s}+1\}$ are defined according to the type of element $\mathcal{K} \in \mathcal{T}_h(\Omega)$.

For a simple pipe element, the functions w_k^{p} are defined by

$$w_k^{\mathsf{p}}(\xi,\eta) = \sum_{i=1}^{\mathsf{p}+1}\sum_{j=1}^{\mathsf{p}+1} w^h_{ijk}\phi_{ij}(\xi,\eta) \qquad k = 1, \ldots, \mathsf{s}+1, \tag{2.48}$$

while, for a transition pipe element, they have the form

$$w_k^{\mathsf{p}}(\xi,\eta) = \begin{cases} \displaystyle\sum_{i=1}^{\mathsf{p}+1}\sum_{j=1}^{\mathsf{p}+1} w^h_{ijk}\phi_{ij}(\xi,\eta) & 1 \le k \le \mathsf{s}, \\ \displaystyle\sum_{i=1}^{\mathsf{p}+1}\sum_{j=1}^{\mathsf{p}+1} \hat{w}^h_{ij}\hat{\phi}_{ij}(\xi,\eta) + \check{w}^h_{ij}\check{\phi}_{ij}(\xi,\eta) & k = \mathsf{s}+1, \end{cases} \tag{2.49}$$

where the transversal interpolants ϕ_{ij}, $\hat{\phi}_{ij}$ and $\check{\phi}_{ij}$ ($1 \le i,j \le \mathsf{p}+1$) are constructed by product of the Lagrange polynomials in the basis $\{\phi_i : i = 1, \ldots, \mathsf{p}+1\}$ of space $\mathbb{P}_{\mathsf{p}}$ and following the structure presented in Equation (2.42).

The introduction of this space allows us to express in a compact way the interpolation strategy in the scope of the TEPEM, and is employed in the next chapters to introduce the discrete spaces where the solution of the problem under consideration is to be sought.

2.4 Further aspects of the pipe-element discretization

In the development of the TEPEM, some numerical details regarding the mesh generation and/or the way in which the approximation of the physical fields is carried out are worth of specific mention.

2.4.1 On the geometrical approximation

Cross-section approximation. The accuracy in the geometrical approximation is closely related to the capabilities of approximating the transversal sections of Ω. The mapping introduced in expression (2.31) between the region $[-1,1]^2$ and a generic transversal section $\mathcal{C}$ is postulated to be as an efficient strategy to approximate the transversal sections commonly encountered when the domain Ω represents a vascular region.

An illustration of the capabilities of the proposed geometrical approximation for transversal sections, are exposed in Figure 2.23 where four luminal areas from a patient-specific arterial geometry (blue dots) are approximated (red line). For typical arterial vessels, the proposed approach delivers reasonable and satisfactory approximations of the transversal sections.

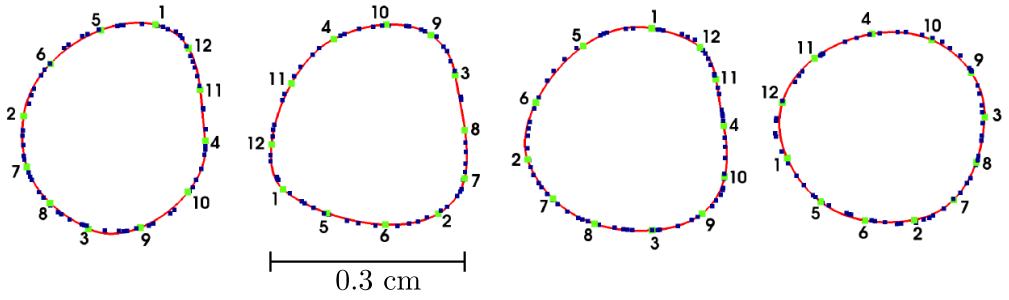

Figure 2.23: Approximation of different cross-sections of patient-specific arterial vessels through the use of Serendipity cubic mapping. In each panel: blue points define each cross-sectional area as given by medical images, solid red line stands for the approximation and green points refer to the geometrical nodes. These four luminal regions correspond to the patient-specific vasculature presented in Section 5.3.1.

A possible undesirable consequence of the mapping of (regular) transversal sections from the two-dimensional region $[-1,1]^2$ is the introduction of four kinks (angular points) in the geometry of the section $\mathcal{C}$. Such additional regularity in the approximated section can be imposed with a modification in the computation of the geometrical nodes which define the mapping. A detailed description of how these nodes are determined is given in Chapter 5.

Another alternative to circumvent the regularity issue is the choice of splines to approximate the transversal geometry or a reformulation of the problem based in cylindrical coordinates. In this last case, explored in [Guzzetti 2014], the accuracy of the map to circular-like transversal shapes generally improves, however at the price of a much more complicated representation of the basis functions (particularly in the absence of symmetry) which could make it difficult to use in patient-specific cases.

Mesh generation. Domain discretization based on simplices, triangular elements in the two-dimensional case and tetrahedral in the three-dimensional, is perhaps the most employed strategy in FEM approaches. For the two-dimensional case, it is also frequent to discretize the domain of the problem into (structured or unstructured) quadrilateral elements, specially for the case where the domain of definition of the problem is a simple and analytically defined region. Such popularity is accompanied with an extensive algorithm/software development technology, looking for the automatic discretization of complex domains, while minimizing the computational effort.

The TEPEM relies on a meshing strategy which is very different from the observed in the literature and which is constructed to take advantage of the nature of the problem, discretizing the domain simply by slicing it along the centerline. The novelty of this meshing approach poses the need to develop correct algorithms to perform an automatic (or, at least, semi-automatic) pipe-discretization for the kind of domains which could appear in the field of interest. For academic examples, for which the domains are constructed in a controlled way to test the capabilities of a certain numerical approach, the geometric partition can be easily constructed in an *ad hoc* way, manually defining the slices without further difficulties.

Concerning the ultimate application of the TEPEM in the simulation of blood flow in patient-specific arterial geometries, the manual definition of a pipe-mesh becomes an impractical and complicated task which could also definitely introduce errors in the mesh generation and, therefore, in the accuracy of the results. A pipe-like mesh generation strategy for patient-specific geometries is described in Chapter 5, where a procedure to accomplish this task is proposed.

2.4.2 On the computation of elemental contributions

The pipe-type finite element introduced by the TEPEM differs from other finite element techniques encountered in the literature also for the large number of degrees of freedom. In fact, for axial and transversal interpolants of order s and p, respectively, the total number of degrees of freedom per element scales with $(\mathsf{s}+1)(\mathsf{p}+1)^{d-1}$, with d the dimension of the problem. This, together with the fact that p is chosen to be large, implies that the simulation time is to be largely dominated by the matrix assembling procedure. At the same time, the large number of degrees of freedom per element is related to the ability of the pipe elements to represent complex transversal dynamics rendering a substantial reduction in the total number of unknowns in the problem, and therefore in the conformation of the system of equations.

It is important to emphasize that the set of Chebyshev-Gauss-Lobatto nodes is employed in the formulation of the TEPEM only for the definition of the Lagrangian interpolants aiming to control the spurious oscillations which naturally appear when an interpolation is performed with high-order polynomials defined at equidistant nodes. For the numerical integration of high-order transversal polynomials, a high-order Gauss quadrature is employed ([Stroud and Secrest 1966]).

2.4.3 On alternative choices for field interpolants

A key aspect in the field interpolation within the TEPEM scheme is the clever combination of high-order polynomials to deal with the transversal dynamics and low-order polynomials for the axial dynamics. In the TEPEM we consider Lagrange polynomials as interpolants, both for axial and transversal directions, due to the flexibility of these functions and also because they provide a clear physical interpretation for the degrees of freedom: the nodal value of approximate solution are the values of the field at the corresponding nodes.

Concerning the choice of CGL nodes for the definition of the Lagrange polynomials employed in the transversal interpolation in contrast with equidistant nodes, a detailed comparison showing the good approximation properties of this choice can be found in [Pena 2009] where an analysis is made based on the Lebesgue number for each interpolant strategy. This number, similar to the condition number, measures the quality in an approximation performed through Lagrange polynomials and Lagrange bases in tensorized geometries. In the aforementioned work, the advantage of the use of CGL nodes to define the Lagrange polynomials is clearly highlighted in comparison to the classical Lagrange polynomials defined at equidistributed points.

Other choices for the definition of interpolants are also possible. In [Mansilla Alvarez 2014] it was explored the approximation of two-dimensional problems by combining low order polynomials for the axial direction with high-order polynomials for the transversal one, constructing this last set of functions only by satisfying the boundary conditions at lateral boundary, therefore losing a physical meaning for the degrees of freedom in the finite element. In [Guzzetti 2014] the problem formulation is recast in cylindrical coordinates and then the field interpolants are constructed also in this system of coordinates, which considerably increases the complexity in their definition but manages to deliver a good quality in the approximation.

2.4.4 Dealing with boundary layers

The accurate approximation of boundary layers in the modeling of blood flow is of the utmost importance. because the accuracy in the approximation of flow-related quantities, such as the WSS, depends directly on the behavior of the solution near the arterial wall.

Crosswind boundary layers, which typically develop in fluid flow simulations near walls where no-slip conditions are prescribed, are accounted for by the transversal interpolants. That is, provided the degree of transversal interpolants is adequately chosen, boundary layers will be accurately simulated. However, since the thickness of the boundary layers depends on the flow regime, the a priori definition of the degree of transversal approximation could be debatable.

In Chapter 4, the boundary layer approximation is assessed for Womersley numbers in the range often encountered in hemodynamic simulations with excellent results for moderate polynomial orders in the transversal interpolants. In turn, if the pipe discretization is performed such that a boundary or stagnation point coincides with the axial boundary of one pipe-element, boundary layers taking place in the streamline direction can occur. In such cases, a Petrov-Galerkin finite element approximation or an axial refinement of the mesh can be employed to circumvent spurious oscillations.

For the case of hemodynamics applications (Chapter 5), we propose a meshing algorithm to perform pipe discretization of vascular regions ensuring that only crosswind boundary layers are possible.

2.5 On the transversal adaptivity

The pipe transition element, introduced in the two- and three-dimensional cases, naturally allows for a local adaptive mesh refinement in the transversal direction in order to gradually divide the partition at junctions.

In the three-dimensional case the transition element is conceived by splitting one plane boundary in the reference element $\mathcal{K}^*$ orthogonal to the axial η direction. Despite this, a further modification make it possible the same splitting in the ξ direction, allowing for an uniform transversal densification by consecutively employing the transition element wherever is needed, even in non-branching domains as outlined in Figure 2.24.

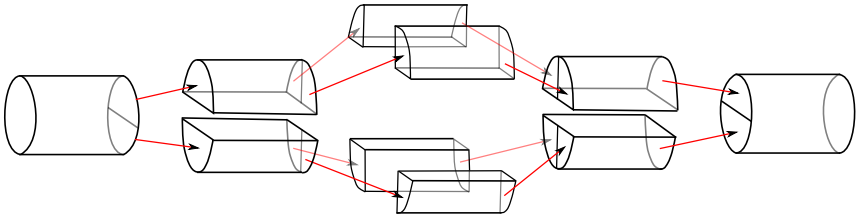

Figure 2.24: Uniform transversal refinement of the pipe-mesh through the consecutive arrangement of transition pipe elements.

The sequential refinement in the mesh, through the coupling between transition and pipe elements in both transversal directions, naturally increases the model capabilities in the selected region, acting like a h-refinement in the scope of standard FEM methods.

Another strategy to improve the transversal capabilities at selected regions is to split the domain of definition of the problem Ω in many subdomains where different transversal orders are selected to approximate the physical field. This type of local adaptivity was explored in [Perotto et al. 2010], in the context of the HiMod technique, where a domain decomposition approach was proposed to couple regions with different enrichment.

Moreover, adaptivity techniques based on *a posteriori* measures of the error in the approximate solution have also been developed in order to adaptively choose the transversal order ([Perotto and Veneziani 2014]). Thus, according to the complexity of the phenomenology, the transversal order is defined at different portions of the domain in an automatic manner. This requires the coupling of pipe elements with different order, which is out of the scope of the present thesis and require significant development.

2.6 Relation with other methodologies

The assumptions for which the TEPEM is expected to perform satisfactorily, particularly the existence of a direction where the phenomenology is richer than in the others, are standard hypotheses introduced in many approaches present in computational mechanics.

To emphasize some characteristics of the proposed approach, here we comment on the similarities and differences of the TEPEM with some well-established techniques.

The p-version of FEM Proposed in [Babuska et al. 1981], the p-version of the FEM consists in fixing a discrete mesh and increasing the model capabilities by augmenting the degree p of the piecewise polynomial approximation.

The TEPEM can be understood as a variant of the p-FEM, assembled on top of a pipe-element partition of the domain of definition of the problem and where the order in the interpolation is modified according to the expected phenomenological dynamics, and where the model capabilities controlled by the polynomial order p is only related to the transversal dynamics.

Unlike the p-FEM, in the TEPEM the polynomials utilized for the approximation of the physical field discretization are not complete, which prevents the latter from featuring the convergence rates of the former.

Semi-analytical FEM The idea of defining a priori the behavior of the physical model across a certain direction, aiming at a reduction in the dimensionality of the domain of definition of the problem, is very old in mechanics. These techniques can be grouped under the name of *Semi-analytical finite element processes* ([Ziekiewicz 1971]) which reduce the computational size of a two- or three-dimensional problem by synthesizing the dynamics across one selected direction through an approximation accomplished by analytical functions, such as that given by a Fourier expansion.

Similar ideas are employed in the TEPEM, in the sense that the a-priori knowledge of the dynamics allows us to choose one direction as the dominant one which is approximated by using a classical FEM approach while the transversal component of the dynamics is also approximated with high-order polynomials, rather than lumped in an approximated analytical way.

Hierarchical model reduction Similar to the TEPEM, the Hierarchical Model Reduction (HiMod) efficiently deals with problems featuring a dominant direction by performing a differentiation in the way in which the fields are approximated, prioritizing the axial (dominant) dynamics through the choice of interpolant functions. For the transverse dynamics, HiMod pursues an *educated basis* approach, where the transverse basis functions are constructed to directly incorporate physical information about the problem, such as the governing equations (or the dominant part of those) and boundary conditions ([Aletti et al. 2017]).

This approach substantially reduces the number of degrees of freedom required in detriment of the presence of an *offline-step* where the transversal basis functions are computed through the solution of Sturm-Liouville eigenvalue problems, which may be non-trivial for non Dirichlet boundary conditions and for general geometries.

2.7 Further remarks

As seen throughout this chapter, even if no specific physical problem was still addressed, the basic idea behind the Transversally Enriched Pipe Element Method (TEPEM) approach is to combine a very special partitioning of the computational domain into *pipe-elements* and the use of low order polynomials for the physical fields in the longitudinal direction of the pipe with high order polynomials for the description across the transversal direction of the domain.

The ingredients presented in this chapter place the TEPEM in-between the orbit of general purpose Finite Element Method (FEM) and the territory of very specific reduced-order strategies, such as HiMod techniques with educated basis functions. Noteworthy, as it will be seen, the TEPEM manages to keep considerable versatility to deal with patient-specific geometries and to yield a reasonably accurate results, while rendering a substantial reduction in the computational cost.

Some of the more remarkable features of the proposed approach are listed below.

The TEPEM family. The family of TEPEM interpolation functions, characterized by the parameters `s` and `p`, approximate the physical fields in such a way that it allows to cautiously tune the model capabilities by adapting the transversal (or axial) polynomial order.

Geometry discretization. The geometrical grid in the TEPEM is composed by pipe-like elements which are defined, in the three-dimensional case, as a combination of piecewise cubic polynomials for the transversal sections with a linear transformation for the axial direction. This approach can easily deal with complex transversal geometries, which is the case of patient-specific arterial vessels in computational hemodynamics. Moreover, it allows a natural and localized mesh adaptation and also a straightforward h-refinement due the simplicity and one-dimensional nature of the mesh.

Boundary conditions. The use of Lagrange polynomial interpolants permits (as it will be seen) the imposition of any kind of boundary condition over the lateral surface of the domain in a very easy and straightforward way. This facilitates the application of the TEPEM in the context of classical computational fluid dynamics in tubular domains, as well as the extension to incorporate fluid-structure interaction phenomena.

Computational cost. The number of degrees of freedom per element in the TEPEM is significantly larger than that of standard FEM. This implies that the simulation time is to be dominated by the matrix assembling procedure (which is highly parallel). Nevertheless, the total number of degrees of freedom in the final system of algebraic equations of the TEPEM is significantly smaller than the case of classical FEM.

The capabilities of the TEPEM approach are exhaustively tested in several examples in the context of scalar transport (Chapter 3) and fluid flow modeling problems (Chapter 4), with particular emphasis in the modeling of the blood flow (Chapter 5).

Chapter 3

TEPEM for transport phenomena

The Transversally Enriched Pipe Element Method (TEPEM), as a generic methodology based in the concept of elements, is developed targeting the application to problems defined in pipe-like regions and featuring a dominant phenomenological direction. Under these assumptions, we claim that the combination of a geometric discretization based on pipe-elements and the transversal enrichment approximation of the physical fields yields a reasonably accurate numerical method with a major reduction in the computational cost when compared with classical FEM strategies, measuring this cost in terms of problem size, computational time and resources needed in the simulation.

In order to highlight the main features of the proposed methodology, in this chapter we apply the TEPEM to approximate the solution of problems in the context of scalar transport phenomena. In particular, we focus our study on the approximation of advection-diffusion problems defined in the two-dimensional space. A detailed description of several aspects of the methodology (such as the discrete structure, elemental contributions of the global problem and sparsity of resulting linear system) is illustrated in this case. Furthermore, convergence studies are carried out.

With the notation and spaces introduced in Chapter 2, in the next section the main characteristics of the discrete problem obtained when employing the TEPEM as approximating strategy are presented. After that, several numerical examples are addressed to study the convergence of the TEPEM against analytical solutions (when available) or a reference solution obtained with FEM in a sufficiently fine triangular mesh with linear interpolants. Also, as a way to study the performance of our approach, a comparison between the accuracy of the TEPEM approximation and that of the FEM approximation in terms of the number of degrees of freedom employed in each strategy is presented. The chapter ends with some final comments summarizing the capabilities of the TEPEM in the scope of scalar transport problems which also hold in other physical situations such as fluid flow modeling.

3.1 The advection-diffusion equation

Let us consider an advection-diffusion-reaction problem set on a generic two-dimensional domain Ω with a dominant direction. Assuming the standard notation for Sobolev spaces, let $\mu \in L^\infty(\Omega)$, with $\mu \geq \mu_0 > 0$ a.e. in Ω, the diffusivity coefficient and $\boldsymbol{\beta} \in [L^\infty(\Omega)]^2$ the convective field. Furthermore, we assume $\nabla \cdot \boldsymbol{\beta} = 0$ in Ω and a forcing term f.

Then, the problem reads: Find $u \in C^2(\Omega)$ such that

$$\begin{cases} -\nabla \cdot (\mu \nabla u) + \boldsymbol{\beta} \cdot \nabla u = f & \text{in } \Omega \\ \mathcal{B}u = \bar{u} & \text{on } \Gamma_D \\ \mu \partial_n u = g & \text{on } \Gamma_N \end{cases} \tag{3.1}$$

with Γ_N and Γ_D portions of the boundary $\partial\Omega$, $\mathcal{B}$ an operator defining the Dirichlet boundary conditions and g defined over Γ_N stands for the Neumann data.

The former equation can be recast in a variational form, resulting in the problem: Find $u \in \mathcal{U}$ such that

$$(\mathcal{L}u, \hat{u})_{\mathcal{Q}' \times \mathcal{Q}} = F(\hat{u}) \qquad \forall\, \hat{u} \in \mathcal{V} \tag{3.2}$$

where $\mathcal{U} = \{u \in \mathcal{Q} : \mathcal{B}u = \bar{u}\}$ is the set of admissible solutions, $\mathcal{V}$ the subspace of admissible variations, $\mathcal{L} : \mathcal{Q} \to \mathcal{Q}'$ stands for the differential operator $\mathcal{L}u = -\nabla \cdot (\mu \nabla u) + \boldsymbol{\beta} \cdot \nabla u$, from the Hilbert space $\mathcal{Q} \subset \mathcal{U}$ (whose definition depends on the boundary conditions) to its dual $\mathcal{Q}'$, and $\mathcal{B}u = \bar{u}$ denotes essential boundary conditions, possibly coexistent on different portions of $\partial\Omega$. Moreover, $(\cdot, \cdot)_{\mathcal{Q}' \times \mathcal{Q}}$ is a duality product defining the equilibrium state involving the operator $\mathcal{L}(\cdot)$. Assuming the case in which the essential boundary conditions are homogeneous, i.e. $\bar{u} = 0$, the problem can be rewritten as: Find $u \in \mathcal{V}$ such that

$$a(u, \hat{u}) = F(\hat{u}) \qquad \forall\, \hat{u} \in \mathcal{V} \tag{3.3}$$

where $a : \mathcal{V} \times \mathcal{V} \to \mathbb{R}$ is a bilinear form related to the differential operator $\mathcal{L}$, $F : \mathcal{V} \to \mathbb{R}$ is a linear functional depending on the data f defined in Ω and g, defined in Γ_N, is naturally embedded in the problem. This is, the Equation (3.3) can be explicitly as

$$\int_\Omega \left(\mu \nabla u \cdot \nabla \hat{u} + (\boldsymbol{\beta} \cdot \nabla u)\, \hat{u} \right) d\Omega = \int_\Omega f \hat{u}\, d\Omega + \int_{\Gamma_N} g \hat{u}\, d\Gamma \qquad \forall\, \hat{u} \in \mathcal{V} \tag{3.4}$$

where Γ_N is the portion of the boundary of Ω where the natural boundary conditions are considered. With the assumptions imposed over the coefficients, the well posedness of the problem follows from the *Lax-Milgram Lemma* ([Evans 1997, Brezis 2010]).

3.1.1 The discrete problem

To employ the Transversally Enriched Pipe Element Method to approximate the solution of the former problem, the first step is to perform a pipe-discretization of the domain, aligning the elements along the dominant direction according to the phenomenology. To this, let us assume that the geometrical domain Ω follows the setting presented in Figure 3.1, where the dominant direction is coincident with the dotted line and the partition is constructed following the schematic division of the domain shown in such figure.

Let us denote by $\mathcal{T}_h(\Omega) = \{K_i; i = 1, \cdots, \mathrm{n_{el}}\}$ such partition. In this case we have only considered simple pipe elements, but transition pipe elements are also allowed. This mesh must satisfy the relations

$$\Omega = \bigcup_{\mathcal{K}_i \in \mathcal{T}_h(\Omega)} \overline{\mathcal{K}}_i \qquad \text{and} \qquad \mathcal{K}_i^\circ \cap \mathcal{K}_j^\circ = \emptyset \qquad i \neq j \tag{3.5}$$

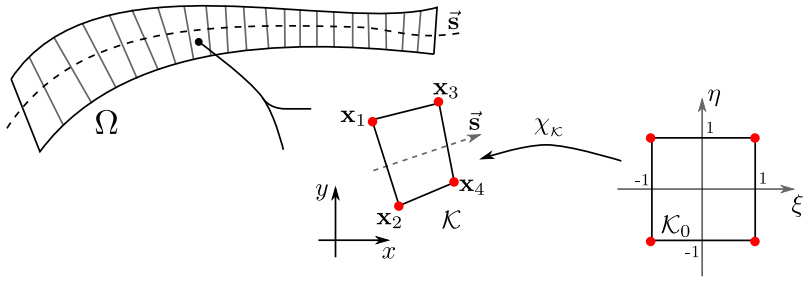

Figure 3.1: TEPEM mesh of domain Ω based on pipe-type elements. The dotted line in Ω stands for the dominant direction of the dynamics. Vector $\vec{\mathbf{s}}$ stands for the axial direction which is related with the $\eta-$axis in the reference element.

Once the pipe discretization of the domain Ω to approximate the solution of the continuous problem statement in Equation (3.4) is established, for a fixed integer value p, the discrete space is defined as

$$\mathcal{V}_h = \mathcal{V} \cap \mathbb{T}_h^{\mathsf{p},1} \cap C(\overline{\Omega}) \tag{3.6}$$

where $\mathbb{T}_h^{\mathsf{p},1}$ is the space of transversally enriched functions defined in each pipe element of $\mathcal{T}_h(\Omega)$, of order p in the transversal direction and where the interpolation in the axial direction is performed through linear polynomials. This space, introduced in the Chapter 2, is characterized as

$$\mathbb{T}_h^{\mathsf{p},1} = \left\{ v \in H^1(\Omega) : v \circ \chi(\boldsymbol{\xi}) = \sum_{k=1}^{2} \sum_{i=1}^{\mathsf{p}+1} v_{ik} \phi_i(\xi) \varphi_k(\eta),\ \mathcal{K} \in \mathcal{T}_h(\Omega) \right\} \tag{3.7}$$

with χ the geometrical mapping between a pipe-element $\mathcal{K}$ and the reference element $\mathcal{K}_0$, $\{\varphi_k, k = 1, 2\}$ the Lagrangian basis for $\mathbb{P}_1$ and $\{\phi_i, i = 1, \ldots, \mathsf{p}+1\}$ the Lagrangian basis for $\mathbb{P}_\mathsf{p}$, both defined at the CGL nodes in $[-1, 1]$.

With the introduction of the discrete space where an approximate solution is to be sought, the discrete counterpart of Equation (3.4) reads as: Find $u_\mathrm{T} \in \mathcal{V}_h$ such that

$$\int_\Omega \left(\mu \nabla u_\mathrm{T} \cdot \nabla \hat{u} + (\boldsymbol{\beta} \cdot \nabla u_\mathrm{T})\, \hat{u} \right) d\Omega = \int_\Omega f \hat{u}\, d\Omega + \int_{\Gamma_N} g \hat{u}\, d\Gamma \qquad \forall\, \hat{u} \in \mathcal{V}_h \tag{3.8}$$

The well-posedness here immediately stems from the conformity of the discrete space $\mathcal{V}_h \subset \mathcal{V}$ and the well-posedness of the continuous problem. Here, as usual, the notation u_T stands for the approximation of the field u when utilizing the TEPEM as the approximation scheme. From here, the process to obtain a matrix structure equivalent to the discrete problem follows the same procedure than FEM schemes, that is, the computation of elemental contributions by exploiting the locality of the compact support of field interpolants (axial interpolants in the TEPEM case).

3.1.2 Elemental contributions

The discrete problem in compact form can be expressed in term of the restrictions in $\mathcal{V}_h$ of the bilinear form $a : \mathcal{V} \times \mathcal{V} \to \mathbb{R}$ and the functional $F : \mathcal{V} \to \mathbb{R}$ as: Find $u_{\mathrm{T}} \in \mathcal{V}_h$ such that

$$a(u_{\mathrm{T}}, \hat{u}) = F(\hat{u}) \qquad \forall\, \hat{u} \in \mathcal{V}_h \tag{3.9}$$

where each term can be computed through the corresponding contribution in each pipe-element. For example, the bilinear form is expressed as

$$a(u_{\mathrm{T}}, \hat{u}) = \sum_{\mathcal{K} \in \mathcal{T}_h(\Omega)} a_{\mathcal{K}}(u_{\mathrm{T}}, \hat{u}) \qquad \forall\, \hat{u} \in \mathcal{V}_h \tag{3.10}$$

where $a_{\mathcal{K}} : \mathcal{V} \times \mathcal{V} \to \mathbb{R}$ is the restriction of $a(\cdot, \cdot)$ to the pipe-element $\mathcal{K}$. As detailed in Figure 3.1, and also as introduced in Section 2.2, each pipe-element $\mathcal{K}$ is determined by four geometrical nodes. Denoting these nodes by $\{\mathbf{x}_i : i = 1, \dots 4\}$, the relation between $\mathcal{K}$ and the reference element $\mathcal{K}_0$ is established through the mapping

$$\chi(\boldsymbol{\xi}) = \sum_{i=1}^{4} \mathbf{x}_i G_i(\boldsymbol{\xi}) \tag{3.11}$$

where

$$\begin{aligned} G_1(\boldsymbol{\xi}) &= -0.25(1-\xi)(1-\eta) \qquad & G_2(\boldsymbol{\xi}) &= 0.25(1+\xi)(1-\eta) \\ G_3(\boldsymbol{\xi}) &= -0.25(1-\xi)(1+\eta) \qquad & G_4(\boldsymbol{\xi}) &= 0.25(1+\xi)(1+\eta) \end{aligned} \tag{3.12}$$

Each term in the $a_{\mathcal{K}}(\cdot, \cdot)$, defined in the actual pipe-element $\mathcal{K}$, can be recast in the reference element $\mathcal{K}_0 = [-1, 1]^2$ through the geometrical mapping $\chi : \mathcal{K}_0 \to \mathcal{K}$ and the relations become

$$\begin{aligned} \int_{\mathcal{K}} \mu(\mathbf{x}) \nabla_{\mathbf{x}} u_{\mathrm{T}} \cdot \nabla_{\mathbf{x}} \hat{u}\, d\mathcal{K} &= \int_{\mathcal{K}_0} \mu \circ \chi(\boldsymbol{\xi}) J^{-T} \nabla_{\boldsymbol{\xi}} u_{\mathrm{T}} \cdot J^{-T} \nabla_{\boldsymbol{\xi}} \hat{u}\, |\det J|\, d\mathcal{K}_0 \\ \int_{\mathcal{K}} \left(\boldsymbol{\beta}(\mathbf{x}) \cdot \nabla_{\mathbf{x}} u_{\mathrm{T}}\right) \hat{u}\, d\mathcal{K} &= \int_{\mathcal{K}_0} \left(\boldsymbol{\beta} \circ \chi(\boldsymbol{\xi}) \cdot J^{-T} \nabla_{\boldsymbol{\xi}} u_{\mathrm{T}}\right) \hat{u}\, |\det J|\, d\mathcal{K}_0 \end{aligned} \tag{3.13}$$

where $\nabla_{\mathbf{x}}(\cdot)$ ($\nabla_{\boldsymbol{\xi}}(\cdot)$) stands for the gradient in the reference element configuration. The transformation of the pipe-element to the material coordinates is carried out through the jacobian matrix J expressed as

$$J = \nabla_{\boldsymbol{\xi}} \chi = \sum_{i=1}^{4} \begin{bmatrix} x_i \partial_\xi G_i(\boldsymbol{\xi}) & x_i \partial_\eta G_i(\boldsymbol{\xi}) \\ y_i \partial_\xi G_i(\boldsymbol{\xi}) & y_i \partial_\eta G_i(\boldsymbol{\xi}) \end{bmatrix} \tag{3.14}$$

where

$$\begin{aligned} \nabla_{\boldsymbol{\xi}} G_1 &= \left[-\frac{1}{4}(1-\eta), -\frac{1}{4}(1-\xi)\right] \qquad & \nabla_{\boldsymbol{\xi}} G_2 &= \left[\frac{1}{4}(1-\eta), -\frac{1}{4}(1+\xi)\right] \\ \nabla_{\boldsymbol{\xi}} G_3 &= \left[-\frac{1}{4}(1+\eta), \frac{1}{4}(1-\xi)\right] \qquad & \nabla_{\boldsymbol{\xi}} G_4 &= \left[\frac{1}{4}(1+\eta), \frac{1}{4}(1+\xi)\right] \end{aligned} \tag{3.15}$$

By the definition of the discrete space $\mathcal{V}_h$, for each function $v \in \mathcal{V}_h$ there exist real values $\{v_{ik} : i = 1, 2; k = 1, \ldots, \mathsf{p}+1\}$ such that in the pipe-element $\mathcal{K}$ the following relation holds

$$v \circ \chi(\boldsymbol{\xi}) = \sum_{k=1}^{2} \sum_{i=1}^{\mathsf{p}+1} v_{ik} \phi_i(\xi) \varphi_k(\eta) = \sum_{j=1}^{2(\mathsf{p}+1)} v_j \psi_j(\boldsymbol{\xi}). \tag{3.16}$$

Thus, by expressing

$$u_{\mathrm{T}} \circ \chi(\boldsymbol{\xi}) = \sum_{j=1}^{2(\mathsf{p}+1)} u_j \psi_j(\boldsymbol{\xi}) \qquad \hat{u}_{\mathrm{T}} \circ \chi(\boldsymbol{\xi}) = \sum_{i=1}^{2(\mathsf{p}+1)} \hat{u}_i \psi_i(\boldsymbol{\xi}), \tag{3.17}$$

we can recast the form $a_{\mathcal{K}}(u_{\mathrm{T}}, \hat{u})$, employing the relations in Equation (3.13), as

$$\begin{aligned} a_{\mathcal{K}}(u_{\mathrm{T}}, \hat{u}) &= \int_{\mathcal{K}} \left[\mu(\mathbf{x}) \nabla_{\mathbf{x}} u_{\mathrm{T}} \cdot \nabla_{\mathbf{x}} \hat{u} + (\boldsymbol{\beta}(\mathbf{x}) \cdot \nabla_{\mathbf{x}} u_{\mathrm{T}})\, \hat{u} \right] d\mathcal{K} \\ &= \int_{\mathcal{K}_0} \left[\hat{\mu}(\boldsymbol{\xi}) J^{-T} \nabla_{\boldsymbol{\xi}} u_{\mathrm{T}} \cdot J^{-T} \nabla_{\boldsymbol{\xi}} \hat{u} + \left(\hat{\boldsymbol{\beta}}(\boldsymbol{\xi}) \cdot J^{-T} \nabla_{\boldsymbol{\xi}} u_{\mathrm{T}} \right) \hat{u} \right] |\det J|\, d\mathcal{K}_0 \\ &= \sum_{i=1}^{2(\mathsf{p}+1)} \sum_{j=1}^{2(\mathsf{p}+1)} u_j \hat{u}_i A_{ij}^{\mathcal{K}} \end{aligned}$$

with

$$A_{ij}^{\mathcal{K}} = \int_{\mathcal{K}_0} \left[\hat{\mu}(\boldsymbol{\xi}) J^{-T} \nabla_{\boldsymbol{\xi}} \psi_j \cdot J^{-T} \nabla_{\boldsymbol{\xi}} \psi_i + \left(\hat{\boldsymbol{\beta}}(\boldsymbol{\xi}) \cdot J^{-T} \nabla_{\boldsymbol{\xi}} \psi_j \right) \psi_i \right] |\det J|\, d\mathcal{K}_0 \tag{3.18}$$

Here the notation $\hat{(\cdot)}$ stands for the field in $(\cdot)$ expressed in the reference element coordinates, this is $\hat{(\cdot)}(\boldsymbol{\xi}) = (\cdot) \circ \chi(\boldsymbol{\xi})$.

Analogously, the elemental contribution of the forcing term $F : \mathcal{V} \to \mathbb{R}$ can be written as

$$\begin{aligned} F_{\mathcal{K}}(\hat{u}) &= \int_{\mathcal{K}} f \hat{u}\, d\mathcal{K} + \int_{\Gamma_N \cap \mathcal{K}} g \hat{u}\, d\Gamma \\ &= \int_{\mathcal{K}_0} f \circ \chi(\boldsymbol{\xi}) \hat{u} |\det J|\, \mathcal{K}_0 + \int_{\Gamma_0} g \circ \chi(\boldsymbol{\xi}) \hat{u} \| J^T \mathbf{n}_0 \| |\det J|\, ds \\ &= \sum_{i=1}^{2(\mathsf{p}+1)} \hat{u}_i F_i^{\mathcal{K}} \end{aligned} \tag{3.19}$$

where Γ_0 is the portion of $\partial\mathcal{K}_0$ such that $\chi(\Gamma_0) = \Gamma_N \cap \mathcal{K}$, $\mathbf{n}_0$ the outward unit normal to Γ_0, and

$$F_i^{\mathcal{K}} = \int_{\mathcal{K}_0} f \circ \chi(\boldsymbol{\xi}) \psi_i |\det J|\, \mathcal{K}_0 + \int_{\Gamma_0} g \circ \chi(\boldsymbol{\xi}) \psi_i \| J^T \mathbf{n}_0 \| |\det J|\, ds. \tag{3.20}$$

3.1.3 Numerical integration

An important numerical aspect in the discretization of the scalar transport problem by employing the TEPEM is the correct numerical quadrature rules to exactly integrate the elemental contributions. Because of the polynomial nature of the interpolants, we can perform the numerical integration using standard Gauss quadrature rules for both axial and transversal directions.

Even when the numerical quadrature is a standard process in schemes based on the element concept, special attention must be given to the quadrature along the transversal direction due to the use of high-order interpolants. For example, let us consider the elemental contribution of the convective velocity (second integral in Equation (3.13)). Considering the convective field ($\boldsymbol{\beta}$) constant in $\mathcal{K}$, the integrating term in $\mathcal{K}_0$ is an element of the space conformed by polynomials up to degree 2 along the axial direction and up to degree $2\mathsf{p}$ on the transversal direction (space denoted as $\mathbb{P}_{2,2\mathsf{p}}$) and the numerical rule to integrate this term has the form

$$\int_{\mathcal{K}_0} v(\xi,\eta)\, d\mathcal{K}_0 = \sum_{i=1}^{2}\sum_{j=1}^{\mathsf{p}+1} \omega_i \alpha_j v(\xi_i,\eta_j) \tag{3.21}$$

where $\{(\omega_i,\xi_i), i = 1,2\}$ is the classical pair of weights and points for the Gauss quadrature rule of order $n = 2$, this is

$$(\omega_1,\xi_1) = \left(1, \frac{-1}{\sqrt{3}}\right) \qquad (\omega_2,\xi_2) = \left(1, \frac{1}{\sqrt{3}}\right) \tag{3.22}$$

and $\{(\alpha_j,\eta_j), j = 1,\ldots,\mathsf{p}+1\}$ is the pair of weights and points for the Gauss quadrature rule of order $n = \mathsf{p}+1$. These quadrature rules have been reported in literature, see for example [Stroud and Secrest 1966]. As it can be appreciated, the numerical integration of a function within the TEPEM scope requires a large number of evaluations if compared with classical low order hFEM strategies. Nevertheless, it results in a reduction in the number of elements in the pipe-element mesh compared with the elements in a triangular mesh in the two-dimensional case, and therefore in the total number of unknowns in the problem. Furthermore, since the assembling procedure can be efficiently parallelized, this step is not regarded as being a bottleneck. These ponderations will be confirmed through the numerical experiments, where the reduction in the problem while maintaining accurate results will be shown.

3.1.4 System of algebraic equations

From an algebraic viewpoint, the TEPEM discretization leads to a system of linear equations that is written in matrix form as:

$$\mathbf{A}\mathbf{d} = \mathbf{F} \tag{3.23}$$

where $\mathbf{A} \in \mathbb{R}^{D\times D}$ is the stiffness matrix, $\mathbf{d} \in \mathbb{R}^{D}$ is the vector of unknown coefficients, $\mathbf{F} \in \mathbb{R}^{D}$ is the load vector associated to the linear functional F and $D = (\mathrm{n}_{\mathrm{el}}+1)(\mathsf{p}+1)$. Each of these entities is computed by assembling the local contributions at each element (pipe-element in the TEPEM case) of the mesh.

The ordering of the degrees of freedom in this problem is performed such that we obtain a block tridiagonal matrix as shown in Figure 3.2. This is possible by noting the (almost) 1D architecture of the pipe-mesh. This algebraic structure is formed when considering the transversal interpolation as an inner summation in the assembling procedure and the axial interpolation as the outer one.

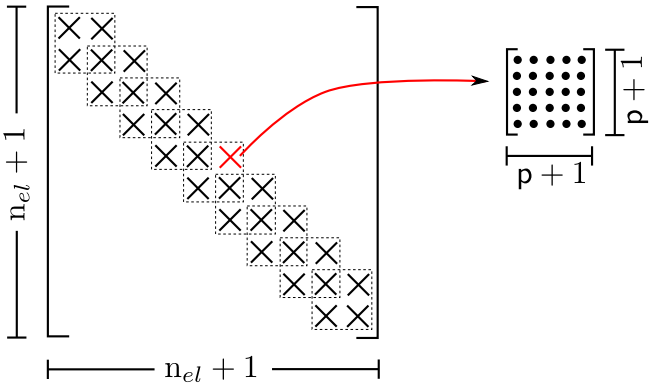

Figure 3.2: Algebraic structure of the global matrix in the 2D ADR problem. Here the dotted square stands for the local contribution computed at each pipe-element of the geometrical discretization.

Measuring the sparsity in the linear system as the ratio between the zero entries of the matrix and the total number of elements, we can compute directly this quantity for the TEPEM by the relation

$$\text{sparsity} = 1 - \frac{3n_{el}+1}{(n_{el}+1)^2} \tag{3.24}$$

i.e., the sparsity of the system provided by the TEPEM is only dependent on the axial discretization. The transversal order p characterizes the matrix bandwidth. A comparison between the matrix sparsity when employed the TEPEM against the FEM is shown in Figure 3.3.

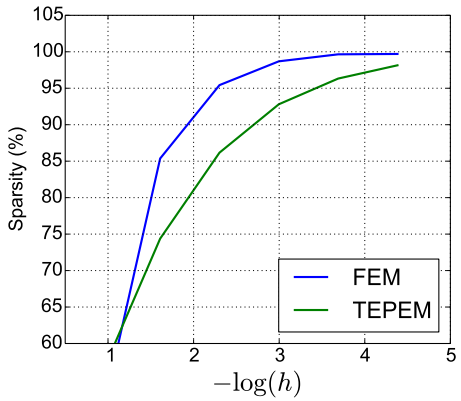

Figure 3.3: Comparison in the sparsity of the global matrix obtained when the TEPEM and FEM schemes are employed.

3.2 Approximation properties

The well posedness of the continuous problem: Find $u \in \mathcal{V}$ such that

$$a(u, \hat{u}) = F(\hat{u}) \qquad \forall\, \hat{u} \in \mathcal{V} \tag{3.25}$$

is guaranteed by ensuring that both the bilinear form $a : \mathcal{V} \times \mathcal{V} \to \mathbb{R}$ and the functional $F : \mathcal{V} \to \mathbb{R}$ satisfy the hypotheses in the Lax-Milgram lemma:

i) $a(\cdot, \cdot)$ is continuous, i.e., there exist $M > 0$ such that $|a(w, v)| \leq M\|w\|_{\mathcal{V}}\|v\|_{\mathcal{V}}$ for all $w, v \in \mathcal{V}$.

ii) $a(\cdot, \cdot)$ is coercive, i.e., there exist $\alpha > 0$ such that $a(v, v) \geq \alpha\|v\|^2_{\mathcal{V}}$ for all $v \in \mathcal{V}$.

iii) $F \in \mathcal{V}'$, i.e. $F(\cdot)$ is a linear and continuous functional.

In this scenario, it is possible to guarantee the existence of a unique solution $u_0 \in \mathcal{V}$ of the continuous problem. Moreover, this function u_0 satisfy

$$\|u_0\|_{\mathcal{V}} \leq \frac{1}{\alpha}\|F\|_{\mathcal{V}'}. \tag{3.26}$$

For the discrete problem: Find $u_{\mathrm{T}} \in \mathcal{V}_h$ such that

$$a(u_{\mathrm{T}}, \hat{u}) = F(\hat{u}) \qquad \forall\, \hat{u} \in \mathcal{V}_h \tag{3.27}$$

where $\mathcal{V}_h = \mathcal{V} \cap \mathbb{T}_h^{\mathsf{p},1} \cap C(\overline{\Omega})$, once the conformity of the discrete space holds (i.e. $\mathcal{V}_h \subset \mathcal{V}$) the continuous and coercive characteristics of the bilinear form are maintained also for the finite-dimensional space. This also holds for the functional $F : \mathcal{V}_h \to \mathbb{R}$. With this, it is guaranteed the existence of a unique solution $u_{\mathrm{T}} \in \mathcal{V}_h$ for the discrete problem.

The relation between u_0 and u_{T}, the approximation error, can be expressed in terms of the continuity and coercive constants as

$$\|u_0 - u_{\mathrm{T}}\|_{\mathcal{V}} \leq \frac{M}{\alpha} \inf_{v \in \mathcal{V}_h} \|u_0 - v\|_{\mathcal{V}} \tag{3.28}$$

By virtue of this last estimate, the convergence of the TEPEM follows from the fact that $\mathcal{V}_h$ is dense in $\mathcal{V}$. This is, for each $v \in \mathcal{V}$ it is satisfied:

$$\lim_{h \to 0} \lim_{\mathsf{p} \to \infty} \inf_{v_h \in \mathcal{V}_h} \|v - v_h\|_{\mathcal{V}} = 0. \tag{3.29}$$

3.2.1 Convergence estimates

An interesting characteristic of high-order schemes, and possibly one of the major reasons for their popularity, is the capacity to achieve exponential convergence rates. The interpolation error of a function $u \in H^m(\Omega)$ in the L^2-norm and H^1-norm is

$$\|u - u_I\|_{L^2(\Omega)} \leq c\mathsf{p}^{-m}\|u^{(m)}\|_{L^2(\Omega)}, \qquad \|u - u_I\|_{H^1(\Omega)} \leq c\mathsf{p}^{1-m}\|u^{(m)}\|_{L^2(\Omega)}. \tag{3.30}$$

These results, available in [Canuto et al. 1988, 2010], reveal that we can achieve an exponential decay in the interpolation error if the approximating function is smooth enough.

Regarding a mixed-order interpolation scheme, like the one proposed in the TEPEM, no *a priori* estimates are available in the literature yet, but some similar schemes can provide insights about the convergence behavior. Specifically, in [Canuto et al. 1982] it was proposed a hybrid finite element and Fourier interpolation scheme and it was established upper bounds for the approximation error, in function of the axial characteristic length (h) and the degree of trigonometric polynomials (N), as

$$\begin{aligned} \|u - u_h\|_{L^2(\Omega)} &\leq c\left(h^2 + N^{-2}\right)\|u\|_{H^2(\Omega)}, \\ \|u - u_h\|_{H^1(\Omega)} &\leq c\left(h^1 + N^{-1}\right)\|u\|_{H^2(\Omega)}, \end{aligned} \tag{3.31}$$

with u_h the approximate solution and c a constant independent of h, N and u. That is, in the hybrid FEM/Fourier scheme, we can infer a convergence rate to be quadratic for the L^2-norm and linear for the H^1-norm, with respect to both N^{-1} and h. Similar estimates are also available within the Hierarchical Modeling (HiMod) technique, where estimates also follow the relation quadratic and linear for the L^2-norm and H^1-norm, in terms of the polynomial order employed for the transversal interpolants (p^{-1}) and the finite element mesh size (h) (see, [Aletti et al. 2017]).

It is important to highlight that in these both contexts, in the combined finite element/Fourier interpolation as well as in the HiMod, the estimates in L^2 and H^1-norm were achieved for a general elliptic problem without considering the presence of a dominant direction or a sort of mixed regularity for the approximating function u. For the TEPEM, whenever a full decoupling between axial and transversal dynamics occurs, we can expect a combination of linear convergence in terms of the axial mesh size (h) with an exponential convergence order in terms of the the polynomial order employed for the approximation of the transversal dynamics (p). For a general case, we can infer a convergence rate like in the estimates given by Equation (3.31) with a possible improvement due to the nature of the problems in which we are interested in. Several numerical examples will be addressed in next section to provide a complete picture of the convergence rates of the TEPEM for scalar problems.

3.2.2 Stabilization techniques

When approximating the solution of the advection-diffusion equation, it is well-known that the Galerkin method can provide unstable results when the diffusion term is largely dominated by the convection one and the element characteristic size h is not small enough to properly model boundary layers. This is explained considering the optimal error estimate in Equation (3.28) since, up to a constant, the upper bound is determined by

$$\frac{M}{\alpha} = \frac{\|\mu\|_{L^\infty(\Omega)} + \|\boldsymbol{\beta}\|_{L^\infty(\Omega)}}{\mu_0}, \tag{3.32}$$

which grows with ratio $\dfrac{\|\boldsymbol{\beta}\|_{L^\infty(\Omega)}}{\|\mu\|_{L^\infty(\Omega)}}$. A non-dimensional parameter, which measures the extent of the domination of the diffusion term over the convection term at the discrete level, is the local Péclet number, defined as

$$\mathrm{Pe}_{\mathcal{K}} = \frac{\|\boldsymbol{\beta}\|_{L^\infty(\Omega)} h_{\mathcal{K}}}{2\|\mu\|_{L^\infty(\Omega)}} \tag{3.33}$$

where $h_{\mathcal{K}} = diam(\mathcal{K})$ is the element dimension in the mesh, defined for the element $\mathcal{K}$. When $\mathrm{Pe} \gg 1$, the standard Galerkin formulation produces an unstable discretization of the differential non-symmetric operator if the solution presents regions with high gradients. Although a detailed description of stabilization schemes within the TEPEM context is out of the scope of this work, it is important to stress the possibility to integrating the proposed methodology with stabilization techniques available in the literature.

A popular alternative to overcome the unphysical solutions in convection dominated problems is the so-called *Streamline Upwind Petrov-Galerkin (SUPG)* method proposed in [Hughes and Brooks 1979, Brooks and Hughes 1982]. In the SUPG, the admissible variation is modified and the weighted formulation has the form:

$$\left(-\nabla \cdot (\mu \nabla u) + \boldsymbol{\beta} \cdot \nabla u - f, \hat{u} + \frac{k_s}{\|\boldsymbol{\beta}\|^2} \boldsymbol{\beta} \cdot \nabla \hat{u} \right)_{L^2(\Omega)} = 0 \qquad \forall\, \hat{u} \in \mathcal{V}. \tag{3.34}$$

Here, the parameter k_s is defined in terms of the Péclet number α_s related with the dominant direction $\vec{\mathbf{s}}$ as

$$k_s = \mu \alpha_s \left[\coth \alpha_s - \frac{1}{\alpha_s} \right], \qquad \alpha_s = \frac{1}{2\mu} \boldsymbol{\beta} \cdot \vec{\mathbf{s}}\, h. \tag{3.35}$$

Note that the stabilization is performed in a similar way that stabilization in one-dimensional problems, considering that the high gradients in the solution are presented only in the axial direction.

3.2.3 Condition number

The ratio between the maximum and minimum eigenvalues of a matrix A is defined as the spectral condition number of the matrix. It plays crucial roles in many aspects of scientific computing. Classical estimates of the condition number are available in the literature when considering the matrix A as being the mass matrix associated to the discretization of a bilinear form $a : \mathcal{V}_h \times \mathcal{V}_h \to \mathbb{R}$ ([Fried 1972, Ciarlet 1978, Melenk 2002]). For the h- and p-version of the FEM, the condition number $c(A)$ is bounded by the following relations

$$c(A) \leq ch^{-2}, \qquad c(A) \leq c\mathsf{p}^4 \tag{3.36}$$

where h is the element size in and p the polynomial order.

For a mixed-interpolation scheme like the TEPEM, in which the accuracy on the approximation depends upon both axial element size and the transversal order of the interpolants, the condition number is expected to depend on these two parameters. To numerically test this hypothesis, the condition number for the matrix A is computed on the domain $\Omega = [0, 1]^2$ and considering the pipe meshes constructed as presented in Figure 3.4. In Figure 3.5, is observed a linear increase of the condition number in terms of the transversal order and quadratic in terms of the axial length. In the same figure, it is also possible to appreciate an almost linear relation between the condition number and the total number of degrees of freedom when increasing both h and p in the TEPEM.

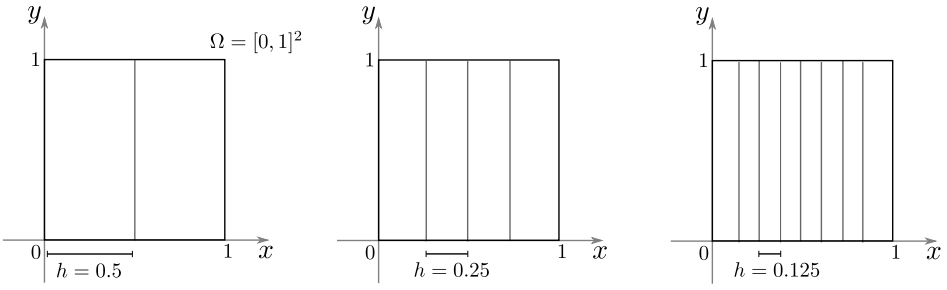

Figure 3.4: Geometry for the condition number test. Pipe element meshes are also outlined.

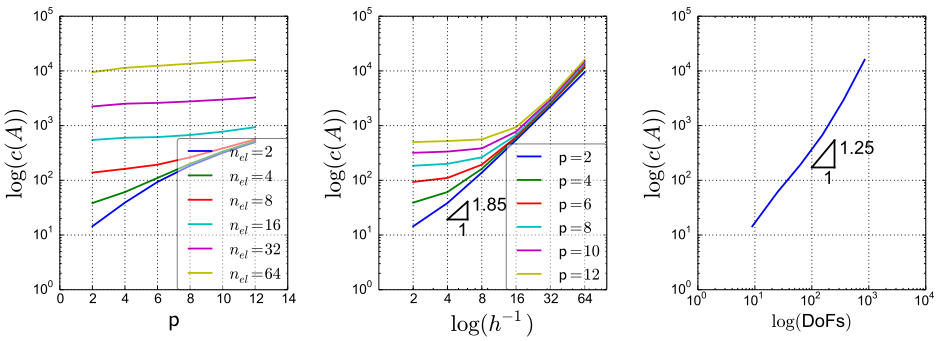

Figure 3.5: Condition number of the mass matrix for the TEPEM approach: Comparison against axial length of the pipe-mesh (h), transversal polynomial order p and degrees of freedom (DoFs).

3.3 Numerical verification

In order to highlight the convergence properties of the TEPEM, several numerical experiments are reported in this section. Specifically, we are interested in analyzing the sensitivity of the TEPEM approximation with respect to the axial discretization size h and the transversal order p. This sensitivity is measured in each example by the computation of the approximation error when compared against the analytical solution, when available, or with a reference solution obtained by the FEM approach with a very fine triangular mesh.

The efficiency of the proposed approach is also measured by comparing the computational cost in the numerical simulation against FEM approximations when varying the elemental size. The comparison is performed by counting the total number of degrees of freedom in each approach and the accuracy achieved by the solution as a function of this parameter.

Regarding the computational implementation, the TEPEM approach is implemented in an in-house general purpose parallel solver, written in FORTRAN language and which is under continuous development by the HeMoLab research group. For the construction of the pipe-type mesh, in each example the geometrical discretization is performed *ad-hoc*, manually slicing the geometry along the defined mainstream direction. For the FEM approximation, it is employed the FreeFem software ([Hecht et al. 2005, Pironneau et al. 2006, Hecht 2012]) which is specially developed for the resolution of partial differential equations by the finite element method, and also provides an integrated meshing algorithm to perform triangular discretization on complex geometries.

For a convergence study, classical norm for the L^2-space and seminorm for the H^1-space are employed for scalar functions. For a scalar field $u \in H^1(\Omega)$ we define

$$\|u\|^2_{L^2(\Omega)} = \int_\Omega u^2 \, d\Omega \qquad |u|^2_{H^1(\Omega)} = \|\nabla u\|^2_{L^2(\Omega)} = \int_\Omega \nabla u \cdot \nabla u \, d\Omega \tag{3.37}$$

and, denoting by u_T an approximation for the field u by the TEPEM approach, we consider the following metrics for the relative approximation error as

$$\|u - u_\mathrm{T}\| = \frac{\|u - u_\mathrm{T}\|_{L^2(\Omega)}}{\|u\|_{L^2(\Omega)}} \qquad |u - u_\mathrm{T}| = \frac{\|\nabla u - \nabla u_\mathrm{T}\|_{L^2(\Omega)}}{\|\nabla u\|_{L^2(\Omega)}} \tag{3.38}$$

These metrics are employed to measure the relative error, in L^2-norm and H^1-seminorm, of TEPEM and also FEM solutions for steady state problems. We also consider transient problems, for which the numerical approximation is obtained by combining a finite difference based scheme for the temporal variable and the TEPEM approach for the spatial dimension. Performing a subdivision of the temporal domain $[0, T]$ into a discrete grid $t_0 = 0 < t_1 < \ldots < t_{N_T} = T$, at each temporal step t_i the TEPEM is employed to obtain the approximated field $u_\mathrm{T}(t_i) = u_\mathrm{T}(\mathbf{x}, t_i)$. The former metrics are employed for frozen temporal instants to measure the relative error at these instants. For a global metric of the quality of approximation along the whole simulation, we define the discrete average time error

$$\|u - u_\mathrm{T}\|^2_{(0,T)} = \sum_{n=0}^{N_T} \Delta t_n \left(\frac{\|u(t_n) - u_\mathrm{T}(t_n)\|_{L^2(\Omega)}}{\|u(t_n)\|_{L^2(\Omega)}} \right)^2 \tag{3.39}$$

where $\Delta t_n = t_{n+1} - t_n$ is the step between consecutive time instants.

3.3.1 Discretization of curved domains

One important detail with respect to a consistent comparison between FEM and TEPEM is to guarantee that both schemes are used to solve the same discrete problem and, more difficulty to achieve, in the same geometrical domain. Both approaches, FEM and TEPEM, perform a geometrical discretization of the real geometry Ω by subdividing into finite/pipe elements with linear lateral boundaries which implies in a geometrical error whenever Ω has curved boundaries. However, both methods yield the same approximated geometry concerning the definition of the approximated boundary.

Recall the type of domains we are interested in, pipe-type geometries such as that outlined in Figure 3.1. Then, if lateral boundaries of Ω are piecewise linear we can guarantee an exact geometry representation through a pipe- or triangular-element discretization. For domains with curved lateral boundaries, the adopted strategy is to replace these lateral curves by piecewise linear segments coincident with an initial pipe-element mesh fine enough to consider this new domain Ω_h to be close enough to the original one. This geometrical approximation step is shown in Figure 3.6 where a coarse initial pipe-mesh is employed.

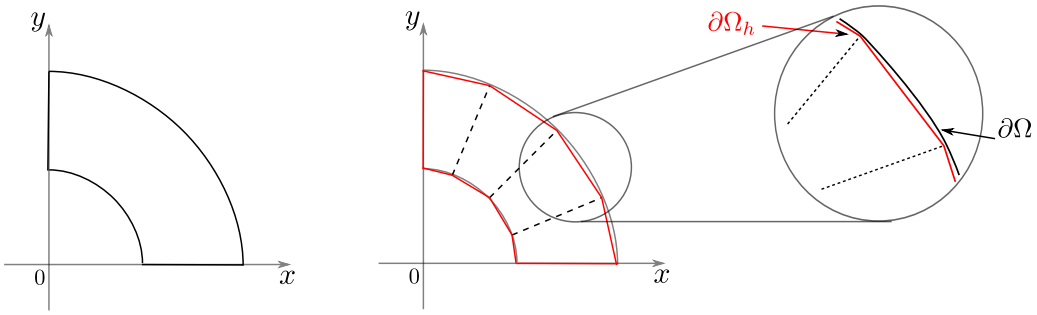

Figure 3.6: Approximation of a curved domain Ω (left) by a domain with piecewise linear boundary Ω_h, highlighted in red (right). The dotted lines demarcate the coarser pipe-element mesh employed for the geometrical approximation.

The pipe-mesh refinement is then performed by axially splitting this initial pipe-mesh. The FEM discretization matches with the Ω_h rendering no geometrical discretization error. An example of both FEM and TEPEM meshes is outlined in Figure 3.7.

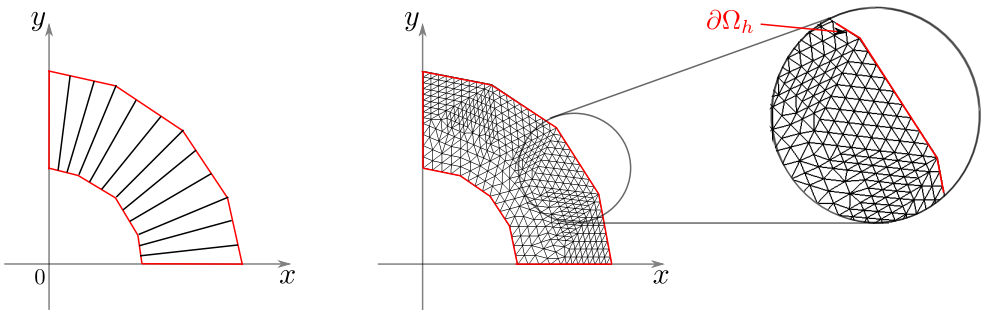

Figure 3.7: Examples of pipe and triangular meshes, for TEPEM and FEM respectively, constructed based in the domain with piecewise linear boundary Ω_h.

3.3.2 Convergence test: Poisson problem

Let us consider the domain Ω as the rectangular region outlined in Figure 3.8, and in this domain we define three Poisson problems such that we manufacture analytical solutions:

(i) A field only with axial dynamics.

(ii) A field with only transversal dynamics.

(iii) A field defined as the product of both former problems.

The goal of this example is to analyze the convergence behavior of the TEPEM, in these three scenarios.

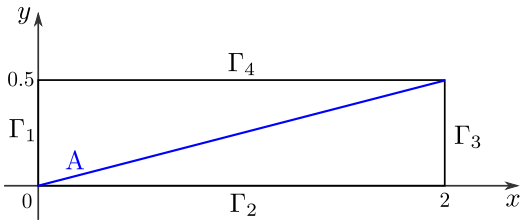

$$\Gamma_1 = \{(x,y) : x = 0, 0 \leq y \leq 0.5\}$$
$$\Gamma_2 = \{(x,y) : 0 \leq x \leq 2, y = 0\}$$
$$\Gamma_3 = \{(x,y) : x = 2, 0 \leq y \leq 0.5\}$$
$$\Gamma_4 = \{(x,y) : 0 \leq x \leq 2, y = 0.5\}$$

Figure 3.8: Domain for the convergence test in the Poisson problem. The boundary $\partial\Omega$ is divided in the four segments Γ_1, Γ_2, Γ_3 and Γ_4. A blue straight segment, denoted by A and highlighted in blue, is selected for a detailed comparison of the TEPEM approximation.

These problems, say *case 1*, *case 2* and *case 3*, correspond to the following variational setting: Find $u \in \mathcal{U}$ such that

$$\int_\Omega \mu \nabla u \cdot \nabla \hat{u} \, d\Omega = \int_\Omega f \hat{u} \, d\Omega \quad \forall \hat{u} \in \mathcal{V}, \tag{3.40}$$

where, as usual, $\mathcal{V}$ stands for the space of admissible variations and $\hat{u}$ is an element of this space. The set of admissible solutions $\mathcal{U}$ as well as the source function f are defined accordingly in each case.

In each problem, we consider a constant diffusion coefficient $\mu = 1$. So, let us specify the three problems next.

Case 1: Homogeneous Dirichlet boundary conditions over $\Gamma_1 \cup \Gamma_3$ and the source term f given by

$$\begin{aligned} f(x,y) = \Bigg[& \left(2 + \left(3\pi + 72\pi^2\right) x - \left(\frac{5}{2}\pi + 36\pi^2\right) x^2 - \frac{1}{2}\pi^2 x^3 + \frac{1}{4}\pi^2 x^4\right) \cos(6\pi x) \\ & + \left(24\pi - 24\pi x - 12\pi^2 x^2 + 6\pi^2 x^3\right) \sin(6\pi x) \Bigg] \exp\left(-\frac{1}{4}\pi x^2\right), \end{aligned} \tag{3.41}$$

which yields the exact solution

$$u(x,y) = x(2-x)\cos(6\pi x)\exp\left(-\frac{1}{4}\pi x^2\right). \tag{3.42}$$

Case 2: Homogeneous Dirichlet boundary conditions over $\Gamma_2 \cup \Gamma_4$ and the source term f given by

$$f(x,y) = (128 + 256\pi - 1024\pi y - 512\pi^2 y + 1024\pi^2 y^2)\exp(-4\pi y), \tag{3.43}$$

which yields the exact solution

$$u(x,y) = 32(1-2y)y\exp(-4\pi y). \tag{3.44}$$

Case 3: Homogeneous Dirichlet boundary conditions over the whole boundary $\partial\Omega$ and the source term f given by the linear combination of the source terms defined in the former cases, such that resulting in the exact solution

$$u(x,y) = [32(1-2y)y\exp(-4\pi y)]\left[x(2-x)\cos(6\pi x)\exp\left(-\frac{1}{4}\pi x^2\right)\right] \tag{3.45}$$

Each case is constructed to accentuate a different dynamics, as can be appreciated in the analytical solution plotted in Figure 3.9. In *Case 1*,the transversal dynamics can be exactly approached by the constant component, so it suggest a convergence depending solely on the axial refinement. In *Case 2* we have the opposite situation because the dynamics is strictly transversal, the axial component is exactly represented by the linear approximation, so that the convergence will depend on the transversal order. Finally, in *Case 3* we combine the others two cases, with a more complex dynamics and for which axial and transversal refinements are required to achieve convergence. Concerning to the geometry, the rectangular domain is exactly represented by a pipe-type discretization. This discrete mesh is composed by n_{el} pipe-elements, with a single element spanning the entire transversal cross-section.

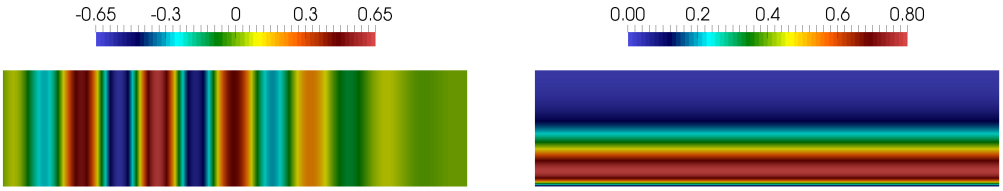

(a) Case 1 solution. $\|u\|_{L^2} = 3.90246 \cdot 10^{-1}$, $\|\nabla u\|_{L^2} = 7.39838 \cdot 10^{0}$

(b) Case 2 solution. $\|u\|_{L^2} = 5.55728 \cdot 10^{-1}$, $\|\nabla u\|_{L^2} = 8.40078 \cdot 10^{0}$

(c) Case 3 solution. $\|u\|_{L^2} = 1.53347 \cdot 10^{-1}$

(d) Case 3 magnitude of the gradient. $\|\nabla u\|_{L^2} = 3.71833 \cdot 10^{0}$

Figure 3.9: Analytical solutions for (a) Case 1, (b) Case 2 and (c-d) Case 3. In each subfigure it is also reported the reference values employed to compute the relative error in the convergence study.

As previously commented, for each case convergence tests are performed with respect to the axial length (h) and to the transversal enrichment order (p). For the axial dynamics in the TEPEM, linear interpolation is employed. For the *Case 1* the convergence is linear with respect to the axial length and, as expected, independent from the transversal order chosen. For the *Case 2* the convergence with respect to the transversal order is exponential and independent from the number of elements in the axial direction.

These results are reported in Table 3.1 where the relative errors are presented as well as the number of degrees of freedom employed in each simulation (for the *Case 1* it was employed $\mathsf{p} = 2$ and for *Case 2* it was employed $\mathrm{n_{el}} = 4$). This information is complemented with the Figure 3.10 where the convergence order for both cases are displayed.

Table 3.1: Comparison of the relative error of TEPEM approximation in L^2-norm and H^1-seminorm for Poisson problem, named *Case 1* and *Case 2*. For each case, the number of degrees of freedom (DoFs) is also reported.

Case 1 ($\mathsf{p} = 2$)				*Case 2* (n_{el}= 4)			
$\mathrm{n_{el}}$	DoFs	$\|u - u_\mathrm{T}\|$	$\|u - u_\mathrm{T}\|$	p	DoFs	$\|u - u_\mathrm{T}\|$	$\|u - u_\mathrm{T}\|$
8	27	$1.10902 \cdot 10^{0}$	$9.57259 \cdot 10^{-1}$	4	25	$2.18789 \cdot 10^{-1}$	$4.01216 \cdot 10^{-1}$
16	51	$4.60486 \cdot 10^{-1}$	$6.33569 \cdot 10^{-1}$	5	30	$7.83213 \cdot 10^{-2}$	$1.72332 \cdot 10^{-1}$
32	99	$1.26689 \cdot 10^{-1}$	$3.38389 \cdot 10^{-1}$	6	35	$2.30509 \cdot 10^{-2}$	$5.85753 \cdot 10^{-2}$
64	195	$3.24445 \cdot 10^{-2}$	$1.70788 \cdot 10^{-1}$	7	40	$5.74755 \cdot 10^{-3}$	$1.68462 \cdot 10^{-2}$
128	387	$8.13772 \cdot 10^{-3}$	$8.16761 \cdot 10^{-2}$	8	45	$1.24187 \cdot 10^{-3}$	$4.69831 \cdot 10^{-3}$
256	771	$2.01829 \cdot 10^{-3}$	$3.74502 \cdot 10^{-2}$	9	50	$2.38339 \cdot 10^{-4}$	$2.52622 \cdot 10^{-3}$
512	1 539	$4.93853 \cdot 10^{-4}$	$1.55572 \cdot 10^{-2}$	10	55	$1.05769 \cdot 10^{-4}$	$2.38255 \cdot 10^{-3}$

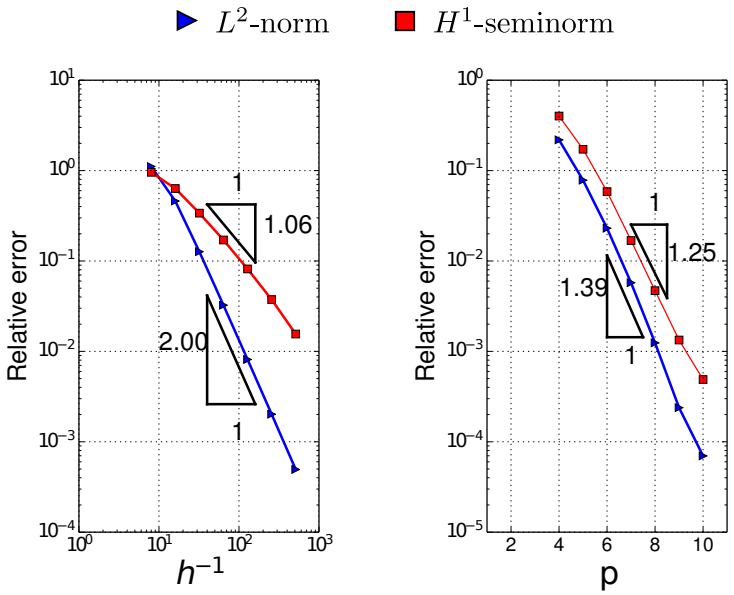

Figure 3.10: Convergence rates for Poisson problem. Errors in *Case 1* (left) with respect to the axial characteristic length (h) and in *Case 2* (right) with respect to the transversal enrichment order (p). In each figure, the relative error in the L^2-norm (▲) and H^1-seminorm (■) are reported.

The *Case 3* is a little more complex in the sense that it requires an increase in the transversal order and also a refinement in the axial length to achieve convergence. A convergence study is also performed in this case, demonstrating the good approximation properties of the TEPEM. The errors in the approximation of the field and also of its derivative, for different combinations of h and p, are documented in Table 3.2.

Table 3.2: Comparison of the relative error of TEPEM approximation in L^2-norm and H^1-seminorm for the *Case 3*.

	n_{el}	64	128	256	512
	h	$3.125 \cdot 10^{-2}$	$1.5625 \cdot 10^{-2}$	$7.8125 \cdot 10^{-3}$	$3.90625 \cdot 10^{-3}$
$\|u - u_T\|$	$\mathsf{p} = 4$	$1.97314 \cdot 10^{-1}$	$1.97618 \cdot 10^{-1}$	$1.97999 \cdot 10^{-1}$	$1.98113 \cdot 10^{-1}$
	$\mathsf{p} = 6$	$3.29639 \cdot 10^{-2}$	$2.20338 \cdot 10^{-2}$	$2.12769 \cdot 10^{-2}$	$2.12556 \cdot 10^{-2}$
	$\mathsf{p} = 8$	$2.58202 \cdot 10^{-2}$	$6.50422 \cdot 10^{-3}$	$1.96229 \cdot 10^{-3}$	$1.23976 \cdot 10^{-3}$
	$\mathsf{p} = 10$	$2.57947 \cdot 10^{-2}$	$6.39766 \cdot 10^{-3}$	$1.56811 \cdot 10^{-3}$	$3.74061 \cdot 10^{-4}$
$\|u - u_T\|$	$\mathsf{p} = 4$	$3.21201 \cdot 10^{-1}$	$2.98247 \cdot 10^{-1}$	$2.92698 \cdot 10^{-1}$	$2.91462 \cdot 10^{-1}$
	$\mathsf{p} = 6$	$1.40748 \cdot 10^{-1}$	$7.54221 \cdot 10^{-2}$	$4.94369 \cdot 10^{-2}$	$4.16181 \cdot 10^{-2}$
	$\mathsf{p} = 8$	$1.34785 \cdot 10^{-1}$	$6.40329 \cdot 10^{-2}$	$2.94602 \cdot 10^{-2}$	$4.52886 \cdot 10^{-3}$
	$\mathsf{p} = 10$	$1.34755 \cdot 10^{-1}$	$6.39758 \cdot 10^{-2}$	$2.93389 \cdot 10^{-2}$	$2.62988 \cdot 10^{-3}$

As expected, for a fixed axial discretization, the approximation is improved when the transversal order is increased but with a lower threshold defined by the model capabilities relatives to that axial mesh. The same pattern appears when analyzing the convergence regarding the axial length, a threshold appears (for a fixed transversal order) which only can be enhanced by increasing the value of p. This saturation behavior, that appears in schemes where the capabilities are depending of more than one parameter (like hp-FEM schemes), is better appreciate in the Figure 3.11 where the linear and exponential convergence, regarding h and p respectively, are affected by a threshold controlled by the other parameter.

The convergence in the TEPEM approximation as well as the predictive capabilities for different values of p are highlighted in Figure 3.12. In that figure, the FEM and TEPEM profiles along the straight segment A (see Figure 3.8) are compared for two different pipe meshes: one the composed by 32 elements and the second one composed by 64 elements. The convergence, in the selected segment, for the field and its derivative are clearly achieved.

For the FEM approximation, we perform a convergence study by analyzing the behavior of the error (in L^2-norm and H^1-seminorm) when refining the triangular mesh. In Table 3.3, we present the error in both norms and also the geometrical characteristics of each triangular mesh. A more direct comparison of the efficiency of the approximation scheme against the TEPEM can be achieved by comparing the error in both schemes against the number of degrees of freedoms. This comparison, outlined in Figure 3.13, expose the larger predictive capabilities of the TEPEM approach when compared to the FEM, not only for the approximation of the primary field but also in the approximation of the derivative which, in the particular case of hemodynamic simulations, play a fundamental role in the computation of some derived-bases quantities.

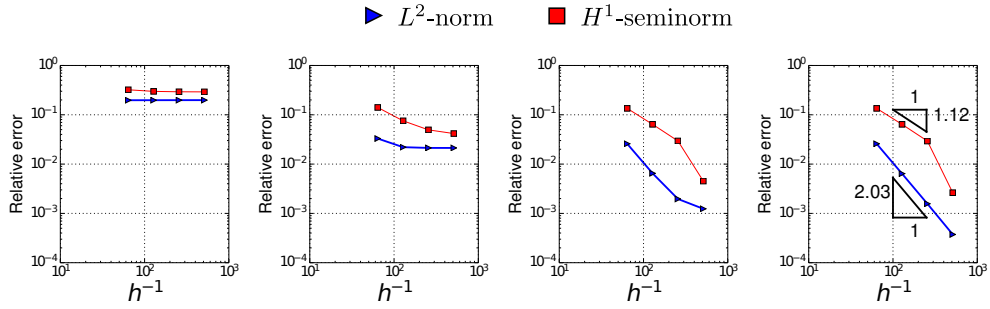

(a) Convergence against axial length (h) for four different transversal polynomial orders. From left to right: $\mathsf{p} = 4$, $\mathsf{p} = 6$, $\mathsf{p} = 8$ and $\mathsf{p} = 10$.

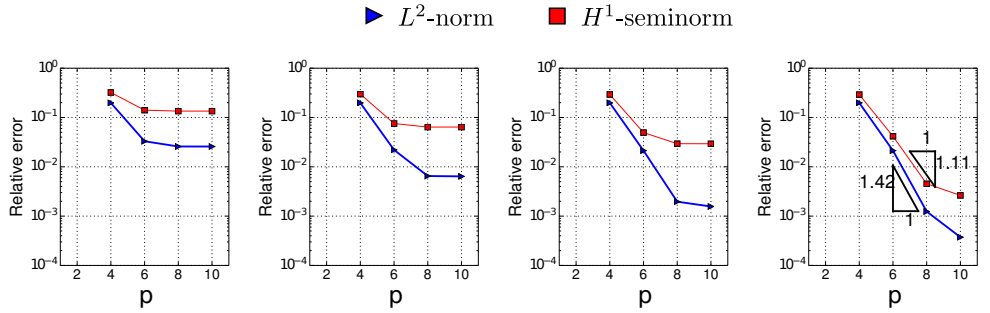

(b) Convergence against transversal polynomial order (p) for four different axial elemental lengths. From left to right: $\mathrm{n_{el}}$= 64, $\mathrm{n_{el}}$= 128, $\mathrm{n_{el}}$= 256 and $\mathrm{n_{el}}$= 512.

Figure 3.11: Convergence rates for the *Case 3*. Errors against axial characteristic length (top row) and against transversal polynomial order (bottom row). In each figure, the relative error in the L^2-norm (▲) and H^1-seminorm (■) are reported.

Table 3.3: Comparison of the relative error of FEM approximation in L^2-norm and H^1-seminorm for the *Case 3* and different discretization sizes. Also, the number of triangular elements and the total number of degrees of freedom are presented.

	Element size				
h	$1.00 \cdot 10^{-1}$	$5.00 \cdot 10^{-2}$	$2.50 \cdot 10^{-2}$	$1.25 \cdot 10^{-2}$	$6.25 \cdot 10^{-3}$
Elements	552	2 208	8 832	35 328	141 312
DoFs	317	1 185	4 577	17 985	71 297
$\|u - u_\mathrm{F}\|$	$1.9704 \cdot 10^{-1}$	$5.6992 \cdot 10^{-2}$	$1.4724 \cdot 10^{-2}$	$3.5667 \cdot 10^{-3}$	$7.3644 \cdot 10^{-4}$
$\|u - u_\mathrm{F}\|$	$3.8512 \cdot 10^{-1}$	$2.0941 \cdot 10^{-1}$	$1.0662 \cdot 10^{-1}$	$5.2356 \cdot 10^{-2}$	$2.3452 \cdot 10^{-2}$

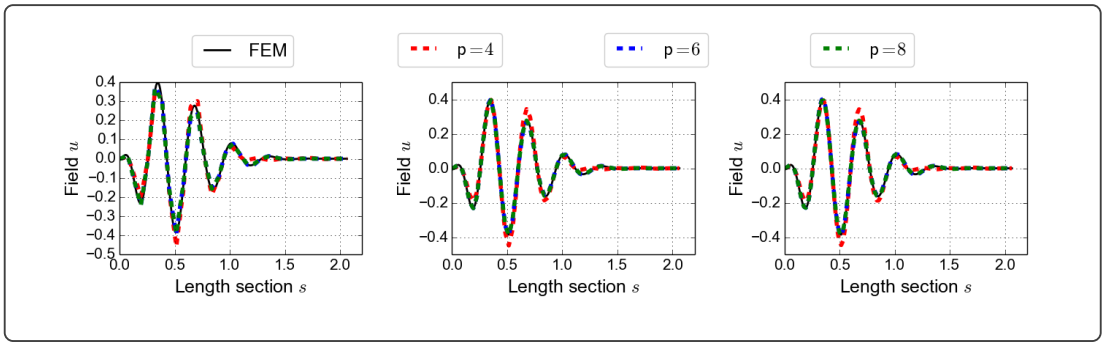

(a) Comparison of field approximation for different axial mesh

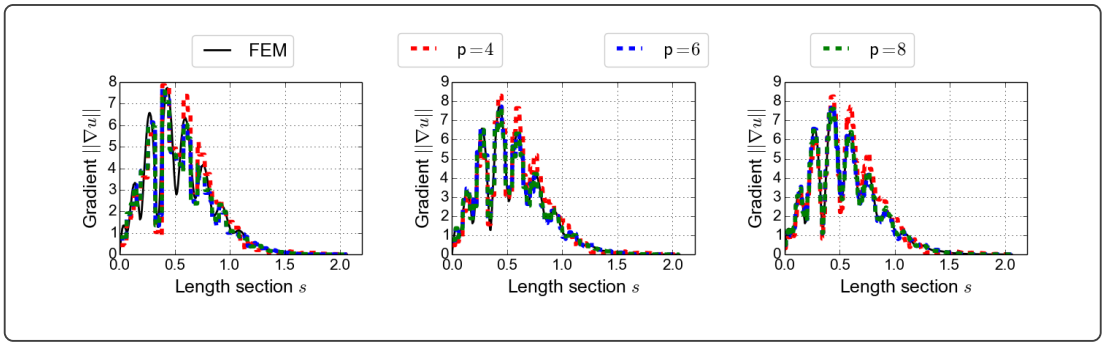

(b) Comparison of the derivative of field approximation for different axial mesh

Figure 3.12: Poisson problem: Comparison of TEPEM solutions (for different polynomial order p) in the Section A. In each panel, and from left to right, the axial mesh is composed by 32, 64 and 128 pipe elements.

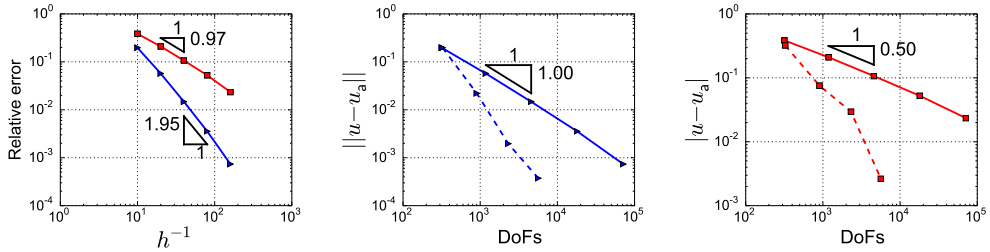

Figure 3.13: Behavior of L^2-norm (▲) and H^1-seminorm (■) for FEM (left panel). Comparison of FEM (solid line) and TEPEM (dotted line) against the total number of degrees of freedom in the L^2-norm (middle panel) and H^1-seminorm (right panel). The notation u_a stands for the approximation (TEPEM or FEM) of the field u.

3.3.3 Advection-diffusion problem and SUPG stabilization

The second example is the approximation of an advection-diffusion problem defined in the annular region Ω defined by the curves

$$\begin{aligned}
\Gamma_1 &= \{\mathbf{x} = (x, y) \in \mathbb{R}^2 : x = 0,\ 0.5 \leq y \leq 1\} \\
\Gamma_2 &= \{\mathbf{x} = (x, y) \in \mathbb{R}^2 : \|\mathbf{x}\|^2 = 0.25\} \\
\Gamma_3 &= \{\mathbf{x} = (x, y) \in \mathbb{R}^2 : 0.5 \leq x \leq 1,\ y = 0\} \\
\Gamma_4 &= \{\mathbf{x} = (x, y) \in \mathbb{R}^2 : \|\mathbf{x}\|^2 = 1\}
\end{aligned} \tag{3.46}$$

Furthermore, this domain will be split by the curve $\{y = x\}$ into two subdomains denoted by Ω_1 (corresponding to $\{y \geq x\}$) and Ω_2 (corresponding to $\{y < x\}$). In Ω, we consider two cases defined by the variational problem: Find $u \in \mathcal{V} = \{v \in H^1(\Omega) : v = 0 \text{ on } \Gamma_2 \cup \Gamma_4\}$ such that:

$$\int_\Omega \Big(\mu(\mathbf{x})\nabla u \cdot \nabla \hat{u} + (\boldsymbol{\beta} \cdot \nabla u)\hat{u}\Big)\, d\Omega = \int_\Omega f\hat{u}\, d\Omega \qquad \forall\, \hat{u} \in \mathcal{V} \tag{3.47}$$

where, defining $\theta = \tan^{-1}(y/x)$, we set $\boldsymbol{\beta} = [10\sin(\theta), -10\cos(\theta)]^T$ and where the source term is defined as follows

$$f(\mathbf{x}) = \begin{cases} 20 & \text{for} \quad \mathbf{x} \in \mathcal{C}_1 = \{(x, y) : (x - 0.25)^2 + (y - 0.75)^2 < 0.1\} \\ 10 & \text{for} \quad \mathbf{x} \in \mathcal{C}_2 = \{(x, y) : (x - 0.75)^2 + (y - 0.25)^2 < 0.1\} \end{cases} \tag{3.48}$$

We consider the two cases:
Case 1: The same diffusion in both subdomains Ω_1 and Ω_2, i.e. $\mu(\mathbf{x}) = 1 \in \Omega$.
Case 2: Different diffusion in each subdomain, say

$$\mu(\mathbf{x}) = \begin{cases} 10^{-4} & \text{for } \mathbf{x} \in \Omega_1 \\ 10^{1} & \text{for } \mathbf{x} \in \Omega_2 \end{cases} \tag{3.49}$$

For the convergence study, we assume as a reference solution an approximation obtained with FEM into a very fine triangular mesh composed by 1 985 946 elements, 994 974 degrees of freedom and linear interpolants for the field approximation. For the *Case 1*, the mesh is uniform while for the *Case 2* the mesh is refined along the curve $\{y = x\}$ to effectively deal with the inner discontinuity created by the difference in the diffusion coefficient. The geometrical domain as well as the reference solution for both cases are outlined in Figure 3.14.

The goal of this example is twofold. First we perform a convergence study for the *Case 1* with respect to the axial length and also to the transversal enrichment. It is expected a linear (exponential) convergence behavior corresponding to the axial (transversal) parameter but with the characteristic saturation behavior shown in the previous example. For the *Case 2* we are interested in the impact of the stabilization into the TEPEM scheme to deal with the internal discontinuity layer and the oscillations due to the high local Péclet number. For the latter case, we consider a pipe mesh composing by 60 elements which results into a local Péclet number around of $\mathrm{Pe} \approx 1\,000$, while for the *Case 1* the coarser pipe mesh results into a very low local Péclet number ($\mathrm{Pe} \approx 0.1$). For both cases, the error in the geometry approximation is neglected.

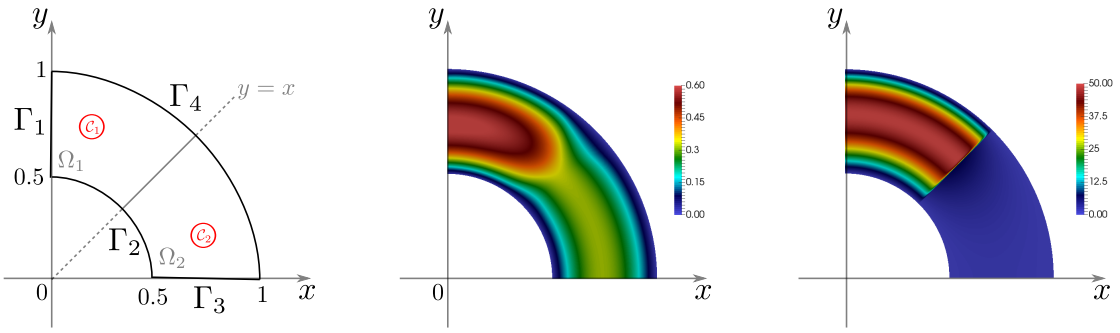

(a) Geometrical setting (b) FEM solution for *Case 1*. (c) FEM solution for *Case 2*.

Figure 3.14: Geometry and reference solution, for *Case 1* and *Case 2*, computed by FEM in a triangular mesh composed by 1 985 946 elements and 994 974 degrees of freedom.

For the numerical convergence study in *Case 1* we use an uniform pipe-element mesh characterized by $\mathrm{n_{el}} \in \{40, 80, 160, 320\}$ while for the transversal order we consider the values $\mathsf{p} \in \{4, 6, 8, 10\}$. In this range, the degrees of freedom associated to the TEPEM approximation vary between 205 for the combination $(\mathrm{n_{el}}, \mathsf{p}) = (40, 4)$ and 3531 for $(\mathrm{n_{el}}, \mathsf{p}) = (320, 10)$, which implies in an approximation with approximately 1% of the degrees of freedom employed in obtaining the reference solution.

A comparison between the relative errors in the norm of L^2 and the semi-norm of H^1 is outlined in Table 3.4 and reflects the excellent capabilities of the TEPEM not only in the approximation of the field but also of its derivative. The coupling between the axial length and transversal enrichment order in the convergence behavior can be seen in Figure 3.15. In this figure, besides the convergence order against h and p, is easy to see (mostly in the first plots) the saturation in the model capabilities when either h or p are fixed. Finally, a visual comparison between the reference solution obtained with FEM and the TEPEM approximate solution is outlined in Figure 3.16 in which it is possible to see that the TEPEM solution follows closely the reference one even with $\mathsf{p} = 6$ and a discretization with 80 pipe-elements.

Table 3.4: Comparison of the relative error of the TEPEM approximation in L^2-norm and H^1-seminorm for the advection-diffusion problem (*Case 1*). As reference values for the computation of the relative error it was employed: $\|u\|_{L^2} = 3.53774 \cdot 10^{-1}$ and $\|\nabla u\|_{L^2} = 2.25367 \cdot 10^{0}$.

	$\mathrm{n_{el}}$	40	80	160	320
	h	$2.95 \cdot 10^{-2}$	$1.475 \cdot 10^{-2}$	$7.375 \cdot 10^{-3}$	$3.6875 \cdot 10^{-3}$
$\|u - u_{\mathrm{T}}\|$	$\mathsf{p} = 4$	$6.51163 \cdot 10^{-3}$	$2.21352 \cdot 10^{-3}$	$2.11244 \cdot 10^{-3}$	$2.22213 \cdot 10^{-3}$
	$\mathsf{p} = 6$	$2.57033 \cdot 10^{-3}$	$1.05408 \cdot 10^{-3}$	$8.04512 \cdot 10^{-4}$	$7.61254 \cdot 10^{-4}$
	$\mathsf{p} = 8$	$2.50315 \cdot 10^{-3}$	$1.25575 \cdot 10^{-3}$	$3.86286 \cdot 10^{-4}$	$3.35062 \cdot 10^{-4}$
	$\mathsf{p} = 10$	$1.20456 \cdot 10^{-3}$	$6.20852 \cdot 10^{-4}$	$3.00496 \cdot 10^{-4}$	$2.28154 \cdot 10^{-4}$
$\|u - u_{\mathrm{T}}\|$	$\mathsf{p} = 4$	$2.46007 \cdot 10^{-2}$	$1.62465 \cdot 10^{-2}$	$1.42390 \cdot 10^{-2}$	$1.38171 \cdot 10^{-2}$
	$\mathsf{p} = 6$	$2.31825 \cdot 10^{-2}$	$1.12220 \cdot 10^{-2}$	$7.85558 \cdot 10^{-3}$	$6.88944 \cdot 10^{-3}$
	$\mathsf{p} = 8$	$2.15023 \cdot 10^{-2}$	$1.02384 \cdot 10^{-2}$	$5.86927 \cdot 10^{-3}$	$4.50414 \cdot 10^{-3}$
	$\mathsf{p} = 10$	$2.12954 \cdot 10^{-2}$	$9.75125 \cdot 10^{-3}$	$5.71621 \cdot 10^{-3}$	$3.76943 \cdot 10^{-3}$

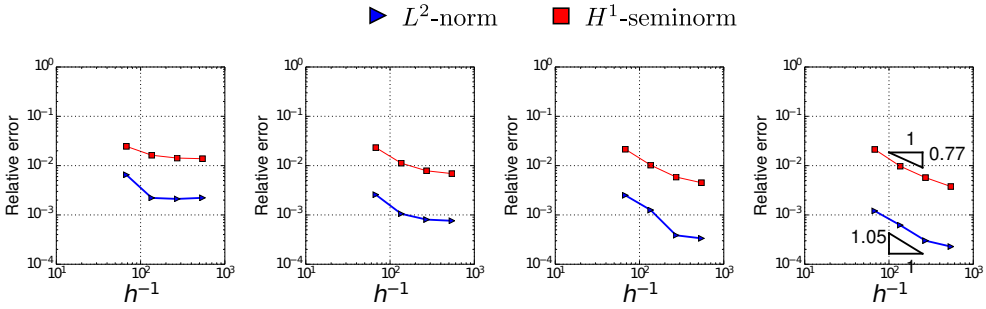

(a) Convergence against axial length (h) for four different transversal polynomial orders. From left to right: $\mathsf{p} = 4$, $\mathsf{p} = 6$, $\mathsf{p} = 8$ and $\mathsf{p} = 10$.

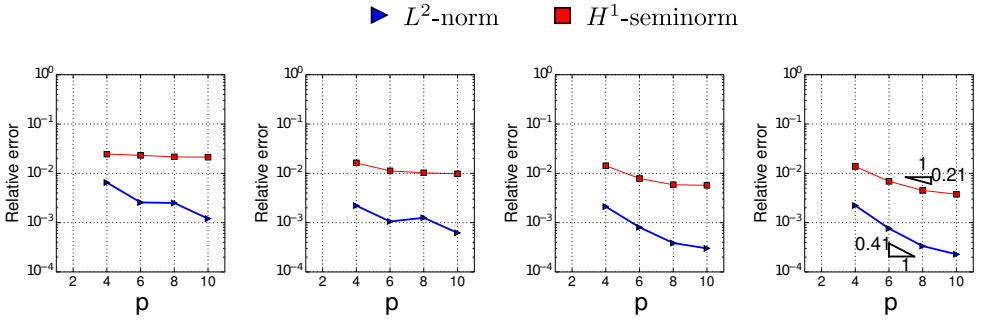

(b) Convergence against transversal polynomial order (p) for four different axial element lengths. From left to right: n_{el}= 40, n_{el}= 80, n_{el}= 160 and n_{el}= 320.

Figure 3.15: Convergence rates for the *Case 1*. Errors with respect to the axial characteristic length (top row) and to the transversal polynomial order (bottom row). In each figure, the relative error in the L^2-norm (▲) and H^1-seminorm (■) are reported.

(a) Reference FEM solution (b) TEPEM $\mathsf{p} = 6$,n_{el}=80. (c) TEPEM $\mathsf{p} = 8$,n_{el}=160.

(d) Reference FEM solution (e) TEPEM $\mathsf{p} = 6$,n_{el}=80. (f) TEPEM $\mathsf{p} = 8$,n_{el}=160.

Figure 3.16: Comparison between the reference solution and TEPEM approximate solutions. Top row: Primary field. Bottom row: Magnitude of the gradient field.

A similar convergence study is performed for the FEM. In this case, due to the curved boundaries of the geometrical domain, we perform a initial geometrical discretization as explained in previous section by considering an initial pipe-mesh composed by 40 elements. In Table 3.5 and Figure 3.17 we present the error behavior and also the geometrical characteristic of the triangulation.

Particularly, in Table 3.5, theoretical convergence order for the FEM in L^2-norm and H^1-seminorm are achieved when compared with the axial length size (quadratic and linear for L^2 and H^1). Regarding the convergence in terms of the number of degrees of freedom, order 1 and 0.5 are obtained, respectively, for L^2-norm and H^1-seminorm. Similar convergence rates are observed for the TEPEM but with improved predictive capabilities, that is, it is possible to obtain solutions with the same level of accuracy but with a considerable reduction in the problem size.

Table 3.5: Comparison of the relative error of FEM approximation in L^2-norm and H^1-seminorm for the *Case 1* and different discretization sizes. Also the number of triangular elements and the total number of degrees of freedom are presented.

	Element size				
h	$1.46 \cdot 10^{-1}$	$7.32 \cdot 10^{-2}$	$3.66 \cdot 10^{-2}$	$1.83 \cdot 10^{-2}$	$9.15 \cdot 10^{-3}$
Elements	142	568	2 272	9 088	36 352
DoFs	90	321	1 209	4 689	18 465
$\|\|u - u_{\mathrm{F}}\|\|$	$3.1004 \cdot 10^{-1}$	$9.9101 \cdot 10^{-2}$	$2.1692 \cdot 10^{-2}$	$6.3436 \cdot 10^{-3}$	$1.6309 \cdot 10^{-3}$
$\|u - u_{\mathrm{F}}\|$	$1.5017 \cdot 10^{-1}$	$7.7559 \cdot 10^{-2}$	$3.9492 \cdot 10^{-2}$	$1.9954 \cdot 10^{-2}$	$9.8654 \cdot 10^{-3}$

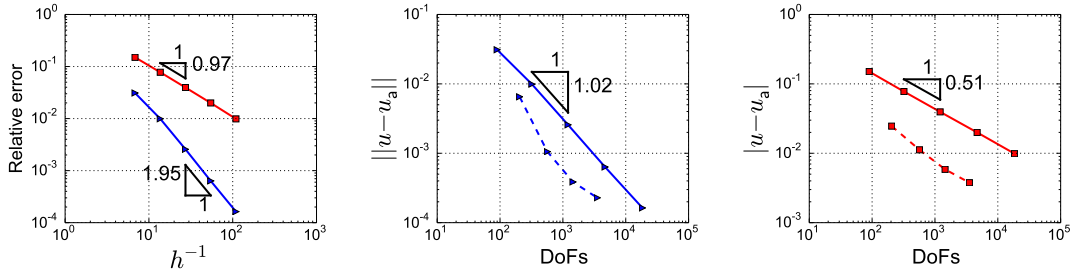

Figure 3.17: Behavior of L^2-norm (▲) and H^1-seminorm (■) for FEM (left panel). Comparison of FEM (solid line) and TEPEM (dotted line) with respect to the number of degrees of freedom in the L^2-norm (middle panel) and H^1-seminorm (right panel). The notation u_{a} stands by the approximation (TEPEM or FEM) for the field u.

For the second case, we use an uniform mesh composed by 60 pipe-elements which results in a local Péclet number Pe $\approx 1\,000$ sufficiently high to generate spurious oscillations. In this case, we perform a visual comparison of TEPEM approximate solutions without stabilization and the results with SUPG, as commented in Section 3.2.2.

As expected, the solution provided by the standard TEPEM, which is reported in Figure 3.18(a;b), features numerical instabilities which completely pollute the numerical solution and which increase as the transversal order increases. When considering the SUPG formulation integrated to the TEPEM strategy, the numerical solution is physically satisfactory even with low transversal polynomial order ($\mathsf{p} = 6$), see Figure 3.18 (c).

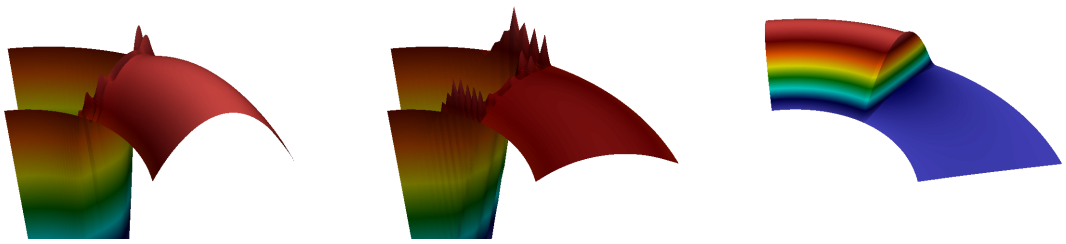

(a) TEPEM with $\mathsf{p} = 6$. (b) TEPEM with $\mathsf{p} = 12$. (c) TEPEM-SUPG with $\mathsf{p} = 6$.

Figure 3.18: Comparison of approximate solutions for the advection-diffusion problem in the *Case 2* obtained with: standard TEPEM strategy with (a) $\mathsf{p} = 6$, (b) $\mathsf{p} = 12$, and (c) with SUPG stabilization with $\mathsf{p} = 6$. In each case, $\mathrm{n_{el}}$= 60 and Pe $\approx 1\,000$.

3.3.4 Convection in wavy channel

In this example, we are interested in the approximation of the advection-diffusion problem: Find $u \in \mathcal{U}$ such that

$$\int_\Omega \left(\mu \nabla u \cdot \nabla \hat{u} + (\boldsymbol{\beta} \cdot \nabla u)\hat{u} \right) d\Omega = \int_\Omega f \hat{u}\, d\Omega \qquad \forall\, \hat{u} \in \mathcal{V} \tag{3.50}$$

where the diffusion coefficient is considered constant ($\mu = 1$) as well as the advection vector $\boldsymbol{\beta} = [10, 0]^T$ and the source term is $f = 10$. This problem is defined in the wavy channel domain limited by the curves:

$$\begin{aligned}
\Gamma_1 &= \{\mathbf{x} = (x, y) \in \mathbb{R}^2 : x = 0,\ 1 \leq y \leq 2\} \\
\Gamma_2 &= \{\mathbf{x} = (x, y) \in \mathbb{R}^2 : 0 \leq x \leq 2, y = 1 - 0.25\sin(2\pi x)\} \\
\Gamma_3 &= \{\mathbf{x} = (x, y) \in \mathbb{R}^2 : x = 2, 1 \leq y \leq 2\} \\
\Gamma_4 &= \{\mathbf{x} = (x, y) \in \mathbb{R}^2 : 0 \leq x \leq 2, y = 2 + 0.25\sin(2\pi x)\}
\end{aligned} \tag{3.51}$$

Hence, the spaces involved in the problem definition are $\mathcal{U} = \{u \in H^1(\Omega) : u = 0 \text{ on } \Gamma_2 \cup \Gamma_4\}$ and $\mathcal{V} = \mathcal{U}$. In this case, no stabilization is employed.

As stated in the previous section, to measure the quality of the TEPEM approximations and due to the lack of an analytical solution, we employ a FEM approximation computed in a very fine triangular mesh as a reference solution. This solution, displayed in Figure 3.19 and denoted by u_{F}, features lateral boundary layers which require, in the context of the FEM, an extremely fine triangulation in order to get accurate solutions.

We perform a convergence study to analyze the capabilities of the TEPEM approach employing an uniform pipe-type partition composed by $\mathrm{n_{el}} = \{64, 128, 256, 512\}$ elements and a moderate transversal polynomial order p in the range $4 \leq \mathsf{p} \leq 10$. For the coarser mesh, a small local Péclet number is obtained (Pe≈ 0.1).

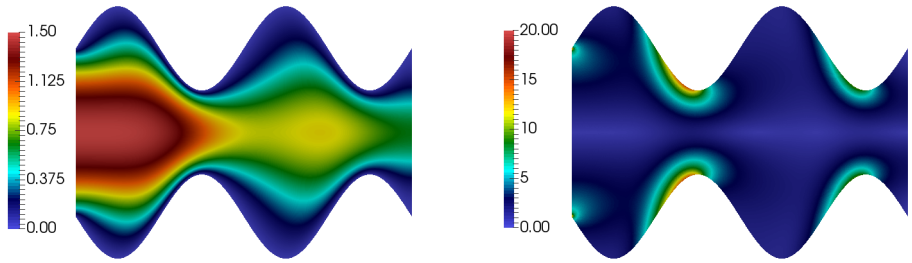

(a) Reference solution obtained with FEM. $\|\nabla u\|_{L^2} = 1.53544 \cdot 10^0$

(b) Magnitude of the gradient of the reference solution. $\|\nabla u\|_{L^2} = 6.10055 \cdot 10^0$

Figure 3.19: Reference solution, for the wavy channel problem, computed by FEM in an uniform triangular mesh composed by 1 196 660 elements and 600 331 degrees of freedom.

The relative errors in the TEPEM approach for the approximation of u_{F} are presented in Table 3.6 and also in Figure 3.20 where convergence rates with respect to the axial characteristic length and to the transversal order are presented. The convergence trend features the characteristic saturation for schemes depending on more than one parameter. For example, in the first panel in Figure 3.20(a) we can appreciate that the model capabilities with $\mathsf{p} = 4$ reach their limit for the first axial discretization and cannot be improved just by axial refinement of the mesh. For higher values for the transversal order, the saturation threshold is modified, improving the approximation.

Table 3.6: Comparison of the relative error of TEPEM approximation in L^2-norm and H^1-seminorm for the wavy channel problem. As reference values for the computation of relative error it was employed: $\|u\|_{L^2} = 1.53544 \cdot 10^0$ and $\|\nabla u\|_{L^2} = 6.10055 \cdot 10^0$.

	$\mathrm{n_{el}}$	64	128	256	512
	h	$3.125 \cdot 10^{-2}$	$1.5625 \cdot 10^{-2}$	$7.8125 \cdot 10^{-3}$	$3.90625 \cdot 10^{-3}$
$\|u - u_{\mathrm{T}}\|$	$\mathsf{p} = 4$	$7.28597 \cdot 10^{-3}$	$6.81256 \cdot 10^{-3}$	$6.98764 \cdot 10^{-3}$	$6.72181 \cdot 10^{-3}$
	$\mathsf{p} = 6$	$3.50336 \cdot 10^{-3}$	$3.39494 \cdot 10^{-3}$	$3.29214 \cdot 10^{-3}$	$3.22173 \cdot 10^{-3}$
	$\mathsf{p} = 8$	$1.38980 \cdot 10^{-3}$	$1.30385 \cdot 10^{-3}$	$7.91865 \cdot 10^{-4}$	$7.87471 \cdot 10^{-4}$
	$\mathsf{p} = 10$	$1.41741 \cdot 10^{-3}$	$1.30269 \cdot 10^{-3}$	$3.92861 \cdot 10^{-4}$	$2.63833 \cdot 10^{-4}$
$\|u - u_{\mathrm{T}}\|$	$\mathsf{p} = 4$	$1.39822 \cdot 10^{-2}$	$1.30818 \cdot 10^{-2}$	$1.28848 \cdot 10^{-2}$	$1.28814 \cdot 10^{-2}$
	$\mathsf{p} = 6$	$1.21667 \cdot 10^{-2}$	$7.77318 \cdot 10^{-3}$	$7.70197 \cdot 10^{-3}$	$7.50230 \cdot 10^{-3}$
	$\mathsf{p} = 8$	$1.05482 \cdot 10^{-2}$	$6.42748 \cdot 10^{-3}$	$4.10823 \cdot 10^{-3}$	$2.79222 \cdot 10^{-3}$
	$\mathsf{p} = 10$	$8.65283 \cdot 10^{-3}$	$5.92177 \cdot 10^{-3}$	$3.04369 \cdot 10^{-3}$	$8.36958 \cdot 10^{-4}$

For the FEM, we also perform a convergence study with respect to the element size of the mesh. The number of elements employed in the triangulation, the number of degrees of freedom as well as the relative error are displayed in Table 3.7. Note that, while for the TEPEM the number of degrees of freedom is in the range of 325 (for $\mathsf{p} = 4$ and $\mathrm{n_{el}} = 64$) and 5643 (for $\mathsf{p} = 10$ and $\mathrm{n_{el}} = 512$), the minimum number of unknowns for the FEM is of the order of $1 \cdot 10^3$.

A comparison of the convergence with respect to the number of degrees of freedom for the TEPEM and FEM, as observed in Figure 3.21, reveals a linear convergence for the relative error in the L^2-norm and reduced to one half when measured in the H^1-seminorm. Moreover, and similar to the previous examples, a direct comparison indicates better results for the TEPEM (in comparison with the FEM) for the same number of degrees of freedom.

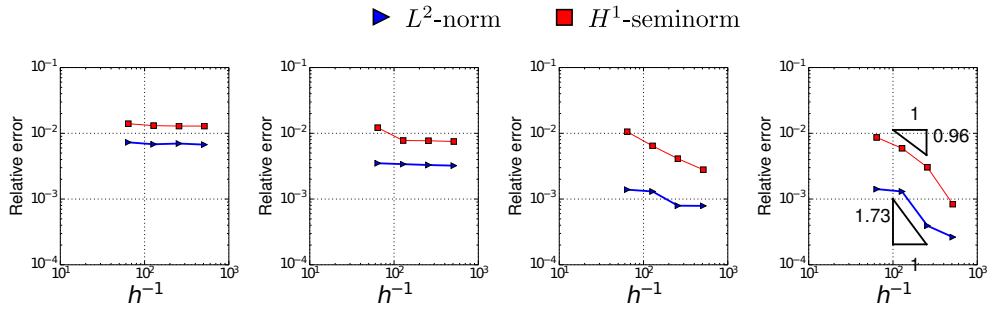

(a) Convergence with respect to the axial length (h) for four different transversal polynomial orders. From left to right: $\mathsf{p} = 4$, $\mathsf{p} = 6$, $\mathsf{p} = 8$ and $\mathsf{p} = 10$.

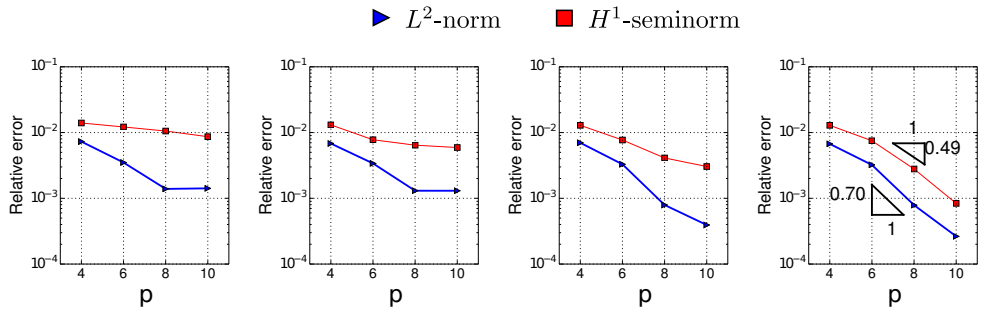

(b) Convergence with respect to the transversal polynomial order (p) for four different axial element lengths. From left to right: $\mathrm{n_{el}} = 64$, $\mathrm{n_{el}} = 128$, $\mathrm{n_{el}} = 256$ and $\mathrm{n_{el}} = 512$.

Figure 3.20: Convergence rates for the wavy channel problem with respect to the axial length and transversal polynomial order. In each figure, the relative error in the L^2-norm (▲) and H^1-seminorm (■) are reported.

Table 3.7: Comparison of the relative error of FEM approximation in L^2-norm and H^1-seminorm for the wavy channel problem with different discretization sizes. The number of triangular elements and the number of degrees of freedom are also reported.

	Element size				
h	$8.57 \cdot 10^{-2}$	$4.28 \cdot 10^{-2}$	$2.14 \cdot 10^{-2}$	$1.07 \cdot 10^{-2}$	$5.35 \cdot 10^{-3}$
Elements	2 008	8 032	32 128	128 512	514 048
DoFs	1 085	4 177	16 385	64 897	258 305
$\|u - u_{\mathrm{F}}\|$	$1.6115 \cdot 10^{-2}$	$4.1708 \cdot 10^{-3}$	$1.0794 \cdot 10^{-3}$	$2.7938 \cdot 10^{-4}$	$7.2309 \cdot 10^{-5}$
$\|u - u_{\mathrm{F}}\|$	$2.6468 \cdot 10^{-1}$	$1.3418 \cdot 10^{-1}$	$6.8031 \cdot 10^{-2}$	$3.4490 \cdot 10^{-2}$	$1.7485 \cdot 10^{-2}$

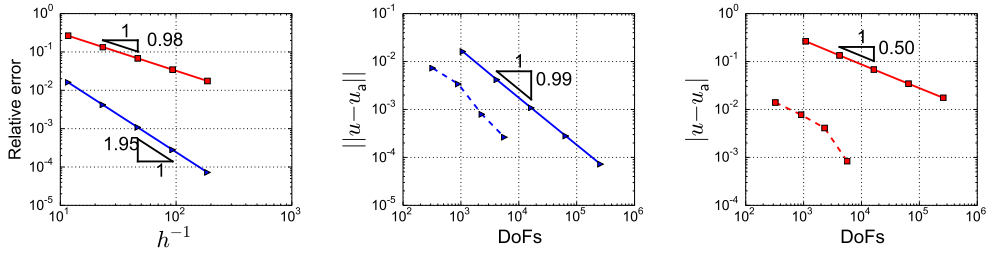

Figure 3.21: Behavior of L^2-norm (▲) and H^1-seminorm (■) for FEM (left panel). Comparison of FEM (solid line) and TEPEM (dotted line) with respect to the number of degrees of freedom in the L^2-norm (middle panel) and H^1-seminorm (right panel). The notation u_a stands for the approximation of field u.

3.3.5 Heat conduction in an L-shaped domain

In this final numerical example, we are interested in studying the TEPEM approach when applied to a transient problem. In particular, we analyze the approximation of the problem: Find $u(x,t) \in \mathcal{V} \times (0,T)$ such that

$$\int_\Omega \left(\frac{\partial u}{\partial t} \hat{u} + \mu \nabla u \cdot \nabla \hat{u} \right) d\Omega = \int_\Omega f(x,t) \hat{u} \, d\Omega \qquad \forall \, \hat{u} \in \mathcal{V} \tag{3.52}$$

where the diffusion coefficient is chosen to be $\mu = 0.1$ and the source term is time-dependent and given by $f(x,t) = 5\cos(2\pi t)$. The geometrical domain is the L-shaped region outlined in Figure 3.22 where the structure of the pipe-mesh employed in the TEPEM approximation is also depicted. The problem is fully characterized by considering homogeneous Dirichlet conditions over the whole boundary.

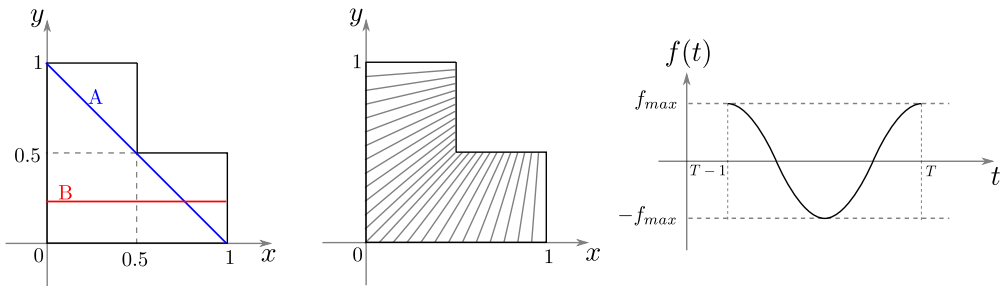

Figure 3.22: L-shaped geometry and source term profile for the transient heat conduction problem. Two straight segments, denoted as A (in blue) and B (in red), are chosen for a detailed comparison of the solutions.

For this problem, we fix an axial partition of the domain composed by 60 pipe-elements and we study the model capabilities when the transversal order p is increased. As detailed at the beginning of this section, the approximation is obtained by combining a finite difference based scheme for the temporal domain and the TEPEM approach for the spatial dimension. The period $T = 1$ defines the periodic characteristic of the source term. The temporal range in the problem $t \in [0,2]$ is divided into a discrete uniform grid of size $\Delta t = 1 \cdot 10^{-3}$ (chosen to ensure the temporal convergence) and a forward explicit Euler scheme is employed to discretize the temporal variation.

For the convergence study, a FEM simulation with 19 243 degrees of freedom and 37 884 triangular elements is performed. In Table 3.8, we show the relative error for four different time instants within the temporal cycle. For each time step, we can appreciate the convergence against the transversal order in the same pattern that the one observed in steady state problems. The same convergence is obtained when measuring the mean error in the L^2-norm and the H^1-seminorm. It is important to note that these convergence rates are obtained, for the TEPEM, with a total number of degrees of freedom in the range between 305 ($\mathsf{p} = 4$) and 671 ($\mathsf{p} = 10$) which represents a relative reduction larger than 96% in contrast to the FEM reference solution.

Table 3.8: Comparison of the relative error of TEPEM approximation in L^2-norm and H^1-seminorm for the transient heat conduction problem in the L-shaped domain measured at four time instants, and also the mean error in the TEPEM approximation.

		Punctual error			
		$t = 0.0T$	$t = 0.3T$	$t = 0.6T$	$t = 0.9T$
$\|u - u_{\mathrm{T}}\|$	$\mathsf{p} = 4$	$1.0131 \cdot 10^{-1}$	$1.1668 \cdot 10^{-1}$	$4.7464 \cdot 10^{-2}$	$5.4664 \cdot 10^{-1}$
	$\mathsf{p} = 6$	$9.6207 \cdot 10^{-2}$	$1.0957 \cdot 10^{-1}$	$3.6091 \cdot 10^{-2}$	$5.3381 \cdot 10^{-1}$
	$\mathsf{p} = 8$	$9.5217 \cdot 10^{-2}$	$1.0696 \cdot 10^{-1}$	$3.1622 \cdot 10^{-2}$	$5.3562 \cdot 10^{-1}$
	$\mathsf{p} = 10$	$9.4637 \cdot 10^{-2}$	$1.0530 \cdot 10^{-1}$	$2.9424 \cdot 10^{-2}$	$5.3152 \cdot 10^{-1}$
$\|u - u_{\mathrm{T}}\|$	$\mathsf{p} = 4$	$2.2074 \cdot 10^{-1}$	$1.8214 \cdot 10^{-1}$	$1.6357 \cdot 10^{-1}$	$4.3651 \cdot 10^{-1}$
	$\mathsf{p} = 6$	$1.6585 \cdot 10^{-1}$	$1.5385 \cdot 10^{-1}$	$1.1103 \cdot 10^{-1}$	$3.7296 \cdot 10^{-1}$
	$\mathsf{p} = 8$	$1.4489 \cdot 10^{-1}$	$1.4409 \cdot 10^{-1}$	$8.7406 \cdot 10^{-2}$	$3.5799 \cdot 10^{-2}$
	$\mathsf{p} = 10$	$1.3324 \cdot 10^{-1}$	$1.4158 \cdot 10^{-1}$	$7.4689 \cdot 10^{-2}$	$3.4726 \cdot 10^{-2}$

	Mean error			
	$\mathsf{p} = 4$	$\mathsf{p} = 6$	$\mathsf{p} = 8$	$\mathsf{p} = 10$
$\|u - u_{\mathrm{T}}\|_{(0,T)}$	$6.1289 \cdot 10^{-2}$	$5.9339 \cdot 10^{-2}$	$5.9122 \cdot 10^{-2}$	$5.8670 \cdot 10^{-2}$
$\|u - u_{\mathrm{T}}\|_{(0,T)}$	$7.5933 \cdot 10^{-2}$	$6.2013 \cdot 10^{-2}$	$5.7581 \cdot 10^{-2}$	$5.5025 \cdot 10^{-2}$
DoFs reduction	98.41%	97.78%	97.14%	96.51%

For a visual comparison of the approximate TEPEM solution against the reference one, in Figure 3.23 both solutions are outlined at four selected time instants. Also, in the same figure, the magnitude of the gradient of both solutions is also compared. In each case, it is easy to see the high quality delivered by the TEPEM approximation (for the primal field as well as for its gradient) with a considerable reduction in the problem size.

A more detailed comparison between the FEM reference solution and the TEPEM approximation (with $\mathsf{p} = 4$ and $\mathsf{p} = 6$) is addressed considering the straight segments highlighted in Figure 3.22. In each segment is compared the solution profile and the magnitude of its derivative, showing a high agreement in the approximation in both segment A (Figure 3.3.5) and segment B (Figure 3.25).

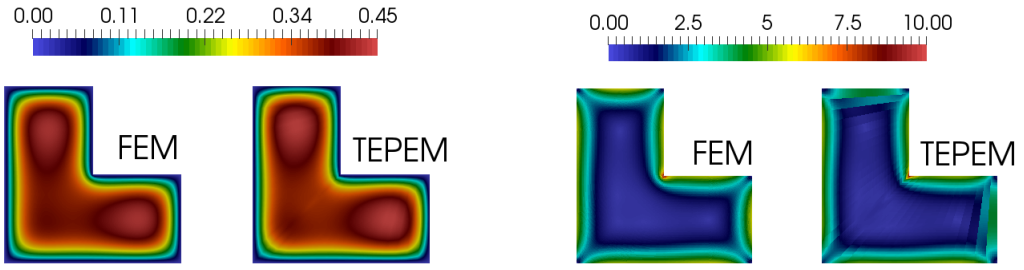

(a) Comparison against reference solution at time: $t/T = 0$

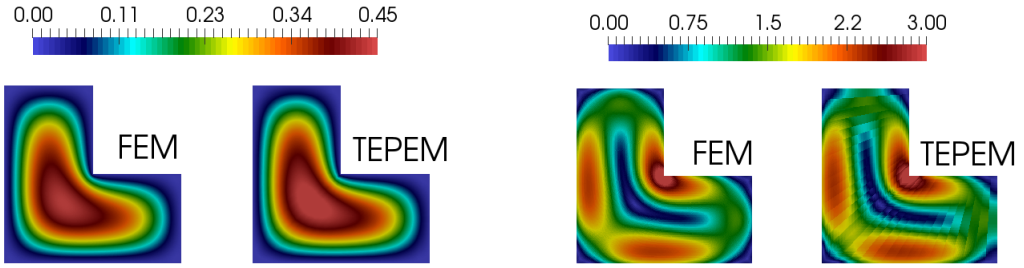

(b) Comparison against reference solution at time: $t/T = 0.30$

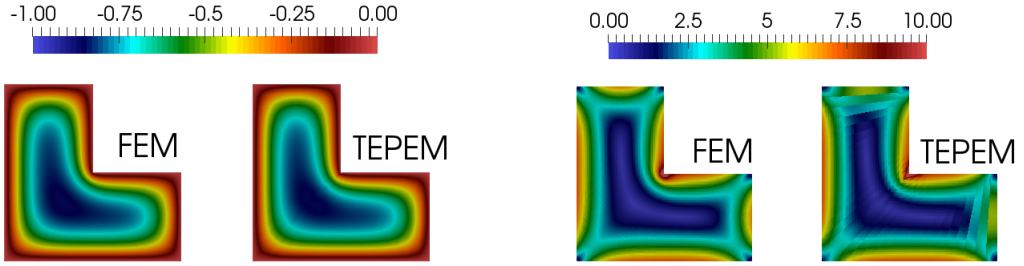

(c) Comparison against reference solution at time: $t/T = 0.60$

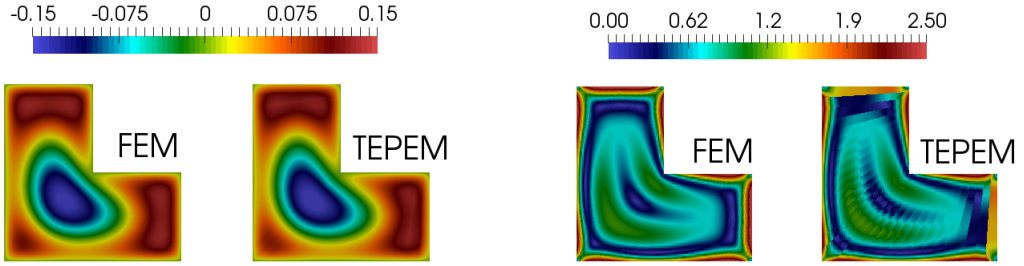

(d) Comparison against reference solution at time: $t/T = 0.90$

Figure 3.23: Comparison between TEPEM approximation ($\mathsf{p} = 6$) and FEM reference solution at four selected time instants. In each row, a comparison between the primal field (left two panels) and the magnitude of the gradient (right two panels) is performed. Scales are conveniently adjusted at each time instant.

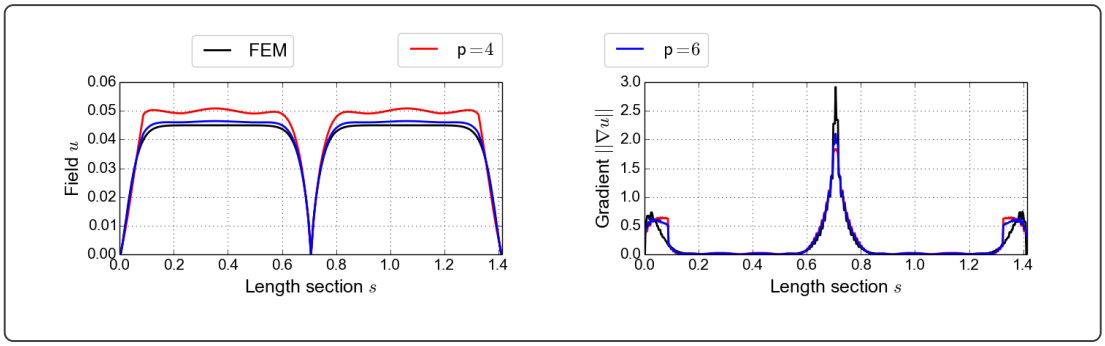

(a) Comparison against reference solution at time: $t/T = 0$

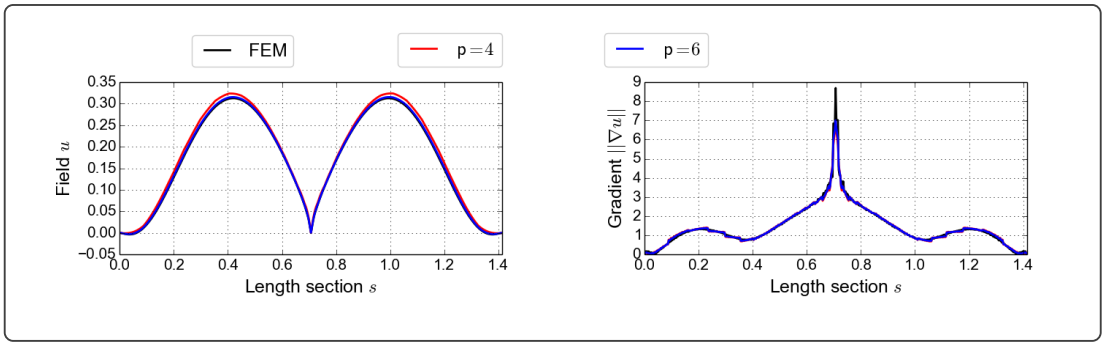

(b) Comparison against reference solution at time: $t/T = 0.30$

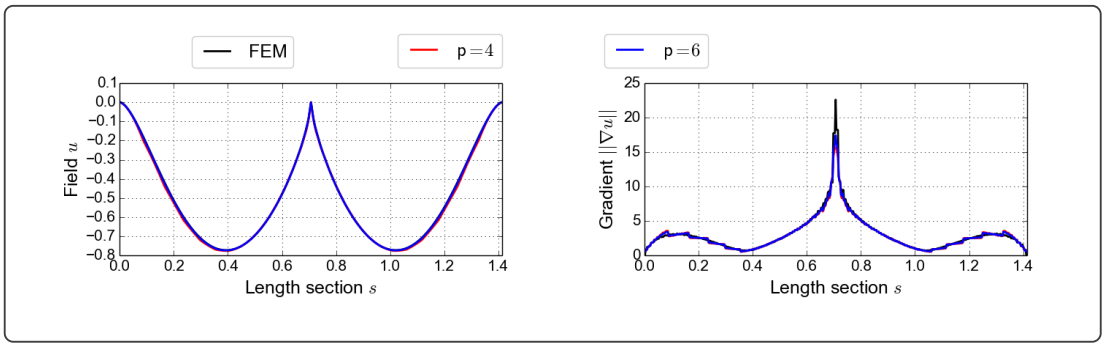

(c) Comparison against reference solution at time: $t/T = 0.60$

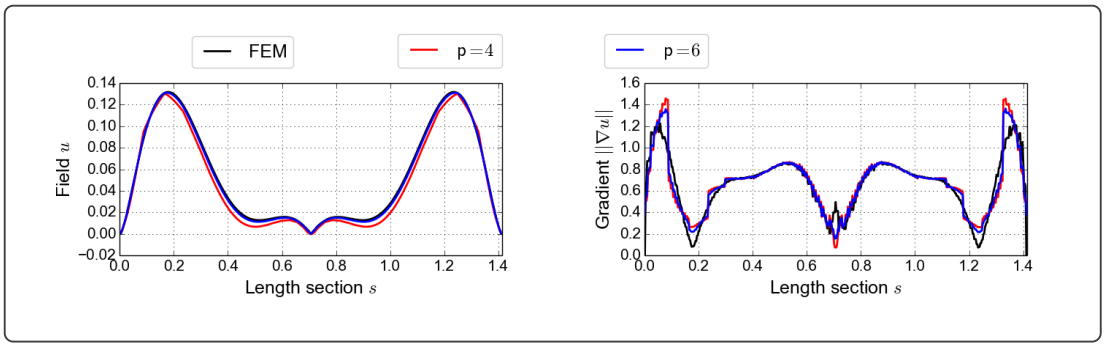

(d) Comparison against reference solution at time: $t/T = 0.90$

Figure 3.24: Comparison between TEPEM approximation ($\mathsf{p} = 4$ and $\mathsf{p} = 6$) and FEM reference solution at four selected time instants and in the segment A. In each row, a comparison between the primal field and the magnitude of the gradient is performed.

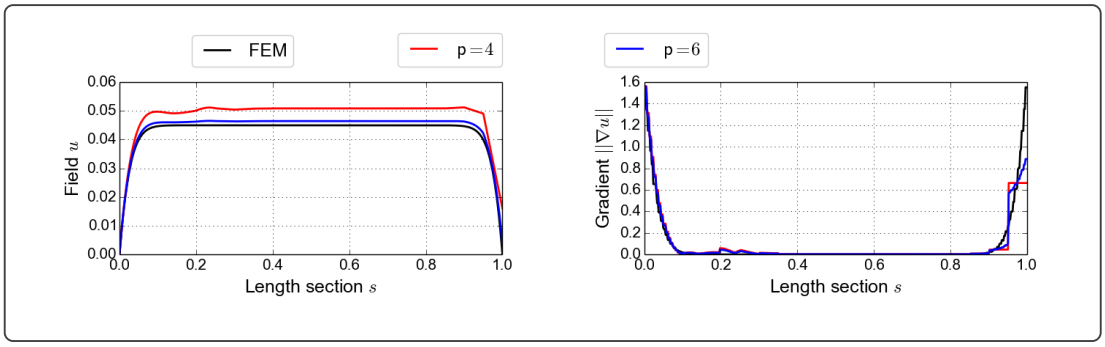

(a) Comparison against reference solution at time: $t/T = 0$

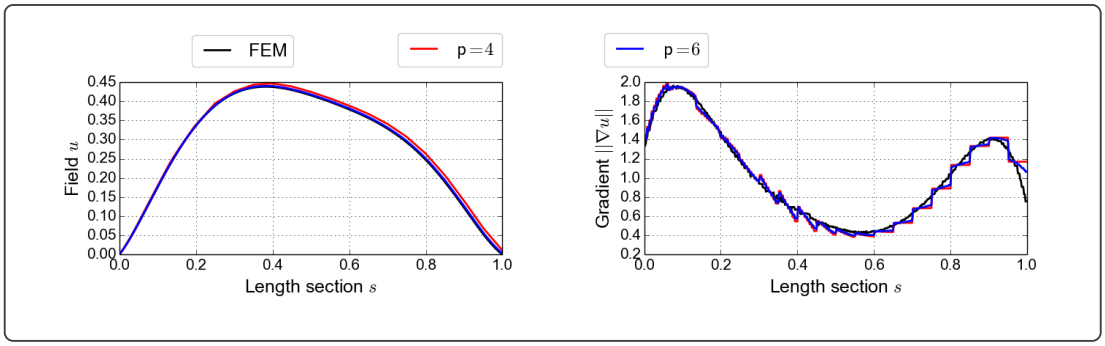

(b) Comparison against reference solution at time: $t/T = 0.30$

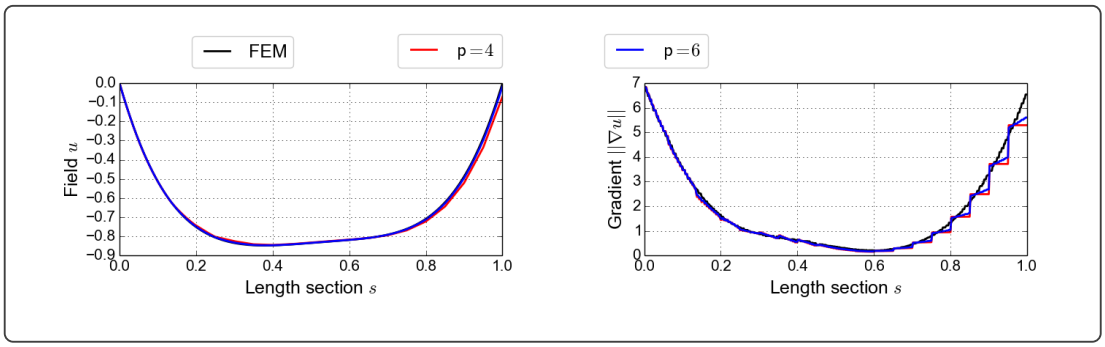

(c) Comparison against reference solution at time: $t/T = 0.60$

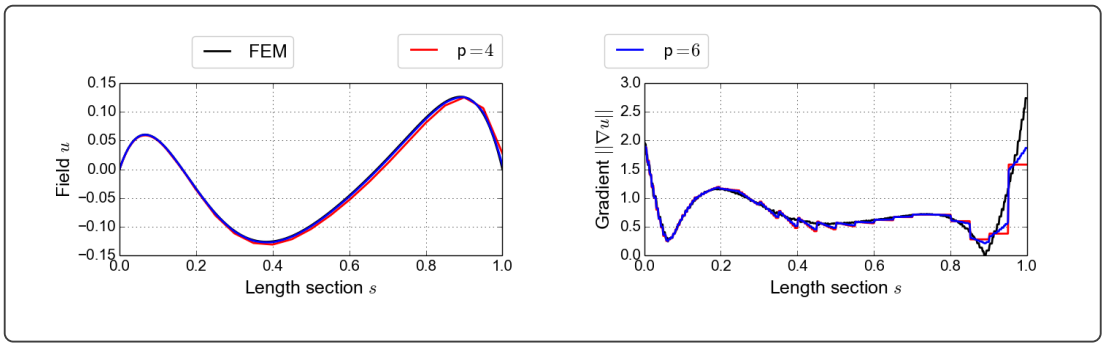

(d) Comparison against reference solution at time: $t/T = 0.90$

Figure 3.25: Comparison between TEPEM approximation ($\mathsf{p} = 4$ and $\mathsf{p} = 6$) and FEM reference solution at four selected time instants and in the segment B. In each row, a comparison between the primal field and the magnitude of the gradient is performed.

3.4 Further remarks

In this chapter, the Transversally Enriched Pipe Element Method (TEPEM), was successfully applied in the approximation of the solution of scalar transport problems (advection-diffusion-reaction problems, specifically) demonstrating a substantial reduction in the problem size while maintaining an accuracy comparable with that obtained with traditional general purpose strategies, such as the Finite Element Method (FEM).

Some remarkable characteristics highlighted throughout this chapter are the following:

The numerical method. The TEPEM is constructed on top of a pipe-element mesh in which proper interpolant functions are defined such that they span the whole transversal direction of the domain. Controlling the order of these polynomial interpolants allows to effectively control the ability of the numerical approach. The TEPEM is conceived as a very special type of finite element. That is, we have started with the variational formulation of the problem for which proper finite dimensional spaces have been defined. Then, elemental contributions can be identified, numerical integration is required so that we finally arrive at a system of algebraic equations to compute the unknown coefficients. This property speaks about the versatility of the proposed method, which permits its extension to other physical models and phenomenological conditions.

System of algebraic equations. After proper arrangement of the degrees of freedom, the algebraic structure of the discrete problem results in a largely sparse system with the global structure similar to the obtained in one-dimensional FEM discretizations (of equal order of the employed for the axial dynamics) and where each block component is a dense submatrix whose size is directly proportional to the transversal polynomial order. Specialized algorithms for this type of system can be exploited to improve the efficiency of this approach.

Integration with other strategies. The versatility in the conception of the TEPEM definition allowed us to integrate it with stabilization techniques without further efforts. The use of SUPG coupling was explored with satisfactory results in the approximation of inner discontinuity layers.

Computational efficiency. Through several examples it has been demonstrated the abilities of the TEPEM to reduce the size of the problem (achieving a reduction of most than the 90% in the degrees of freedom) while providing excellent approximations for the physical field in all tested cases.

The predictive capabilities of the model are effectively controlled by the parameter p, which defines the transversal order of the interpolants, and by the mesh parameter h which defines the axial pipe element length.

Chapter 4

The TEPEM for incompressible fluid flow

In the search for numerical techniques capable of being applied in the medical practice, and specifically in the hemodynamics field, the solution of the Navier-Stokes equations has caught a lot of attention. These equations provide a suitable model to describe the blood flow in the cardiovascular system, although, the numerical simulation of three-dimensional incompressible flows poses challenging problems. These challenges have driven the research towards the reduction of the dimension of the problem, which is nowadays a topic of paramount interest. In fact, many approaches are available at literature which furnish a dimensional reduction based on, for example, the introduction of kinematical constrains, in detriment of the lack on the representation of several three-dimensional features.

The Transversally Enriched Pipe Element Method can be envisioned as a promising strategy to deal with three-dimensional fluid flow problems, naturally reducing the problem size at discrete level but maintaining an accuracy that is, to some extent, comparable with full 3D FEM strategies. The advantage of the TEPEM scheme in the approximation of Navier-Stokes equation relies in: (i) the structure of the linear system, whose global algebraic structure is similar to the one obtained for one-dimensional models allowing a natural parallelism in the assembly and solution and (ii) the major reduction in the problem size as well as the natural way in which model capabilities are controlled, as was highlighted in the last chapter. It is expected that the efficiency demonstrated in the last chapter within the scope of a scalar transport problem is maintained in the vector case, reducing the number of unknowns and reflecting this into accurate approximations but with considerable reduction in the computational time, which is of fundamental importance in real large-scale problems.

In this Chapter we explore the numerical advantages when the TEPEM is employed to approximate the velocity and pressure fields. For the discretization of the Navier-Stokes problem we have chosen to work with a combination of quadratic and linear polynomials for the velocity/pressure pair, for the axial dynamics, while for the transversal dynamics the pair velocity/pressure is approximated by polynomial orders given by $\mathbb{P}_{\mathsf{p}}/\mathbb{P}_{\mathsf{p}/2}$. In practice, we propose a family of finite element spaces commanded by the parameter p which controls the model capabilities. Inspired in classical inf-sup stable spaces employed in FEM and spectral methods, the stability of this pair is numerically investigated in this chapter. Several numerical examples are also addressed, both in 2D and 3D domains, to confirm the stability of the discrete pair, as well as to perform a study of the convergence properties and efficiency when compared against a traditional FEM scheme. These numerical examples are performed in controlled academic domains, constructed to ensure a correct convergence study and comparison with FEM reference solutions.

4.1 The Navier-Stokes equations

Let us consider $\Omega \subset \mathbb{R}^d$ $(d = 2, 3)$ being an open and bounded domain with Lipschitz continuous boundary $\partial\Omega$, as the outlined in Figure 4.1. We will split the boundary $\partial\Omega$ in three disjointed parts Γ_i, Γ_o and Γ_L. Inlet and outlet boundaries, Γ_i and Γ_o, are considered as flat boundaries and where either Neumann or Dirichlet boundary conditions can be prescribed.

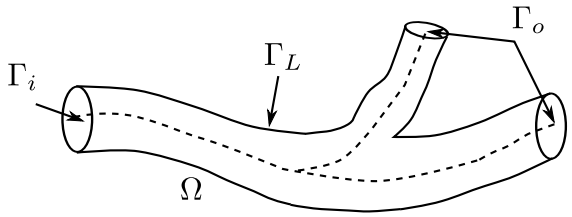

Figure 4.1: Schematic setting for the fluid flow problem. Domain boundary is divided in flat inlet/outlet boundaries Γ_i and Γ_o and the lateral surface Γ_L.

Let T be a positive and fixed real value. The equations of motion of an incompressible fluid, with density ρ and viscosity μ, are

$$\begin{aligned} &\rho\left(\frac{\partial \mathbf{u}}{\partial t} + (\mathbf{u}\cdot\nabla)\mathbf{u}\right) + \nabla p - 2\mu\nabla\cdot(\nabla\mathbf{u})^s = \mathbf{f} && \text{in}\,\Omega, t \in (0,T) \\ &\nabla\cdot\mathbf{u} = 0 && \text{in}\,\Omega, t \in (0,T) \end{aligned} \tag{4.1}$$

where $\mathbf{u}$ and p are the velocity and pressure fields, respectively. The problem is fully characterized by considering a divergence free initial condition $\mathbf{u}(\mathbf{x}, 0) = \mathbf{u}_0(\mathbf{x})$ and suitable boundary conditions over the surface $\partial\Omega$. Particularly, over the lateral boundary (Γ_L) homogeneous Dirichlet boundary conditions are considered (no-slip condition).

To recast the Navier-Stokes equations in a variational framework, we introduce the space

$$\boldsymbol{\mathcal{V}} = \left\{\mathbf{u} \in [H^1(\Omega)]^d : \mathbf{u}|_{\Gamma_L} = 0, (\boldsymbol{\Pi}\mathbf{u})|_{\Gamma_i} = 0, (\boldsymbol{\Pi}\mathbf{u})|_{\Gamma_o} = 0\right\} \tag{4.2}$$

of all $[H^1(\Omega)]^d$ functions with zero trace in Γ_L and where the projector operator $\boldsymbol{\Pi} = \boldsymbol{I} - \mathbf{n}\otimes\mathbf{n}$ is introduced to impose a fully developed flow over the surface of normal $\mathbf{n}$. This last assumption is justified considering that, in the field of hemodynamics, it is natural to consider that the domain has been isolated from the rest of the system at places where the flow is assumed to be fully developed.

Given a divergence free datum $\mathbf{u}_0 \in \boldsymbol{\mathcal{V}}$ and an external field $\mathbf{f} \in [L^2(0,T;H^{-1}(\Omega)]^d$, we define the weak form for the Navier-Stokes problem as: Find the velocity field $\mathbf{u} \in [L^2(0,T;\boldsymbol{\mathcal{V}}) \cap L^\infty(0,T;L^2(\Omega)]^d$ and pressure field $p \in L^2(0,T;L^2(\Omega))$ such that

$$\int_\Omega \left[\rho\frac{\partial \mathbf{u}}{\partial t}\cdot\hat{\mathbf{u}} + \rho(\mathbf{u}\cdot\nabla)\mathbf{u}\cdot\hat{\mathbf{u}} + 2\mu\boldsymbol{\varepsilon}(\mathbf{u})\cdot\nabla(\hat{\mathbf{u}}) - p\,\mathrm{div}\,\hat{\mathbf{u}} - \hat{p}\,\mathrm{div}\,\mathbf{u}\right] d\Omega = \int_\Omega \mathbf{f}\cdot\hat{\mathbf{u}}\,d\Omega + \int_{\Gamma_i} t_i\mathbf{n}\cdot\hat{\mathbf{u}}\,d\Gamma_i + \int_{\Gamma_o} t_o\mathbf{n}\cdot\hat{\mathbf{u}}\,d\Gamma_o \qquad \forall\,(\hat{\mathbf{u}},\hat{p}) \in \boldsymbol{\mathcal{V}}\times L^2(\Omega), \quad (4.3)$$

with ρ and μ being the fluid density and viscosity, respectively, $\boldsymbol{\varepsilon}(\cdot) = (\nabla(\cdot))^s$, and $\hat{(\cdot)}$ denotes an admissible variation of field $(\cdot)$. Finally, t_i and t_o are given data which stand for the magnitude of the normal component of the traction vector imposed at Γ_i and Γ_o, respectively. Mathematical properties of each part in the Navier-Stokes formulation, as continuity of forms, can be seen in detail in [Teman 1977, Girault and Raviart 1986, Evans 1997].

In hemodynamic applications, the vector field $\mathbf{f}$ is usually set to zero. This hypothesis corresponds to consider negligible the effects of gravity. From a mechanical point of view, the solution of the Navier-Stokes equation may develop instabilities called *turbulence* due to the dynamics induced by the non-linear convection term and its relative strength when compared against to the diffusive effects. This predominance of inertial effects over viscous effects is characterized by the Reynolds number

$$Re = \frac{\rho D u^*}{\mu}, \quad (4.4)$$

a dimensionless number that depends on the characteristic length of the vessel D (typically the vessel equivalent diameter), the magnitude of the mean flow velocity u^*, the density ρ and viscosity μ of the fluid. Values for Reynolds number up to $Re = 800$ are the encountered in the blood flow circulation.

4.2 The discrete scheme

A discrete formulation for the Navier-Stokes equation is addressed in this section. For this purpose, we separate the process into three steps:

i) The time discretization to deal with the transient term in the continuous model.

ii) The adoption of a linearization scheme to overcome the nonlinearity implied by the convective term $(\mathbf{u}\cdot\nabla)\mathbf{u}$.

iii) The spatial discretization of velocity and pressure fields, at each time step, for which transversally enriched discrete spaces are introduced.

The result is an scheme which treat iteratively both the time and the nonlinear nature of the problem described in Equation 4.3. Also, a penalization process for the pressure is discussed to supplement the incompressibility constrain.

4.2.1 Scheme for time discretization

We start by approximating the time derivative by a backward Euler scheme at the following way: Given $\Delta t \in \mathbb{R}$, we set $t_0 = 0$, $t_n = t_0 + n\Delta t$ $(n \geq 1)$ and, denoting $\mathbf{u}^n = \mathbf{u}(t_n)$, we consider the approximation for the time derivative as

$$\frac{\partial \mathbf{u}}{\partial t}(t_n) = \frac{\mathbf{u}^n - \mathbf{u}^{n-1}}{\Delta t}, \tag{4.5}$$

which allows us to recast the continuous-in-time problem as the following implicit formulation: Given an initial velocity $\mathbf{u}^0$, for each $n > 1$ find the solution $(\mathbf{u}^n, p^n) \in \boldsymbol{\mathcal{V}} \times L^2(\Omega)$ of

$$\begin{aligned}\int_\Omega \left[\rho \frac{\mathbf{u}^n}{\Delta t} \cdot \hat{\mathbf{u}} + \rho(\mathbf{u}^n \cdot \nabla)\mathbf{u}^n \cdot \hat{\mathbf{u}} + 2\mu\boldsymbol{\varepsilon}(\mathbf{u}^n) \cdot \nabla(\hat{\mathbf{u}}) - p^n \operatorname{div} \hat{\mathbf{u}} - \hat{p} \operatorname{div} \mathbf{u}^n\right] d\Omega = \\ \int_\Omega \rho \frac{\mathbf{u}^{n-1}}{\Delta t} \cdot \hat{\mathbf{u}} + \int_{\Gamma_i} t_i^n \mathbf{n} \cdot \hat{\mathbf{u}}\, d\Gamma_i + \int_{\Gamma_o} t_o^n \mathbf{n} \cdot \hat{\mathbf{u}}\, d\Gamma_o \qquad \forall (\hat{\mathbf{u}}, \hat{p}) \in \boldsymbol{\mathcal{V}} \times L^2(\Omega),\end{aligned} \tag{4.6}$$

with the initial condition $\mathbf{u}^0 = \mathbf{u}_0$. Clearly, no initial pressure needs to be specified.

4.2.2 Linearization of the convective term

The convective term $(\mathbf{u} \cdot \nabla)\mathbf{u}$ in the Equation (4.3), and their time-discrete counterpart, introduces an evident nonlinearity in the problem. The usual approach to deal with this aspect is to solve a linearized version of the equations at each time step. Two numerical schemes stand out as the most popular methods for implicit time marching algorithms:

Picard iteration. A widely used scheme to linearize the convective term is based in Picard (fixed-point) linearization. In this approach, the nonlinear term is substituted by

$$(\mathbf{u}^{k+1} \cdot \nabla)\mathbf{u}^{k+1} \approx (\mathbf{u}^k \cdot \nabla)\mathbf{u}^{k+1} \tag{4.7}$$

where the vector field $\mathbf{u}^k$ is the approximation of the velocity field in the k-th Picard iteration.

Another apparently possible way to linearize the convective term, and still in a fixed-point fashion, is to employ the approximation

$$(\mathbf{u}^{k+1} \cdot \nabla)\mathbf{u}^{k+1} \approx (\mathbf{u}^{k+1} \cdot \nabla)\mathbf{u}^k \tag{4.8}$$

Physically speaking, understanding the term $(\mathbf{u} \cdot \nabla)$ as the convection operator and solving for the flow at the $(k+1)$th iteration: $(\mathbf{u}^k \cdot \nabla)\mathbf{u}^{k+1}$ implies an approximate convection operator $(\mathbf{u}^k \cdot \nabla)$ convecting the velocity field $\mathbf{u}^{k+1}$ while the term $(\mathbf{u}^{k+1} \cdot \nabla)\mathbf{u}^k$ involves the exact convection operator $(\mathbf{u}^{k+1} \cdot \nabla)$ convecting a previously calculated velocity field $\mathbf{u}^k$. The difference between both linearizing strategies is explored in detail in [DeBlois 1997]. There, the author demonstrates that linearize the term $(\mathbf{u} \cdot \nabla)\mathbf{u}$ by employing the expression in Equation (4.8) leads to wrong fixed points and, therefore, unfeasible solutions of the Navier-Stokes equations. For a proof of the global convergence of this method, we refer to [Karakashian 1982].

Newton iteration. Assuming that the approximated solution for the iteration $k+1$ can be expressed as the previous iteration solution plus a correction, this is

$$\mathbf{u}^{k+1} = \mathbf{u}^k + \delta\mathbf{u}^k \tag{4.9}$$

so, the convective term can be written as:

$$\begin{aligned}(\mathbf{u}^{k+1}\cdot\nabla)\mathbf{u}^{k+1} &= ((\mathbf{u}^k+\delta\mathbf{u}^k)\cdot\nabla)(\mathbf{u}^k+\delta\mathbf{u}^k)\\ &= (\mathbf{u}^{k+1}\cdot\nabla)\mathbf{u}^k + \delta(\mathbf{u}^k\cdot\nabla)\mathbf{u}^k + \delta^2(\mathbf{u}^k\cdot\nabla)\mathbf{u}^k\\ &= (\mathbf{u}^{k+1}\cdot\nabla)\mathbf{u}^k + (\mathbf{u}^k\cdot\nabla)\mathbf{u}^{k+1} - (\mathbf{u}^k\cdot\nabla)\mathbf{u}^k + \delta^2(\mathbf{u}^k\cdot\nabla)\mathbf{u}^k\end{aligned} \tag{4.10}$$

where, by neglecting the quadratic term in δ, we obtain the Newton linearization of the Navier-Stokes equation.

Although Newton methods features faster convergence rates, they typically have radii of convergence smaller than Picard methods. Hence, in most applications and particularly for our approach, the Picard iterative method is employed. This strategy gives rise, at each time step $n \geq 1$, to the so-called Oseen problem: Find the converged solution $(\mathbf{u}^n, p^n) \in \boldsymbol{\mathcal{V}} \times \mathcal{Q}$ such that $\mathbf{u}^{n,k} \to \mathbf{u}^n$ and $p^{n,k} \to p^n$ (when $k \to \infty$) where, for each $k \geq 1$, it holds

$$\begin{aligned}\int_\Omega \left[\rho\frac{\mathbf{u}^{n,k}}{\Delta t}\cdot\hat{\mathbf{u}} + \rho(\mathbf{u}^{n,k-1}\cdot\nabla)\mathbf{u}^{n,k}\cdot\hat{\mathbf{u}} + 2\mu\boldsymbol{\varepsilon}(\mathbf{u}^{n,k})\cdot\nabla(\hat{\mathbf{u}}) - p^{n,k}\operatorname{div}\hat{\mathbf{u}} - \hat{p}\operatorname{div}\mathbf{u}^{n,k}\right] d\Omega =\\ \int_\Omega \rho\frac{\mathbf{u}^{n-1}}{\Delta t}\cdot\hat{\mathbf{u}} + \int_{\Gamma_i} t_i^n\mathbf{n}\cdot\hat{\mathbf{u}}\, d\Gamma_i + \int_{\Gamma_o} t_o^n\mathbf{n}\cdot\hat{\mathbf{u}}\, d\Gamma_o \qquad \forall\,(\hat{\mathbf{u}},\hat{p}) \in \boldsymbol{\mathcal{V}}\times L^2(\Omega),\end{aligned} \tag{4.11}$$

with the initial solution $\mathbf{u}^{n,0} = \mathbf{u}^n$.

4.2.3 Improving the condition of the system

The incompressibility nature of the velocity field imposed in the Navier-Stokes equations makes the system difficult to solve numerically. From an algebraic point of view, the discretization of the problem with this constrain results in a saddle-point system with a zero diagonal block which may involve several numerical challenges. For a detailed discussion of this type of problem see, for example, [Benzi et al. 2005].

A popular strategy to overcome this difficulty is to modify the continuous variational formulation in Equation (4.3) in an appropriate way so that we arrive at the so-called *pseudocompressibility* methods. One of the most popular of this kind is the penalty method, introduced in [Courant 1943], where the left hand side in Equation (4.3) is substituted by:

$$\int_\Omega \left[\rho\frac{\partial\mathbf{u}^\epsilon}{\partial t}\cdot\hat{\mathbf{u}} + \rho(\mathbf{u}^\epsilon\cdot\nabla)\mathbf{u}^\epsilon\cdot\hat{\mathbf{u}} + 2\mu\boldsymbol{\varepsilon}(\mathbf{u}^\epsilon)\cdot\nabla(\hat{\mathbf{u}}) - p^\epsilon\operatorname{div}\hat{\mathbf{u}} - \hat{p}\operatorname{div}\mathbf{u}^\epsilon - \epsilon p^\epsilon\hat{p}\right] d\Omega \tag{4.12}$$

Notice that the equation is now defined in the variables $(\mathbf{u}^\epsilon, p^\epsilon)$ and also the term $\epsilon p^\epsilon\hat{p}$ was introduced. At a continuous level, the solution $(\mathbf{u}^\epsilon, p^\epsilon)$ converges to $(\mathbf{u}, p)$, when $\epsilon \to 0$. At the discrete level, this problem introduces an error commanded by the parameter ϵ.

Another option is to penalize the Navier-Stokes equation by adding at the Equation (4.6) the term

$$\epsilon \int_\Omega p^{n,k}\hat{p}\, d\Omega - \epsilon \int_\Omega p^{n,k-1}\hat{p}\, d\Omega \tag{4.13}$$

where $p^{n,k}$ is the pressure field at the temporal step n and at the iteration step k. This strategy leads to a variational consistent modification of the continuous model. When needed, we will include this last term in the model to improve the conditioning of the resulting discrete structure. The convergence of the pressure field is found along the Picard iterations performed to deal with the nonlinearities already present in the Navier-Stokes equations.

4.2.4 Spatial TEPEM discretization

After discretizing in time by backward Euler, and linearizing using Picard iterations, we arrive at the following time-discrete linearized variational problem: For each $n > 1$ find $(\mathbf{u}^n, p^n) \in \mathcal{V} \times \mathcal{Q}$ solution of the iterative scheme:

$$\begin{aligned}\int_\Omega \left[\rho\frac{\mathbf{u}^{n,k}}{\Delta t}\cdot\hat{\mathbf{u}} + \rho(\mathbf{u}^{n,k-1}\cdot\nabla)\mathbf{u}^{n,k}\cdot\hat{\mathbf{u}} + 2\mu\boldsymbol{\varepsilon}(\mathbf{u}^{n,k})\cdot\nabla(\hat{\mathbf{u}}) - p^{n,k}\,\mathrm{div}\,\hat{\mathbf{u}} - \hat{p}\,\mathrm{div}\,\mathbf{u}^{n,k}\right] d\Omega = \\ \int_\Omega \rho\frac{\mathbf{u}^{n-1}}{\Delta t}\cdot\hat{\mathbf{u}} + \int_{\Gamma_i} t_i^n\mathbf{n}\cdot\hat{\mathbf{u}}\, d\Gamma_i + \int_{\Gamma_o} t_o^n\mathbf{n}\cdot\hat{\mathbf{u}}\, d\Gamma_o \qquad \forall\,(\hat{\mathbf{u}},\hat{p}) \in \boldsymbol{\mathcal{V}} \times L^2(\Omega),\end{aligned} \tag{4.14}$$

defined for $k \geq 0$ and with initial solution $\mathbf{u}^{n,0} = \mathbf{u}^{n-1}$, $p^{n,0} = p^{n-1}$. Here $\mathbf{u}^{n,k}$ and $p^{n,k}$ are the fluid velocity and pressure at time $t = t_n$ and at the current iteration k.

For the spatial discretization of the Navier-Stokes equations, we employ the TEPEM strategy to discretize both velocity and pressure fields at each time and at each Picard iteration. For a pipe-type partition $\mathcal{T}_h(\Omega)$ of the geometrical domain and a fixed even parameter $\mathsf{p} \in \mathbb{N}$, we introduce the finite-dimensional spaces to approximate the velocity and pressure fields as

$$\boldsymbol{\mathcal{V}}_h = \left[\mathbb{T}_h^{\mathsf{p},2}\right]^d \cap C(\overline{\Omega}) \cap \boldsymbol{\mathcal{V}} \qquad \mathcal{Q}_h = \mathbb{T}_h^{\frac{\mathsf{p}}{2},1} \cap C^*(\overline{\Omega}) \tag{4.15}$$

where $C^*(\overline{\Omega})$ stands for the space of functions which are continuous at interfaces between adjacent simple pipe elements and are discontinuous at interfaces between simple and transition pipe elements. Hence, the velocity is a continuous field while the pressure presents discontinuities over the cross-sectional interfaces between transition-pipe elements and simple pipe elements.

It is important to recall that the space $\mathbb{T}_h^{\mathsf{p},\mathsf{s}}$ (for $\mathsf{s} \in \{1,2\}$) is constructed over the partition $\mathcal{T}_h(\Omega)$ and is defined, in the three-dimensional case, as

$$\mathbb{T}_h^{\mathsf{p},\mathsf{s}} = \left\{ w^h \in L^2(\Omega) : w^h \circ \chi_{\mathcal{K}}(\xi,\eta,\zeta) = \sum_{k=1}^{\mathsf{s}+1} w_k^{\mathsf{p}}(\xi,\eta)\varphi_k(\zeta),\ \ \mathcal{K} \in \mathcal{T}_h(\Omega) \right\} \tag{4.16}$$

where $\{\varphi_k : k = 1,\ldots,\mathsf{s}+1\}$ is the Lagrangian basis for $\mathbb{P}_\mathsf{s}$ ($\mathsf{s} \in \{1,2\}$) and the functions $\{w_k^{\mathsf{p}} : k = 1,\ldots,\mathsf{s}+1\}$ are constructed in terms of the basis $\{\phi_i : i = 1,\ldots,\mathsf{p}+1\}$ for the space $\mathbb{P}_\mathsf{p}$ according to the definition provided in Section 2.3.3.

With the combination of spaces for velocity and pressure proposed in Equation (4.15), the velocity and pressure are considered continuous fields. We will denote by $\mathbf{u}_{\mathrm{T}}$ (p_{T}) the approximation of the velocity (pressure) field in the TEPEM spaces.

4.3 Further numerical and computational aspects

The former finite-dimensional combination of spaces for velocity and pressure yields an approximation of the velocity, on the reference element, with quadratic polynomials in the axial direction and polynomials up to degree p for the transversal direction. Equivalently, the pressure field is approximated through the combination of linear polynomials for the axial direction and polynomials up to $\mathsf{p}/2$ for the transversal dynamics.

This special combination defines a finite-element with a higher number of degrees of freedom if compared with the finite elements available in the literature for the same problem. For the three-dimensional case, the case $\mathsf{p} = 4$ defines a pipe-element with 75 degrees of freedom for each scalar component of the velocity and 18 for the pressure. For the transition pipe-element, this number increases to 95 for velocity and 24 for the pressure. The distribution of the velocity/pressure nodes for $\mathsf{p} = 4$ is displayed in Figure 4.2. Note that considering order $\mathsf{p}/2$ to define the discrete pressure space allows to match the pressure nodes with a subset of the velocity nodes, reusing the mesh structure and avoiding the need to consider two different meshes.

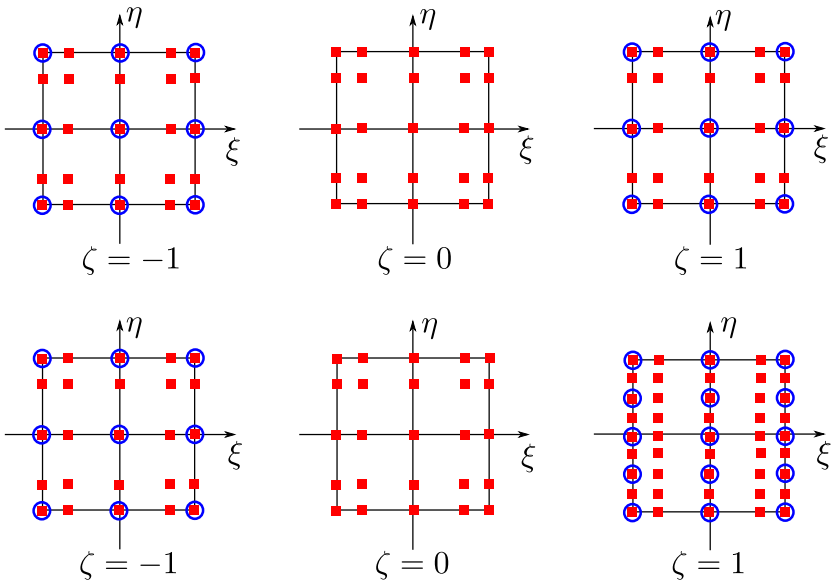

Figure 4.2: Velocity (red ■) and pressure (blue ◯) nodes in each transversal section of the reference element for transversal order $\mathsf{p} = 4$. Top: Nodes for a simple slab element. Bottom: Nodes for a transition element.

Notwithstanding this increase in the degrees of freedom per element, it is expected that the total number of unknowns is drastically reduced due the 1D-like structure of the mesh, which allows to employ a reduced number of elements while maintaining a good geometric approximation. Moreover, the use of a distributed computing paradigm can be used to exploit the simple connectivity among elements to improve the efficiency of the method. Several numerical examples are addressed in Sections 4.4-4.5 to evaluate this efficiency by comparing against a FEM approach.

4.3.1 Algebraic system of equations

As happens with finite difference ([Peyret and Taylor 2012]) and classical finite elements schemes ([Quarteroni and Valli 2008, Elman et al. 2014]), the implicit discretization of the Navier-Stokes equations employing the TEPEM with the previously defined finite-dimensional spaces results in, for each $n \geq 1$, a generalized saddle point system of the form:

$$\begin{pmatrix} \mathbf{A}_n & \mathbf{B}_n \\ \mathbf{B}_n^T & \mathbf{0} \end{pmatrix} \begin{pmatrix} \mathbf{U}_n \\ P_n \end{pmatrix} = \begin{pmatrix} \mathbf{F}_n \\ \mathbf{0} \end{pmatrix} \tag{4.17}$$

where $\mathbf{U}_n \in \mathbb{R}^{N_u \cdot d}$ and $P_n \in \mathbb{R}^{N_p}$ are the degrees of freedom for velocity $\mathbf{u}^n$ and pressure p^n in the time $t = t^n$, with d the dimension of the problem and N_u and N_p the dimension of the finite-dimensional spaces for velocity and pressure, respectively. The matrix $\mathbf{B}_n = [B_i]_{1 \leq i \leq d}$ is the discrete counterpart of the gradient operator, $\mathbf{B}_n^T$ of the divergence operator and matrix $\mathbf{A}_n = [A_{ij}]_{1 \leq i,j \leq d}$ accounts for the discretization of the diffusive term, the linearized convective term and the mass matrix.

The algebraic system in Equation (4.17) is obtained by adding the elemental contributions in the pipe-mesh partition as was detailed in Chapter 3 in the context of scalar transport problems. The structure of each inner block, $A_{ij} \in \mathbb{R}^{N_u \times N_u}$ and $B_i \in \mathbb{R}^{N_u \times N_p}$ (for $1 \leq i \leq d$), features the global structure seen in one-dimensional FEM discretizations with ordered numbering. By denoting $\mathsf{p}_u = (\mathsf{p}+1)^{d-1}$ and $\mathsf{p}_p = (\frac{\mathsf{p}}{2}+1)^{d-1}$, the algebraic structure of these blocks is outlined in Figure 4.3. Note that by considering the axial discretization at the outer level of approximation, blocks that form the global matrices are block banded matrices with dense sub-blocks.

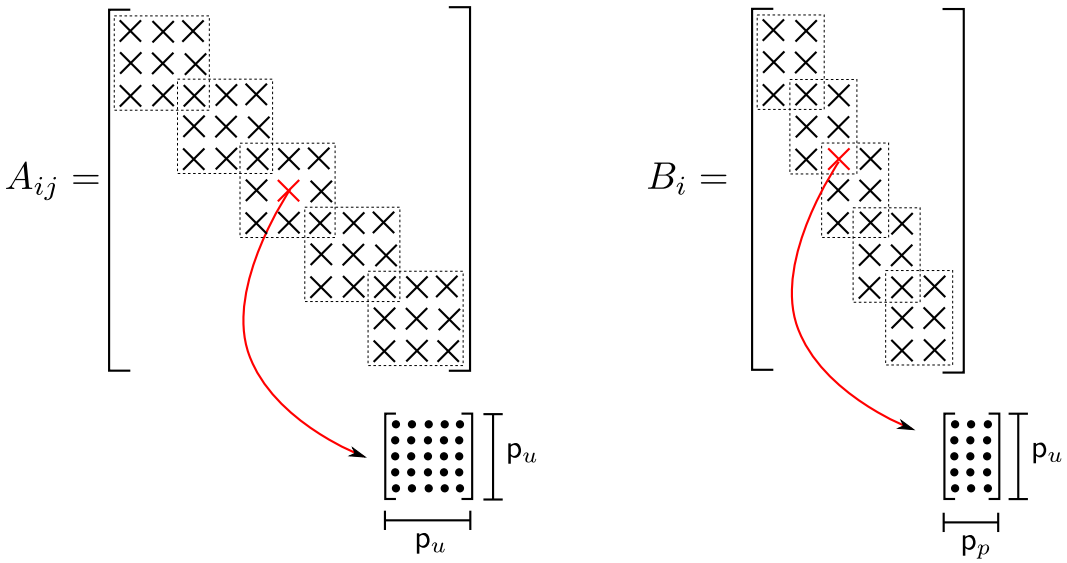

Figure 4.3: Algebraic structure of the block matrices in the discretization of Navier-Stokes equations. Dotted regions stands for the local contribution computed in each pipe-element.

4.3.2 Inf-sup stability

From the theoretical point of view, it is well known the fundamental role that the inf-sup condition plays in the theory of mixed and penalty methods. Also known as LBB condition due to the works of Ladyzhenskaya-Babuska-Brezzi ([Ladyzhenskaya 1969, Babuška 1971, Brezzi 1974]), this condition holds for the weak form of the continuous problem, but it is not a priori guaranteed by the corresponding discrete formulation. While the issue has largely been investigated for finite element and spectral methods ([Maday and Patera 1989, Bernardi and Maday 1997, Brenner and Scott 2007, Quarteroni and Valli 2008, Canuto et al. 2010]), we are not aware of any theoretical result for hybrid methods that involve both of techniques.

For the TEPEM, the pair of velocity/pressure finite-dimensional spaces was initially inspired in some compatibility condition results for FEM and spectral schemes:

i) For FEM, a classical stable combination is the first element of Taylor-Hood family: quadratic polynomials to interpolate the velocity and linear interpolants for the pressure.

ii) In turn, a difference of two degrees in the approximation of velocity in contrast with the pressure is also an usual pair that ensures the inf-sup stability in spectral methods.

These approaches contribute to the conjecture that the combination

$$\boldsymbol{\mathcal{V}}_h = \left[\mathbb{T}_h^{\mathtt{p},2}\right]^d \cap C(\overline{\Omega}) \cap \boldsymbol{\mathcal{V}} \qquad \mathcal{Q}_h = \mathbb{T}_h^{\frac{\mathtt{p}}{2},1} \cap C^*(\overline{\Omega}) \tag{4.18}$$

is a plausible inf-sup stable pair of spaces for the approximation of Navier-Stokes equations precluding the appearance of unphysical phenomena. Even when an ultimate proof for this combination is not yet available, it is possible to gain insight into the compatibility of the pair through numerical tools. In this context, it is specially interesting the so-called *inf-sup test* proposed in [Chapelle and Bathe 1993, Bathe 2001], in which a numerical approximation of the inf-sup constant (here called IS) is obtained as the solution of an eigenvalue problem.

Roughly speaking, the inf-sup test is described as follows: Let us denote by $(\boldsymbol{\mathcal{U}}_h, \mathcal{P}_h)$ the combination of finite-dimensional spaces for velocity and pressure that we are interested in to test and also define the forms $a : \boldsymbol{\mathcal{U}}_h \times \boldsymbol{\mathcal{U}}_h \to \mathbb{R}$ and $b : \mathcal{P}_h \times \boldsymbol{\mathcal{U}}_h \to \mathbb{R}$ as

$$a(\mathbf{u}, \hat{\mathbf{u}}) = \int_\Omega \boldsymbol{\varepsilon}(\mathbf{u}) \cdot \nabla \hat{\mathbf{u}} \, d\Omega \qquad b(p, \hat{\mathbf{u}}) = \int_\Omega p \operatorname{div} \hat{\mathbf{u}} \tag{4.19}$$

Denoting by A_h (B_h) the discrete representation of form $a(\cdot,\cdot)$ ($b(\cdot,\cdot)$), by M_h the pressure mass matrix related to the L^2-norm and defining $R_h = M_h^{-1}(B_h A_h^{-1} B_h^T)$, we can obtain a numerical value of the inf-sup constant (for a given fixed mesh) as

$$IS = \sqrt{\lambda_0} = \inf_{q_h \in \mathcal{P}_h} \sup_{u_h \in \boldsymbol{\mathcal{U}}_h} \frac{1}{\|q_h\| \|u_h\|} \int_\Omega q_h \operatorname{div} u_h \, d\Omega \tag{4.20}$$

where λ_0 is the smaller non-zero eigenvalue of the problem

$$R_h \mathbf{v}_h = \lambda \mathbf{v}_h \tag{4.21}$$

The stability of the pair $(\boldsymbol{\mathcal{U}}_h, \mathcal{P}_h)$, in the inf-sup test, is now reduced to analyzing the behavior of IS when the dimension of these spaces increases. If the value IS is bounded away from zero, the velocity/pressure pair passes the test, otherwise it fails. Moreover, the number of zero eigenvalues (denoted as k_{pm}) immediately tells whether spurious modes are possible to be manifested. The main attractive in this numerical test is that, since its appearance in [Chapelle and Bathe 1993], it has been applied in several contexts and finite elements with analytical proof (for stable and unstable discrete pairs) and has provided in each case a numerical prediction matching with the theoretical one, testifying his excellent reliability to assess the behavior of finite elements for which no a priori theoretical results exist, like the case of the TEPEM family of spaces.

The inf-sup test is employed to evaluate the compatibility of the pair proposed in the expression (4.18), denoted as $\mathcal{S}_0$, and three other combinations for the velocity/pressure spaces, named:

i) Same axial/transversal order: $\mathcal{S}_1 = \left(\left[\mathbb{T}_h^{\mathsf{p},1} \right]^d \cap C(\overline{\Omega}) \cap \boldsymbol{\mathcal{V}} \right) \times \left(\mathbb{T}_h^{\mathsf{p},1} \cap C^*(\overline{\Omega}) \right)$

ii) Same axial order: $\mathcal{S}_2 = \left(\left[\mathbb{T}_h^{\mathsf{p},1} \right]^d \cap C(\overline{\Omega}) \cap \boldsymbol{\mathcal{V}} \right) \times \left(\mathbb{T}_h^{\frac{\mathsf{p}}{2},1} \cap C^*(\overline{\Omega}) \right)$

iii) Same transversal order: $\mathcal{S}_3 = \left(\left[\mathbb{T}_h^{\mathsf{p},2} \right]^d \cap C(\overline{\Omega}) \cap \boldsymbol{\mathcal{V}} \right) \times \left(\mathbb{T}_h^{\mathsf{p},1} \cap C^*(\overline{\Omega}) \right)$

recalling that, in the proposed context, a transversally enriched pipe element defined by velocity and pressure must have the inf-sup constant IS bounded away from zero when the number of pipe-elements increases (h decreases) and when the transversal polynomial order increases (p increases).

The behavior of the IS value for the pair denoted as $\mathcal{S}_0$ is presented in the Figure 4.4. For this choice, the IS value features a saturation when h decreases and when p increases, allowing us to conclude that the pair of velocity/pressure spaces passes the inf-sup test. Also, the absence of zero eigenvalues is confirmed, which implies the absence of spurious modes.

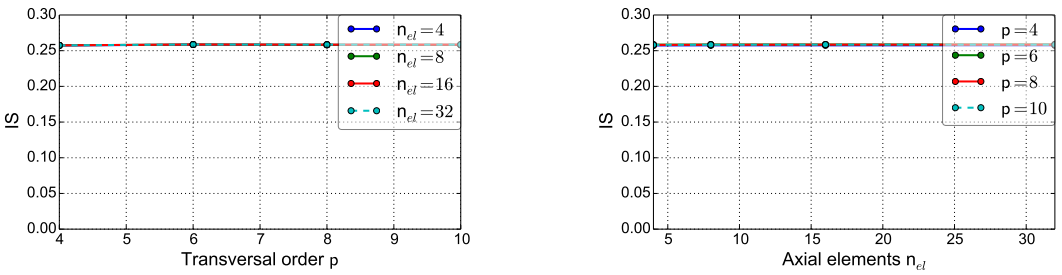

Figure 4.4: Behavior of the IS value for the velocity/pressure combination $\mathcal{S}_0$ when decreasing the axial elemental length and increasing the transversal order.

Similarly, the inf-sup test is applied in the pairs denoted by $\mathcal{S}_1$, $\mathcal{S}_2$ and $\mathcal{S}_3$. None of these cases passed the numerical test. The value of IS and the number of spurious nodes k_{pm}, for each case, decreases with the decreasing of h and also with the increasing of p. Figures 4.5-4.7 presents the behavior of IS and k_{pm} for these three cases, making evident the decrease of the numerical value of the inf-sup constant without the existence of a threshold away from zero and the presence of spurious nodes.

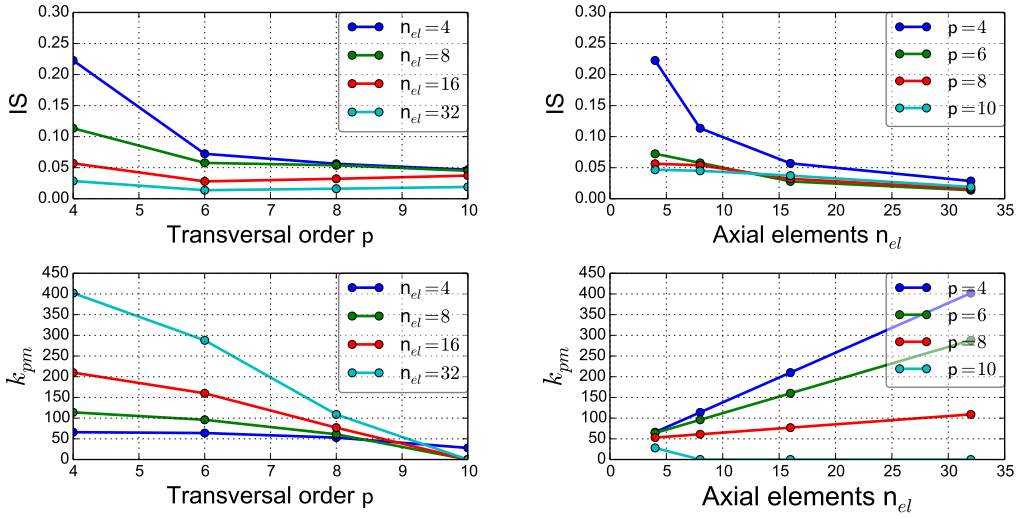

Figure 4.5: Behavior of the IS value and number of spurious nodes k_{pm} for the velocity/pressure combination $\mathcal{S}_1$ when decreasing the axial elemental length and increasing the transversal order.

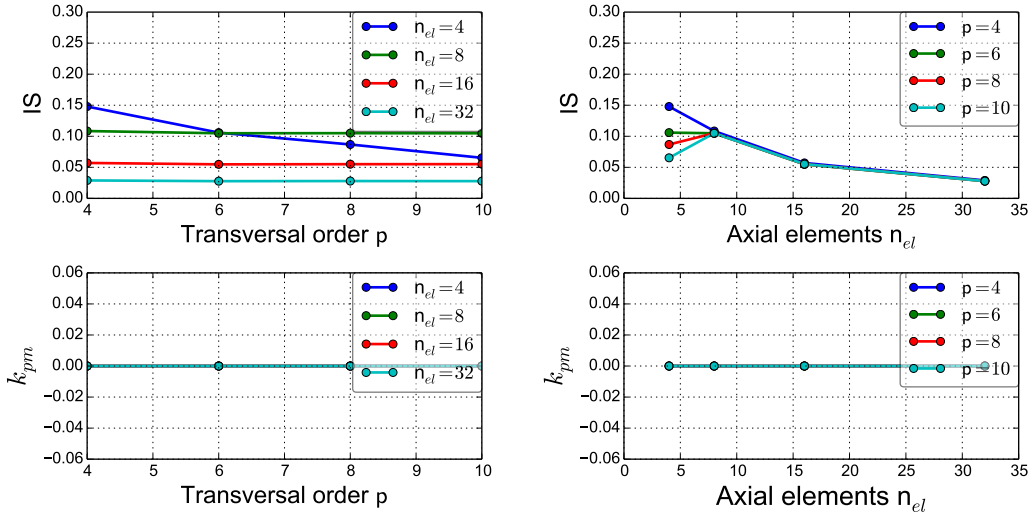

Figure 4.6: Behavior of the IS value and number of spurious nodes k_{pm} for the velocity/pressure combination $\mathcal{S}_2$ when decreasing the axial elemental length and increasing the transversal order.

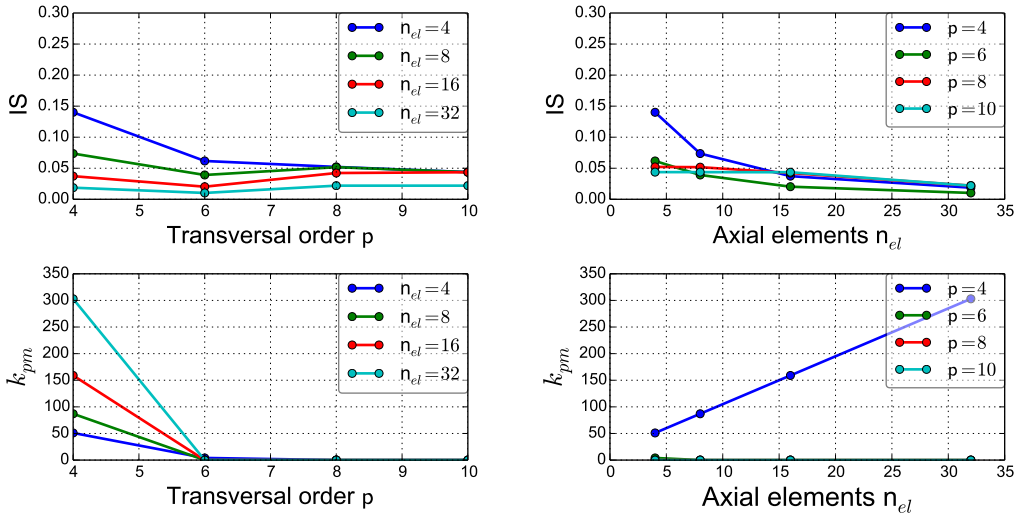

Figure 4.7: Behavior of the IS value and number of spurious nodes k_{pm} for the velocity/pressure combination $\mathcal{S}_3$ when decreasing the axial elemental length and increasing the transversal order.

This numerical evidence, together with the absence of any spurious modes in all the numerical cases addressed during the development of the TEPEM both in two- and three-dimensional cases, leads us to consider the pair $\mathcal{S}_0$ as stable in the inf-sup sense.

4.3.3 Initial conditions for the velocity field

The numerical solution of the time-dependent Navier-Stokes equations requires the consideration of an initial condition for the velocity field. In the field of hemodynamics it is impossible to set the correct initial conditions because of the periodic nature of the physiological flows. Instead, it is usually proposed to start with $\mathbf{u}(\mathbf{x}, 0) = \mathbf{0}$ and then simulate several cardiac periods in order to erase the initial conditions and reach a periodic state.

An alternative to setting null velocity is to solve a stationary Stokes problem. The velocity solution is compatible with boundary/incompressibility condition and accounts already for part of the physics of the problem, by neglecting the inertia effects. Another option is to employ cheaper models to the assessment and then construct an initial data in base of that low-cost solution. In the TEPEM, as the geometrical structure is independent of the transversal order employed to approximate the velocity/pressure fields, the projection of an approximate solution into richer spaces can easily be performed, and will be exploited in some numerical simulations presented here. This is, in contrast to projections within the context of FEM where the refinement in the approximate space is attached to a modification in the geometry.

4.3.4 Boundary conditions

The computational implementation of boundary conditions at inlet/outlet regions within the TEPEM scope is performed taken into account that all the degrees of freedom corresponding to the desired flat boundary are connected when considering one single pipe-element for the transversal section. In practice, it is possible to understand each inlet/outlet boundary as a single element composed by $(\mathsf{p}+1)^2$ nodes, as exemplified in Figure 4.8.

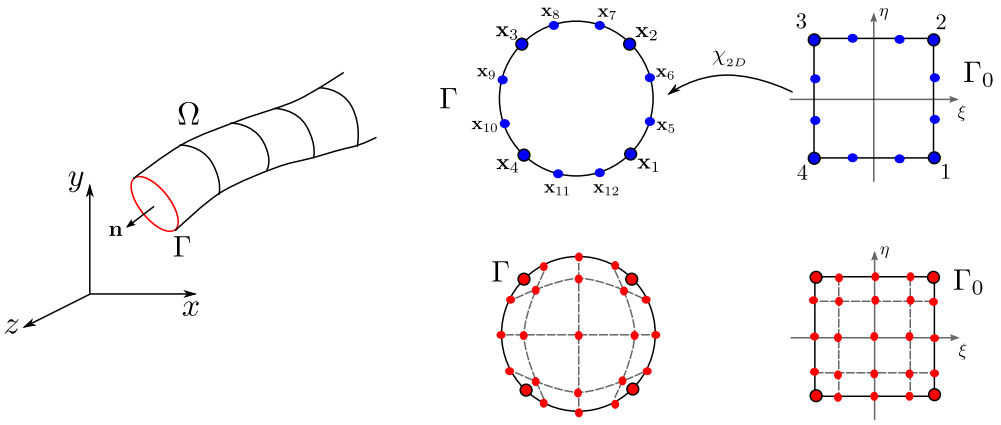

Figure 4.8: Geometrical components of flat boundary Γ. In blue the geometrical nodes and in red the nodes where physical fields are approximated (case $\mathsf{p}=4$).

The geometrical mapping χ_{2D} is constructed in base of the Serendipity basis as

$$\chi_{2D}(\xi,\eta)=\sum_{i=1}^{12}\mathbf{x}_i\mathcal{S}_i(\xi,\eta) \tag{4.22}$$

while the velocity field is approximated as

$$\mathbf{u}\circ\chi_{2D}|_{\Gamma_0}(\boldsymbol{\xi})=\sum_{i=1}^{(\mathsf{p}+1)}\sum_{j=1}^{(\mathsf{p}+1)}\mathbf{u}_{ij}\phi_i(\xi)\phi_j(\eta) \tag{4.23}$$

where the set $\{\phi_i : i=1,\ldots,\mathsf{p}+1\}$ is the basis of $\mathbb{P}_\mathsf{p}$ where each element is a Lagrangian polynomial defined in the CGL set of nodes and, for $1\leq i,j\leq \mathsf{p}+1$, $\mathbf{u}_{ij}\in\mathbb{R}^3$ are the degrees of freedom for the velocity field. Note that both the geometrical mapping and the approximation of velocity field are constructed as a restriction of the field defined for a pipe-element but restricted to one transversal slice.

Among different possible boundary conditions that could be imposed at inlet/outlet boundaries, here we limit ourselves to two cases: (i) Non-homogeneous Dirichlet BC, in particular the imposition of a parabolic profile for the velocity and (ii) The imposition of non-homogeneous Neumann BC. In Chapter 5.2, some other types of boundary conditions are addressed in the context of hemodynamics simulations.

Dirichlet condition Considering Γ being a circular region of center $\mathbf{x}_0$ and radius R, we are interested in imposing at Γ a velocity field with parabolic profile and maximum velocity prescribed as α. This is, for each $\mathbf{x} \in \Gamma$

$$\mathbf{u}(\mathbf{x}) \cdot \mathbf{n} = \pm\alpha \left(1 - \frac{r^2}{R^2}\right), \qquad \mathbf{u}(\mathbf{x}) \cdot \mathbf{t}_1 = 0, \qquad \mathbf{u}(\mathbf{x}) \cdot \mathbf{t}_2 = 0 \tag{4.24}$$

where $r^2 = \|\mathbf{x} - \mathbf{x}_0\|^2$, $\mathbf{n}$ is the outward unit normal of Γ and the in-plane vectors $\mathbf{t}_1$ and $\mathbf{t}_2$ are such that $\mathbf{t}_1 \times \mathbf{t}_2 = \mathbf{n}$. The sign at the first equation is positive if Γ is an outlet boundary and negative in the case of inlet boundary, this because the normal $\mathbf{n}$ is chosen always to be outward. Note also that, when choosing this boundary as being a flat surface, the vectors $\mathbf{n}$, $\mathbf{t}_1$ and $\mathbf{t}_2$ are uniform in Γ.

The natural way to impose this condition is by computing the exact values of coefficients $\mathbf{u}_{ij} \in \mathbb{R}^3$ in the Equation (4.23) such that the last relations must be satisfied. Then, these values are imposed in the discrete linear system in direct way, modifying the rows corresponding to these degrees of freedom.

The computation of each velocity coefficient is trivially performed by appealing to the Lagrangian nature of the interpolants. Defining for each $1 \leq i, j \leq \mathsf{p} + 1$ the values

$$\xi_i = -\cos\left(\frac{(i-1)\pi}{\mathsf{p}}\right), \quad \eta_j = -\cos\left(\frac{(j-1)\pi}{\mathsf{p}}\right), \tag{4.25}$$

it is immediate the relation $\mathbf{u}_{ij} = \mathbf{u} \circ \chi_{2D}(\xi_i, \eta_j)$.

Finally, each coefficient is the solution of the problem

$$\mathbf{u}_{ij} \cdot \mathbf{n} = \pm\alpha \left(1 - \frac{r_{ij}^2}{R^2}\right), \qquad \mathbf{u}_{ij} \cdot \mathbf{t}_1 = 0, \qquad \mathbf{u}_{ij} \cdot \mathbf{t}_2 = 0, \tag{4.26}$$

where $r_{ij}^2 = \|\chi_{2D}(\xi_i, \eta_j) - \mathbf{x}_0\|^2$.

Neumann boundary condition Neumann BC are naturally imposed in the variational formulation of the problem. The normal component of the traction imposed at Γ, expressed here as $t = -p$, being p a given time-dependent datum, is then expressed as

$$\int_\Gamma t\mathbf{n} \cdot \hat{\mathbf{u}}(\mathbf{x})\, d\Omega = \int_\Gamma (-p(\mathbf{x}, t)\mathbf{n}) \cdot \hat{\mathbf{u}}(\mathbf{x})\, d\Omega. \tag{4.27}$$

For time-dependent values of pressure, and recalling that the vector $\mathbf{n}$ is constant in Γ, the last integral can be recast into the reference surface Γ_0 as

$$\int_\Gamma t\mathbf{n} \cdot \hat{\mathbf{u}}(\mathbf{x})\, d\Omega = -p(t)\mathbf{n} \cdot \int_{\Gamma_0} \hat{\mathbf{u}} \circ \chi_{2D}(\boldsymbol{\xi}) \|J^{-T}\mathbf{n}_0\| \det J\, d\Gamma_0, \tag{4.28}$$

where $J = \nabla\chi_{2D}$ and $\mathbf{n}$ and $\mathbf{n}_0$ the outward unit normal vector of Γ and Γ_0, respectively.

4.4 Academic fluid flow simulations: 2D case

The numerical assessment of the proposed methodology, for the approximation of fluid-flow problems defined in a two-dimensional case, is addressed in this section. The three-dimensional case will be studied in the next section. As carried out in the case of scalar transport problems, and to highlight the accuracy properties in the approximation of Navier-Stokes equations an efficiency study is performed for several test problems.

The convergence properties are studied through the comparison of the approximate velocity/pressure field against analytical solutions, when available, or reference solutions obtained with a traditional FEM scheme. This convergence study is performed against variations in the mesh axial size (h) and in the transversal order p. Denoting by $(\mathbf{u}_{\mathrm{T}}, p_{\mathrm{T}})$ the approximate solution via the TEPEM and by $(\mathbf{u}, p)$ the reference solution (analytical or obtained with FEM), we define the relative error metrics for velocity and pressure in the L^2-norm as

$$\|\mathbf{u}-\mathbf{u}_{\mathrm{T}}\|=\frac{\|\mathbf{u}-\mathbf{u}_{\mathrm{T}}\|_{L^2(\Omega)}}{\|\mathbf{u}\|_{L^2(\Omega)}} \qquad \|p-p_{\mathrm{T}}\|=\frac{\|p-p_{\mathrm{T}}\|_{L^2(\Omega)}}{\|p\|_{L^2(\Omega)}} \tag{4.29}$$

and also, for the velocity, is defined the relative error in the H^1-seminorm by

$$|\mathbf{u}-\mathbf{u}_{\mathrm{T}}|=\frac{\|\nabla\mathbf{u}-\nabla\mathbf{u}_{\mathrm{T}}\|_{L^2(\Omega)}}{\|\nabla\mathbf{u}\|_{L^2(\Omega)}} \tag{4.30}$$

where $\|\cdot\|_{L^2(\Omega)}$ is the classical norm

$$\|\mathbf{u}\|^2_{L^2(\Omega)}=\int_\Omega \mathbf{u}\cdot\mathbf{u}\,d\Omega \tag{4.31}$$

The errors measured through these norms are complemented with the calculation of the reduction in the total number of degrees of freedom needed in the TEPEM problem ($\mathrm{DoFs_T}$) against the employed for the reference solution ($\mathrm{DoFs_0}$). The percentage reduction is defined as

$$\text{DoFs reduction} = \frac{\mathrm{DoFs_0}-\mathrm{DoFs_T}}{\mathrm{DoFs_0}}\times 100\% \tag{4.32}$$

For the cases in which no analytical solution is available, the reference solution is chosen as the approximation of the Navier-Stokes problem employing classical FEM approach into a sufficiently fine mesh. The mesh is composed by triangular elements and the finite element $\mathbb{P}_2-\mathbb{P}_1$ is employed to approximate velocity and pressure fields. The computational implementation of this strategy is performed using the FreeFem software due to: (i) its facility to implement and solve two-dimensional problems, (ii) the self-contained meshing software and (iii) for a comparison exclusively based on the reduction of the problem size, it is not mandatory to ensure the same computational paradigm of implementation for FEM and TEPEM.

Related to the geometrical discretization, an ad-hoc pipe mesh is constructed in each case to study the convergence of the proposed methodology against the axial size h. The inclusion of transition-pipe elements is detailed in the cases in which be employed. These elements are related to the respective reference element through the mapping described in Section 2.2.1 and which is defined through the combination of linear functions for both axial and transversal direction.

For transient cases, the temporal discretization is performed with a time step small enough to ensure the convergence in the time. The discrete linear system is solved by a direct solver based in LU decomposition. Tolerance value for non-linear iterations is fixed as $tol = 1 \cdot 10^{-2}$ for FEM and TEPEM simulations. No stabilization is employed for neither of approaches.

4.4.1 Poiseuille and Womersley flows

The first numerical example in 2D is devoted to test the numerical capabilities of the TEPEM in two cases where the analytical solution is available. Consider the flow of a fluid between parallel plates driven by a pressure gradient. When considering a constant pressure gradient, the flow is known as the Poiseuille flow. Conversely, if the pressure gradient is sinusoidal in time, this problem is known as Womersley flow. Both cases are defined in the domain described in Figure 4.9. Homogeneous Dirichlet boundary conditions are considered for the transversal (vertical) direction of the velocity field at $\Gamma_1 \cup \Gamma_3$ and no-slip conditions are applied over the lateral boundaries ($\Gamma_2 \cup \Gamma_4$).

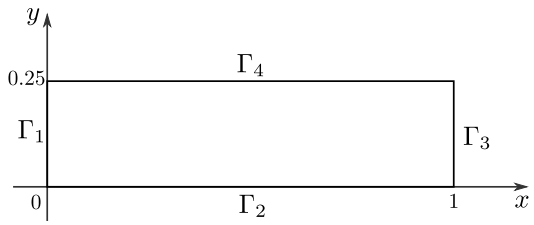

$$\Gamma_1 = \{(x, y) : x = 0, 0 \leq y \leq 0.25\}$$
$$\Gamma_2 = \{(x, y) : 0 \leq x \leq 1, y = 0\}$$
$$\Gamma_3 = \{(x, y) : x = 1, 0 \leq y \leq 0.25\}$$
$$\Gamma_4 = \{(x, y) : 0 \leq x \leq 1, y = 0.25\}$$

Figure 4.9: Geometrical setting for the Poiseuille and Womersley flows.

Poiseuille flow. Considering the flow driven by a constant pressure difference between inlet and outlet (Δp), the analytic solution for velocity $\mathbf{u} = (u, v)$ and pressure p are given by

$$u(x, y) = \frac{\Delta p}{2\mu} y(y - L_y), \qquad v(x, y) = 0, \qquad p(x, y) = p_{in} + \Delta p\, x \tag{4.33}$$

where $L_y = 0.25$ is the transversal length and μ is the (constant) viscosity coefficient.

Notice that, for this particular case, the pressure field is a linear function of the axial direction while the velocity is fully characterized by quadratic function of the transversal direction. With this, the TEPEM must be able to provide the exact solution even with a few number of pipe-elements and lower transversal order for each field.

To test a particular case, let us consider the viscosity $\mu = 1$ and the inlet/outlet pressure given by $p_{in} = 128$ and $p_{out} = 0$ (this is $\Delta p = -128$). This pressure difference is imposed through non-homogeneous and homogeneous Neumann boundary conditions at inlet and outlet for the axial component of the traction, respectively.

For the TEPEM approximation, we consider an uniform discretization of Ω composed by only three pipe-elements ($h = 1/3$) and a transversal enrichment $\mathsf{p} = 4$ for the velocity field and $\mathsf{p} = 2$ for the pressure. The discrete spaces defined for velocity and pressure contain the analytical solution, and so the approximation obtained with the TEPEM matches the analytical one. The approximate solution is outlined in Figure 4.10. To complement these results, a comparison between the axial velocity profile and pressure drop along the axial direction for the TEPEM solution against the analytical solution is shown in Figure 4.11. The total number of degrees of freedom is 123.

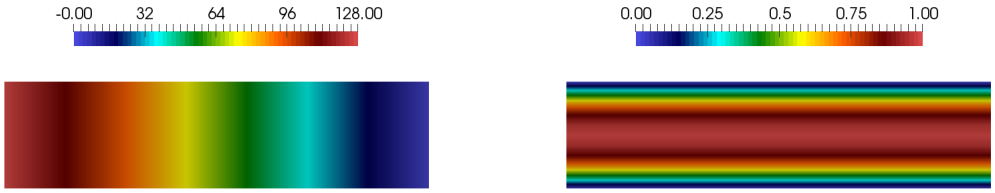

(a) Pressure drop (b) Velocity profile

Figure 4.10: Approximate solution with TEPEM for the Poiseuille flow problem. Only three pipe-elements were employed and transversal order $\mathsf{p} = 4$ for the velocity. Exact solution is achieved.

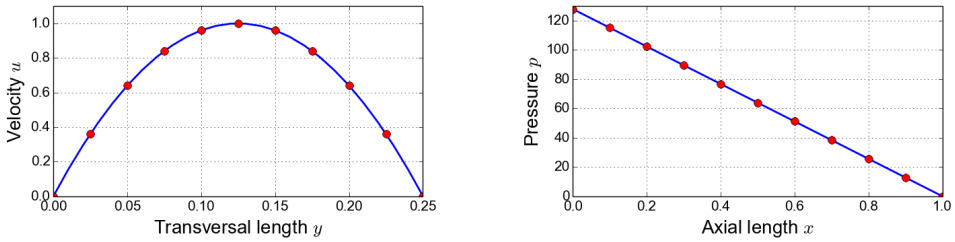

Figure 4.11: Comparison of the approximate solution with TEPEM (red dots) against analytical solution (blue solid line). Left: Velocity profile in the transversal section $x = 0.5$. Right: Pressure drop along the axial direction (line $y = 0.125$).

Womersley flow. The Womersley flow is described as the flow between parallel plates driven by a sinusoidal pressure gradient. Considering the pressure drop as a function of time as $\Delta p = -A\cos\left(\frac{\tau}{T}\right)$, with fixed values for amplitude (A) and period (T), the analytical solution is available and described by

$$\begin{aligned} u(x,y,t) &= -\text{Real}\left[i\frac{A}{\tau\rho}\left(1-\frac{\cos(\lambda(2y/L_y-1))}{\cos(\lambda)}\right)e^{i\tau t}\right] \\ v(x,y,t) &= 0 \\ p(x,y,t) &= p_{in}(t) + x\Delta p \end{aligned} \tag{4.34}$$

where L_y is the transversal length, ρ is the (constant) density of the fluid, Real$(\cdot)$ stands for the real part of the argument $(\cdot)$, $i = \sqrt{-1}$ the imaginary unity and the imaginary coefficient $\lambda = (-i\kappa^2)^{1/2}$ is given by the dimensionless number κ known as Womersley number and defined by $\kappa = \frac{L_y}{2}\left(\frac{\tau}{\mu}\right)^{1/2}$ with μ the (constant) viscosity.

The pressure difference is imposed through non-homogeneous and homogeneous Neumann boundary conditions at inlet and outlet for the axial component of the traction. The complexity of the dynamics is determined by the Womersley number. By increasing this number we obtain thinner transversal boundary layers that are difficult to be accurately predicted by classical FEM in uniform meshes. For a fixed time $t = t_0$, the velocity profile cannot be described as a polynomial, which leads to an error when comparing the TEPEM approximation against the analytical solution. As the exact solution is purely dependent of the transversal component, the approximation error only depends on the transversal enrichment order considered for velocity and pressure.

For the numerical simulations, we fix the values: $\rho = 1$, $\tau = 2\pi$, $A = 1$ and $T = 1$. The discrete mesh for the TEPEM is composed by three pipe elements of equal axial length ($h = 1/3$) and the range considered for the transversal enrichment order for the velocity is $4 \leq \mathsf{p} \leq 12$. To test the TEPEM capabilities, we simulate the transient flow for three different Womersley numbers $\kappa \in \{4, 12, 20\}$, these values were reached by varying the viscosity. For the temporal discretization, we take $\Delta t = T/1000$ and $\mathbf{u} = \mathbf{0}$ as initial condition. Three periods were simulated and the error analysis is performed within the third period. The computational cost of the TEPEM for the transient simulations can be measured by the degrees of freedom (DoFs) needed in each case. In Table 4.1 DoFs employed by the TEPEM, for different transversal orders, are displayed together with the simulation time for the whole third cycle in a sequential implementation.

Table 4.1: Degrees of freedom and simulation time (in minutes) for the Womersley flow simulation with TEPEM and different transversal order.

	Transversal enrichment				
	$\mathsf{p}=4$	$\mathsf{p}=6$	$\mathsf{p}=8$	$\mathsf{p}=10$	$\mathsf{p}=12$
DoFs	123	171	219	267	315
Time (min)	0.42	0.70	1.35	2.03	2.68

A comparison between the TEPEM approximation and the analytical solution, for different times instants, is presented in Figure 4.12. For the three values of Womersley number, it is evident the high accuracy obtained with the proposed methodology not only into the approximation of the velocity profiles but also into the approximation of the derivative, which is of fundamental importance in hemodynamics simulations to compute derivative-based variables such as for example the wall shear stress (WSS).

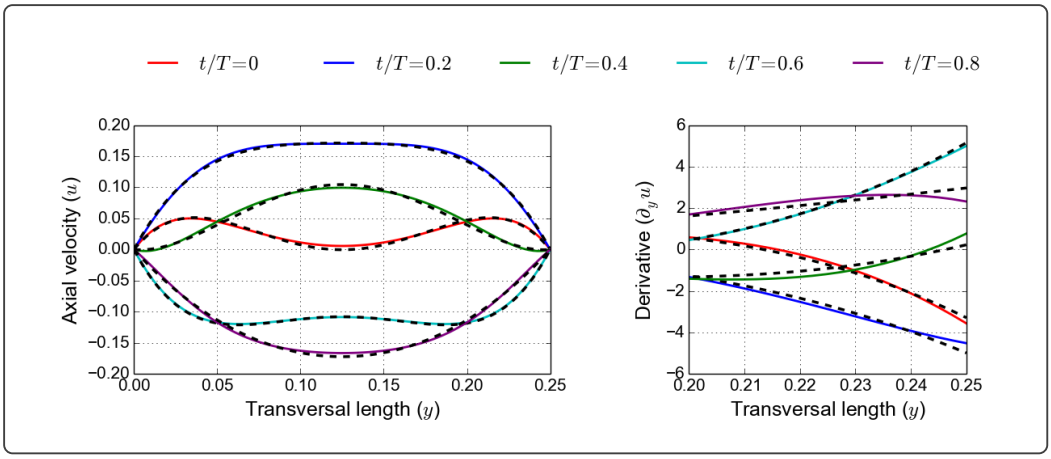

(a) Case $\kappa = 4$ with $\mathsf{p} = 4$.

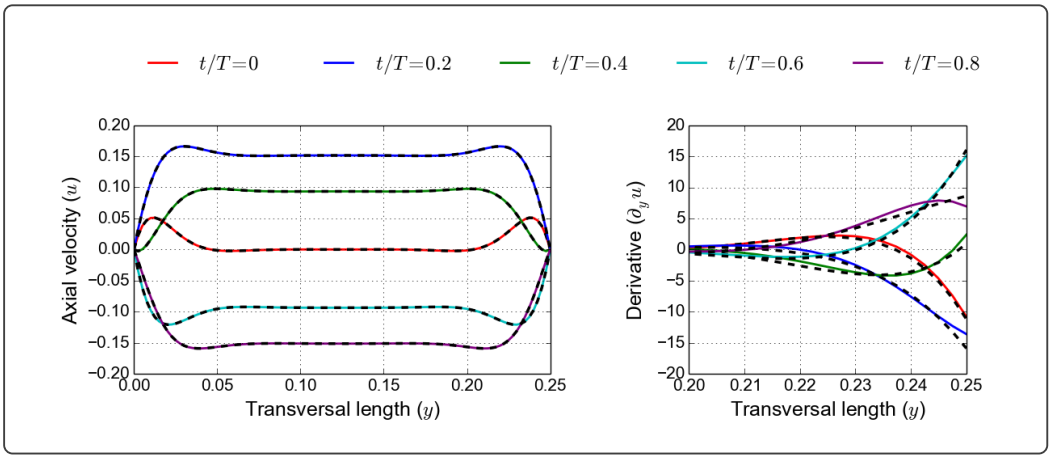

(b) Case $\kappa = 12$ with $\mathsf{p} = 8$.

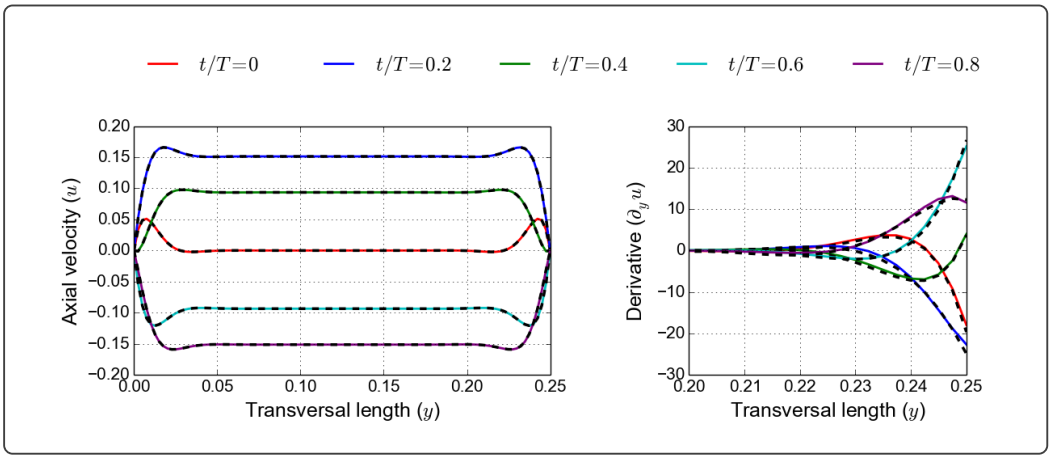

(c) Case $\kappa = 20$ with $\mathsf{p} = 12$.

Figure 4.12: Comparison of analytical (solid line) and approximate (dashed line) velocity profile for the Womersley problem at different times. From top to bottom: $(\kappa = 4, \mathsf{p} = 4)$, $(\kappa = 12, \mathsf{p} = 8)$ and $(\kappa = 20, \mathsf{p} = 12)$. At each panel, a comparison between velocity profiles along a transversal section $(x = 0.5)$ as well as a detail of the velocity gradient near right boundary are presented.

4.4.2 Backward-facing step

The laminar backward-facing step (BFS) flow problem is now considered. Extensively studied in the literature (see, for example, [Armaly et al. 1983, Kim and Moin 1985, Sohn 1988]), the BFS flow is considered as a benchmark problem employed to study the accuracy of new numerical methods as well as their capacity to deal with the presence of recirculation patterns. According to Arnali et al [Armaly et al. 1983], the Reynolds number is measured based on the average value of the inlet velocity profile and the cross-sectional width of the whole domain. For $\mathrm{Re} < 500$ there only exists a single recirculation zone behind the step while, for higher values, another recirculation zone appears at the top wall of the channel.

The geometry for this problem is the suddenly expanded domain shown in Figure 4.13. Aspect ratio of the BFS to the overall sectional width is 1:2 and the total length in the horizontal direction is 20. In this region, four straight segments are selected and denoted as: A (vertical segment $x = 4$), B (vertical segment $x = 10$), C (horizontal segment defined by $1 \leq x \leq 10$ and $y = 1$) and D (diagonal along the whole domain).

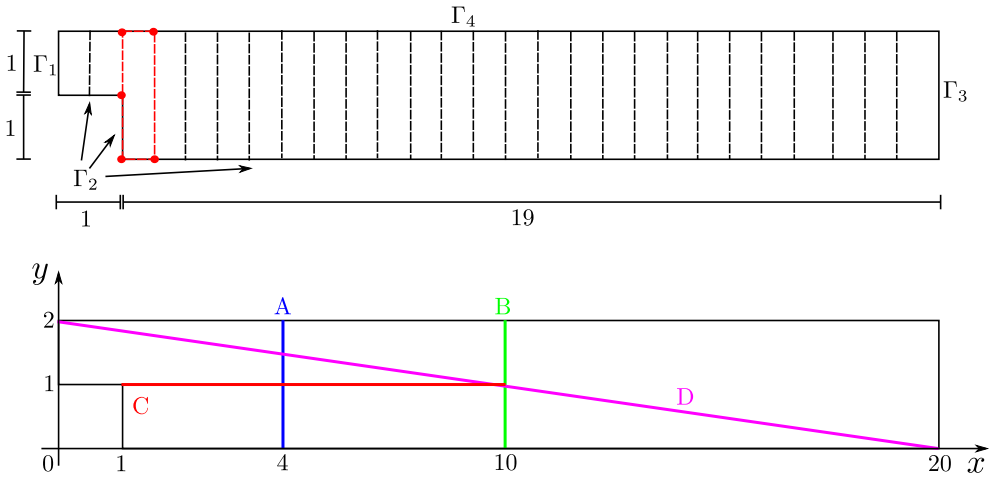

Figure 4.13: Geometrical setting for the backward-facing step benchmark problem. In dotted lines, the structure for a pipe-type discretization is outlined. Highlighted in red, only one transition pipe element is employed for the discretization. Also, three straight segments are demarcated and denoted as: A (in blue), B (in green), C (in red) and D (in magenta).

A fully developed parabolic velocity profile, with unitary maximum velocity, is prescribed at the inlet boundary (Γ_1) and at the outlet boundary (Γ_3) homogeneous Neumann boundary conditions for the axial component of the traction and homogeneous Dirichlet boundary conditions are considered for the transversal direction of the velocity field. The problem is fulfilled with no-slip conditions over the lateral boundaries ($\Gamma_2 \cup \Gamma_4$).

The flow regime in this example is $\mathrm{Re} \in \{250, 500\}$ which is achieved by changing the value of the viscosity, and the domain is discretized in a pipe-type mesh formed by 200 elements ($h = 0.1$). Among these elements, one transition pipe element is considered in the expansion, as can be seen in Figure 4.13). The degrees of freedom for each case of transversal enrichment ($\mathsf{p} \in \{4, 6, 8, 10, 12\}$) as well the characteristics in the FEM mesh are outlined in Table 4.2

Table 4.2: Comparison of number of elements and degrees of freedom employed in FEM and TEPEM simulations. We also indicate the relative reduction in the number of degrees of freedom associated to each TEPEM simulation (for different transversal order) against the employed to obtain the reference FEM solution.

	FEM	Transversal order				
		$p = 4$	$p = 6$	$p = 8$	$p = 10$	$p = 12$
Elements	32 552			200		
DoFs	263 940	4 613	6 418	8 223	10 028	11 833
DoFs reduction	-	98.25%	97.56%	96.88%	96.20%	95.51%

For the first case Re = 250, the computation starts with zero velocity as initial condition. A comparison between the reference FEM solution and the TEPEM approximation ($p = 8$) is presented in Figure 4.14. The velocity field provided by the TEPEM with transversal order $p = 8$ (which represents a reduction higher than 90% in the problem size against the reference solution) is in highly agreement with the reference one.

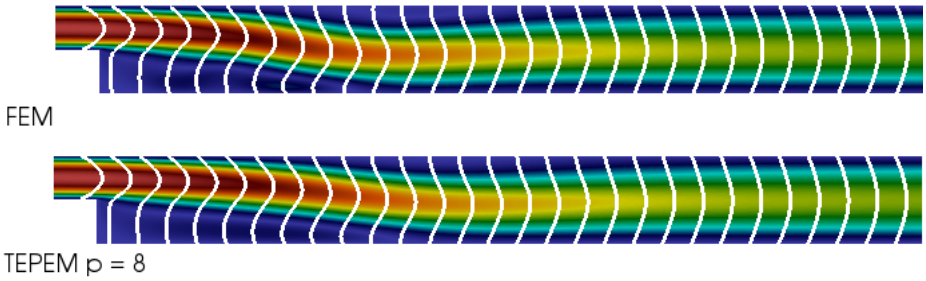

Figure 4.14: Comparison of the magnitude of the velocity field approximated with the TEPEM against the FEM reference solution for the case Re = 250. Velocity profiles (white lines) are also compared for each approach.

The approximation obtained in the case Re = 250 is employed as initial guess for the case Re = 500. A comparison of the magnitude of the velocity provided by the TEPEM and the reference one is displayed in Figure 4.15. In that figure, the comparison is performing in the velocity profiles along the mainstream direction. The proposed approach, with $p = 8$, is able to predict accurately the flow dynamics as well as the vortical structures (see Figure 4.16), whose position and size are in agreement with existing literature.

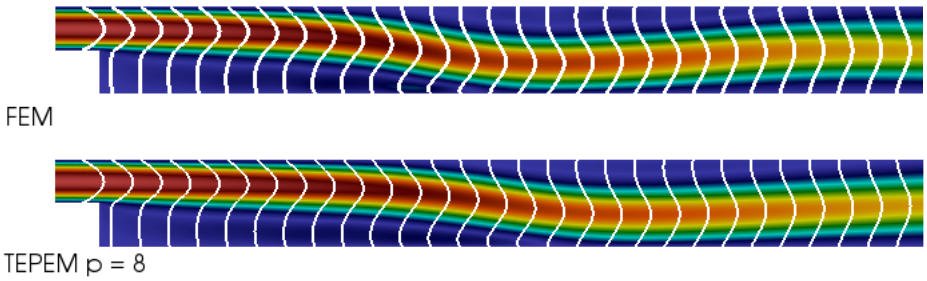

Figure 4.15: Comparison of the magnitude of the velocity field approximated with the TEPEM against the FEM reference solution for the case Re = 500. Velocity profiles (white lines) are also compared for each approach.

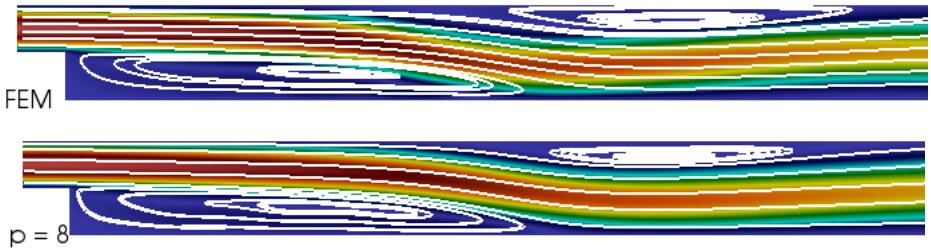

Figure 4.16: Comparison of velocity streamlines for the reference FEM solution and the TEPEM ($\mathsf{p} = 8$) for the case $Re = 500$.

The global comparison presented in the former figures is complemented with a comparison between the approximated fields and the reference ones focused in the straight segments demarcated in Figure 4.13. The scalar components of the velocity (axial and transversal) as well as the pressure field obtained with both FEM and TEPEM are presented for the case Re = 250 (Figure 4.17) and Re = 500 (Figure 4.18).

For both Reynolds cases, these comparisons evidence the convergence in the TEPEM when increased the transversal order p. Notice that no further differences are appreciated between the approximate TEPEM solution with $\mathsf{p} = 8$ and $\mathsf{p} = 10$, neither for different straight sections nor both Reynolds regime.

Once the discretization in pipe-elements is fixed, there exist a threshold in the model capabilities of the TEPEM which is commanded by the axial characteristic length h. This threshold in the predictive capabilities when fixed the parameter h (evidenced in all the convergence studies addressed so far) justify the difference between the field approximation obtained with TEPEM and $\mathsf{p} = 10$ (that can be understood as a converged solution regarding p) and the reference solution. An improvement in the accuracy can be obtained by refining the axial mesh.

4.4.3 Partially obstructed channel

The flow through a region with a partial obstruction is addressed here. The geometry for this problem is described in Figure 4.19. The flow is driven by the imposition of a parabolic velocity profile (with maximum value u_0) at the boundary $\Gamma_1 = \{\mathbf{x} \in \mathbb{R}^2 : x = 0, 0 \leq y \leq 1\}$. At boundary Γ_3, we consider a mixed boundary condition with homogeneous Dirichlet condition for the transversal (vertical) velocity field and homogeneous Neumann condition for the axial component of the traction. The setting is completed with the imposition of no-slip boundary conditions over the remaining part of the boundary. On this geometry are also selected four segments (A, B, C and D) which will help in a detailed comparison of the fields provided by the FEM and TEPEM.

This numerical example is intended to study the convergence of the approximation of the TEPEM as a function of the transversal order considered for the velocity/pressure fields, and for different values of Reynolds number, in the steady state regime. For this purpose, we fix a pipe mesh and consider as the reference solution the approximation obtained with FEM into a fine mesh. This reference solution is denoted by $(\mathbf{u}_{\mathrm{F}}, p_{\mathrm{F}})$.

The characteristics of both FEM and TEPEM meshes are detailed in Table 4.3 together with the relative reduction in the total number of degrees of freedom when the TEPEM is chosen.

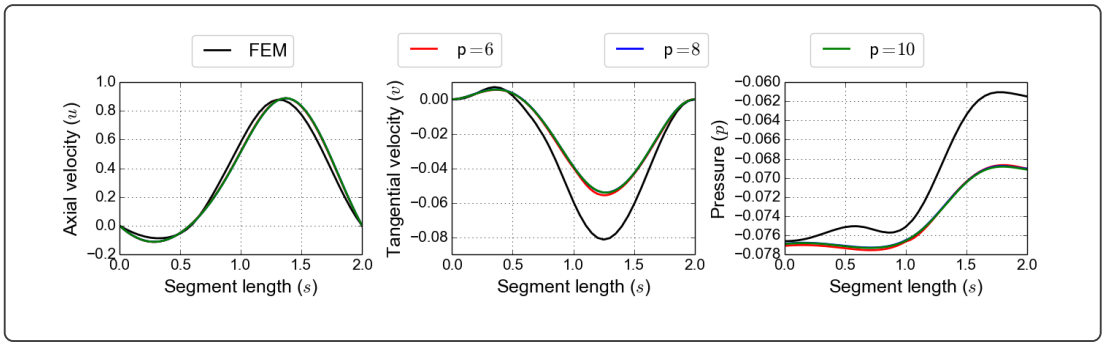

(a) Comparison of fields along the straight segment A

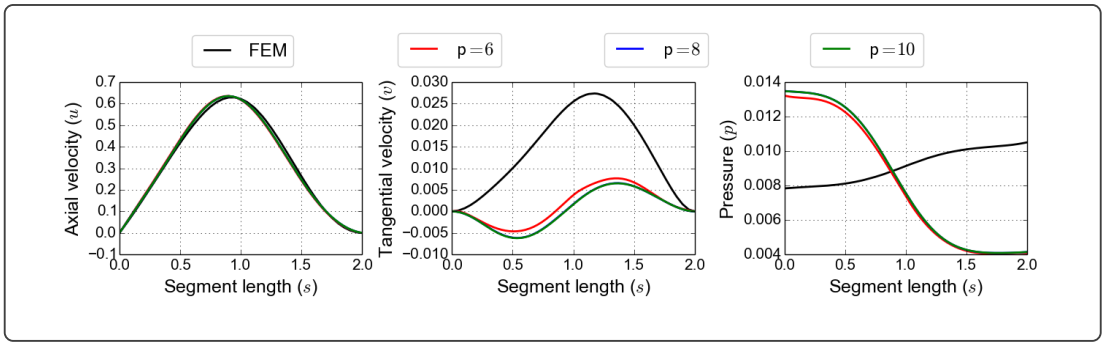

(b) Comparison of fields along the straight segment B

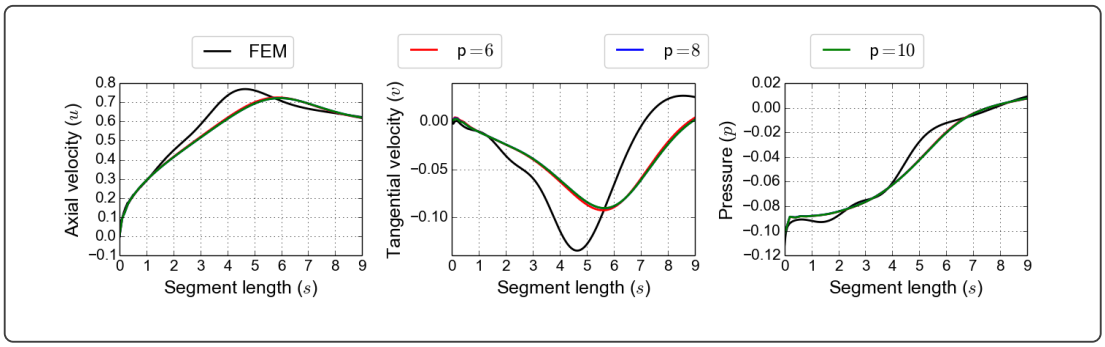

(c) Comparison of fields along the straight segment C

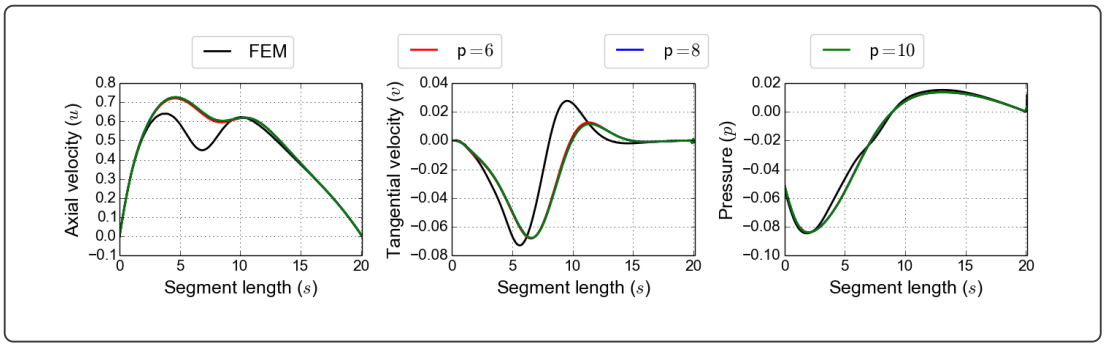

(d) Comparison of fields along the straight segment D

Figure 4.17: Comparison of the scalar components of the velocity and the pressure field approximated with the TEPEM against the FEM solution for the case Re = 250 and in the selected straight segments in Figure 4.13.

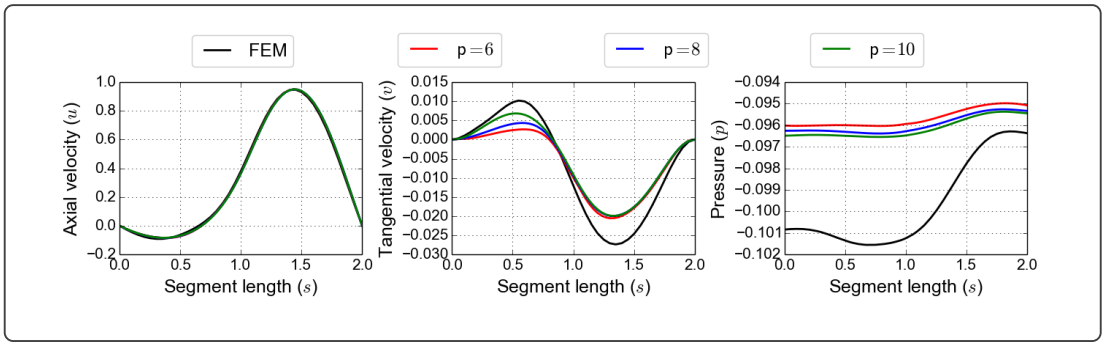

(a) Comparison of fields along the straight segment A

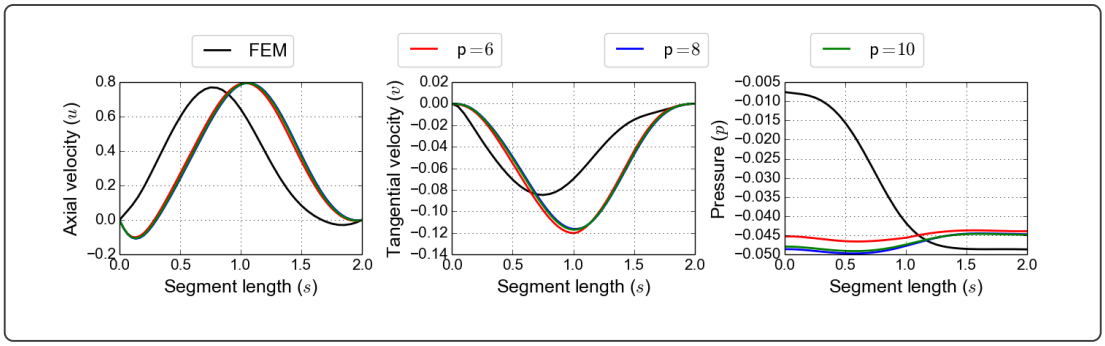

(b) Comparison of fields along the straight segment B

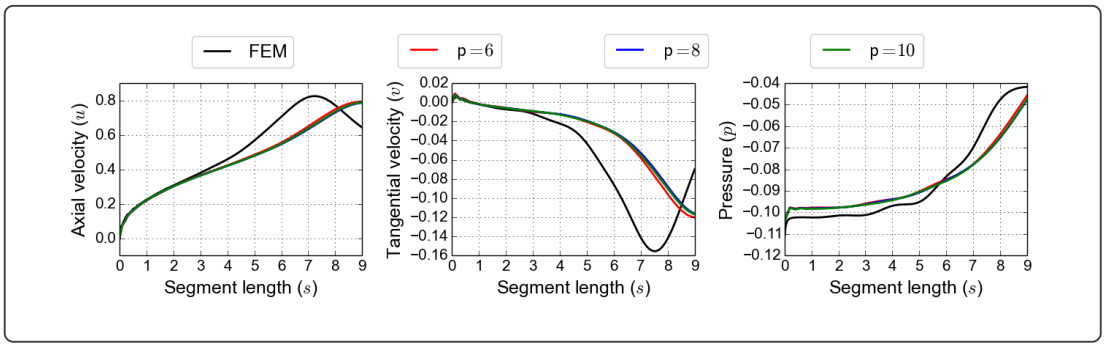

(c) Comparison of fields along the straight segment C

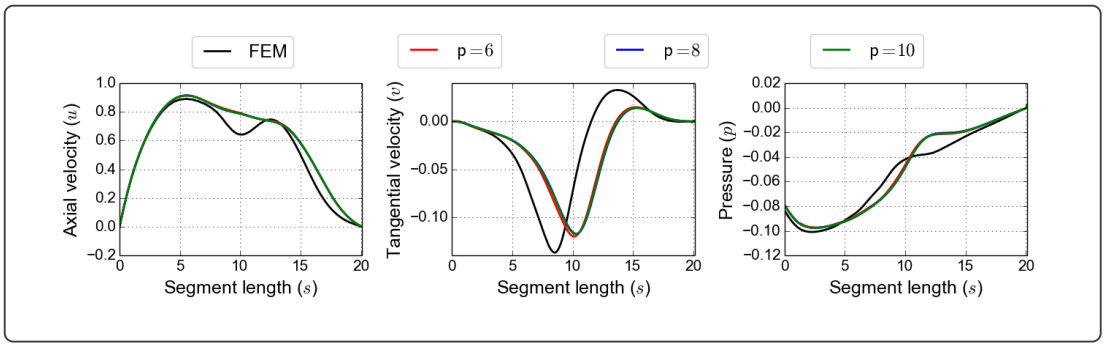

(d) Comparison of fields along the straight segment D

Figure 4.18: Comparison of the scalar components of the velocity and the pressure field approximated with the TEPEM against the FEM solution for the case Re = 500 and in the selected straight segments in Figure 4.13.

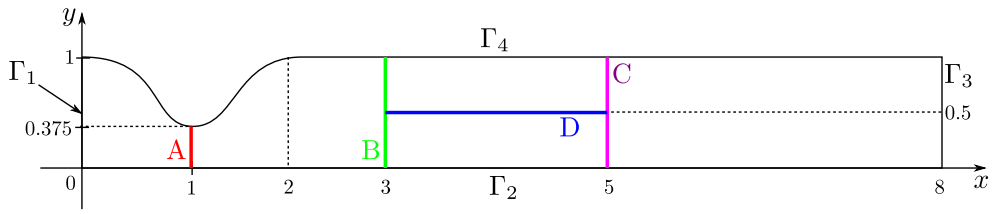

Figure 4.19: Geometrical setting for the constricted region example. Boundary is divided in segments $\partial\Omega = \bigcup_{i=1,2,3,4} \Gamma_i$. Also, four sections are highlighted in the geometry and denoted by: A (in red), B (in green), C (in magenta) and D (in blue).

Table 4.3: Comparison of number of elements and degrees of freedom employed in FEM and TEPEM simulations. We also indicate the relative reduction in the number of degrees of freedom associated to each TEPEM simulation (for different transversal order) against that employed to obtain the reference FEM solution.

	FEM	Transversal order				
		$\mathsf{p}=4$	$\mathsf{p}=6$	$\mathsf{p}=8$	$\mathsf{p}=10$	$\mathsf{p}=12$
Elements	88 246			800		
DoFs	711 252	28 815	40 021	51 227	62 433	73 639
DoFs reduction	-	95.95%	94.37%	92.79%	91.22%	89.64%

The flow regime addressed in this example is $\mathrm{Re} \in \{50, 250, 500\}$. The Reynolds number is based on the average value of the inlet velocity profile and the cross-sectional width of the whole domain. Then, fixing the values for density ($\rho = 1$) and viscosity ($\mu = 0.01$), the Reynolds number in each case is achieved by varying the maximum velocity imposed at the inlet u_0. The relative error in the TEPEM approximation, compared to the reference solution u_{T}, is detailed in Table 4.4 for the three values of Reynolds considered.

The convergence against the transversal order p, for each case, can be better appreciated in Figure 4.20 where the evolution of the error (in L^2-norm and H^1-seminorm) is displayed together with the order of convergence.

Notice that in the case $\mathrm{Re} = 50$, the low complexity in the dynamics is reflected in the presence of a threshold in the approximation error. Therefore, the quality in the approximation cannot be improved by increasing the transversal order, instead of this an axial refinement must be performed to reduce the approximation error.

Nevertheless, the TEPEM approximation with lowest values for transversal enrichment (say $\mathsf{p} = 6$) provides excellent results in velocity and pressure when compared with the reference solution. In Figure 4.21 a comparison between reference and TEPEM solution is shown, focusing in the comparison of velocity profile, pressure and the streamlines in the whole domain. Special attention deserves the development of a recirculation region right after the constriction, which is accurately approximated with the TEPEM.

A more detailed comparison between the FEM reference solution and different TEPEM solutions (for $\mathsf{p} \in \{6, 8, 10\}$) is presented in Figure 4.22. There, axial and transversal components of the velocity and the pressure field obtained with both techniques are compared focusing in the selected segments in Figure 4.19. Notice that, in each section, the TEPEM solution is convergent (as long p is increased) with a threshold related with the axial refinement of the mesh.

Table 4.4: Relative errors in the velocity field, in the velocity gradient and in the pressure field between the TEPEM solution and the reference FEM solution for the partially obstructed channel case and Reynold number Re = 50 (top table), Re = 250 (middle table) and Re = 500 (bottom table). Also, for each Reynolds number, the reference values for FEM solutions are reported.

	Transversal order				
$Re = 50$	$\mathsf{p} = 4$	$\mathsf{p} = 6$	$\mathsf{p} = 8$	$\mathsf{p} = 10$	$\mathsf{p} = 12$
$\|\mathbf{u}_\mathrm{F} - \mathbf{u}_\mathrm{T}\|$	$1.2063 \cdot 10^{-1}$	$1.0453 \cdot 10^{-1}$	$9.9743 \cdot 10^{-2}$	$9.4058 \cdot 10^{-2}$	$9.2609 \cdot 10^{-2}$
$\|\mathbf{u}_\mathrm{F} - \mathbf{u}_\mathrm{T}\|$	$2.0039 \cdot 10^{-1}$	$1.8726 \cdot 10^{-1}$	$1.7160 \cdot 10^{-1}$	$1.6003 \cdot 10^{-1}$	$1.5536 \cdot 10^{-1}$
$\|p_\mathrm{F} - p_\mathrm{T}\|$	$7.8488 \cdot 10^{-2}$	$6.6057 \cdot 10^{-2}$	$7.1975 \cdot 10^{-2}$	$7.3736 \cdot 10^{-2}$	$7.5254 \cdot 10^{-2}$

	Transversal order				
$Re = 250$	$\mathsf{p} = 4$	$\mathsf{p} = 6$	$\mathsf{p} = 8$	$\mathsf{p} = 10$	$\mathsf{p} = 12$
$\|\mathbf{u}_\mathrm{F} - \mathbf{u}_\mathrm{T}\|$	$2.0621 \cdot 10^{-1}$	$1.4943 \cdot 10^{-1}$	$9.9978 \cdot 10^{-2}$	$8.0820 \cdot 10^{-2}$	$8.3904 \cdot 10^{-2}$
$\|\mathbf{u}_\mathrm{F} - \mathbf{u}_\mathrm{T}\|$	$2.9999 \cdot 10^{-1}$	$2.2012 \cdot 10^{-1}$	$1.5934 \cdot 10^{-1}$	$1.3241 \cdot 10^{-1}$	$1.3101 \cdot 10^{-1}$
$\|p_\mathrm{F} - p_\mathrm{T}\|$	$3.2690 \cdot 10^{-1}$	$1.3967 \cdot 10^{-1}$	$3.7788 \cdot 10^{-2}$	$2.7658 \cdot 10^{-2}$	$3.1145 \cdot 10^{-2}$

	Transversal order				
$Re = 500$	$\mathsf{p} = 4$	$\mathsf{p} = 6$	$\mathsf{p} = 8$	$\mathsf{p} = 10$	$\mathsf{p} = 12$
$\|\mathbf{u}_\mathrm{F} - \mathbf{u}_\mathrm{T}\|$	$3.0585 \cdot 10^{-1}$	$3.3172 \cdot 10^{-1}$	$1.4940 \cdot 10^{-1}$	$9.7171 \cdot 10^{-2}$	$8.5708 \cdot 10^{-2}$
$\|\mathbf{u}_\mathrm{F} - \mathbf{u}_\mathrm{T}\|$	$4.5277 \cdot 10^{-1}$	$4.6555 \cdot 10^{-1}$	$2.2767 \cdot 10^{-1}$	$1.5341 \cdot 10^{-1}$	$1.3314 \cdot 10^{-1}$
$\|p_\mathrm{F} - p_\mathrm{T}\|$	$4.4504 \cdot 10^{-1}$	$2.5348 \cdot 10^{-1}$	$1.0826 \cdot 10^{-1}$	$4.0651 \cdot 10^{-2}$	$2.7951 \cdot 10^{-2}$

	Reference values		
	$\|\mathbf{u}_\mathrm{F}\|_{L^2}$	$\|\nabla\mathbf{u}_\mathrm{F}\|_{L^2}$	$\|p_\mathrm{F}\|_{L^2}$
Re = 50	$1.6108 \cdot 10^{0}$	$3.6042 \cdot 10^{1}$	$1.0827 \cdot 10^{0}$
Re = 250	$4.4159 \cdot 10^{0}$	$1.1133 \cdot 10^{2}$	$3.8959 \cdot 10^{0}$
Re = 500	$7.5695 \cdot 10^{0}$	$2.0514 \cdot 10^{2}$	$9.6176 \cdot 10^{0}$

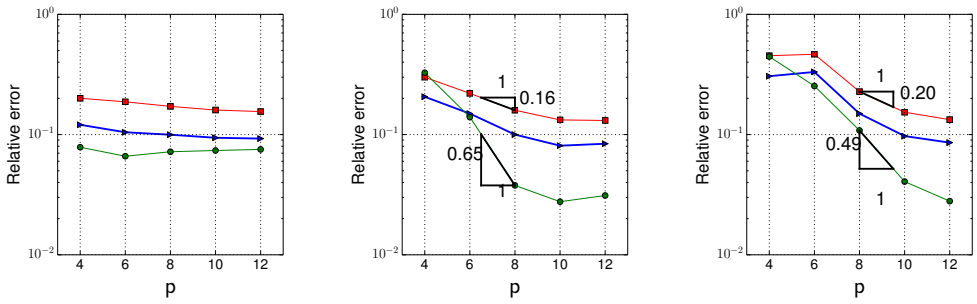

Figure 4.20: Convergence history for the partially obstructed domain in three Reynolds regimes: Re = 50 (left panel), Re = 250 (center panel) and Re = 500 (right panel). In each panel, the relative error in the L^2-norm (▲) and H^1-seminorm (■) for the velocity are reported. For the pressure, the relative error in the L^2-norm (●) is also presented.

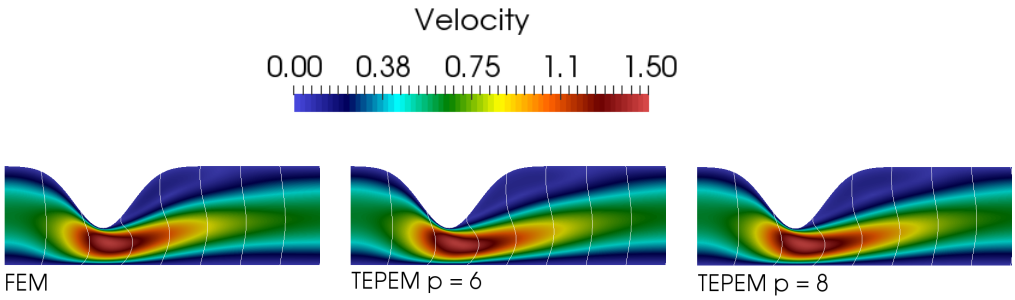

(a) Comparison of the magnitude of the velocity field for the TEPEM and for the reference FEM solution.

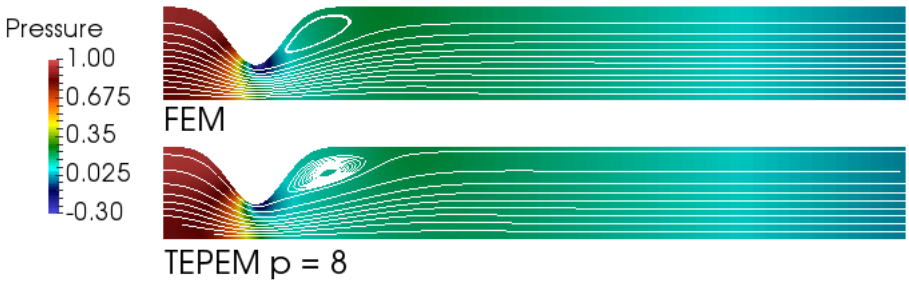

(b) Comparison of the pressure field and velocity streamlines for the TEPEM ($\mathsf{p} = 8$) and the reference FEM solution.

Figure 4.21: Partially obstructed domain with Re = 50. Comparison of velocity and pressure approximation for the TEPEM against the reference FEM solution. Also, streamlines are displayed to appreciate the recirculation zone.

At middle (Re = 250) and right (Re = 500) panels in Figure 4.20 we can appreciate that the increase in the Reynolds number, and therefore the increase in the dynamics complexity, reduces the threshold required for the transversal dynamics to dominate the source of the approximation error.

For the case Re = 250, the improvement in the quality of TEPEM approximation (for different values of transversal enrichment) is presented in Figure 4.23. The agreement in the velocity profile and in the pressure field are highly satisfactory. Moreover, the recirculation region developed after the constricted part of the domain (even when a higher complexity than the one presented in the case Re = 50) is also correctly predicted with $\mathsf{p} = 8$, which implies in an efficient approximation with a reduction of more than 90% in the problem size.

Furthermore, in Figure 4.24 a comparison between the scalar components of the velocity and the pressure field provided by TEPEM and reference FEM solution is addressed in the four straight segments of interest. The convergence of the TEPEM, with respect to the transversal order p, is also evidenced for each scalar field and each selected segment.

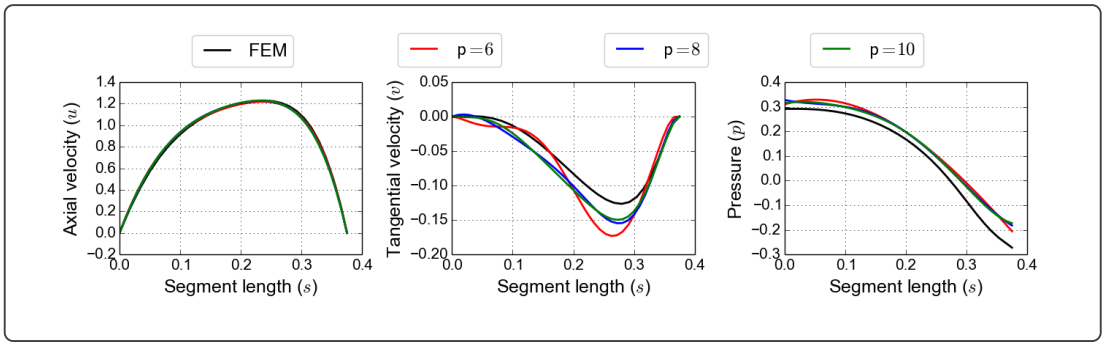

(a) Comparison in section A

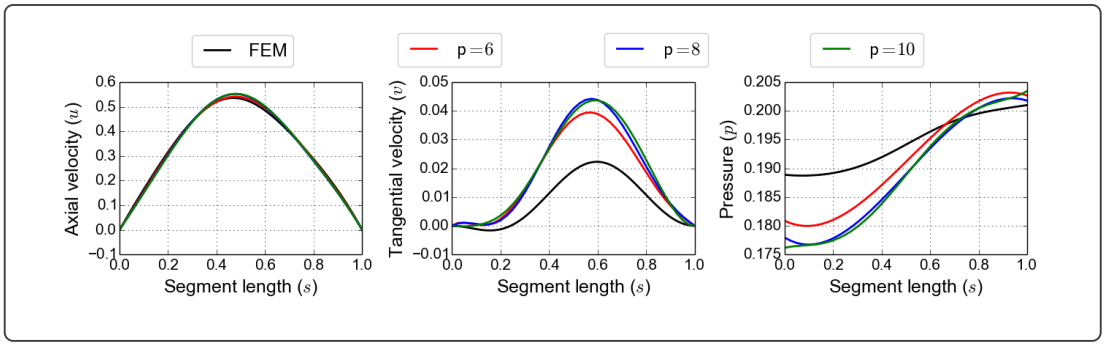

(b) Comparison in section B

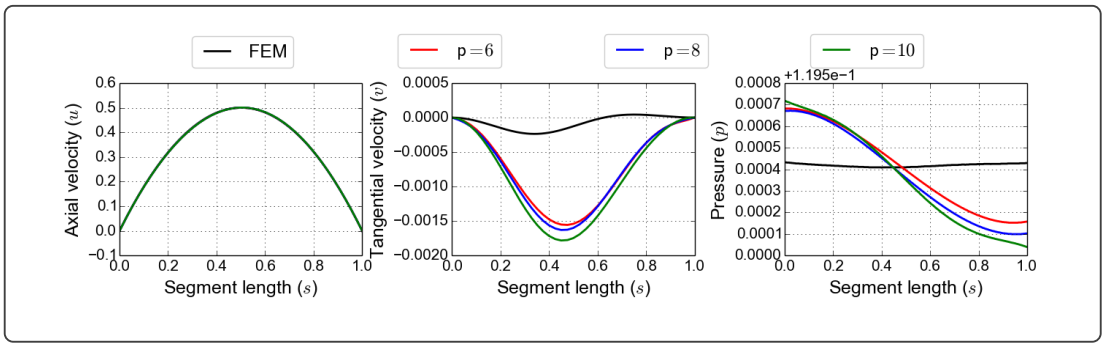

(c) Comparison in section C

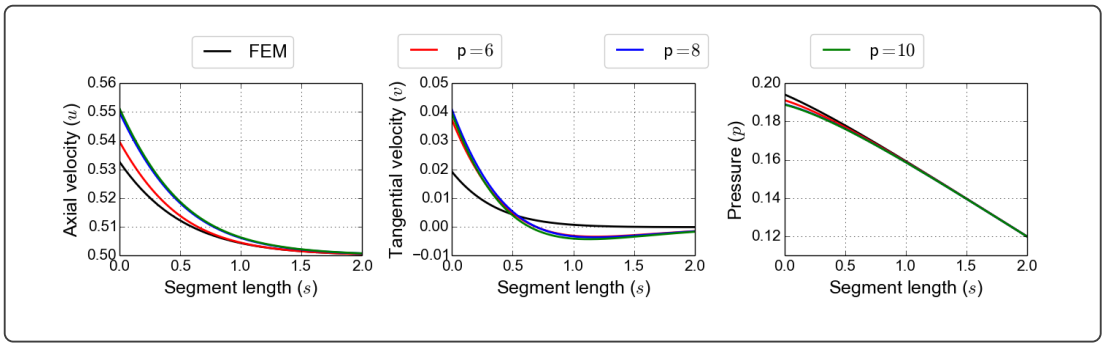

(d) Comparison in section D

Figure 4.22: Comparison of the velocity (axial and transversal components) and pressure, on the selected regions, between the reference FEM solution and different TEPEM solutions (for varying p) and for the case Re = 50.

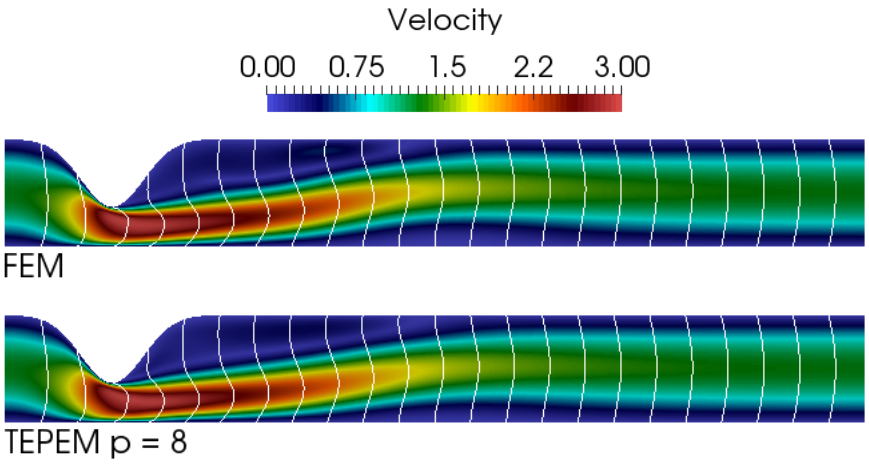

(a) Comparison of the magnitude of the velocity field for the TEPEM and for the reference FEM solution.

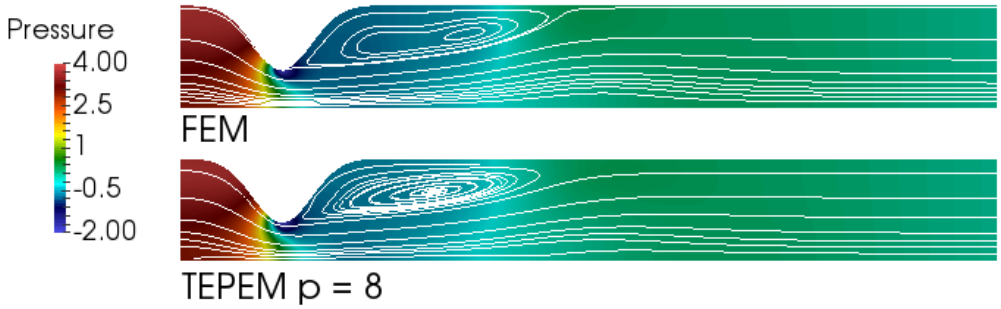

(b) Comparison of the pressure field and velocity streamlines for the TEPEM ($\mathsf{p} = 8$) and the reference FEM solution.

Figure 4.23: Partially obstructed domain with Re = 250. Comparison of velocity and pressure approximation for the TEPEM against the reference FEM solution. Also, streamlines are displayed to appreciate the recirculation zone.

The case Re = 500, the higher regime considered for this example, increase considerably the complexity in the dynamics and also features a new recirculation region at the bottom of the domain, as can be appreciated in Figure 4.25. In the same figure, it is addressed a comparison between the approximate solution obtained with the TEPEM for $\mathsf{p} = 8$ against the reference FEM solution. The two recirculation regions are correctly approximated by the TEPEM.

A comparison in the velocity (axial and transversal components) and pressure along the straight segments of interest is also outlined in Figure 4.26. Notice than while increasing the complexity in the dynamics (increasing the Reynolds number) the difference between TEPEM solutions with low transversal order ($\mathsf{p} = 6$) and high order ($\mathsf{p} = 10$) are more evident. Even for the higher Reynolds number considered here, the convergence of the TEPEM (with respect to the parameter p) can be easily appreciated.

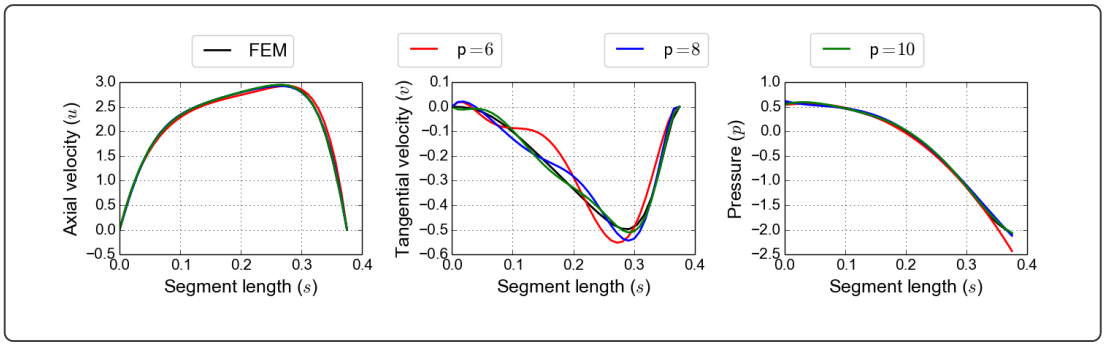

(a) Comparison in section A

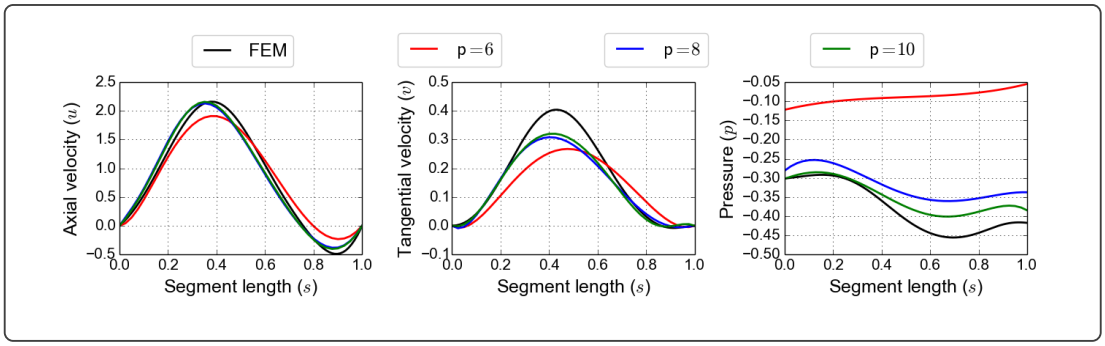

(b) Comparison in section B

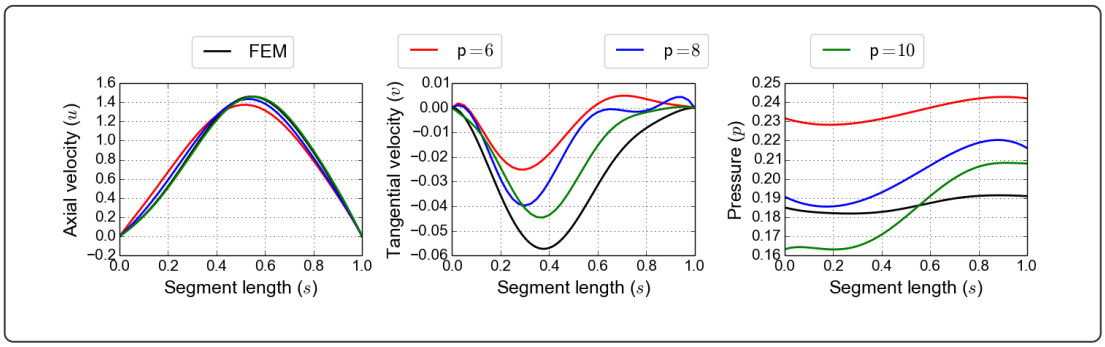

(c) Comparison in section C

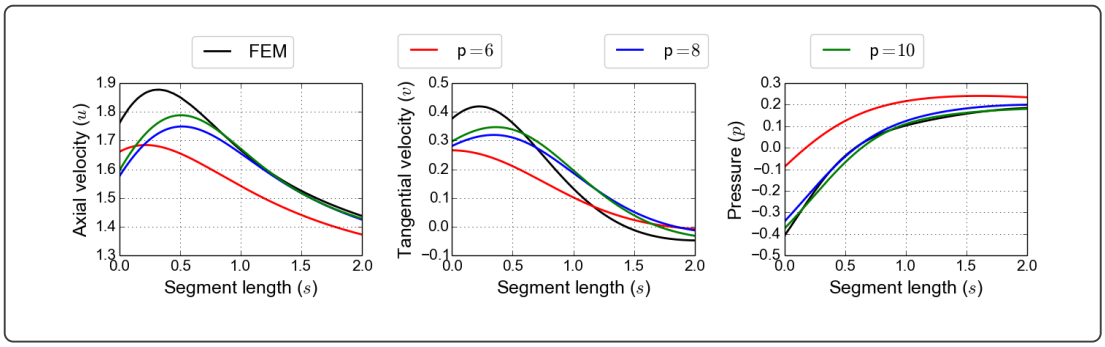

(d) Comparison in section D

Figure 4.24: Comparison of the velocity (axial and transversal components) and pressure, on the selected regions, between the reference FEM solution and different TEPEM solutions (for varying p) and for the case Re = 250.

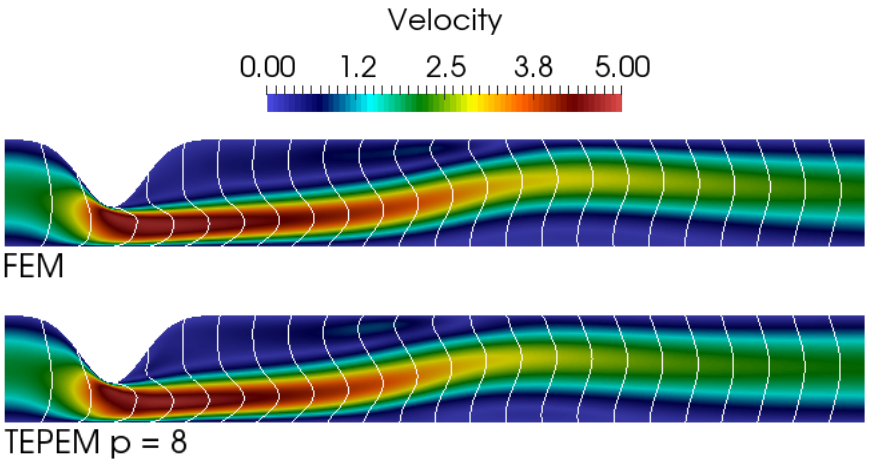

(a) Comparison of the magnitude of the velocity field for the TEPEM and for the reference FEM solution.

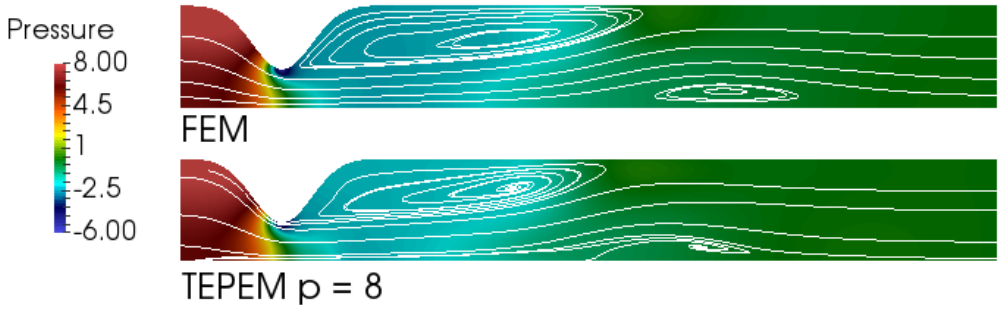

(b) Comparison of the pressure field and velocity streamlines for the TEPEM ($\mathsf{p} = 8$) and the reference FEM solution.

Figure 4.25: Partially obstructed domain with Re = 500. Comparison of velocity and pressure approximation for the TEPEM against the reference FEM solution. Also, streamlines are displayed to appreciate the recirculation zone.

These three cases corroborate the high quality in the TEPEM approximation with a considerable reduction in the problem size. In fact, considering $\mathsf{p} = 8$, the three steady state cases were addressed with high fidelity and performing a reduction in the total number of degrees of freedom over 90%.

To study the TEPEM capabilities in a transient case, we now perform the same comparison against a reference FEM solution for a flow driven by the imposition, at the inlet, of a sinusoidal velocity profile of the form

$$\mathbf{u}(\mathbf{x}, t) = -u_0(1 + \sin(2\pi t))y(1 - y)\mathbf{n} \qquad \mathbf{x} \in \Gamma_1 \tag{4.35}$$

with u_0 the maximum velocity value considered for the case Re = 250 and $\mathbf{n}$ the outer normal ($\mathbf{n} = (-1, 0)$). This inlet condition implies into a flow characterized by a mean Reynolds number Re = 250 and a Womersley number $\kappa \approx 12$.

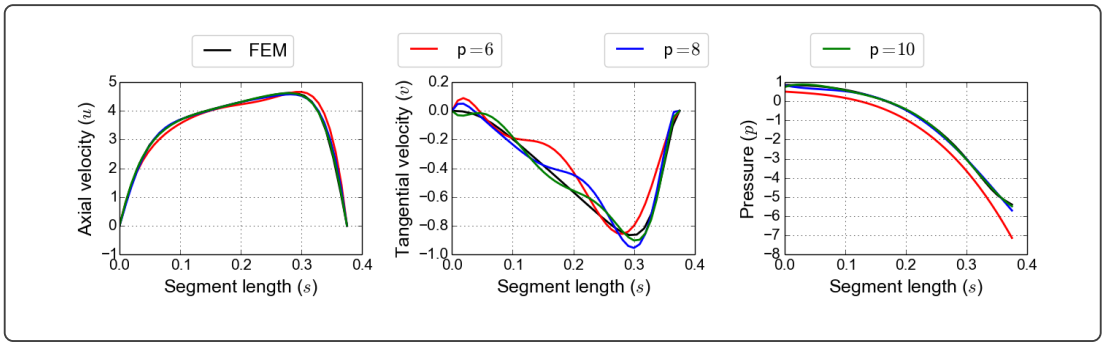

(a) Comparison in section A

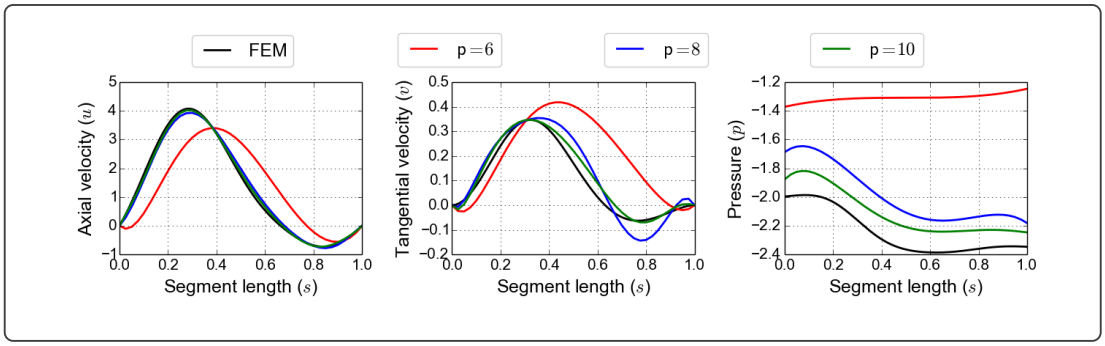

(b) Comparison in section B

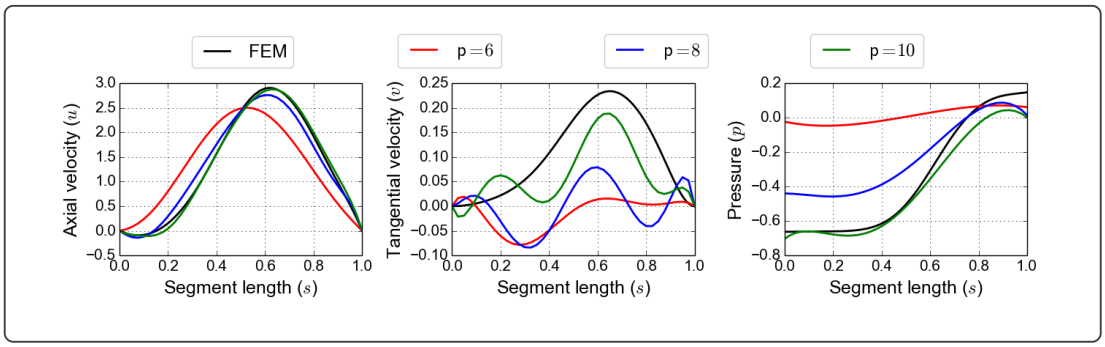

(c) Comparison in section C

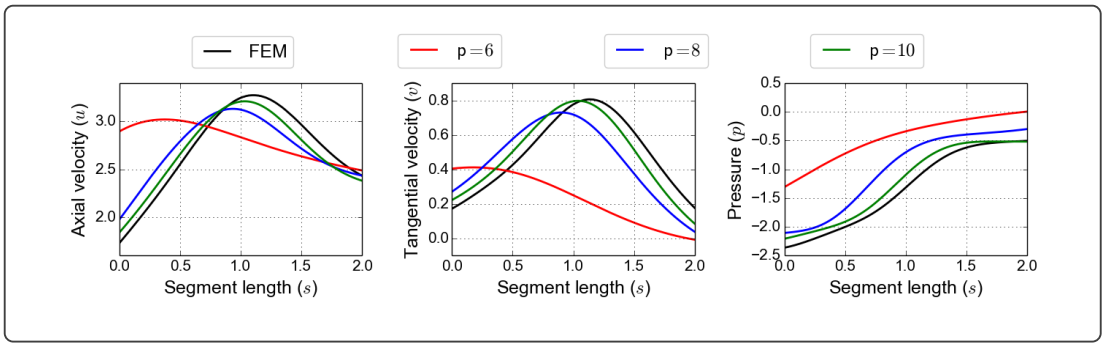

(d) Comparison in section D

Figure 4.26: Comparison of the velocity (axial and transversal components) and pressure, on the selected regions, between the reference FEM solution and different TEPEM solutions (for varying p) and for the case Re = 500.

Denoting by $T = 1s$ the period of the sinusoidal parabolic profile imposed at the inlet boundary of the domain, we study the accuracy of the TEPEM for $\mathsf{p} \in \{6, 8, 10\}$, along two cycles ($0 < t < 2T$), considering a time step of $\Delta t = 1 \cdot 10^{-3}$.

In Table 4.5 we present the relative errors for velocity and pressure measured against the reference FEM solution computed in the same mesh used for the steady state regime. The metrics employed in this table are the discrete equivalent of the L^2-norm in time, this is

$$\|\mathbf{u}_{\mathrm{F}} - \mathbf{u}_{\mathrm{T}}\|^2_{(0,2T)} = \sum_{n=0}^{N_t} \Delta t \left(\frac{\|\mathbf{u}(\mathbf{x}, t_n) - \mathbf{u}_{\mathrm{T}}(\mathbf{x}, t_n)\|}{\|\mathbf{u}(\mathbf{x}, t_n)\|} \right)^2 \tag{4.36}$$

where $0 = t_0 < t_1 < \ldots < t_{N_t} = 2T$.

Table 4.5: Relative errors in the velocity field, in the velocity gradient and in the pressure field between the TEPEM solution and the reference FEM solution for the partially obstructed domain in the time-depending setting. Also, the reference values for FEM solutions are reported.

	TEPEM				FEM
	$\mathsf{p} = 6$	$\mathsf{p} = 8$	$\mathsf{p} = 10$		
$\|\mathbf{u}_{\mathrm{F}} - \mathbf{u}_{\mathrm{T}}\|_{(0,2T)}$	$6.1582 \cdot 10^{-1}$	$4.2918 \cdot 10^{-1}$	$3.0953 \cdot 10^{-1}$	$\|\mathbf{u}_{\mathrm{F}}\|_{L^2}$	$7.7236 \cdot 10^{0}$
$\|\mathbf{u}_{\mathrm{F}} - \mathbf{u}_{\mathrm{T}}\|_{(0,2T)}$	$7.6034 \cdot 10^{-1}$	$5.2603 \cdot 10^{-1}$	$4.0514 \cdot 10^{-1}$	$\|\nabla\mathbf{u}_{\mathrm{F}}\|_{L^2}$	$1.4709 \cdot 10^{2}$
$\|p_{\mathrm{F}} - p_{\mathrm{T}}\|_{(0,2T)}$	$1.5939 \cdot 10^{-1}$	$9.2254 \cdot 10^{-2}$	$7.6326 \cdot 10^{-2}$	$\|p_{\mathrm{F}}\|_{L^2}$	$1.0084 \cdot 10^{2}$

A detailed description of the error behavior along the two cycles is presented in Figure 4.27. Moreover, in Figure 4.28 it is compared the FEM reference solution against the TEPEM approximation (with $\mathsf{p} = 8$) at four different time instants along the simulation. In this last figure it is easy to note the fidelity in the approximation regarding to the location and size of the many recirculation areas.

As said before, the main ability of the TEPEM is the capacity to accurately predict the most interesting characteristics of the dynamics (recirculation in this case) and, even when the accuracy can be improved by increasing the transversal order or/and refining the axial mesh, the level of accuracy presented with $\mathsf{p} = 8$ (or $\mathsf{p} = 6$ for regimes characterized by low Reynolds number) seems to be sufficient for practical applications, where the correct prediction of global characteristics (as for example, regions of recirculation) is many times further important than provide a highly accurate high-fidelity prediction of physical fields.

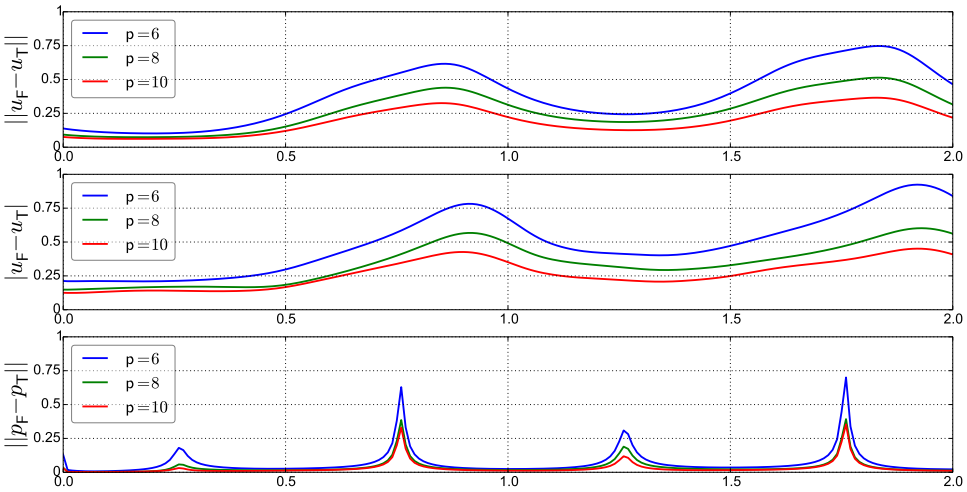

Figure 4.27: Relative error for the partially obstructed domain in the time-dependent setting for velocity (in L^2-norm and H^1-seminorm) and pressure (in L^2-norm) along the two cycles.

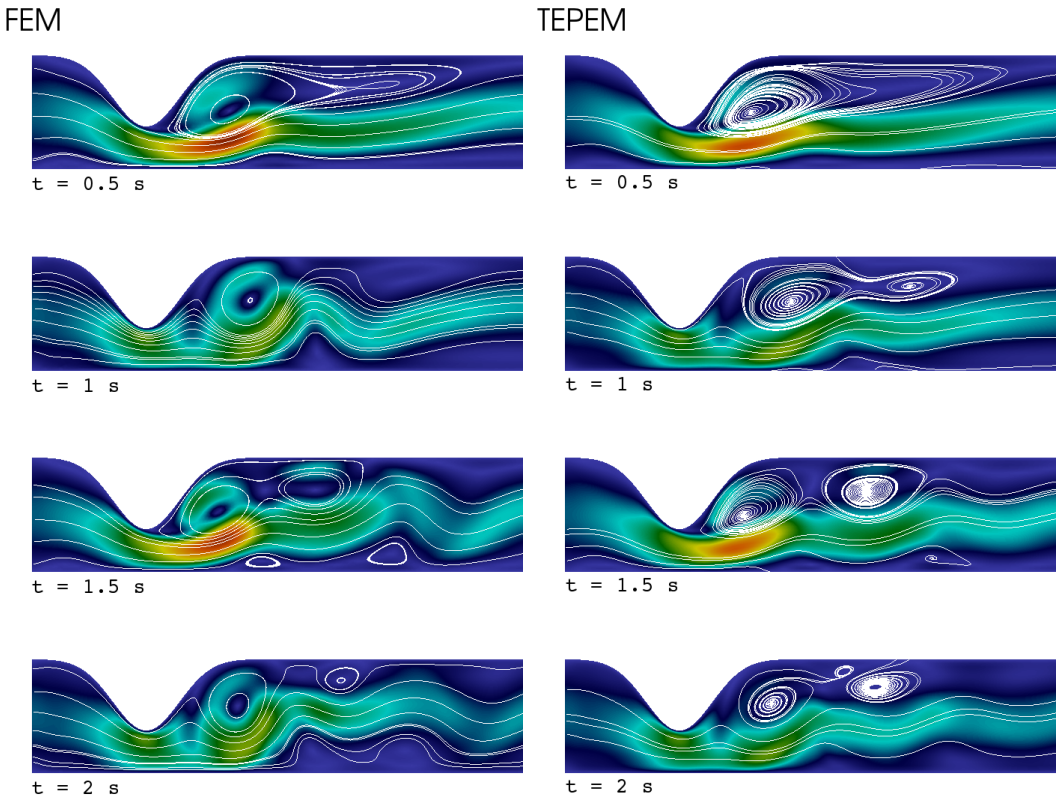

Figure 4.28: Partially obstructed domain in the time-dependent setting with Re = 250. Comparison of velocity and pressure approximation for the TEPEM ($\mathsf{p} = 8$) with the reference FEM solution. Also, the streamlines displayed help to unveil the recirculation zones.

4.4.4 Pulsatile flow in a bifurcated domain

Moving a step forward for the application of the TEPEM in computational hemodynamics, this problem addresses the simulation of a pulsatile flow in the bifurcated domain presented in Figure 4.29. Here, the lateral boundaries are described through the functions

$$\begin{aligned} f(x) &= r_1 \mathbb{1}_{(0,3)} + \left(r_1 + (K - r_1) \exp\left(1 - \frac{m^2}{m^2 - (x-7)^2} \right) \right) \mathbb{1}_{(3,7)} + K \mathbb{1}_{(7,10)} \\ g(x) &= 4 r_1 \left(-\frac{1}{2} + \frac{1}{1 + \exp(-4x + 20)} \right) \\ h(x) &= -\left(1 + \frac{r_2 - r_3}{r_1} \right) g(x) \end{aligned} \tag{4.37}$$

where $\mathbb{1}_I$ is the characteristic function of the set I and the coefficients are chosen as being $r_1 = 0.31386$, $r_2 = 0.11966$, $r_3 = 0.08023$, $K = 2r_1 + 2r_2$ and $m = 4$. These data are chosen such that the inflow and outflow areas are consistent with typical geometrical data in a carotid artery bifurcation.

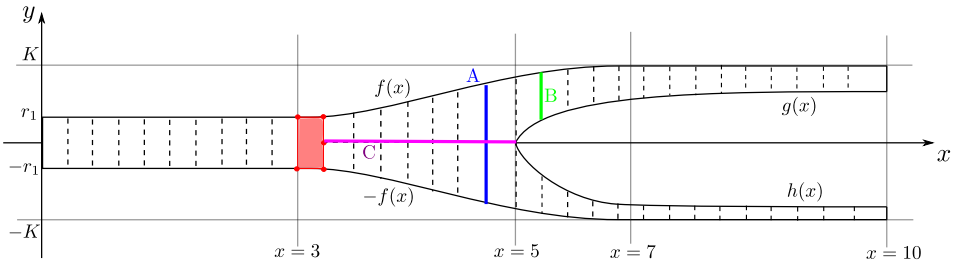

Figure 4.29: Bifurcating channel for a typical problem in computational hemodynamics (dimensions in centimeters). In dotted lines, the structure for the pipe-element discretization is outlined. Transition element is highlighted in red. Also, three segments are demarcate and denoted by: A (in blue), B (in green) and C (in magenta).

Regarding to the boundary conditions considered for this problem, homogeneous Dirichlet conditions are imposed for the velocity over the lateral boundaries defined by the curves $f(x)$, $-f(x)$, $g(x)$ and $h(x)$. At the inflow boundary (leftmost vertical boundary), a parabolic profile is prescribed, which is scaled to define the flow rate waveform presented in Figure 4.30. A description of the scale procedure is addressed in Section 5.2. For the two outflow boundaries (rightmost vertical boundaries), homogeneous Neumann boundary data are considered.

The density and viscosity for this problem are fixed as $\rho = 1$ g/cm^2 and $\mu = 0.01$ P (Poise - 1P = 1 g·cm^{-1}·s^{-1}), respectively, and the time discretization is accomplished with $\Delta t = 1 \cdot 10^{-3}$ s. As initial guess, for TEPEM and FEM, we consider the solution of the stationary Stokes problem defined in the same domain but where the flow is driven by the imposition of a parabolic velocity profile, at the inlet, with maximum velocity such that the flow imposed matches with the flow corresponding to the time $t = 0$ in the waveform presented in Figure 4.30.

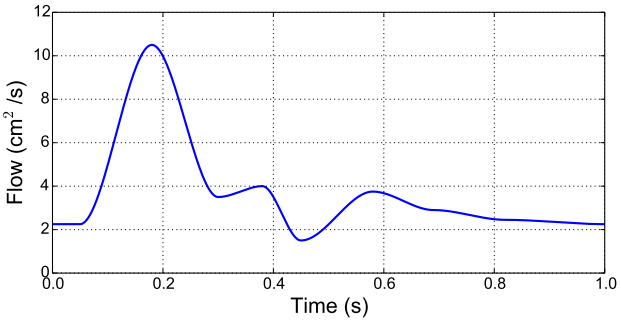

Figure 4.30: Flow rate boundary condition imposed at the inlet.

The pipe-element mesh in TEPEM is constructed with an uniform mesh, with axial length $h = 0.05$ cm, and one transition element is introduced to deal with the bifurcation of the domain. Notice that the transition element (highlighted in red in Figure 4.29) is located at certain distance from the point where the bifurcation of the domain take place (point $x = 5$), generating a region where the transversal area is discretized by two pipe-elements and, therefore, where the model capabilities are naturally increased. This local enhancement in the predictive capabilities is useful due to the lack of a mainstream direction in the bifurcation region between the points $x = 3$ and $x = 5$.

The predictive capabilities of the TEPEM are compared against a reference solution obtained with FEM in a mesh formed by 61 412 triangular elements and a total of 440 119 degrees of freedom. A comparison between the meshes, for FEM and TEPEM, is presented in Table 4.6.

Table 4.6: Comparison in terms of the number of elements and degrees of freedom employed in FEM and TEPEM simulations. Also, it is presented the relative reduction in the number of degrees of freedom associated to each TEPEM simulation (for different transversal order) against the employed to obtain the reference FEM solution.

	FEM	Transversal order				
		$\mathsf{p} = 4$	$\mathsf{p} = 6$	$\mathsf{p} = 8$	$\mathsf{p} = 10$	$\mathsf{p} = 12$
Elements	61 412			3 400		
DoFs	440 119	109 435	153 650	197 865	242 080	286 295
DoFs reduction	-	75.14%	65.08%	55.04%	44.99%	34.95%

In Figures 4.31 - 4.32 a comparison of the magnitude of the velocity field and the velocity streamlines between the FEM reference solution and the TEPEM approximation is presented. In the first figure, the comparison is focused in the bifurcation region (region in between $3 \leq x \leq 7$) and reveals the good agreement between both solutions, at different time instants, even with a low value for the transversal enrichment ($\mathsf{p} = 6$). A typical recirculation is obtained in this region and is effectively predicted for the TEPEM approach. Second figure focus the comparison in the three selected segments presented in Figure 4.29. The pressure field is also predicted by the TEPEM with good fidelity, comparing with the reference FEM solution, as can be appreciated in Figure 4.33.

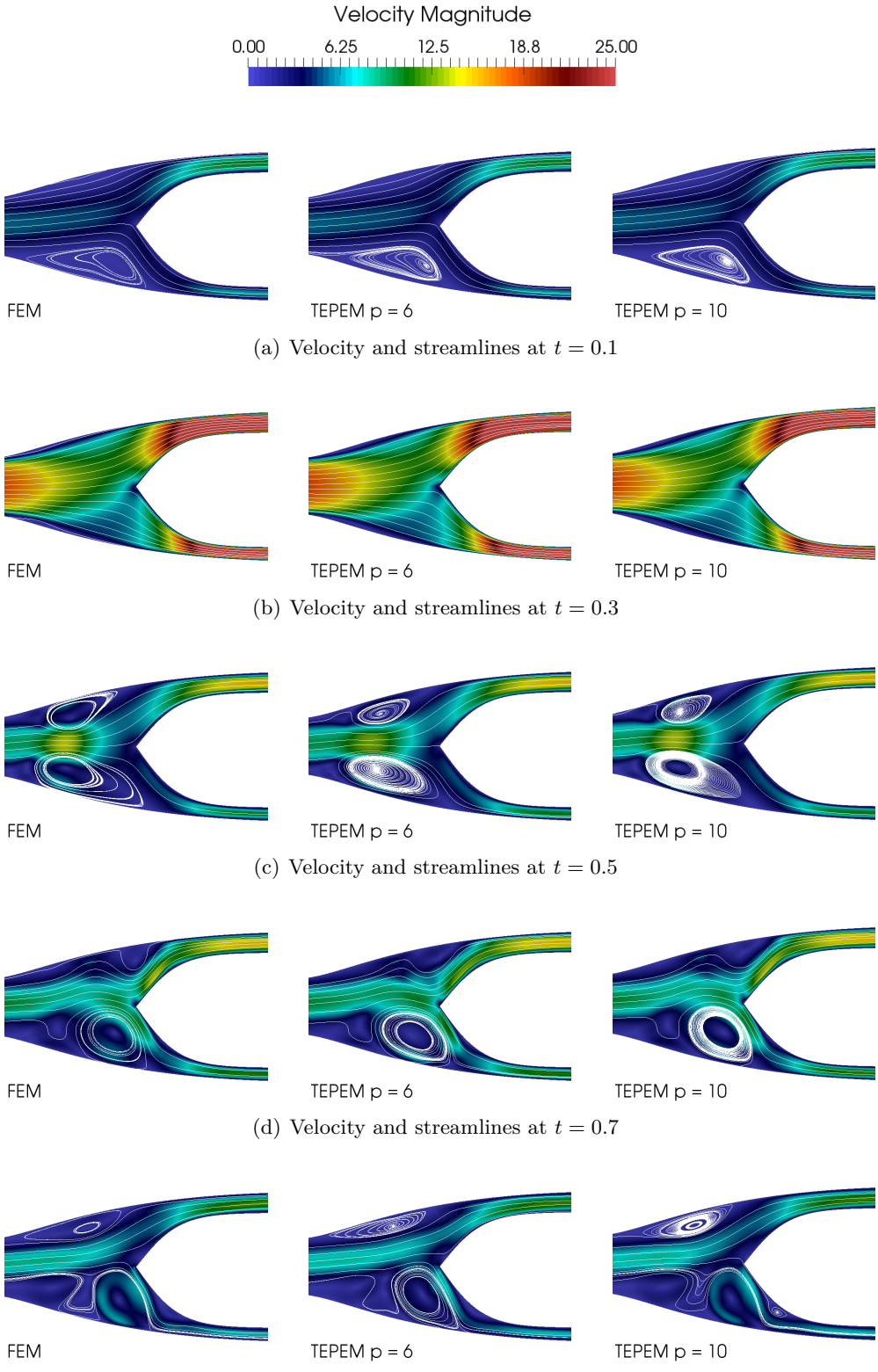

(a) Velocity and streamlines at $t = 0.1$

(b) Velocity and streamlines at $t = 0.3$

(c) Velocity and streamlines at $t = 0.5$

(d) Velocity and streamlines at $t = 0.7$

(e) Velocity and streamlines at $t = 0.9$

Figure 4.31: Comparison of the magnitude of the flow velocity between the FEM reference solution and different TEPEM solutions (for varying p), and streamlines at different time instants.

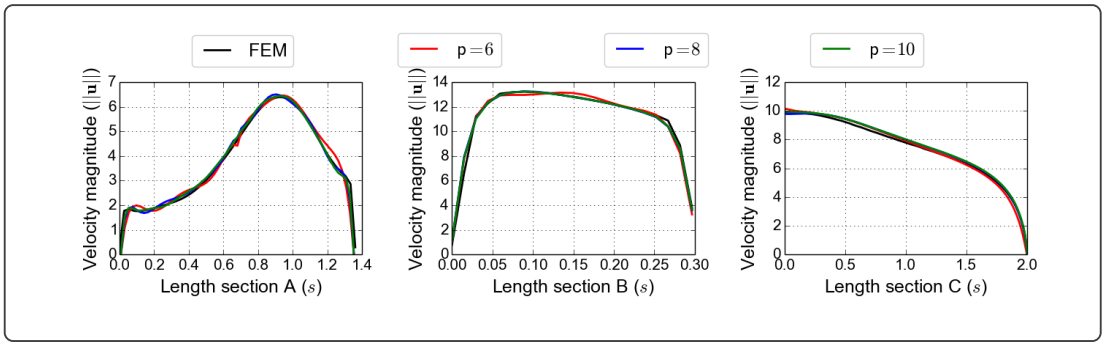

(a) Comparison in velocity magnitude at $t = 0.1$

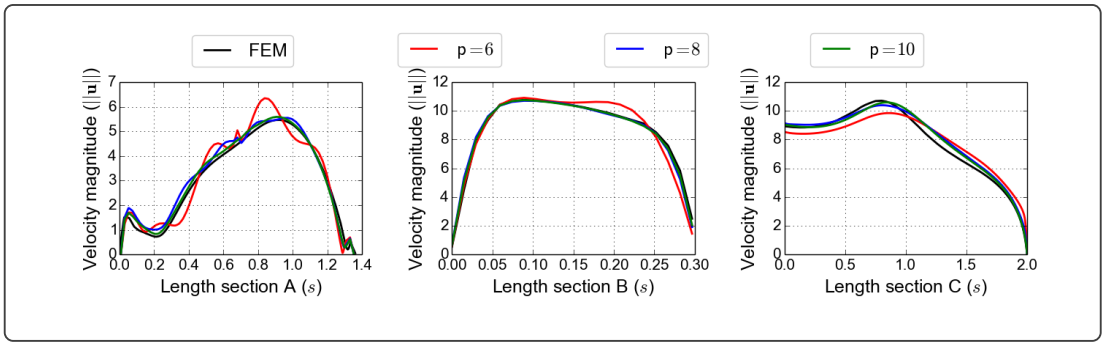

(b) Comparison in velocity magnitude at $t = 0.3$

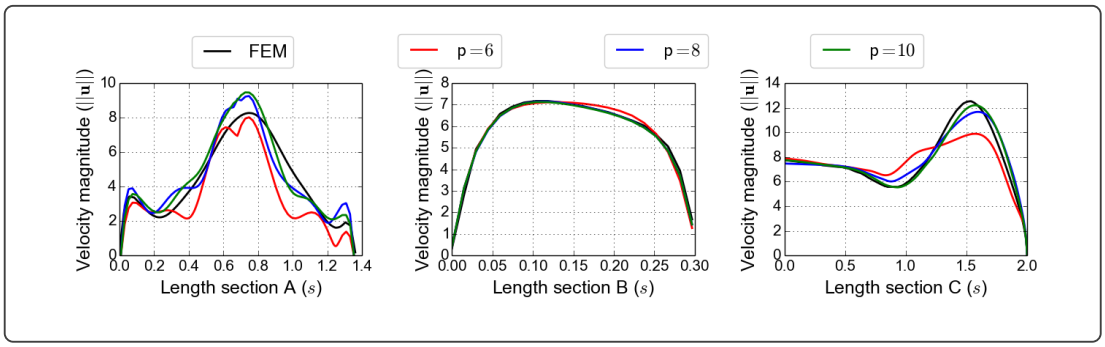

(c) Comparison in velocity magnitude at $t = 0.5$

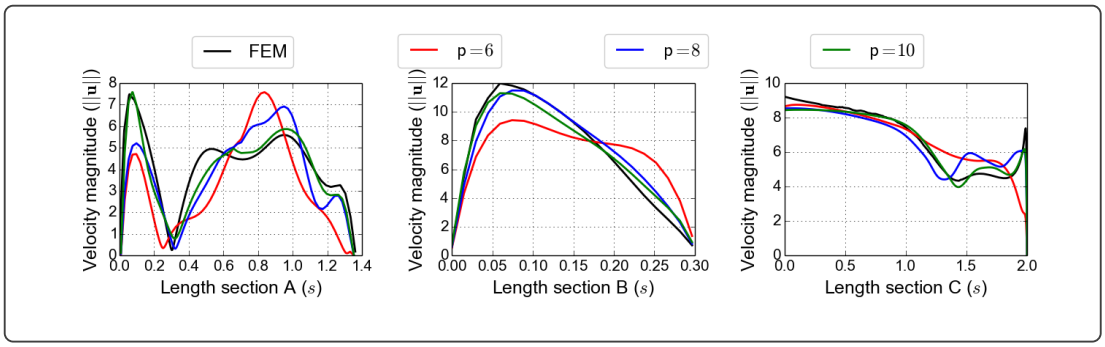

(d) Comparison in velocity magnitude at $t = 0.7$

Figure 4.32: Comparison of the magnitude of the flow velocity between the FEM reference solution and different TEPEM solutions (for varying p) at different time instants and three selected sections.

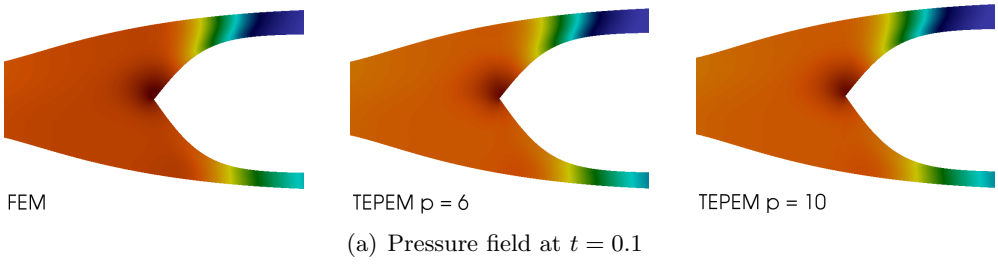

(a) Pressure field at $t = 0.1$

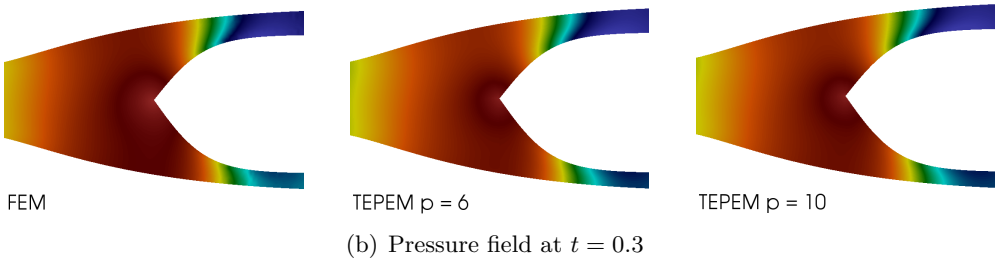

(b) Pressure field at $t = 0.3$

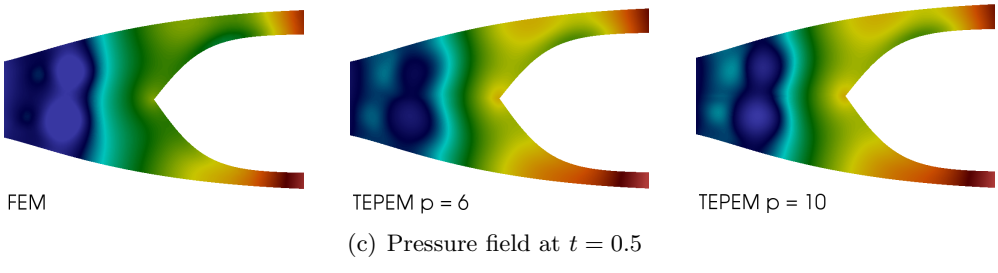

(c) Pressure field at $t = 0.5$

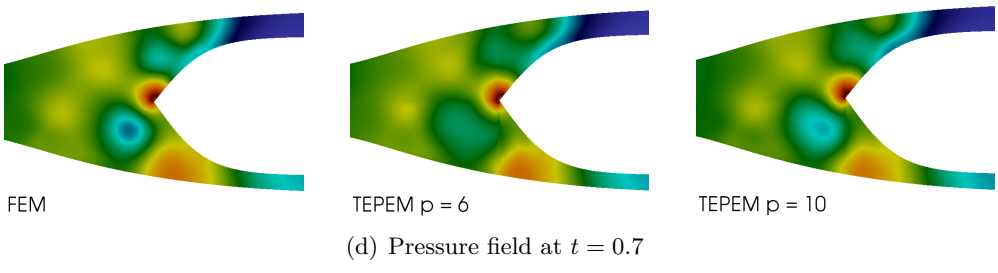

(d) Pressure field at $t = 0.7$

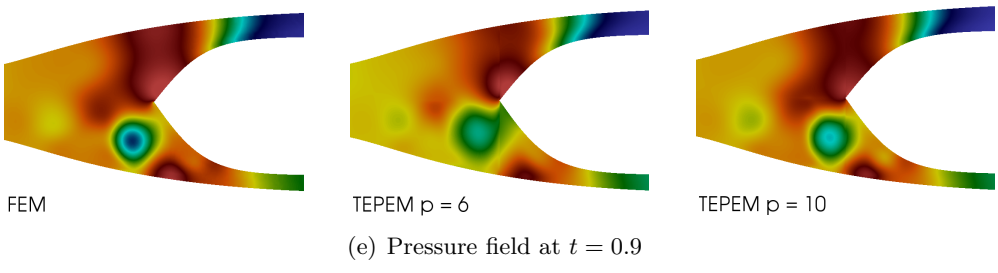

(e) Pressure field at $t = 0.9$

Figure 4.33: Comparison of pressure field between the FEM reference solution and different TEPEM solutions (for varying p) at the bifurcation area. At each time step, scales are conveniently adjusted.

4.4.5 Transient flow through 90° curved pipe

This last example addresses the flow through a two-dimensional curved pipe. The geometrical domain is the one outlined in Figure 4.34, bounded by the curves Γ_i (inlet boundary), Γ_o (outlet boundary) and Γ_l (lateral boundary).

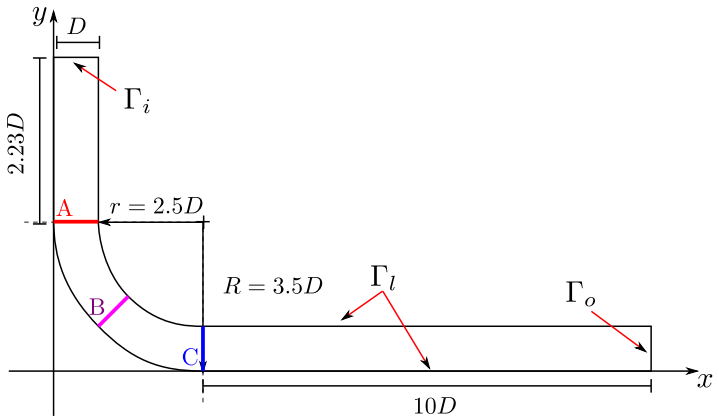

Figure 4.34: Geometric description of the 90° curved pipe. The inlet spacing between the parallel plates is fixed as $D = 0.62$cm. Three segments are selected: Section A in red, Section B in magenta and Section C in blue.

On Γ_l it is imposed a no-slip boundary condition and over Γ_o we consider mixed boundary conditions with homogeneous Dirichlet condition for the transversal component of the velocity field and homogeneous Neumann condition for the axial component of the traction. The flow is driven by the imposition, at Γ_i, of a parabolic velocity profile scaled to yield the sinusoidal flow

$$q(t) = q_0 \left(1 + \sin(2\pi t)\right) \tag{4.38}$$

with $q_0 = 4$ cm^2/s. Values for density and viscosity are fixed as $\rho = 1$ g/cm^2 and $\mu = 0.01$ P. The flow is characterized by a mean Reynolds number equal to $Re = 250$ and a Womersley number $\kappa \approx 8$.

Once the capabilities of the TEPEM proposal were demonstrated in previous examples, for transient cases as well as for problems in complex geometries, the goal of this example is to perform a comparison within the TEPEM and for different values of transversal enrichment. For this purpose, we perform a discretization of the problem domain composed of approximately 200 pipe-elements, each one with the same axial length.

Denoting by $T = 1$s the period of the proposed periodic flow, we approximate the solution in the interval of time $t \in (0, 2T)$ and consider the time step as being $\Delta t = 1 \cdot 10^{-3}$s. The computational cost to perform the transient simulation is illustrated in Table 4.7 where we compare the degrees of freedom, the time employed for a one single time-step iteration and the wall-clock time for different transversal order.

Table 4.7: Comparison of the computational effort in the TEPEM for different transversal order. Only two processors were employed in each case.

		Transversal order				
		$\mathsf{p}=4$	$\mathsf{p}=6$	$\mathsf{p}=8$	$\mathsf{p}=10$	$\mathsf{p}=12$
Time	DoFs	6 057	8 443	10 829	13 215	15 601
	Single time-step (seg)	1.94	2.09	2.59	3.28	3.47
	Wall-clock time (min)	46.76	78.31	103.98	125.73	139.77

In Figures 4.35-4.38, we compare the pressure and velocity profile, for different time instants, provided by different values of transversal enrichment. This comparison is focused in the three segments selected in the curved region and presented in Figure 4.34 and features the improvement in the results when the transversal order is increased. At each time, the profiles provided by $\mathsf{p}=8$ and $\mathsf{p}=10$ are almost overlapping, which can be appreciated as a convergence of the TEPEM as a function of the parameter p.

For $\mathsf{p}=6$, the velocity profiles are very close to the reference profiles, showing very slight differences only appreciable at some time instants. As said before, the main goal of the TEPEM proposal is to reduce the computational effort but maintaining the ability to carry the most relevant information of the dynamics. This is fundamental for hemodynamics applications where sometimes it is more relevant to get a global insight of the blood dynamics rather than to achieve the exact solution. For this regime ($Re = 250$, $\kappa \approx 8$) the transversal order $\mathsf{p}=6$ yields excellent results, if compared with the solution with $\mathsf{p}=10$, with a significantly smaller computational time.

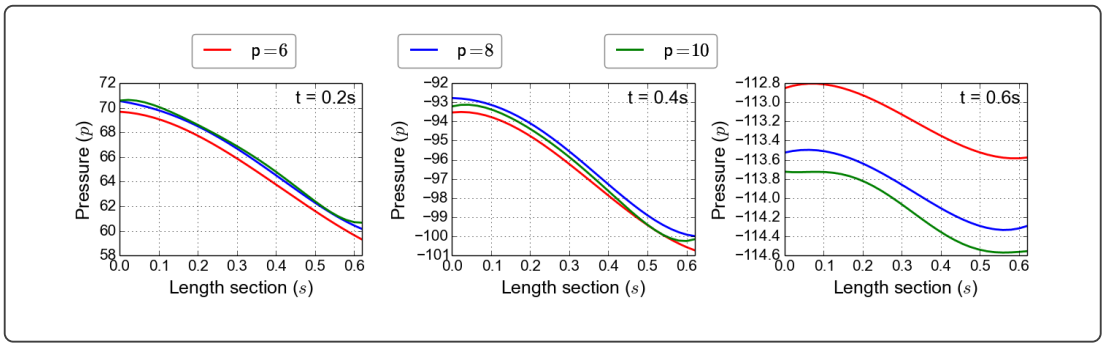

(a) Comparison in pressure at $t = 0.2$s, $t = 0.4$s and $t = 0.6$s

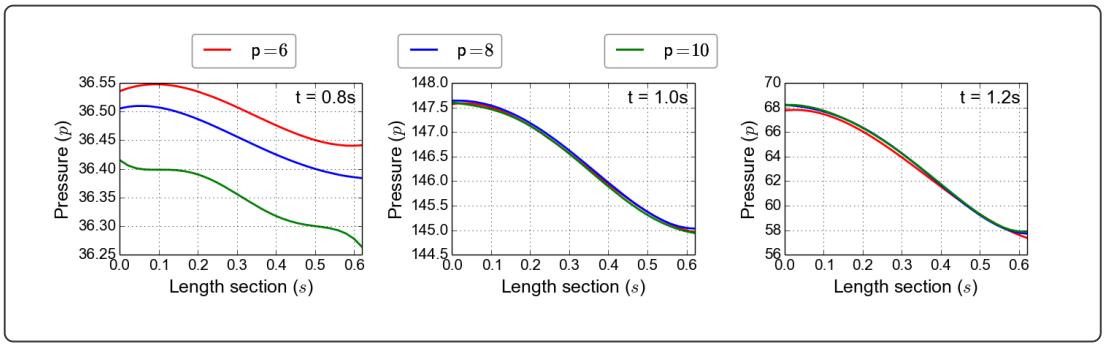

(b) Comparison in pressure at $t = 0.8$s, $t = 1.0$s and $t = 1.2$s

Figure 4.35: Comparison of pressure field, in the section B, given by the TEPEM with different transversal order and at different time instants along the simulation.

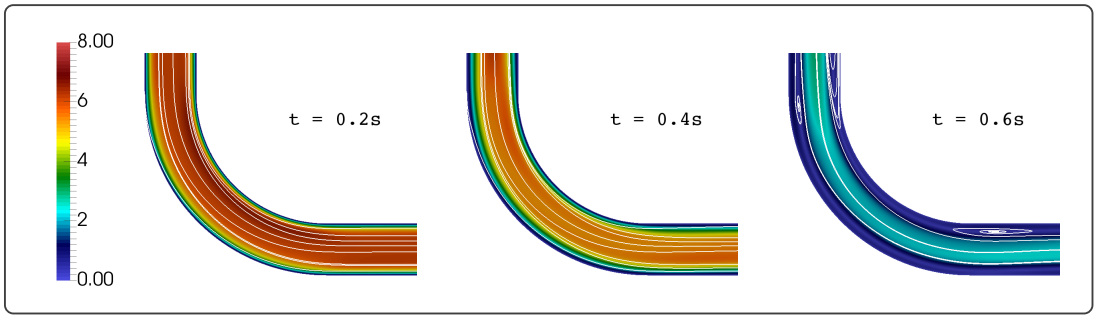

(a) Magnitude of the velocity approximated with $\mathsf{p} = 8$.

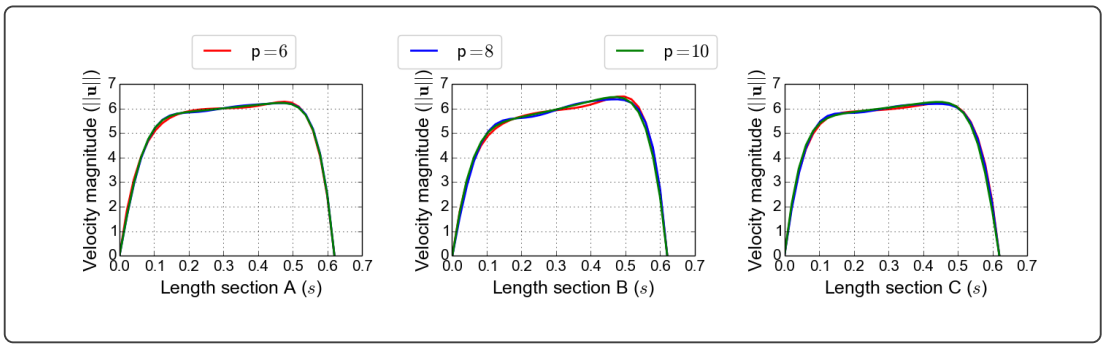

(b) Comparison in velocity magnitude at $t = 0.2$s

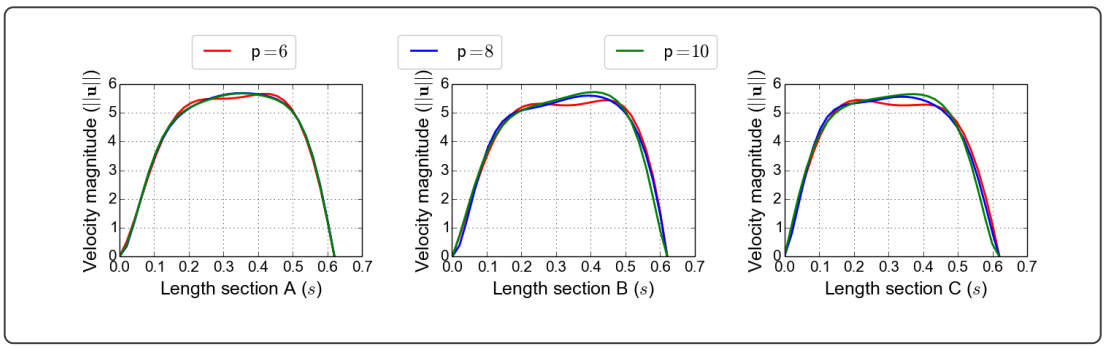

(c) Comparison in velocity magnitude at $t = 0.4$s

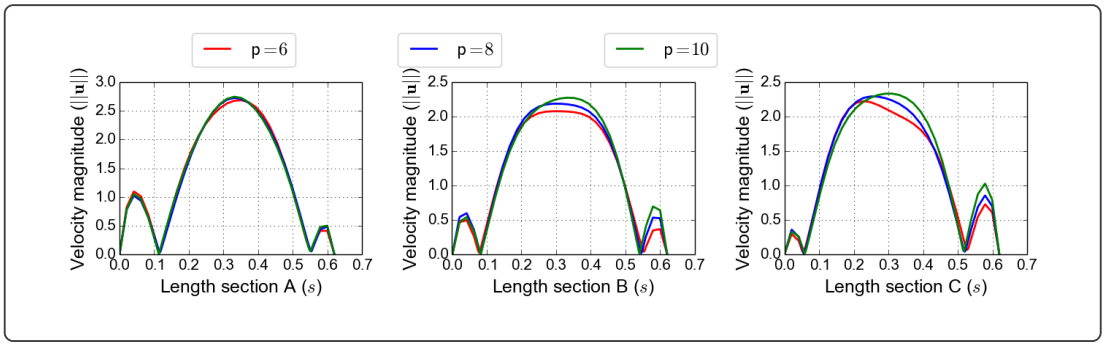

(d) Comparison in velocity magnitude at $t = 0.6$s

Figure 4.36: Comparison of velocity profiles, in the curved region, given by the TEPEM with different transversal order and at different time instants along the simulation.

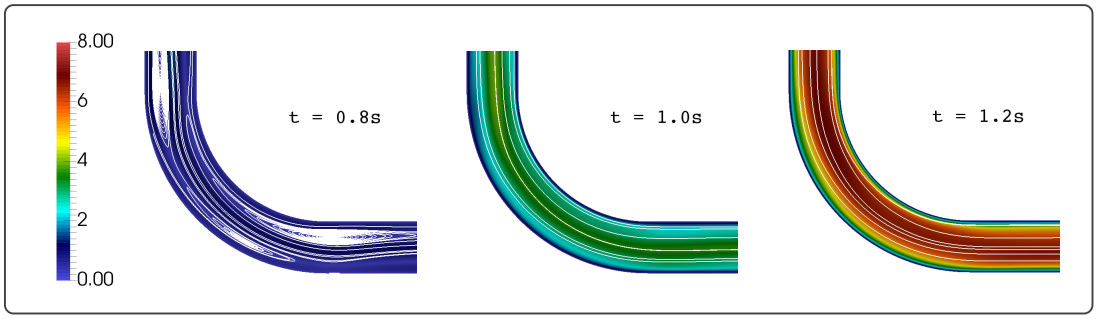

(a) Magnitude of the velocity approximated with $\mathsf{p} = 8$.

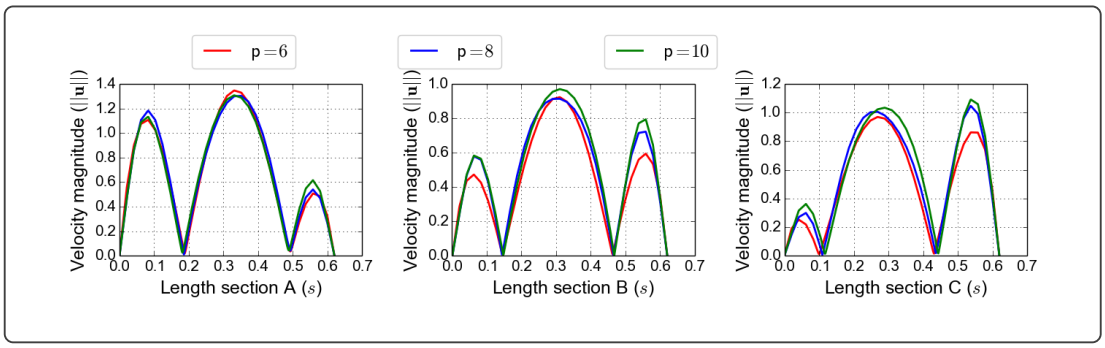

(b) Comparison in velocity magnitude at $t = 0.8$s

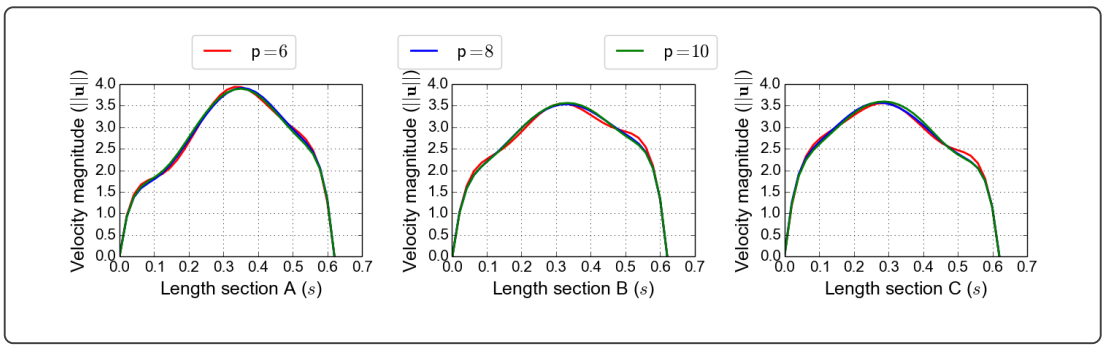

(c) Comparison in velocity magnitude at $t = 1.0$s

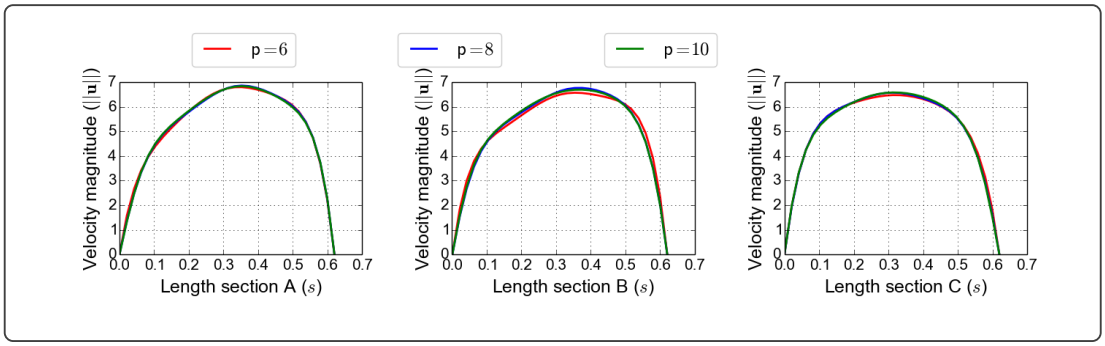

(d) Comparison in velocity magnitude at $t = 1.2$s

Figure 4.37: Comparison of velocity profiles, in the curved region, given by the TEPEM with different transversal order and at different time instants along the simulation.

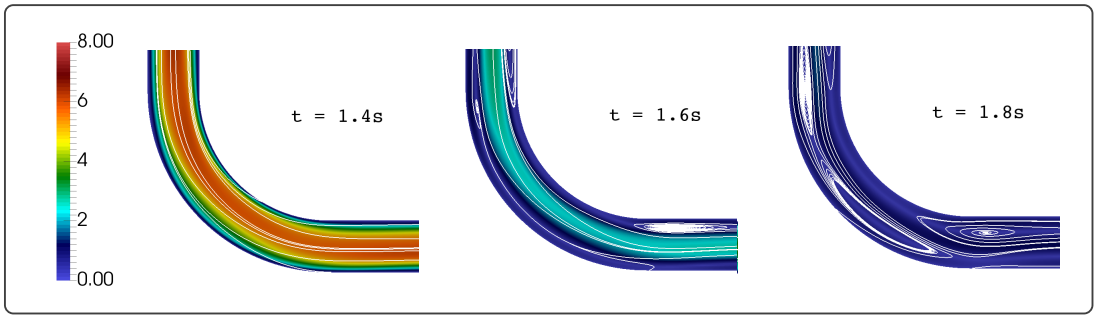

(a) Magnitude of the velocity approximated with $\mathsf{p} = 8$.

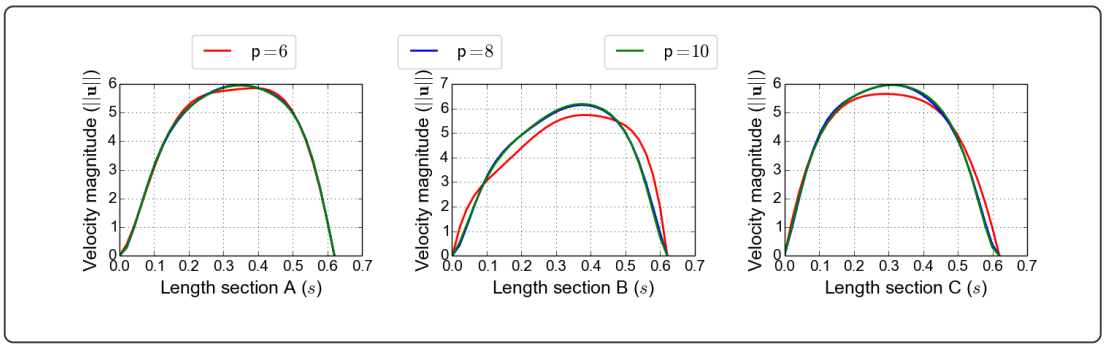

(b) Comparison in velocity magnitude at $t = 1.4$

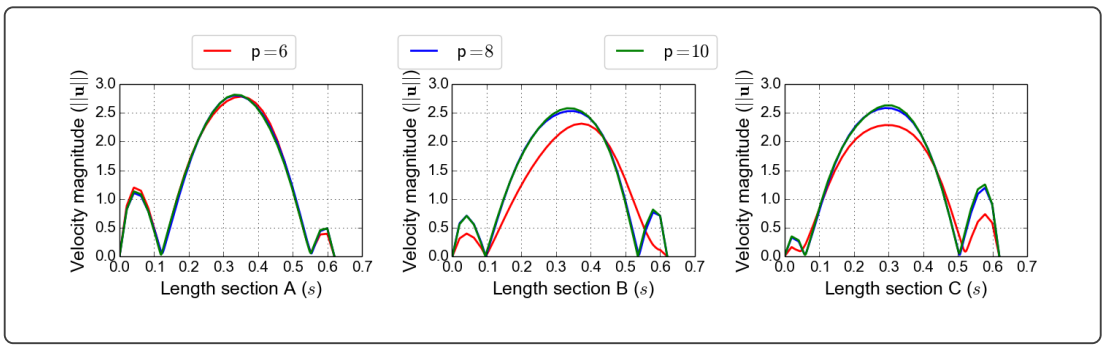

(c) Comparison in velocity magnitude at $t = 1.6$

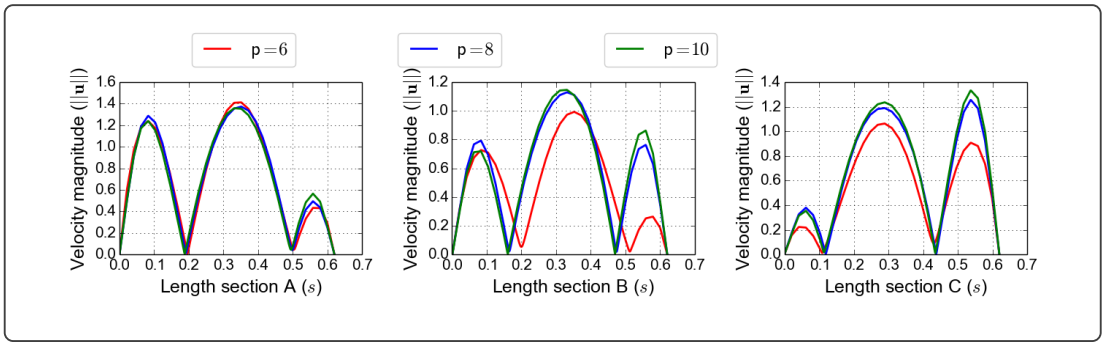

(d) Comparison in velocity magnitude at $t = 1.8$

Figure 4.38: Comparison of velocity profiles, in the curved region, given by the TEPEM with different transversal order and at different time instants along the simulation.

4.5 Academic fluid flow simulations: 3D case

After demonstrating the capabilities of the TEPEM in the two-dimensional case, in this section we perform an equivalent study for problems defined in 3D regions. It is expected that the demonstrated efficiency in the previous section remains valid and in many cases accentuated when dealing with three-dimensional problems.

The accuracy in the approximation of velocity and pressure fields is measured as performed in the two-dimensional case, computing the relative error with respect to a reference solution that is either an analytical solution when available or a FEM solution computed in a sufficiently fine tetrahedral mesh.

In this case, in addition to the comparison between TEPEM and FEM in terms of the number of degrees of freedom, we also compare the computational time required in the simulation with both methods. For this purpose, both TEPEM and FEM techniques have been parallelized within the same general-purpose numerical solver. The number of processors (NP) used in the solution process is set specifically for each case. Then, the wall-clock simulation time is reported as well as the average computational time, which is defined by multiplying the wall-clock time by NP. By assuming linear parallel scalability of both methods, this last parameter can be understood as the theoretical time employed in each simulation if a single core was employed.

For the TEPEM, the geometry discretization is performed in *ad-hoc* way and the velocity and pressure fields are approximated employing the combination of discrete spaces commented in the Equation 4.15. The resulting discrete system is monolithically solved by employing a direct parallel algebraic LU solver. For the problems addressed in this section, the reduction in the problem size performed by the TEPEM allow us the use of a direct solver.

By other hand, for the FEM, the spatial discretization is performed by employing the Vascular Modeling ToolKit [VMTK 2015]. The velocity and pressure fields are approximated based on the mini element ([Arnold et al. 1984]) with SUPG stabilization ([Hughes et al. 1987]). The system of algebraic equations is solved using an iterative GMRES method, with a restricted additive Schwarz preconditioner.

For both, FEM and TEPEM, the Portable, Extensible Toolkit for Scientific Computation (PETSc [Balay et al. 2017b,a]) provide the implementation of the LU solver, the Krylov subspace algorithm and the preconditioner strategy. For transient cases, the time step (Δt) employed for the temporal discretization is fine enough to ensure the convergence.

The simulations, for both strategies, were performed in the INCT-MACC cluster. This heterogeneous cluster, available at the *Laboratório Nacional de Computação Científica* (LNCC, Petrópolis, Brazil), is consisting of 100 nodes with 2 x Intel Xeon X5670 2.93GHz (6 cores), 36GB of RAM and 54 nodes with 2 x Intel Xeon E5-2660 2.20GHz (8 cores), 64GB of RAM interconnected through Infiniband QDR.

A post-processing step is considered for both strategies, FEM and TEPEM, to compute the wall shear stress (WSS). Defined over the boundary that corresponds to the lateral lumen boundary, the WSS is computed from the wall shear rate vector $\tau(t, \mathbf{x}) = (\nabla^s \mathbf{u})\mathbf{n}$ at each surface point $\mathbf{x}$ as

$$\text{WSS} = -2\mu\tau(t, \mathbf{x}). \tag{4.39}$$

4.5.1 Womersley flow

The Womersley flow is a classical benchmark example in fluid dynamics due to the existence of an analytical solution [Womersley 1955]. Consider the incompressible flow of a Newtonian fluid inside a cylindrical pipe driven by a pressure gradient defined as

$$\Delta p = -A\cos\left(\frac{2\pi}{T}t\right) \tag{4.40}$$

with $T = 1$ the period and $A = 2$ the amplitude. The domain of the problem is a cylinder of length equal to $l = 2$ and radius $R = 0.2$.

To ensure that the flow is fully developed, the pressure difference is imposed through homogeneous and non-homogeneous Neumann boundary conditions, at outlet and inlet respectively. No-slip boundary condition is imposed on the lateral boundaries of the pipe.

The analytical solution, for velocity and pressure, can be analytically computed in cylindrical coordinates (r, θ, x). Denoting by $(\mathbf{u}_x, \mathbf{u}_r, \mathbf{u}_\theta)$ the axial, radial and angular components of the velocity, respectively, the solution of the Womersley problem is expressed as

$$\begin{aligned} &\mathbf{u}_x(r,\theta,x,t) = -\text{Real}\left(\frac{A}{i\rho\tau}\left[1 - \frac{J_0\left(\hat{x}r\right)}{J_0(\hat{x}R)}\right]\right)e^{i\tau t} \qquad \mathbf{u}_r = \mathbf{u}_\theta = 0 \\ &p(r,\theta,x,t) = p_{in}(t) + x\Delta p \end{aligned} \tag{4.41}$$

where ρ is the (constant) density of the fluid, r the radial component of the spatial coordinate, $i = \sqrt{-1}$ the imaginary unity, Real$(\cdot)$ the real component of argument $(\cdot)$, $J_0(\cdot)$ the Bessel function of order zero. Also, we have the following parameters

$$\tau = \frac{2\pi}{T}, \qquad \kappa = R\sqrt{\frac{\tau}{\mu}}, \qquad \hat{x} = \frac{\kappa}{R}i^{3/2} \tag{4.42}$$

with κ the Womersley number and μ the fluid viscosity.

A numerical study of the TEPEM is carried out to demonstrate the capabilities of the proposed approach in the cases $\kappa \in \{3, 5, 10, 20\}$, which are Womersley numbers within the range encountered in hemodynamic applications. Keeping the density $\rho = 1$, the Womersley number in each case is reached by varying the fluid viscosity. For the time discretization, we consider $\Delta t = \frac{T}{4000}$.

The errors in the TEPEM approximation, for different Womersley numbers and transversal enrichment orders, are presented in Table 4.8 for the velocity and the gradient. This table is complemented with Figure 4.39 where the convergence of the TEPEM solution with respect to the transversal enrichment is presented for each Womersley number.

Table 4.8: Numerical error in the velocity field between the TEPEM solution and the analytical solution measured in the norm of $L^2(0,T;L^2(\Omega))$-space and the seminorm of $L^2(0,T;H^1(\Omega))$-space.

		Womersley number			
		$\kappa = 3$	$\kappa = 5$	$\kappa = 10$	$\kappa = 20$
$\|\mathbf{u} - \mathbf{u}_T\|$	$\mathsf{p} = 4$	$1.0177 \cdot 10^{-3}$	$1.5820 \cdot 10^{-3}$	$4.5864 \cdot 10^{-3}$	$8.2390 \cdot 10^{-3}$
	$\mathsf{p} = 8$	$2.7518 \cdot 10^{-4}$	$3.8203 \cdot 10^{-4}$	$9.9085 \cdot 10^{-4}$	$1.7180 \cdot 10^{-3}$
	$\mathsf{p} = 12$	$1.6767 \cdot 10^{-4}$	$2.5408 \cdot 10^{-4}$	$4.6867 \cdot 10^{-4}$	$7.6272 \cdot 10^{-4}$
$\|\mathbf{u} - \mathbf{u}_T\|$	$\mathsf{p} = 4$	$2.7938 \cdot 10^{-3}$	$9.4462 \cdot 10^{-3}$	$3.5476 \cdot 10^{-2}$	$7.2035 \cdot 10^{-2}$
	$\mathsf{p} = 8$	$9.3157 \cdot 10^{-4}$	$1.8344 \cdot 10^{-3}$	$9.2567 \cdot 10^{-3}$	$2.8609 \cdot 10^{-2}$
	$\mathsf{p} = 12$	$7.6222 \cdot 10^{-4}$	$1.3994 \cdot 10^{-3}$	$5.8783 \cdot 10^{-3}$	$1.0455 \cdot 10^{-2}$

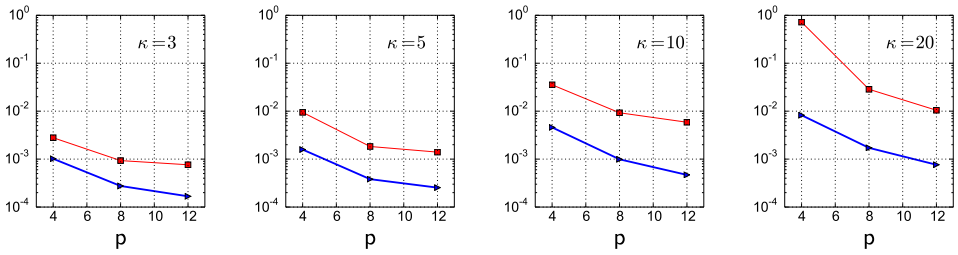

Figure 4.39: Numerical error of the velocity in the $L^2(0,T;L^2(\Omega))$-norm (▲) and the $L^2(0,T;H^1(\Omega))$-seminorm (■) for each Womersley number κ.

For a visual comparison, in Figures 4.40-4.43 the analytical solution and the TEPEM approximation are displayed. For different time instants, the approximate solution (with $\mathsf{p} = 8$), at the middle of the pipe, is presented as a 3D profile together with the analytical solution. It can be seen that even with a low transversal order, say $\mathsf{p} = 4$, the solution is reasonably good near the wall, which is crucial towards a reasonable, and fast, estimation of the endothelial shear stress in hemodynamic simulations. Also, even for high Womersley number, the choice $\mathsf{p} = 8$ offers a very accurate solution.

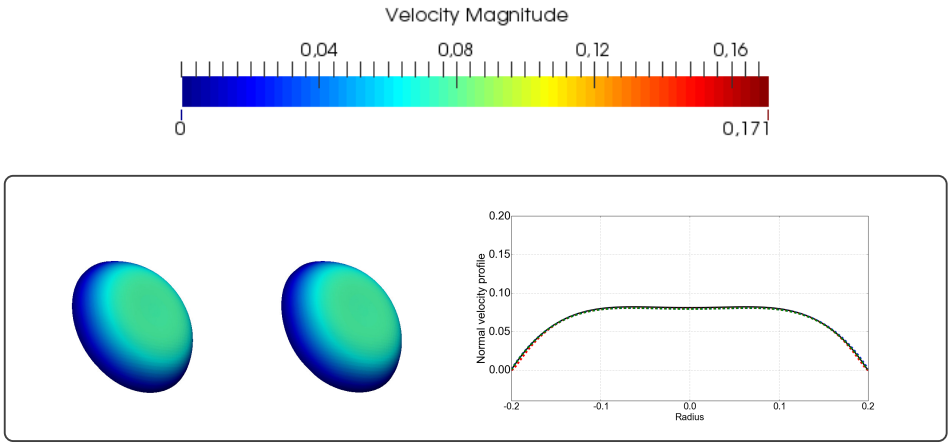

(a) Velocity profile at $t = 0/8$

(b) Velocity profile at $t = 1/8$

(c) Velocity profile at $t = 2/8$

(d) Velocity profile at $t = 3/8$

Figure 4.40: Comparison of velocity profile provided by the TEPEM (right profile at each panel) with respect to the analytical solution (left profile at each panel) for Womersley numbers $\kappa = 3$. On each panel, the solid black line stands for the analytical solution, red dotted line is the approximation with $\mathsf{p} = 4$, blue dotted line corresponds to $\mathsf{p} = 8$ and green dotted line is the solution with transversal order $\mathsf{p} = 12$.

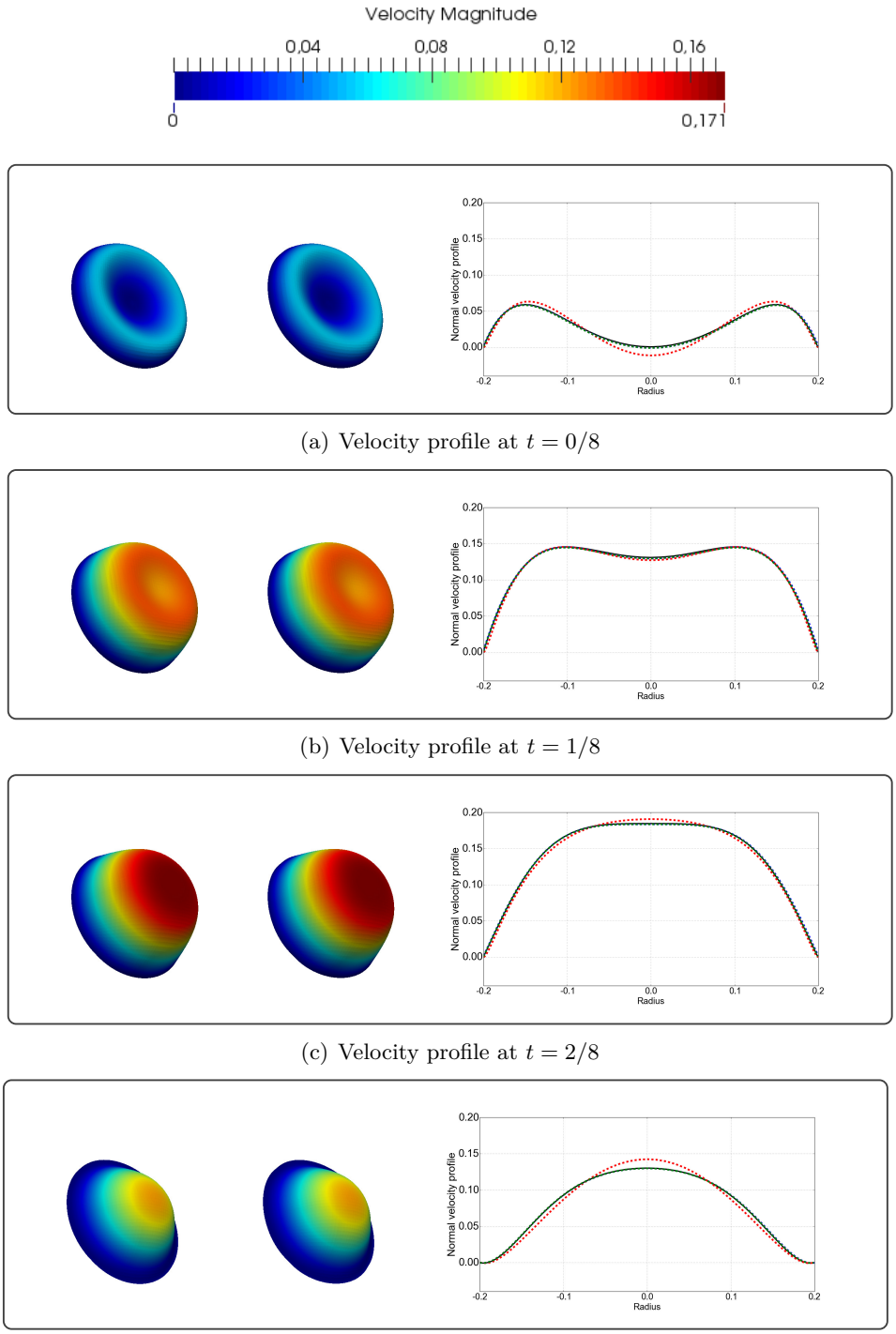

(a) Velocity profile at $t = 0/8$

(b) Velocity profile at $t = 1/8$

(c) Velocity profile at $t = 2/8$

(d) Velocity profile at $t = 3/8$

Figure 4.41: Comparison of velocity profile provided by the TEPEM (right profile at each panel) with respect to the analytical solution (left profile at each panel) for Womersley numbers $\kappa = 5$. On each panel, the solid black line stands for the analytical solution, red dotted line is the approximation with $\mathsf{p} = 4$, blue dotted line corresponds to $\mathsf{p} = 8$ and green dotted line is the solution with transversal order $\mathsf{p} = 12$.

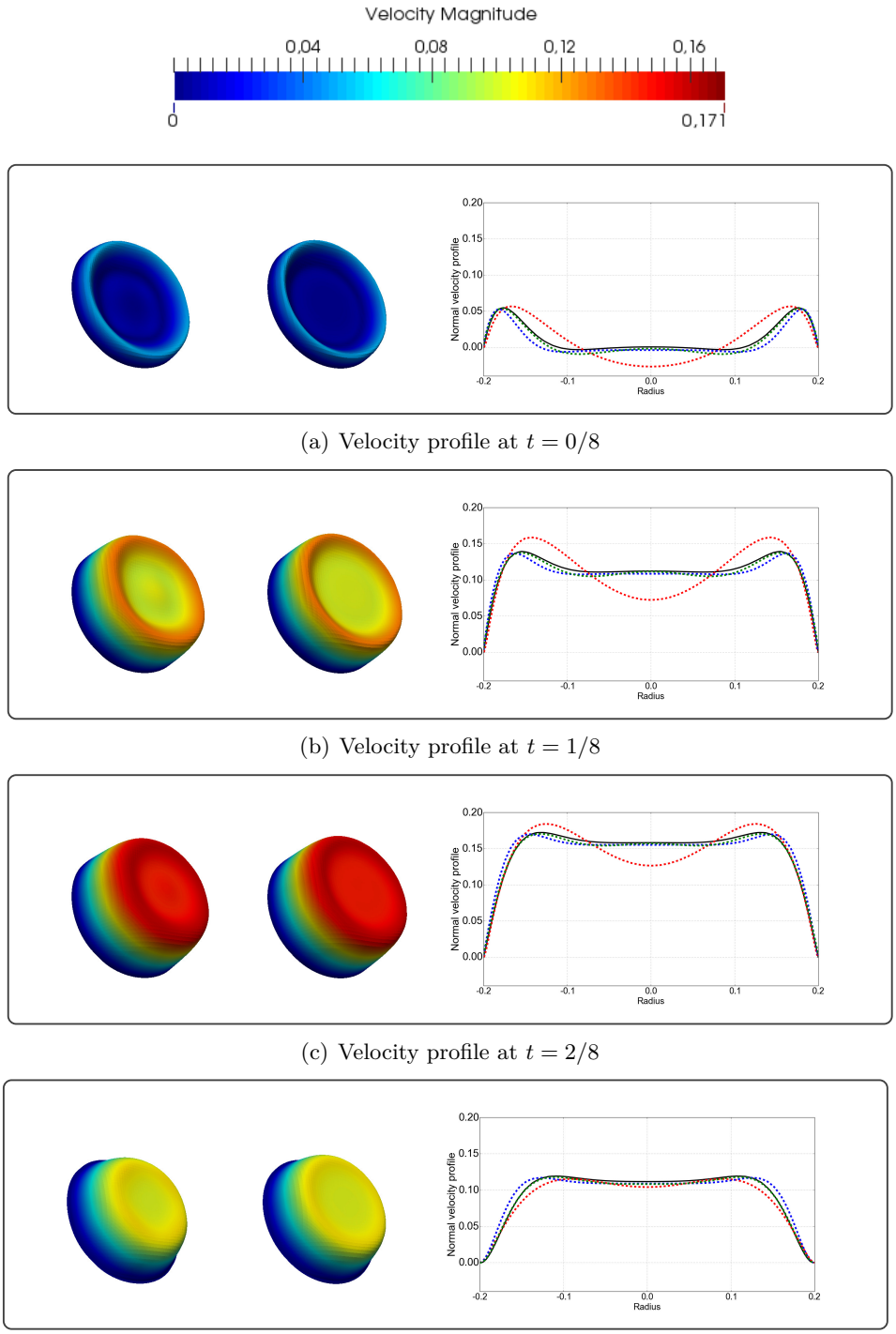

(a) Velocity profile at $t = 0/8$

(b) Velocity profile at $t = 1/8$

(c) Velocity profile at $t = 2/8$

(d) Velocity profile at $t = 3/8$

Figure 4.42: Comparison of velocity profile provided by the TEPEM (right profile at each panel) with respect to the analytical solution (left profile at each panel) for Womersley numbers $\kappa = 10$. On each panel, the solid black line stands for the analytical solution, red dotted line is the approximation with $\mathsf{p} = 4$, blue dotted line corresponds to $\mathsf{p} = 8$ and green dotted line is the solution with transversal order $\mathsf{p} = 12$.

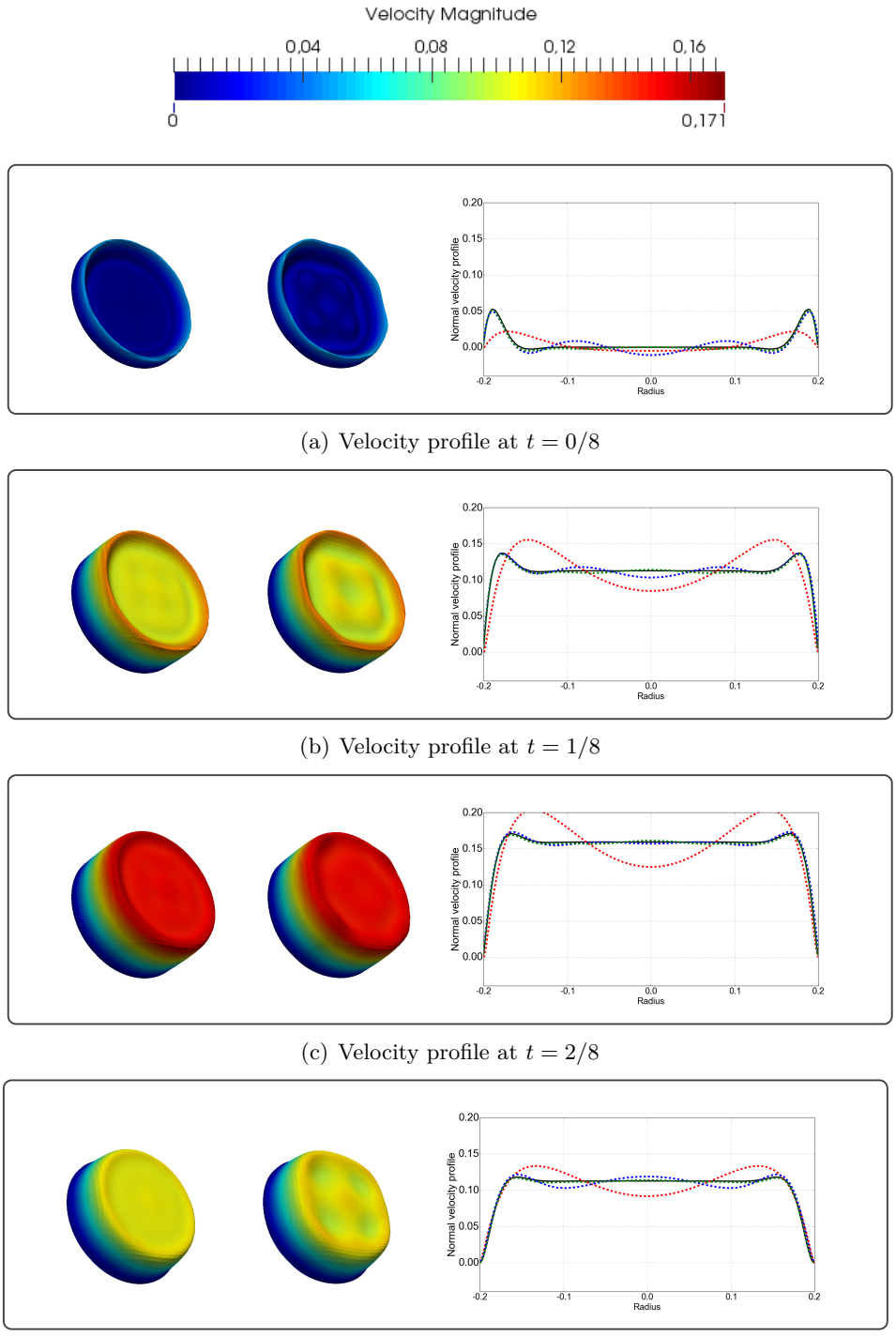

(a) Velocity profile at $t = 0/8$

(b) Velocity profile at $t = 1/8$

(c) Velocity profile at $t = 2/8$

(d) Velocity profile at $t = 3/8$

Figure 4.43: Comparison of velocity profile provided by the TEPEM (right profile at each panel) with respect to the analytical solution (left profile at each panel) for Womersley numbers $\kappa = 20$. On each panel, the solid black line stands for the analytical solution, red dotted line is the approximation with $\mathsf{p} = 4$, blue dotted line corresponds to $\mathsf{p} = 8$ and green dotted line is the solution with transversal order $\mathsf{p} = 12$.

4.5.2 Tortuous pipe flow

Let us define the region Ω where the fluid is flowing as the tortuous pipe with circular cross-sectional area with centerline and radius parametrized by the relation

$$c(t) = 0.4\sqrt{t}\sin(2\pi t), \qquad r(t) = 0.1(1 + 0.5\cos^2(2\pi t)) \qquad 0 \leq t \leq T \tag{4.43}$$

where T is the period. The aim of this example is to study the TEPEM when the complexity in the domain is increased. For this, we consider three domains corresponding to two, four and six turns of the tortuous pipe (corresponding to $T \in \{1, 2, 3\}$). These domains are outlined in Figure 4.44.

Figure 4.44: Geometries for the tortuous sinusoidal pipe example. From left to right: Two, four and six turns.

The efficiency of the TEPEM is measured with respect to a FEM reference solution computed in an extremely fine tetrahedral mesh, comparing the total number of degrees of freedom involved in each strategy, computational time and error for the TEPEM in the velocity field. The characteristics of the meshes for both approaches are summarized in Table 4.9. Notice that the relative reduction in the degrees of freedom is superior to the 98% for all the cases. Specifically it is achieved a reduction between 99.66% (in the case $\mathsf{p} = 6$ and two turns) and 98.04% (in the case $\mathsf{p} = 12$ and six turns).

Table 4.9: Comparison between degrees of freedom and number of elements employed in the FEM and the TEPEM approaches. The relative reduction in the degrees of freedom performed by the TEPEM is superior to the 98%.

	Degrees of Freedom					Elements	
	FEM	$\mathsf{p} = 6$	$\mathsf{p} = 8$	$\mathsf{p} = 10$	$\mathsf{p} = 12$	FEM	TEPEM
Turn 2	1 329 676	4 407	8 466	13 851	20 562	1 901 141	26
Turn 4	3 054 632	10 383	19 950	32 643	48 462	4 395 739	62
Turn 6	4 139 792	17 355	33 348	54 567	81 012	5 840 736	104

In each domain, the steady state flow is simulated (with density and viscosity values fixed at $\rho = 1$ and $\mu = 0.01$) as being driven by a pressure difference imposed to reach a given Reynolds number. For this example, we consider two cases for Reynolds $Re \in \{50, 500\}$. As usual, no-slip boundary condition is imposed on the lateral boundary.

The errors in the velocity approximation ($\mathbf{u}_\mathrm{T}$), computed against the reference FEM velocity ($\mathbf{u}_\mathrm{F}$), are presented in Table 4.10. These results, for both $Re = 50$ and $Re = 500$, evidence the convergence in the TEPEM and the increase in the model capabilities with respect to the transversal order considered for the interpolation of physical fields. Moreover, the convergence rate against p (Figure 4.45) is very similar for the three domains considered here.

Table 4.10: Numerical errors in the velocity field between the TEPEM and the FEM solutions measured in the L^2-norm.

		Transversal order			
		p = 6	p = 8	p = 10	p = 12
Re = 50	Turn 2	$1.04 \cdot 10^{-2}$	$6.88 \cdot 10^{-3}$	$5.04 \cdot 10^{-3}$	$3.93 \cdot 10^{-3}$
	Turn 4	$1.49 \cdot 10^{-2}$	$9.40 \cdot 10^{-3}$	$6.34 \cdot 10^{-3}$	$4.36 \cdot 10^{-3}$
	Turn 6	$5.70 \cdot 10^{-1}$	$1.85 \cdot 10^{-2}$	$8.09 \cdot 10^{-3}$	$6.47 \cdot 10^{-3}$
Re = 500	Turn 2	$6.32 \cdot 10^{-2}$	$3.32 \cdot 10^{-2}$	$1.47 \cdot 10^{-2}$	$8.68 \cdot 10^{-3}$
	Turn 4	$8.90 \cdot 10^{-2}$	$4.80 \cdot 10^{-2}$	$2.45 \cdot 10^{-2}$	$1.29 \cdot 10^{-2}$
	Turn 6	$1.07 \cdot 10^{-1}$	$5.79 \cdot 10^{-2}$	$3.40 \cdot 10^{-2}$	$1.70 \cdot 10^{-2}$

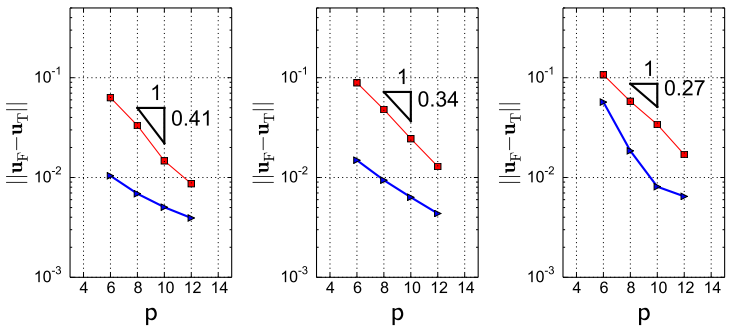

Figure 4.45: Numerical error of the velocity in the $L^2(\Omega)$-norm for the two (left panel), four (middle panel) and six (right panel) turns. At each panel are presented the error for the case Re = 50 (in blue) and Re = 500 (in red).

In addition to the reduction in the size of the discrete problem, a reduction in the computational time is also expected to occur. The total time taken by each strategy to solve the steady state problem is presented in Table 4.11. It is evident the strong reduction in the computational time achieved by the TEPEM, yielding a reduction in the computational time from 10 to 900 times. As we increase the size of the problem, the TEPEM becomes a more efficient strategy.

Table 4.11: Computational time (in minutes) to solve the steady state problem with the FEM and TEPEM approaches. Each case was performed employing one single processor (serial strategy) to allow a better comparison.

		FEM	TEPEM			
			p = 6	p = 8	p = 10	p = 12
Re = 50	Turn 2	90	0.5	4	11	25
	Turn 4	390	1	6	22	70
	Turn 6	1 800	3	11	40	125
Re = 500	Turn 2	450	1	10	35	98
	Turn 4	1 900	5	35	95	320
	Turn 6	9 100	10	75	200	660

To better understand the improvements in the predictive capabilities of the proposed method, for the case Turn 4 and Re = 500 we perform a comparison against FEM solutions obtained with coarser meshes instead of the extremely fine mesh considered before. For each transversal order p, we define a coarse FEM mesh whose characteristic element sizes are of the order of the characteristic distance between the nodes of the TEPEM elements, this is, $h = 1/(\mathsf{p}+1)$. The error in the FEM with these "equivalent" meshes is outlined in Table 4.12 together with the mesh characteristics. To complement this comparison, in Figure 4.46 it is presented the numerical convergence of both methods (TEPEM and FEM in equivalent meshes) with respect to the transversal order and the degrees of freedom, with a higher rate of convergence for the TEPEM in both cases.

Table 4.12: Case Turn 4 and Re = 500. Accuracy of numerical approximation (with respect to a FEM solution with a fine tetrahedral mesh) with the FEM approximation using an "equivalent" tetrahedral mesh. The errors resulting from the TEPEM are also presented.

	Equivalent order			
	$\mathsf{p}=6$	$\mathsf{p}=8$	$\mathsf{p}=10$	$\mathsf{p}=12$
Elements	40 152	90 040	148 007	193 728
DoFs	36 384	72 816	115 776	152 004
$\|\mathbf{u}-\mathbf{u}_{\mathrm{F}}\|$	$1.32\cdot10^{-1}$	$8.13\cdot10^{-2}$	$5.67\cdot10^{-2}$	$4.60\cdot10^{-2}$
$\|\mathbf{u}-\mathbf{u}_{\mathrm{T}}\|$	$8.90\cdot10^{-2}$	$4.80\cdot10^{-2}$	$2.45\cdot10^{-2}$	$1.29\cdot10^{-2}$

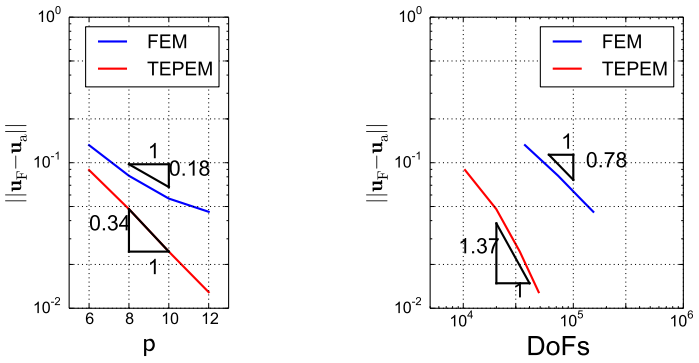

Figure 4.46: Numerical convergence of the velocity field for the TEPEM and FEM, in equivalent meshes, by comparison with a reference FEM solution obtained with an extremely fine tetrahedral mesh. The convergence is measured with respect to the transversal order p and the number of degrees of freedom in each approach (DoFs).

Finally, in Figures 4.47-4.48, we present, at two selected transversal sections, a comparison of the steady state velocity profiles given by the TEPEM, by the reference FEM solution and the coarse FEM solutions computed in the equivalent tetrahedral meshes. As it can be seen, the proposed method can satisfactorily resolve the normal and transversal components of the velocity vector field for a relatively moderate Reynolds number (Re = 500). When increased the transversal order p, the expected convergence is achieved. In turn, using the equivalent FEM meshes, worse quality solutions are obtained.

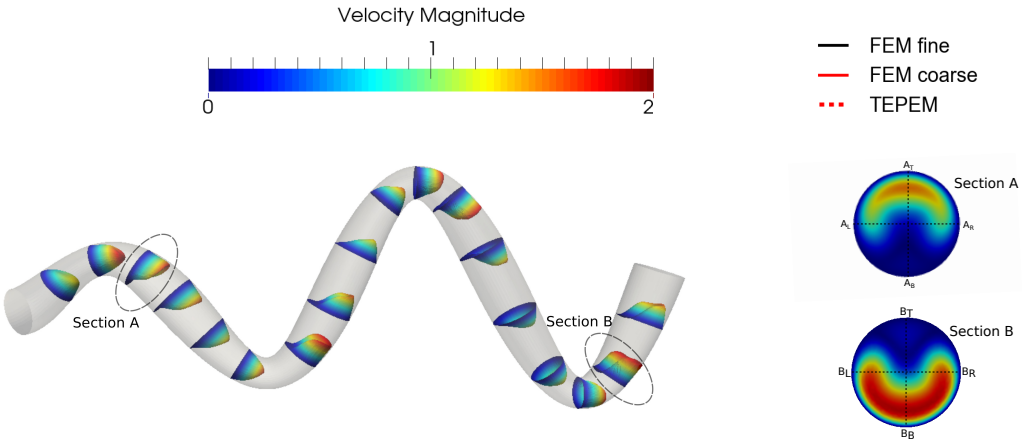

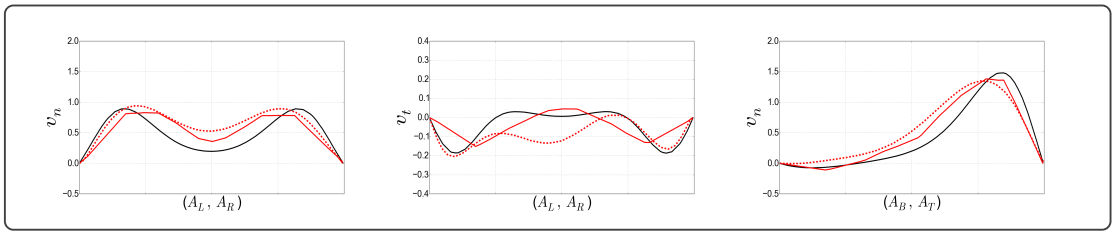

(a) Transversal order $\mathsf{p} = 6$.

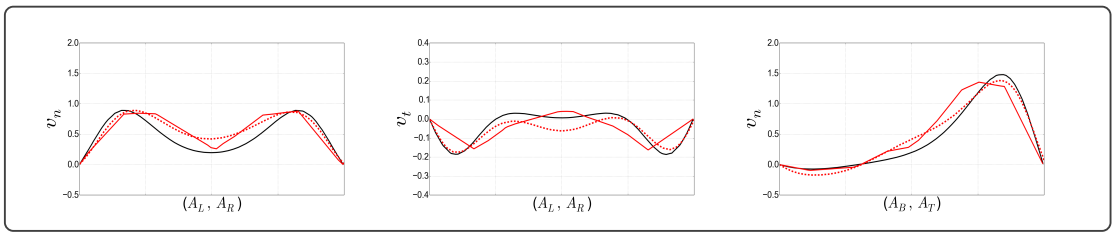

(b) Transversal order $\mathsf{p} = 8$.

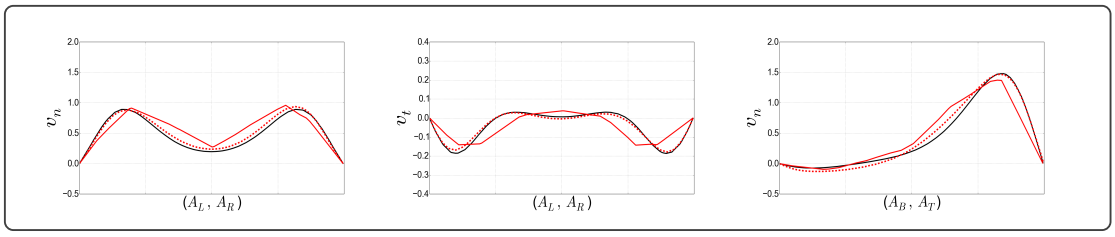

(c) Transversal order $\mathsf{p} = 10$.

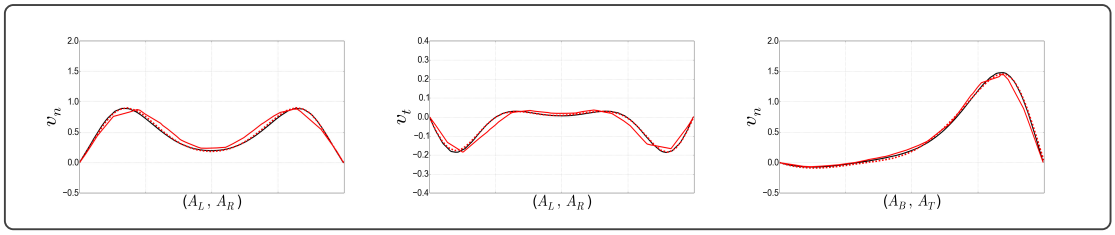

(d) Transversal order $\mathsf{p} = 12$.

Figure 4.47: Comparison of normal and tangential velocity components at region A of the tortuous pipe for the case Turn 4 and Re = 500. Solutions are compared for different approximation orders of the TEPEM and for two (fine and coarse) FEM meshes.

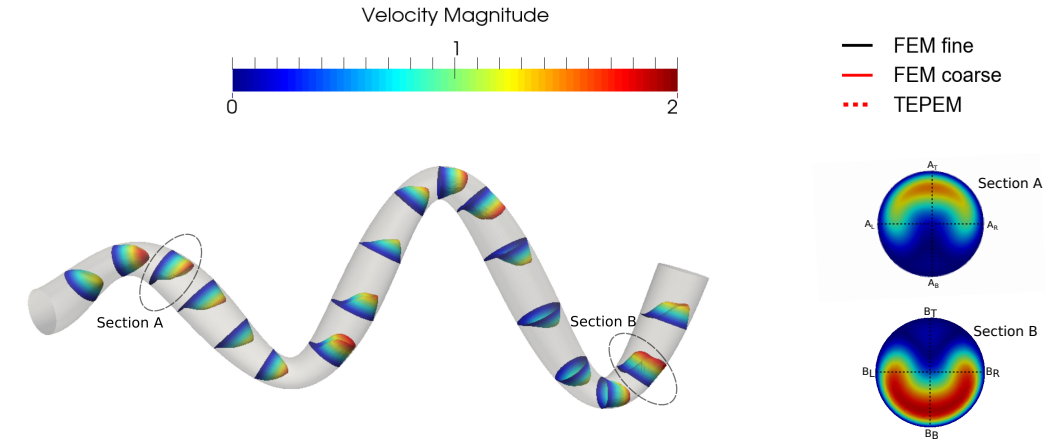

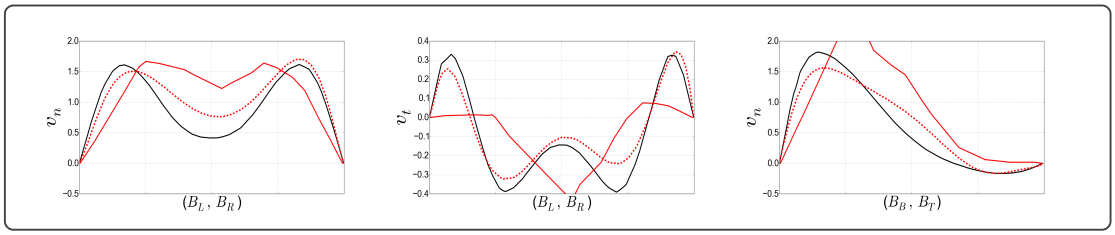

(a) Transversal order $\mathsf{p} = 6$.

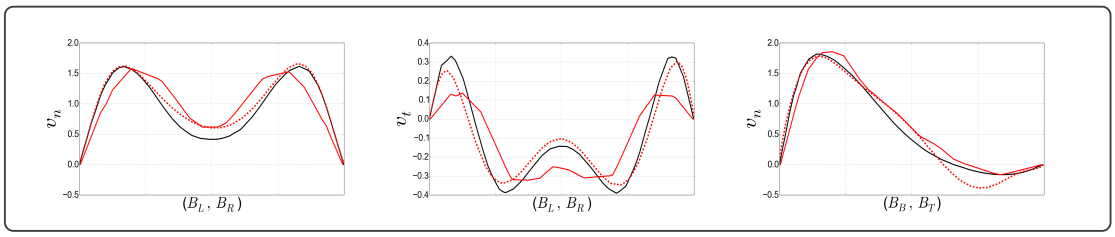

(b) Transversal order $\mathsf{p} = 8$.

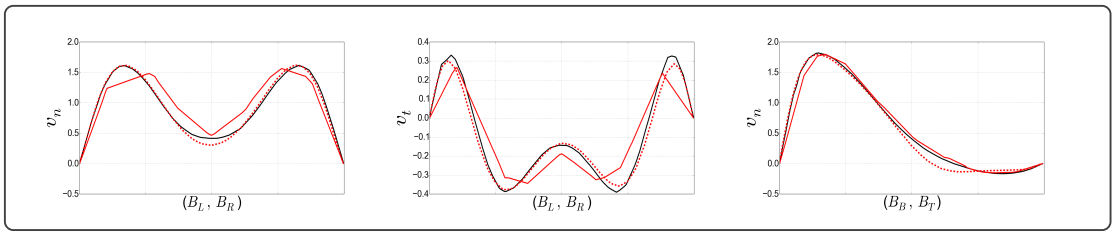

(c) Transversal order $\mathsf{p} = 10$.

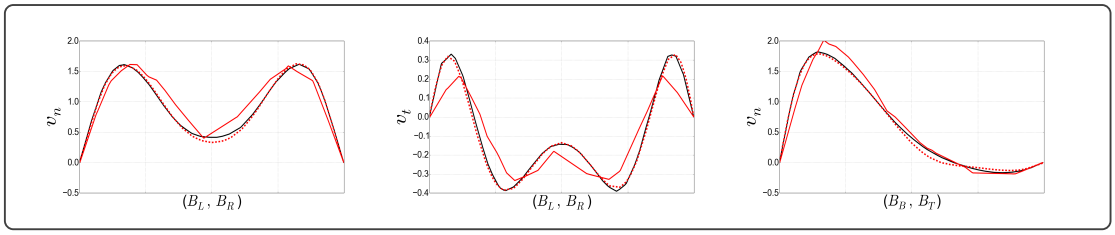

(d) Transversal order $\mathsf{p} = 12$.

Figure 4.48: Comparison of normal and tangential velocity components at region B of the tortuous pipe for the case Turn 4 and Re = 500. Solutions are compared for different approximation orders of the TEPEM and for two (fine and coarse) FEM meshes.

4.5.3 Synthetic carotid artery

The fluid flow through a synthetic carotid artery is addressed in this example. The geometrical domain is based on the phantom carotid structure proposed in [Bharadvaj et al. 1982b,a] and is outlined in Figure 4.49. In that figure, the unit are given in centimeters.

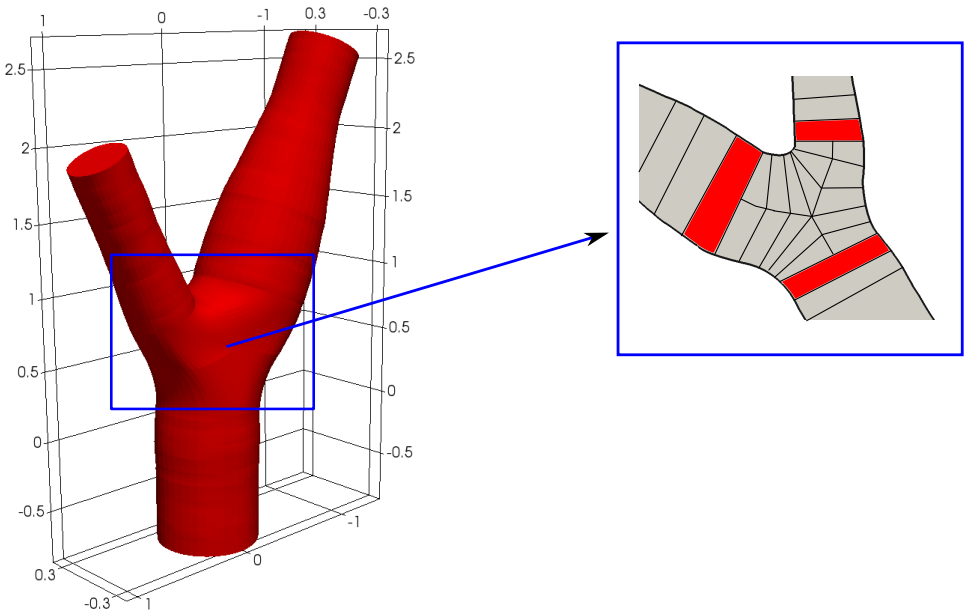

Figure 4.49: Geometry setting for the synthetic carotid artery. Over the right, transversal view of the mesh discretization proposed near the bifurcated region. Transition elements are highlighted in red.

Three different Reynolds numbers are selected for this example, $Re \in \{50, 150, 250\}$. The flow is driven by the imposition of a flow rate at the inlet (bottom axial boundary) chosen to ensure the desired Reynolds number. At outlets, homogeneous Neumann boundary conditions are considered and no-slip conditions for the velocity over the lateral surface is prescribed. As initial condition, zero velocity is considered for the case Re = 50. The case Re = 150 is started with the Re = 50 solution as initial guess and so on.

A sufficiently fine FEM mesh is considered as the reference solution for comparison purposes. This mesh, is composed by a total of 12 276 715 tetrahedral elements. For the TEPEM, the geometry is divided into 95 elements: 72 pipe-elements to discretize the three tubular regions, 20 in the interior of the junction and 3 transition elements to connect the bifurcation and the branches. A comparison between the degrees of freedom employed in each strategy is shown in Table 4.13. Notice that for the larger transversal order considered here ($\mathsf{p} = 12$) the reduction in the problem size is over 98%.

Concerning to the reduction in the computational time, a comparison between the wall-clock time simulation time (in minutes) employed by both methodologies (TEPEM and FEM) is presented in Table 4.14. Even for the largest transversal order considered for the TEPEM, the simulation time is five times smaller when compared with the time employed by the FEM strategy. This reduction is even higher when considering that the FEM solution was achieved with a total of 100 processors (NP = 100) while for the TEPEM it was employed only 10 processors.

Table 4.13: Comparison between degrees of freedom and number of elements employed in the FEM and the TEPEM approaches. Also the relative reduction in the degrees of freedom is presented.

	FEM	TEPEM				
		$\mathsf{p}=4$	$\mathsf{p}=6$	$\mathsf{p}=8$	$\mathsf{p}=10$	$\mathsf{p}=12$
Elements	12 276 715			95		
DoFs	7 880 372	15 121	29 922	49 729	74 542	104 361
DoFs reduction		99.80%	99.62%	99.36%	99.05%	98.67%

Besides the enormous reduction in the computational effort, both in terms of time and resources, the velocity and pressure fields provided by the TEPEM are in good agreement with the reference FEM solution. This can be appreciated in Table 4.15 where it is presented the relative error for each Reynolds case. Note that, for velocity and pressure, the TEPEM approach provides solutions with a relative error in the order of 2% for the case Re = 250 and $\mathsf{p}=4$.

Table 4.14: Computational time (in minutes) to solve the steady state problem, for different Reynolds numbers, with the FEM and TEPEM approaches.

		FEM	TEPEM				
			$\mathsf{p}=4$	$\mathsf{p}=6$	$\mathsf{p}=8$	$\mathsf{p}=10$	$\mathsf{p}=12$
Number of processors (NP)		100			10		
Wall-clock time (min)	Re = 50	58.12	0.06	0.5	2.2	6.2	10.7
	Re = 150	117.24	0.1	0.91	3.96	11.74	20.79
	Re = 250	105.4	0.12	1.04	3.95	13.5	20.7

Remarkably, when inspecting the solutions delivered by the TEPEM, the flow structure is rather close to the FEM solution, being able to predict with high degree of fidelity the velocity profiles and pressure even near the bifurcated region where the dynamics is much more complex when compared with non-branched tubular regions.

For the case Re = 250, in Figures 4.50-4.51 we present a comparison between velocity and pressure fields provided by the FEM and TEPEM strategies for different transversal enrichment orders. The precision in the global velocity behavior as well as in the pressure near the bifurcated region is worth to be highlighted. Furthermore, and in the same figure, a global view of the wall shear stress provided by the FEM and TEPEM approaches stresses the potentialities of the proposed approach once that the estimation of this field is fundamental in hemodynamics applications.

A more detailed comparison in the velocity field reveals the capabilities of the TEPEM to predict secondary flows in the carotid sinus, as can be seen in Figure 4.52. As for the wall shear stress (WSS) field, a detailed comparison is performed by unfolding the surface of the three tubular domains, as shown in Figure 4.53, panel (a). Moreover, a comparison between the average WSS at each cross-section is presented in Figure 4.53, panel (b).

Table 4.15: Relative error in the velocity field, in the velocity gradient and in the pressure field between the TEPEM solution and the reference FEM solution for the synthetic carotid artery bifurcation and Reynolds number Re = 50 (top table), Re = 150 (middle table) and Re = 250 (bottom table). For each Reynolds number, also the reference values for FEM solutions are reported.

	TEPEM					FEM	
	$\mathsf{p}=4$	$\mathsf{p}=6$	$\mathsf{p}=8$	$\mathsf{p}=10$	$\mathsf{p}=12$		
$\|\mathbf{u}_\mathrm{F}-\mathbf{u}_\mathrm{T}\|$	$7.16\cdot10^{-3}$	$6.23\cdot10^{-3}$	$6.14\cdot10^{-3}$	$6.12\cdot10^{-3}$	$6.11\cdot10^{-3}$	$\|\mathbf{u}_\mathrm{F}\|_{L^2}$	3.9410
$\|\mathbf{u}_\mathrm{F}-\mathbf{u}_\mathrm{T}\|$	$3.75\cdot10^{-2}$	$3.62\cdot10^{-2}$	$3.57\cdot10^{-2}$	$3.57\cdot10^{-2}$	$3.56\cdot10^{-2}$	$\|\nabla\mathbf{u}_\mathrm{F}\|_{L^2}$	48.5043
$\|p_\mathrm{F}-p_\mathrm{T}\|$	$1.16\cdot10^{-3}$	$1.13\cdot10^{-3}$	$9.96\cdot10^{-4}$	$5.61\cdot10^{-4}$	$4.81\cdot10^{-4}$	$\|p_\mathrm{F}\|_{L^2}$	42.5005

	TEPEM					FEM	
	$\mathsf{p}=4$	$\mathsf{p}=6$	$\mathsf{p}=8$	$\mathsf{p}=10$	$\mathsf{p}=12$		
$\|\mathbf{u}_\mathrm{F}-\mathbf{u}_\mathrm{T}\|$	$0.14\cdot10^{-2}$	$0.12\cdot10^{-2}$	$8.07\cdot10^{-3}$	$7.03\cdot10^{-3}$	$4.47\cdot10^{-3}$	$\|\mathbf{u}_\mathrm{F}\|_{L^2}$	11.8324
$\|\mathbf{u}_\mathrm{F}-\mathbf{u}_\mathrm{T}\|$	$0.48\cdot10^{-2}$	$0.43\cdot10^{-2}$	$0.36\cdot10^{-2}$	$0.34\cdot10^{-2}$	$0.31\cdot10^{-2}$	$\|\nabla\mathbf{u}_\mathrm{F}\|_{L^2}$	162.1823
$\|p_\mathrm{F}-p_\mathrm{T}\|$	$2.25\cdot10^{-3}$	$1.85\cdot10^{-3}$	$1.56\cdot10^{-3}$	$1.34\cdot10^{-3}$	$1.10\cdot10^{-3}$	$\|p_\mathrm{F}\|_{L^2}$	185.4991

	TEPEM					FEM	
	$\mathsf{p}=4$	$\mathsf{p}=6$	$\mathsf{p}=8$	$\mathsf{p}=10$	$\mathsf{p}=12$		
$\|\mathbf{u}_\mathrm{F}-\mathbf{u}_\mathrm{T}\|$	$0.23\cdot10^{-2}$	$0.22\cdot10^{-2}$	$0.10\cdot10^{-2}$	$8.36\cdot10^{-3}$	$5.50\cdot10^{-3}$	$\|\mathbf{u}_\mathrm{F}\|_{L^2}$	19.8871
$\|\mathbf{u}_\mathrm{F}-\mathbf{u}_\mathrm{T}\|$	$0.69\cdot10^{-2}$	$0.65\cdot10^{-2}$	$0.41\cdot10^{-2}$	$0.37\cdot10^{-2}$	$0.33\cdot10^{-2}$	$\|\nabla\mathbf{u}_\mathrm{F}\|_{L^2}$	296.1083
$\|p_\mathrm{F}-p_\mathrm{T}\|$	$0.21\cdot10^{-2}$	$3.93\cdot10^{-3}$	$3.47\cdot10^{-3}$	$3.05\cdot10^{-3}$	$2.17\cdot10^{-3}$	$\|p_\mathrm{F}\|_{L^2}$	390.2437

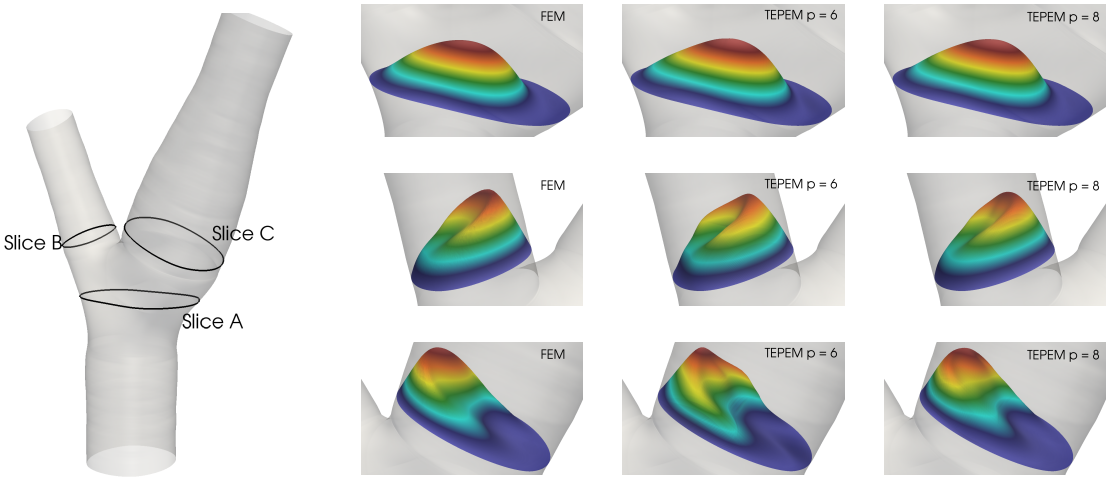

Figure 4.50: Comparison of velocity profiles between the FEM reference solution and the TEPEM for $\mathsf{p}=4$ and $\mathsf{p}=6$ in three transversal sections.

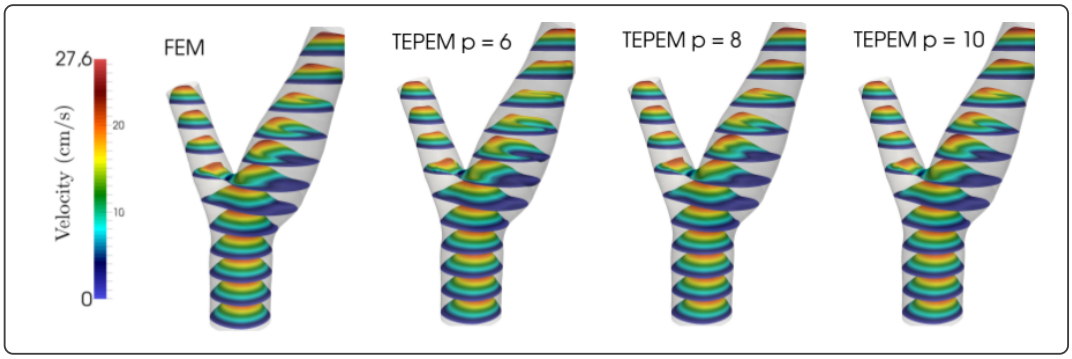

(a) Velocity profiles along the z-axis.

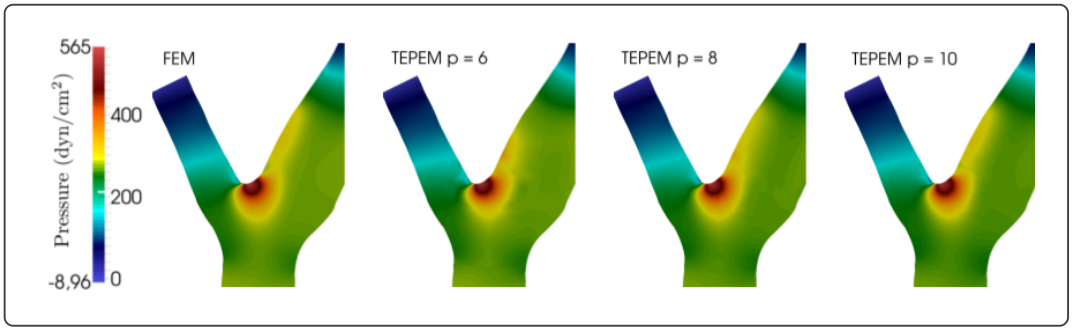

(b) Pressure field in the bifurcated region.

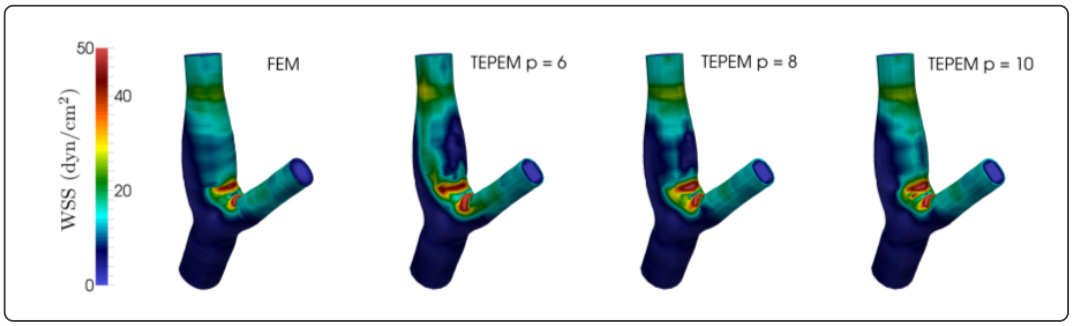

(c) Wall shear distribution.

Figure 4.51: Comparison of velocity, pressure and wall shear stress fields between the FEM reference solution and the TEPEM for different transversal enrichment orders.

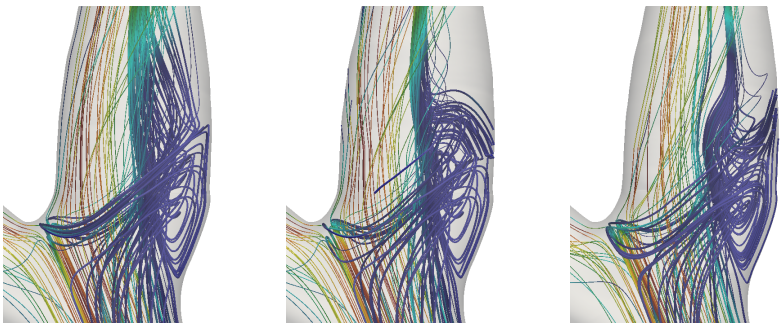

Figure 4.52: Detail of recirculation region in the carotid sinus. Comparison between FEM and TEPEM solutions for different transversal enrichment orders.

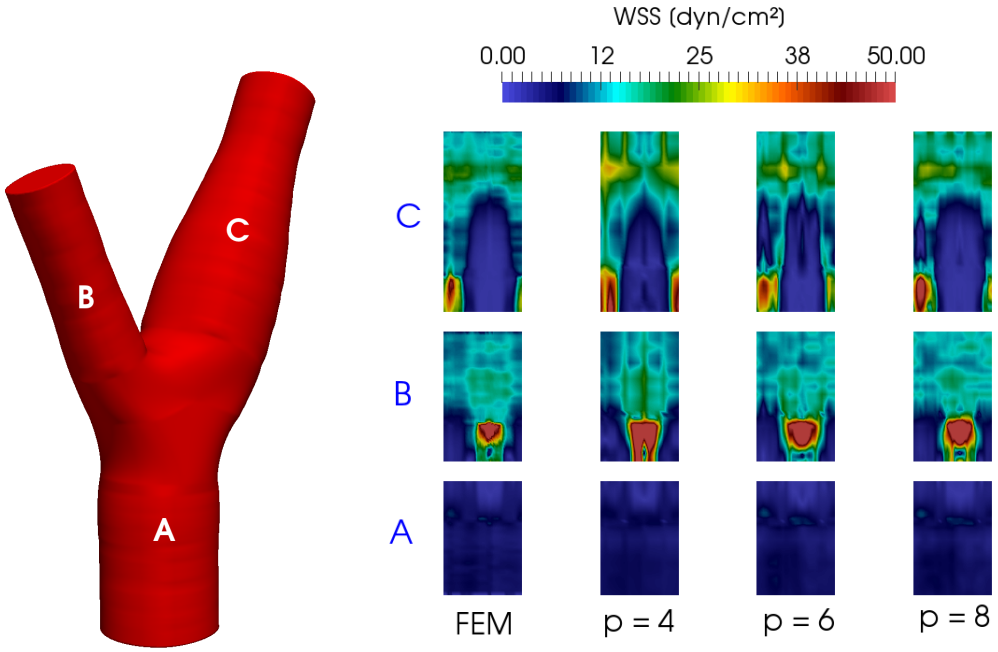

(a) Unfolded view of the WSS along the longitudinal axis

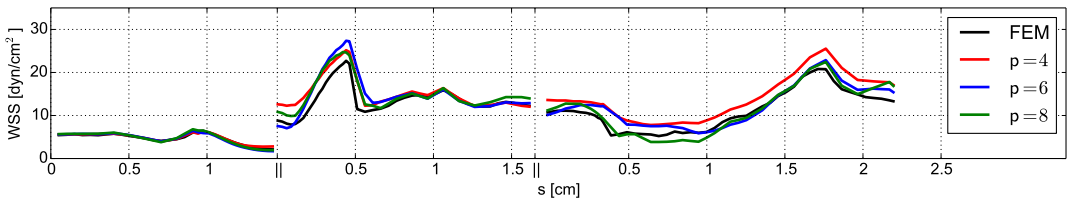

(b) Cross-sectional average of WSS over the lateral wall

Figure 4.53: Comparison of the wall shear stress field between TEPEM and the reference FEM solution for different polynomial transversal orders.

4.5.4 Highly curved pipe

Let us consider the domain Ω as being the curved circular pipe defined by the centerline $\mathcal{C} = \mathcal{C}_1 \cup \mathcal{C}_2 \cup \mathcal{C}_3$ where

$$\begin{aligned} \mathcal{C}_1 &= \{\mathbf{x} \in \mathbb{R}^3 : x = 0, y = 0, 5 \leq z \leq 6\} \\ \mathcal{C}_2 &= \{\mathbf{x} \in \mathbb{R}^3 : x = 0, y \geq 6, (y - 0.4)^2 + (z - 6)^2 = 0.4^2\} \\ \mathcal{C}_3 &= \{\mathbf{x} \in \mathbb{R}^3 : x = 0, y = 0.8, 0 \leq z \leq 6\} \end{aligned} \tag{4.44}$$

The radius of the pipe is constant and $r = 0.2$ cm. In this region, detailed in Figure 4.54, a transient flow is considered. This flow is driven by the imposition at the inlet (transversal section corresponding to the point $\mathbf{x}_0$, a parabolic velocity profile with maximum value $u_0(t) = u^0(1 + \sin(2\pi t))$, homogeneous Neumann boundary condition over the outlet boundary and no-slip conditions over the lateral wall. The problem is fully set by considering as initial condition the solution of the steady state flow problem defined by imposing a velocity profile with maximum velocity u^0 (in cm/s^2) at the inlet and the same conditions for the transient case over lateral and outlet boundaries.

The goal of this problem is twofold. First, for the computation of the initial condition, we study the scalability of the TEPEM with respect to the transversal order. This is performed by fixing a pipe discretization of Ω and computing the solution of the steady state problem for different transversal orders and number of processors (NP). Second, we study the convergence of approximate fields within the TEPEM approach in the transient regime.

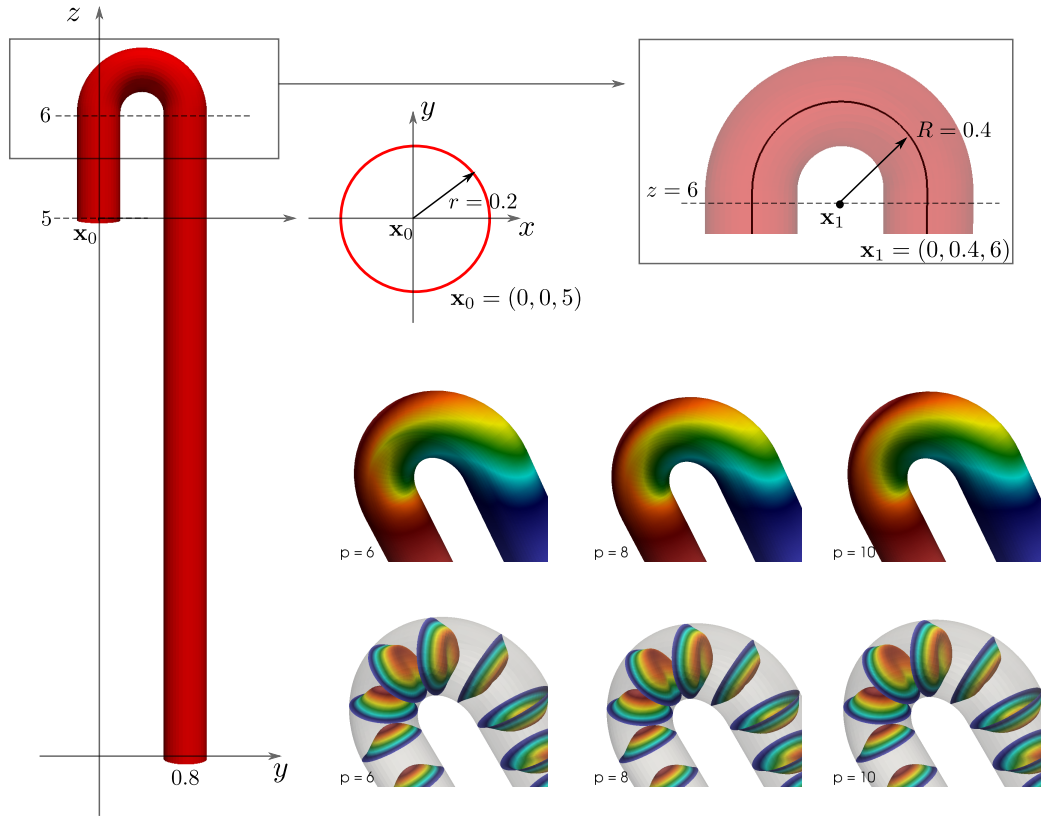

Figure 4.54: Geometrical description of the curved domain and comparison of velocity and pressure approximations for the steady state problem with different transversal orders.

Let us focus first in the steady state problem. Considering $\rho = 1$ g/cm^{-3} and $\mu = 1 \cdot 10^{-3}$ P, the Reynolds number of this problem is Re $= 200$. For the discretization of the domain, we consider an uniform pipe-mesh with axial size $h = 0.1$ cm (composed by approximately 100 pipe elements) and the velocity and pressure fields are approximated considering a transversal order of $\mathsf{p} \in \{4, 6, 8, 10, 12\}$.

For each transversal order, the solution of the flow problem is initially computed by employing one single processor (NP $= 1$) and then duplicating this number until reaching a total of NP $= 32$. The time needed to perform a single Picard (non-linear) iteration, for each combination of p and NP, are presented in Table 4.16, together with the total number of degrees of freedom as a function of p. Moreover, and to complement the data presented in this table, in Figure 4.55 it is detailed both the computational time employed in the assembling process and the time to solve the linear system as a function of the number of processors. As it can be seen, the speedup ratio is almost the ideal one.

Table 4.16: Computational time (in seconds) to perform a single Picard iteration in the TEPEM approach, for different transversal orders and number of processors.

	DoFs	Number of processors					
		1	2	4	8	16	32
$\mathsf{p} = 4$	15 984	3.8	3.9	1.3	0.5	0.2	0.2
$\mathsf{p} = 6$	31 163	26.7	16.3	8.3	3.4	1.7	0.9
$\mathsf{p} = 8$	51 368	141.5	95.7	48.2	21.0	11.1	4.9
$\mathsf{p} = 10$	76 599	497.0	290.0	146.2	66.9	35.5	15.5
$\mathsf{p} = 12$	106 856	1244.8	640.1	357.4	170.4	90.3	39.4

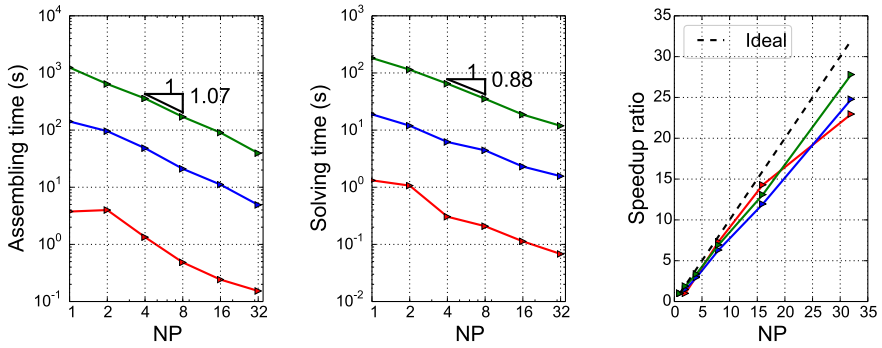

Figure 4.55: Reduction in the computational time taken to perform a single Picard iteration in terms of the number of processors for the TEPEM approach and transversal order $\mathsf{p} = 4$ (red curve), $\mathsf{p} = 8$ (blue curve) and $\mathsf{p} = 12$ (green curve). Also the speedup ratio is presented for these transversal orders.

Once the initial condition has been computed, for each value of p, the transient fluid flow problem is addressed employing a total of 16 processors in each case (NP $= 16$). The transient regime is defined by a mean Reynolds Re $= 200$ and a Womersley number $\kappa \approx 12$. A comparison between velocity profiles for each transversal order is outlined in Figures 4.56-4.57.

In both figures, the convergence of the TEPEM approximation with respect to the transversal order is evident, and it is important to highlight the excellent results when it is employed $\mathsf{p} = 6$. For the case $\mathsf{p} = 4$, the lowest enrichment induces errors that undermine the correct approximation of the velocity in the curved region, but provide very precise results in the tubular inlet/outlet regions as can be seen in Figure 4.57, as expected because the flow becomes developed.

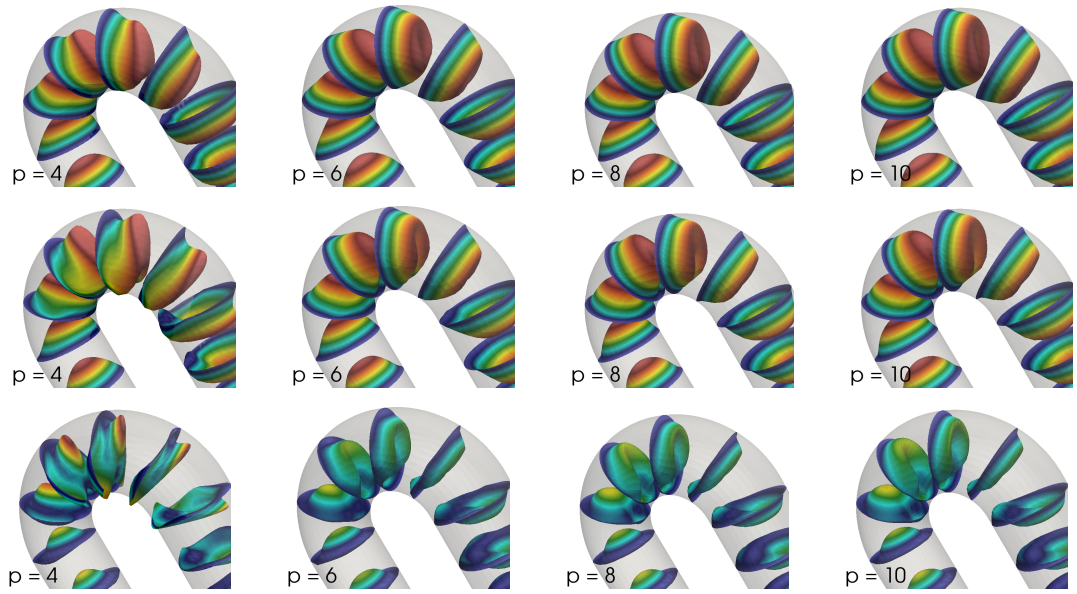

Figure 4.56: Detail of velocity profiles in the curved region. For different orders in the transversal enrichment, the profiles correspond to the time instants $t = 0.2s$ (top row), $t = 0.4s$ (middle row) and $t = 0.6s$ (bottom row).

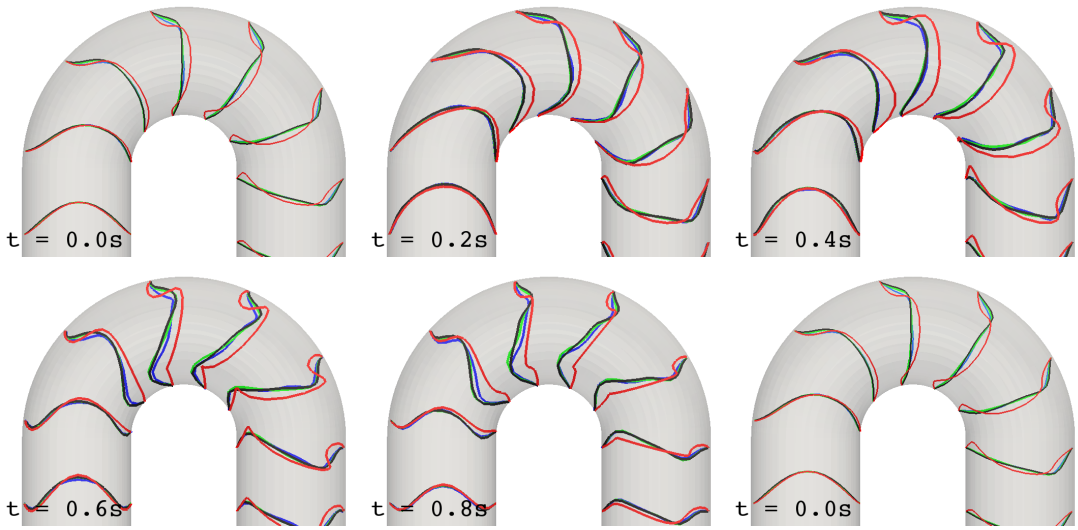

Figure 4.57: Comparison of velocity profiles in two regions of the curved pipe. At each panel it is compared the profiles with $\mathsf{p} = 4$ (red curve), $\mathsf{p} = 6$ (blue curve), $\mathsf{p} = 8$ (green curve) and $\mathsf{p} = 10$ (black curve).

The convergence in the wall shear stress (WSS), as a function of the transversal order, is also observed. For a potential use in hemodynamics, the precise identification of regions where the WSS reaches high/low values is more important than computing the exact value. In Figure 4.58 a comparison between the WSS in the curved region is shown, for different transversal orders and selected time instants, and the capabilities to define the regions featuring high/low WSS is clearly demonstrated even for the lowest enrichment order ($\mathsf{p} = 4$).

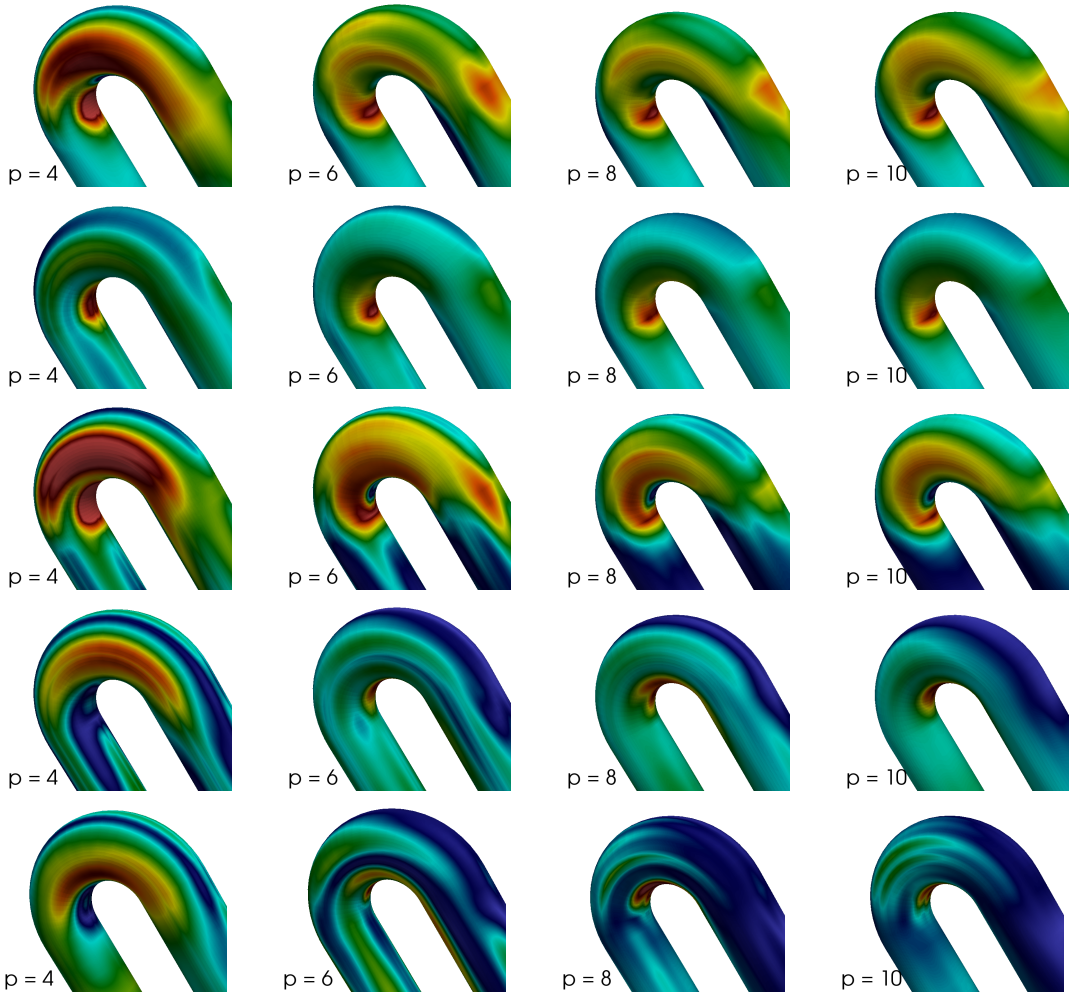

Figure 4.58: Detail of wall shear stress (WSS) in the curved region and for different transversal orders. From top to bottom, the rows correspond to the time instants $t = 0.2s$, $t = 0.4s$, $t = 0.6s$, $t = 0.8s$ and $t = 1s$.

4.6 Further remarks

In this chapter, the TEPEM was successfully employed in the incompressible fluid flow modeling, demonstrating predictive capabilities comparable to those provided by standard FEM approaches but employing a fraction of time, which is fundamental when the ultimate goal of the proposed approach is its application in real problems in computational hemodynamics.

Specifically, in this chapter it was addressed the discretization of the Navier-Stokes equations employing the TEPEM for the approximation of the physical fields, velocity and pressure. Important discrete aspects related to this discretization, like the structure of the discrete system and the suitable choice for finite-dimensional spaces for velocity/pressure, were also addressed. Concerning the last aspect, a combination of discrete spaces for velocity and pressure in the TEPEM approach was proposed and, even without an ultimate theoretical proof of the stability of this pair, numerical evidence in the direction of the inf-sup stability was provided. The numerical test known as *the inf-sup test*, together with the absence of any spurious behavior in the extensive numerical assessment addressed along this chapter strongly suggests the suitability of the proposed pair. Regarding the structure of the discrete system related to the discretization of the physical problem with the TEPEM, the proximity between the pipe-mesh structure and a one-dimensional partition is reflected in the similarity of the discrete structures obtained in both cases. For the TEPEM, the linear system to be solved at each Picard iteration is a block band matrix, which features an interesting sparsity pattern able to be exploited in the future to make the algebraic solution process even more efficient.

The numerical assessment of the TEPEM in the discretization of the NS equations was addressed in both the two and three dimensional cases, aiming of demonstrating the capability of the TEPEM as an efficient tool able to provide relevant hemodynamic information, with high fidelity and at a fraction of the computational cost if compared with standard FEM techniques. Classical benchmarks, steady-state and transient flow regimes were addressed. An extensive comparison between both techniques, FEM and TEPEM, was performed in terms of number of degrees of freedom, computational time and accuracy. For the 3D case, also a comparison between the approximation of the wall shear stress for TEPEM and FEM, in a synthetic carotid artery, was addressed and the results uphold the excellent capabilities of the TEPEM to provide accurate information of this field, of utmost importance in the hemodynamics realm.

It is also worthwhile to highlight that, in all the numerical cases reported throughout this chapter, the reduction in the number of degrees of freedom performed by the TEPEM (compared with that employed to obtain a reference FEM solution) was superior to the 90% even for the largest transversal order considered in the TEPEM to approximate the transversal dynamics of the velocity field ($\mathsf{p} = 12$). This remarkable reduction in the problem size brings a terrific insight about the gains that the use of the TEPEM in real large-scale problems, in which the colossal amount of information demarcate a threshold of application for standard FEM approaches, could offer.

Chapter 5

TEPEM in computational hemodynamics

The core of this work relies into the search for new numerical alternatives able to perform efficient numerical simulations in the hemodynamic realm. In this chapter, we tackle that problem by employing the Transversally Enriched Pipe Element Method (TEPEM) as an efficient numerical strategy capable to provide high fidelity insight about fluid related quantities and reducing considerably the computational effort when compared with current approaches.

The capabilities of the proposed strategy were stated in former Chapters and extensively explored through several numerical examples in two- and three-dimensional settings, for scalar problems (in Chapter 3) and also in the fluid-flow modeling (in Chapter 4). In the latter, the TEPEM proved to be capable to positively deal with the trade-off between accuracy and computational cost, providing results closer to the obtained with 3D FEM simulations at a fraction of time.

The focus of this Chapter is to extend these results into patient-specific geometries and to compare the TEPEM predictions against FEM results obtained in meshes (and with costs) similar to those typically employed in the academic research and medical practice. Regarding the blood flow modeling, the assumption of the blood flow as a Newtonian model, neglecting the shear thinning and viscoelastic effects, is suitable in large vessels or when we are not interested in the finer microscopic details of the flow, and so we assume that the Navier-Stokes equations to model the blood flow are a good model, which is enough for our purposes. Moreover, according to [Formaggia et al. 2010], the flow in large and medium sized vessels (except in the aorta artery) is characterized by Reynolds numbers varying in the range $100 \leq Re \leq 800$ while the Womersley number is in the range $1 \leq \kappa \leq 5$. The results obtained in Chapter 4 covered these dimensional features, and so we expect to have, as in that chapter, high fidelity solutions with the TEPEM.

Two major difficulties are to be mandatorily tackled when aiming the application of the proposed methodology to hemodynamics simulations in patient-specific regions: (i) The introduction of a suitable algorithmic procedure to perform a (semi-)automatic discretization of the vascular region of interest into a pipe-type discrete structure and (ii) A correct imposition of boundary conditions appropriate for the hemodynamics context. Both issues are addressed in this Chapter and the geometrical accuracy as well as the advantages of the TEPEM approach in patient-specific hemodynamics simulations are demonstrated through several numerical examples. For all the CFD simulations, the INCT-MACC cluster is employed.

5.1 Geometric modeling pipeline

The first major issue into the application of the proposed methodology in patient-specific geometries is related to the mesh discretization, which is based on pipe-elements. This discretization, for synthetic domains as the addressed in the last chapter, was performed considering an *ad-hoc* structure which seems unpractical for arbitrary vascular regions as the ones we are interested in. In this Section it is explored a computational framework to perform a pipe-like discretization in a semi-automatic way, covering from the image segmentation step to the final discrete structure based on pipe elements.

Roughly speaking, the proposed pipeline to meet this goal in general arterial domains combines:

i) A certain (but arbitrary) processing pipeline to go from the image segmentation to a finite element surface mesh. This process is also standard for FEM blood flow simulations, because the volume (tetrahedral) mesh is constructed having as starting point the surface triangular mesh.

ii) A centerline extraction process plus the identification of curves that define the cross-sectional luminal areas. The vascular regions are then exclusively described through the centerline/cross-section information removing the subsequent need for the surface triangulation.

iii) The approximation of transversal sections and bifurcation regions. This procedure defines each pipe- and transition-element which composes the discretization.

While the first step is standard in the generation of tetrahedral meshes for hemodynamics simulations, the last two are specific requirements posed by the TEPEM, and supersede the time-consuming step of volume mesh generation (in the FEM approach).

5.1.1 Image segmentation

The image segmentation and mesh processing pipeline employed are illustrated in Figure 5.1, which is specific for extracting arterial structures from coronary computed tomography angiography (CCTA). This pipeline follows the standard steps to perform volume mesh for FEM simulations:

a) After a manual selection of boundaries of the arterial region, a colliding front method is employed to obtain an initial segmentation of the artery. Then, a level set algorithm is initialized with the colliding front output to obtain the final segmentation. Both, colliding front and level set methods are detailed in [Antiga et al. 2008].

b) A raw surface triangulation is constructed using the marching cubes method [Lorensen and Cline 1987], which produces a closed surface.

c) Techniques described in [Antiga et al. 2003] are employed to compute a centerline from the raw triangulation and the inlet/outlet flat boundaries are removed to yield an open tubular surface. This open surface is smoothed and re-meshed to improve quality and achieve quasi-homogeneous triangle size.

d) A tetrahedralization of the refined surface is addressed to produce finite element volume meshes to perform standard finite element simulations.

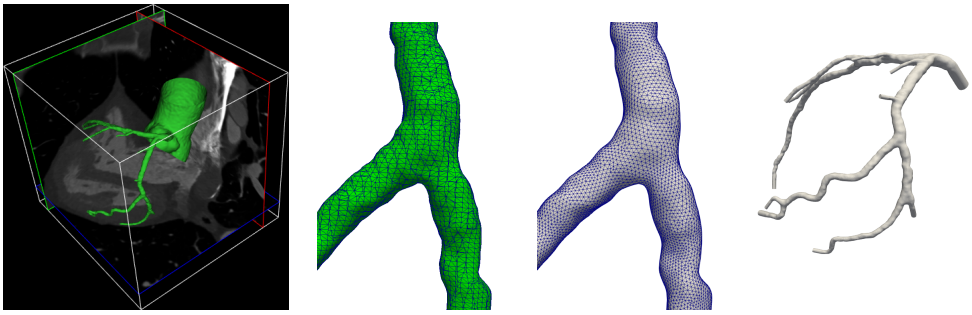

(a) (b) (c) (d)

Figure 5.1: Standard work-flow for arterial segmentation and tetrahedral mesh generation for FEM simulations. (a) input CCTA image; (b) raw triangulation; (c) improved surface mesh; (d) full 3D FEM mesh.

The acquisition protocols, the image processing methodology as well the mesh processing pipeline are described in detail in [Bulant et al. 2017a,b] and make intensive used of the Vascular Modeling ToolKit [VMTK 2015]. It is important to stress that panels (a)-(c) in Figure 5.1 are mandatory for the TEPEM pipeline while the panel (d), the most time-consuming step, is only performed in the context of FEM.

The TEPEM pipeline is completed by replacing the step in panel (d) in Figure 5.1 by the generation of the transversal sections along the arterial region centerline. The steps in the cross-section segmentation process, shown in Figure 5.2, are the following:

i) Arterial centerlines are computed from the lumem surface following [Antiga et al. 2003], which are curves in 3D space represented by polylines defined by approximately equidistant points (typically it is used $\Delta x = 0.05$cm).

ii) Transversal sections of the surface are extracted at each centerline point. A total of N_{1D} nodes defining the centerline yields a set of N_{1D} connected nodes representing the transversal section contour as a closed polyline $\mathcal{P}_i$.

This last step introduces the presence of *double sections* at bifurcation points (as seen in light red in panel (c) in Figure 5.2) which cannot be approximated in the same way that performed for the transversal sections in tubular regions. The approximation of the transversal sections in bifurcation areas is addressed in the next section.

Note that the workflow steps concerning the TEPEM (steps (a)-(d) in Figure 5.2) are independent of the imaging modality. After reaching a surface triangulation of the region of interest, the cross-section extraction turns to be a generic algorithm, allowing its application in phantom geometries also in which the procedure relies on the centerlines dataset and on the vessel radius at each centerline point.

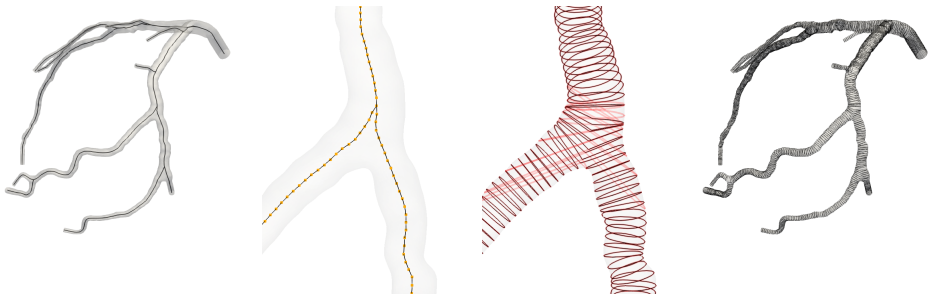

(a) (b) (c) (d)

Figure 5.2: Workflow for the extraction of transversal sections in the TEPEM. (a) Arterial centerline; (b) zoom of centerline at a bifurcation; (c) cross-sectional polylines; (d) transversal sections for the complete vascular region.

5.1.2 Bifurcation reconstruction algorithm

The presence of *double sections* in bifurcation regions prevents the direct approximation of these junctions with the previous strategy, and introduces the need for a reconstruction step before defining the pipe-discretization. This reconstruction step looks for a better description of the junction region which is poorly described by the cross-section cuts because, in this region, the pipe-like structure assumption is broken. Each bifurcation is reconstructed uniquely based on the information provided by the three closest non-intersecting cross-sections coming from the three tubular domains which converge to the bifurcation, and which are constructed as described in the previous section.

Let $\mathcal{C}_i$, $i \in \{A, B, C\}$, denote the three cross-sections reaching the bifurcation domain. Each cross-section features a planar boundary curve with geometric center $\mathbf{p}_i$ and normal $\mathbf{n}_i$. Hence, denoting by $\mathbf{p}_0$ the centroid of $\{\mathbf{p}_A, \mathbf{p}_B, \mathbf{p}_C\}$, we define the following planar regions

$$\Pi_{mn} = \{\mathbf{x} \in \mathbb{R}^3 : (\mathbf{x} - \mathbf{p}_0) \cdot \mathbf{n}_{mn} = 0\} \qquad m, n \in \{A, B, C\}, \tag{5.1}$$

with

$$\begin{aligned} \mathbf{n}_0 &= \frac{(\mathbf{p}_B - \mathbf{p}_A) \times (\mathbf{p}_C - \mathbf{p}_A)}{\|(\mathbf{p}_B - \mathbf{p}_A) \times (\mathbf{p}_C - \mathbf{p}_A)\|}, & \mathbf{n}_{AB} &= \frac{(\mathbf{n}_B - \mathbf{n}_A) \times \mathbf{n}_0}{\|(\mathbf{n}_B - \mathbf{n}_A) \times \mathbf{n}_0\|}, \\ \mathbf{n}_{AC} &= \frac{(\mathbf{n}_C - \mathbf{n}_A) \times \mathbf{n}_0}{\|(\mathbf{n}_C - \mathbf{n}_A) \times \mathbf{n}_0\|}, & \mathbf{n}_{BC} &= \frac{(\mathbf{n}_B + \mathbf{n}_C) \times \mathbf{n}_0}{\|(\mathbf{n}_B + \mathbf{n}_C) \times \mathbf{n}_0\|}. \end{aligned} \tag{5.2}$$

These planes, which share a common line defined by the point $\mathbf{p}_0$ and the unit normal $\mathbf{n}_0$, divide the bifurcation domain into three disjoint regions which are connected with the converging tubular domains. Geometrical entities introduced here, as normal vectors and planar sections, are outlined in Figure 5.3 (see panels (a)-(b)).

The inner axial boundary inside the junction region is defined by the intersection of the previously defined loci Π_{mn} $(m, n \in \{A, B, C\})$ and the tubular connection from each pipe region to the other two, as illustrated in panels (c)-(e) in Figure 5.3. Those intersected sections are directly defined by the following min-max problem: consider the points $\mathbf{a}$ and $\mathbf{c}$ defined over the curves $\mathcal{C}_A$, $\mathcal{C}_C$ (see Figure 5.3, panel (d)) and consider

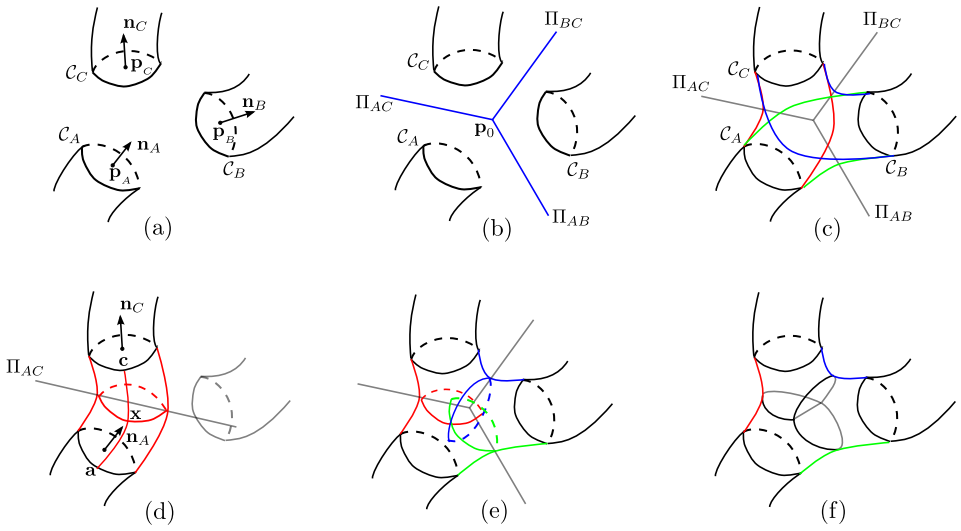

Figure 5.3: Steps in the geometric reconstruction of a bifurcation. (a) Tubular domains converging to the bifurcation. (b) Definition of centroid and planes. (c) Pair-wise smooth extension. (d)-(e) Bifurcation cross-sections are result of intersection of planes with the extensions created to join the non-bifurcated sections. (f) Final bifurcation cross-section is obtained and branches extensions are delimited.

the locus Π_{AC}, the point $\mathbf{x}$ in the intersected section and connecting $\mathbf{a}$ and $\mathbf{c}$ is solution of the problem

$$(\mathbf{x}, \alpha^*, \beta^*, \lambda_0, \lambda_1) = \arg \max_{\gamma_0,\gamma_1 \in \mathbb{R}} \min_{\mathbf{w}\in\mathbb{R}^3} \min_{\alpha,\beta\in\mathbb{R}} \mathcal{F}(\mathbf{w}, \alpha, \beta, \gamma_0, \gamma_1), \tag{5.3}$$

with the following functional

$$\begin{aligned}\mathcal{F}(\mathbf{w}, \alpha, \beta, \gamma_0, \gamma_1) = \int_{-1}^{1} (|f'(\mathbf{w}, \alpha, t)|^2 + |g'(\mathbf{w}, \beta, t)|^2)\, dt \\ + \gamma_0 |f'(\mathbf{w}, \alpha, 1) - g'(\mathbf{w}, \beta, -1)| + \gamma_1 |(\mathbf{w} - \mathbf{p}_0) \cdot \mathbf{n}_{AC}|,\end{aligned} \tag{5.4}$$

where, for $t \in [-1, 1]$, and $\{Q_1, Q_2, Q_3\}$ being the function basis for $\mathbb{P}_2$, we define

$$\begin{aligned} f(\mathbf{w}, \alpha, t) &= \mathbf{a}Q_1(t) + \frac{1}{2}\left(\alpha^2 \mathbf{n}_A + \frac{1}{2}\mathbf{w} + \frac{3}{2}\mathbf{a}\right) Q_2(t) + \mathbf{w}Q_3(t), \\ g(\mathbf{w}, \beta, t) &= \mathbf{w}Q_1(t) + \frac{1}{2}\left(\frac{1}{2}\mathbf{w} + \frac{3}{2}\mathbf{c} - \beta^2 \mathbf{n}_C\right) Q_2(t) + \mathbf{c}Q_3(t), \end{aligned} \tag{5.5}$$

with $\mathbf{n}_A$ and $\mathbf{n}_C$ the normal unit vectors to the curves $\mathcal{C}_A$ and $\mathcal{C}_C$, respectively. In equation (5.4), the derivative $(\cdot)'$ is with respect to variable t.

In a few words, the min-max problem guarantees that each point $\mathbf{x}$ in the intersected section provides the minimum piecewise quadratic path between the two tubular regions while prescribing a certain axial regularity. The same process is employed to determine the other two intersected sections. The final step consists in finding the intersection between the three planar sections, provided by the min-max problem, to characterize the boundary (internal to the bifurcation) which demarcates the branches extensions. These extensions ultimately compose the bifurcation, as seen in Figure 5.3 panel (f).

Notice also that this reconstruction algorithm provides a continuous description of the lateral surface of the junction, based only on the three closest non-intersecting cross-sections and on an inner boundary (in black in panel (f) in Figure 5.3). The discretization of this region, into pipe-elements, is addressed in the next section.

5.1.3 Cross-section approximation

The segmentation process provides a representation of the vascular region in terms of N_{1D} points, defining the centerline, and a closed polyline $\mathcal{P}_i$, for each node in the centerline, describing the contour of each transversal section. These cross-sections are the basis for the pipe-discretization of tubular regions in the vascular domain. For the discretization of the junctions, the reconstruction step described before allows a pipe meshing with the introduction of transition elements to deal with the complex topological structure of these regions.

Approximation in tubular regions. Let us focus first in the tubular regions in the vascular geometry. According to the geometrical structure of the TEPEM (introduced in Chapter 2), each of these closed polylines is approximated as an element of the space $\mathbb{S} = \{\mathcal{S}_i, i = 1, \ldots, 12\}$ of cubic Serendipity functions defined in $[-1, 1]^2$. This is, the closed curve $\mathcal{P}_i$ $(i = 1, \ldots, N_{1D})$ is approximated through

$$\chi_{\mathbf{x}}(t) = \sum_{n=1}^{12} \mathbf{x}_n \mathcal{S}_n(\boldsymbol{\xi}(t)), \qquad \boldsymbol{\xi}(t) = \begin{cases} (8t-1, -1) & 0 \leq t < 1/4 \\ (1, 8t-3) & 1/4 \leq t < 1/2 \\ (5-8t, 1) & 1/2 \leq t < 3/4 \\ (-1, 7-8t) & 3/4 \leq t \leq 1 \end{cases} \tag{5.6}$$

where $\boldsymbol{\xi}(t+n) = \boldsymbol{\xi}(n)$ for all $n \in \mathbb{Z}$ and the geometrical nodes $\{\mathbf{x}_n, n = 1, \ldots, 12\}$ control the accuracy in the approximation.

To achieve a better approximation (in some sense), a least-square problem is introduced to compute the geometrical nodes (for each closed curve $\mathcal{P}_i$), and also to ensure that the approximated curve has continuous first derivative at points $t_0 = 0$, $t_1 = 1/4$, $t_2 = 1/2$ and $t_3 = 3/4$ (points related with the corners of the reference element $[-1, 1]^2$). We compute the linear coefficients in Equation (5.6) by solving the min-max problem

$$(\mathbf{x}_1, \ldots, \mathbf{x}_{12}, \lambda_0, \ldots, \lambda_3) = \arg \max_{\gamma_0, \ldots, \gamma_3 \in \mathbb{R}} \min_{\mathbf{w}_1, \ldots, \mathbf{w}_{12} \in \mathbb{R}^3} \mathcal{L}(\mathbf{w}_1, \ldots, \mathbf{w}_{12}, \gamma_0, \ldots, \gamma_3), \tag{5.7}$$

with

$$\mathcal{L}(\mathbf{w}_1, \ldots, \mathbf{w}_{12}, \gamma_0, \ldots, \gamma_3) = \int_0^1 |\chi_{\mathbf{x}}(t) - \mathcal{P}(t)|^2 \, dt + \sum_{i=0}^{3} \gamma_i [\![\chi'_{\mathbf{x}}(t_i)]\!], \tag{5.8}$$

where $\mathcal{P}(t)$ $(0 \leq t \leq 1)$ is a parametrization of the polyline $\mathcal{P}_i$, $[\![g(t_i)]\!] = g(t_i^+) - g(t_i^-)$ is the jump of function g at $t = t_i$, and $\lambda_0, \ldots, \lambda_3$ are the Lagrange multipliers to enforce continuity of the solution at points $t_0, \ldots, t_3$ defined above.

The accuracy of the least-square problem to find the geometrical nodes, for each closed polyline, is exemplified in Figure 5.4 where four luminal regions are approximated with the proposed strategy. The comparison between the data representing the transversal section (blue dots in referred figure) and the approximated curve corresponding to the geometrical nodes provided by the least-square problem (red curve) demonstrates the capabilities of this, yet simple, efficient approximation strategy. Notice also that the

required regularity is naturally imposed in each approximated curve.

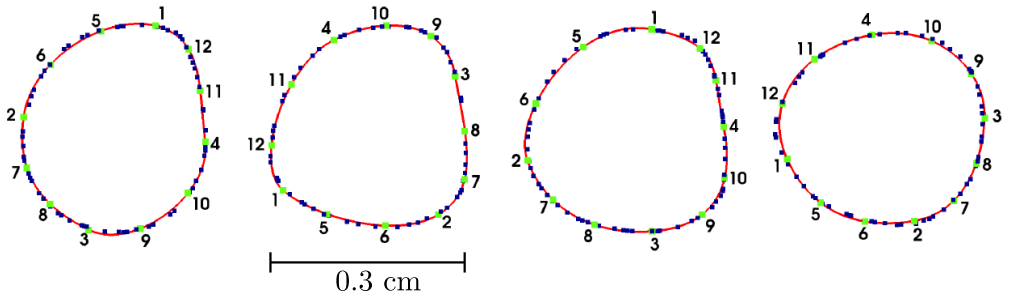

Figure 5.4: Approximation of different cross-sections via the least square problem. In each panel: blue points define the polyline $\mathcal{P}$, solid red line stands for the approximated section and green points are the geometrical nodes. These four luminal regions correspond to the patient-specific vasculature presented in Section 5.3.1

Approximation in reconstructed junctions. Concerning the reconstructed junctions, the pipe mesh is defined incorporating a transition element for coupling each tubular region converging to the junction with the corresponding junction inlet/outlet. The incorporation of these elements allows us to perform a smooth transition from a single element spanning the whole cross-section to a two-element bifurcated mesh. The richer discretization of the interior of the junction achieved by two pipe elements in the transversal direction provides a compensation for the geometrical complexity in such region and also to the lack of a mainstream direction.

The structure of the pipe-element mesh for a bifurcating domain region is outlined in Figure 5.5. The axial length of pipe elements in the interior of the bifurcation is defined according to the characteristic length to the elements in the tubular regions.

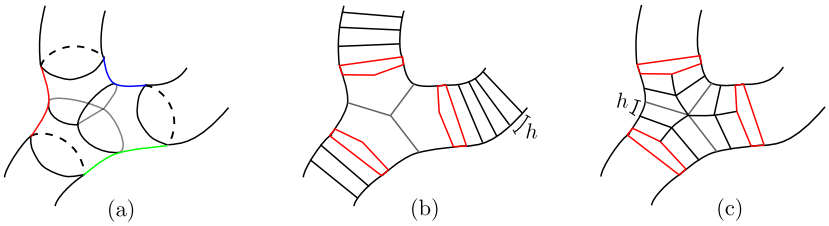

Figure 5.5: Detail of pipe-type mesh discretization within the bifurcation. (a) Reconstructed junction. (b) Lateral view of the pipe elements in the non-branching tubular domains. (c) Lateral view of the discretization at the junction. Transition elements are highlighted in red.

Here, the geometrical nodes defining each transition element are selected as forming an equidistant set on the corresponding planar sections. These sections are automatically described in the reconstruction step, therefore no least-square problem is needed to be solved in the meshing of a junction.

Notice that the geometrical discretization workflow proposed results in a mesh structure in which the boundary layer regions are associated with the transversal direction of the pipe-elements. In this way, the presence of cross-wind boundary layers is naturally tackle by the high-order polynomials which, as seen in previous chapters, are able to effectively deal with this phenomenon without the need of a mesh refinement or of using stabilizing techniques.

5.2 Physiological boundary conditions

In the modeling of the blood flow through isolated regions of the cardiovascular system, the imposition of physiologically reasonable conditions at the artificial (axial) boundaries is mandatory to accurately model the blood flow without neglecting the effects of the downstream circulation. The most adequate strategy to set a consistent hemodynamic environment in a given vessel is to make use of 3D models coupled to dimensionally-reduced blood flow models (1D models for example) [Blanco et al. 2009]. In this work, due to time constrains, we shall not couple 3D models with 1D models, and pursue less sophisticated strategies to define boundary data.

Consider the generic bifurcated region in Figure 5.6. The fluid is attached to the lateral wall, corresponding to a rigid wall model, so no-slip conditions are considered over Γ_L. The boundary Γ_i represents the inlet boundary, while Γ_o the outlet boundary.

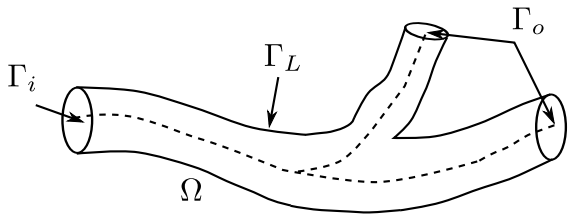

Figure 5.6: Schematic setting for a generic vascular region.

Note that the axial boundaries, Γ_i and Γ_o, are artificial boundaries, that appear once the vascular region was considered isolated from the rest of the cardiovascular system and where appropriate conditions are needed. A common practice, is to prescribe a velocity profile at the inlet, say Γ_i, while suitable Neumann condition on the outlets.

Among these conditions, at each axial boundary the flow is assumed to be fully developed, which implies in a uniform normal component of the traction and null in-plane velocity component. This is, at each inlet/outlet boundary Γ, it is imposed

$$(\mathbf{I} - \mathbf{n} \otimes \mathbf{n})\mathbf{u} = 0 \qquad \text{and} \qquad \mathbf{t}_i = -p_i \mathbf{n} \tag{5.9}$$

where $\mathbf{n}$ is the outward unit normal and p_i the prescribed value for the pressure at Γ (when the flow is fully developed, this value matches the fluid pressure, otherwise it is actually the normal component of the traction). Alternative formulations to the imposition of velocity profile and pure Neumann condition on the axial boundaries can be found in the specialized literature, see for example [Olufsen 1999, Formaggia et al. 2002, Lagana et al. 2002, Vignon-Clementel et al. 2006, Grinberg and Karniadakis 2008].

In this section we are interested in addressing two particular variations for the boundary conditions aiming at the introduction of physiological data into the simulations: (i) the imposition of a pulsatile flow rate waveform and (ii) the relation between the pressure p_i and the flow rate Q, through a 0D element.

5.2.1 Flow rate boundary condition

Let us assume that we are interested in prescribing a realistic volumetric flow rate, at the inlet Γ_i, described by the scalar function $Q(t) : (0, T) \to \mathbb{R}$, with T defining the period of the heart beat. Two possibilities can be identified for the inlet boundary: (i) Γ_i being a circular region of radius R or (ii) Γ_i a generic flat surface.

Circular inlet region. For the first case, the inlet boundary being a circular region of center $\mathbf{x}_0$ and radius R, a closed form for the velocity at Γ_i can be provided if we postulate that the desired flow, at each time instant, is realized through a parabolic profile. In fact, assuming a parabolic profile for the velocity, it is immediate the relation

$$Q(t) = \int_{\Gamma_i} \mathbf{u} \cdot \mathbf{n} d\,\Gamma = 2\pi \int_0^R u_n(r)\, dr = 2\pi \int_0^R u_0(t) \left(1 - \frac{r^2}{R^2}\right) d\, r \tag{5.10}$$

with r is the radial spatial component in radial coordinates, u_n the normal component of the velocity field $\mathbf{u}$ and $u_0(t)$ the maximum velocity as function of time. Then the flow waveform is directly achieved by imposing the Dirichlet condition for the normal component of the velocity over Γ_i

$$u_n(\mathbf{x}, t) = \frac{2}{\pi R^2} Q(t) \left(1 - \frac{r^2}{R^2}\right) \tag{5.11}$$

where $r = \|\mathbf{x} - \mathbf{x}_0\|$. In addition, the in-plane components of the velocity field are set to zero.

Generic inlet region. The previous strategy, although computationally simple, is limited for domains where Γ_i are circular regions, which is unrealistic for patient-specific geometries. A more generic approach is based on the imposition of the flow rate, at each time, through the use of a Lagrange multiplier directly in the variational formulation of the fluid flow problem. Specifically, the strategy employed to prescribe the flow at the inlet Γ_i is based on adding to the original fluid flow variational problem: Find $(\mathbf{u}, p) \in \mathcal{U} \times L^2(\Omega)$ such that

$$\begin{aligned} &\int_\Omega \left[\rho \frac{\partial \mathbf{u}}{\partial t} \cdot \hat{\mathbf{u}} + \rho(\mathbf{u} \cdot \nabla)\mathbf{u} \cdot \hat{\mathbf{u}} + 2\mu\boldsymbol{\varepsilon}(\mathbf{u}) \cdot \nabla(\hat{\mathbf{u}}) - p \operatorname{div} \hat{\mathbf{u}} - \hat{p} \operatorname{div} \mathbf{u}\right] d\Omega = \\ &\quad \int_\Omega \mathbf{f} \cdot \hat{\mathbf{u}}\, d\Omega + \int_{\Gamma_i} t_i \mathbf{n} \cdot \hat{\mathbf{u}}\, d\Gamma_i + \int_{\Gamma_o} t_o \mathbf{n} \cdot \hat{\mathbf{u}}\, d\Gamma_o \qquad \forall\, (\hat{\mathbf{u}}, \hat{p}) \in \boldsymbol{\mathcal{V}} \times L^2(\Omega), \end{aligned} \tag{5.12}$$

the terms

$$\hat{\lambda} \left(\int_{\Gamma_i} \mathbf{u} \cdot \mathbf{n}\, d\Gamma - Q(t)\right) + \lambda \left(\int_{\Gamma_i} \hat{\mathbf{u}} \cdot \mathbf{n}\, d\Gamma\right) \qquad \forall\, \hat{\lambda} \in \mathbb{R} \tag{5.13}$$

where $\lambda \in \mathbb{R}$ is a Lagrange multiplier introduced to ensure the constraint relating the velocity field with the flow rate.

Hence, the flow rate is directly imposed at the variational formulation level allowing their numerical implementation in a very straightforward way. A detailed discussion on the theoretical aspects of this approach is described in [Formaggia et al. 2002].

5.2.2 Resistance boundary condition

Let us denote by Γ_o the boundary in which we are interested in imposing a Neumann boundary condition. The hypothesis of uniform traction over Γ_o implies that the traction is expressed as $\mathbf{t} = -p_o\mathbf{n}$ where p_o is the value for the pressure at Γ_o. The simplest way to describe the outflow is by applying a zero traction boundary condition at the outflow. However, this choice may be unfeasible to correctly reflect the flow division in a bifurcation, which depends mostly on the downstream vasculature.

For a physiological description of the outlet pressure p_o, we can correlate this value with the flow rate $Q(t)$ through the introduction of a resistance $\tilde{R}$ satisfying the relation $\tilde{R}Q(t) = p_o - p_{\text{ref}}$, where p_{ref} is a reference pressure value (for instance, a far away constant pressure value, such as the venous pressure).

Assuming for simplicity $p_{\text{ref}} = 0$, this relation modifies the term related to the traction in the variational formulation as

$$-\int_{\Gamma_o} \mathbf{t}\cdot\hat{\mathbf{u}}\,d\Gamma = \int_{\Gamma_o}\Big(\tilde{R}Q(t)\mathbf{n}\Big)\cdot\hat{\mathbf{u}}\,d\Gamma = \tilde{R}\Big(\int_{\Gamma_o}\mathbf{u}\cdot\mathbf{n}\,d\Gamma\Big)\Big(\int_{\Gamma_o}\hat{\mathbf{u}}\cdot\mathbf{n}\,d\Gamma\Big). \quad (5.14)$$

The value for the resistance has to be given in order to represent the opposition of the downstream vasculature to the flowing of the blood through the corresponding vessel. In the following section we address this issue. Physiological data for the resistance can be found in [Stergiopulos et al. 1992, Alastruey et al. 2007], with values varying in a range between $9.3\cdot 10^3$ and $8.43\cdot 10^5$ dyn $\cdot$ s $\cdot$ cm^{-5}.

5.2.3 Power law for multiple inlet/outlet

In the presence of several inlet/outlet boundaries (denoted by Γ_i, $i = 1,\dots,N$ each one with equivalent radius $r_i^2 = |\Gamma_i|/\pi$), the imposition of flow rate or resistance conditions requires the introduction of a strategy to distribute the desired quantity. The hypothesis employed in this work is to distribute the flow (and resistance) data following a power law based on the vessel radii.

For the imposition of flow data ($Q(t)$, $t\in(0,T)$) we proceed as follows: For each Γ_i, a Lagrange multiplier λ_i is introduced at the variational formulation to impose the flow using the following power law rule to divide the flow rate among the boundaries

$$Q_i(t) = r_i^3\left(\sum_{j=1}^{N} r_j^3\right)^{-1} Q(t), \qquad t\in(0,T). \quad (5.15)$$

Observe that it is not possible to prescribe the flow rate at all the inlet/outlet boundaries because of the incompressibility constraint.

In turn, the total resistance $\tilde{R}$ is distributed among the boundaries Γ_i ($i = 1,\dots,N$) according to the following power law relation between the resistance and the equivalent vessel radius at the corresponding boundary

$$\tilde{R}_i = r_i^{-3}\left(\sum_{j=1}^{N} r_j^3\right)\tilde{R}. \quad (5.16)$$

The effects of the imposition of these type of boundary conditions in hemodynamics simulations can be appreciated in [Bulant 2017].

5.3 Blood flow in the left anterior descending artery

The potentialities of the TEPEM in hemodynamics applications, the geometrical pipeline proposed for the pipe mesh generation, as well as the boundary conditions explained earlier in this chapter, are studied through the application of the proposed methodology into the blood flow simulation in patient-specific arterial regions.

Specifically, in this section, a patient-specific coronary blood flow simulation is performed. Three geometries of the left anterior descending (LAD) artery are evaluated: (i) A geometry obtained from optical coherence tomography (OCT); (ii) a geometry obtained from CCTA and (iii) a geometry reconstructed based on centerline/radius information. Each of these regions are non-branching arterial segments.

The boundary condition at the inlet boundary is given by a prescribed flow rate, which is also shown in Figure 5.7. This inflow waveform was designed on the basis of available clinical data from Doppler measurements, to guarantee realistic conditions. At the outlet, homogeneous Neumann boundary conditions are imposed. The time step is the same for all the test cases, with $\Delta t = 0.001$ s. Physiological values for density and viscosity are considered, these parameters are set to $\rho = 1.04$ g/cm^3 and $\mu = 0.04$ P. Two cardiac cycle are simulated. A distributed computing paradigm is employed here for both, TEPEM and FEM, because of the size of the problem.

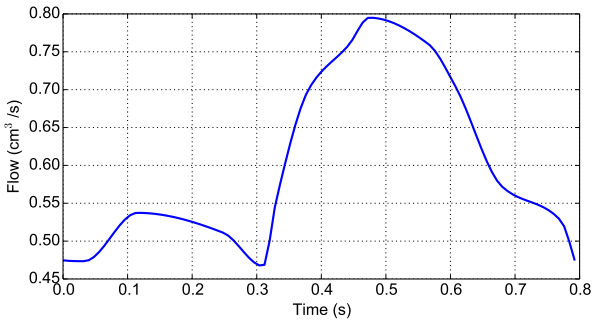

Figure 5.7: Flow rate signature for the coronary blood flow simulation.

The comparison of the computational burden of FEM and TEPEM is addressed at each example. Problem size (through the total number of degrees of freedom), physical resources needed to perform the simulation and the computational time employed are the relevant indexes in which we will focus for the comparison. A direct comparison for degrees of freedom and physical resources is performed at each case. For the comparison of the computational time, the wall-clock time and the average computational time (defined by multiplying the wall-clock time and the number of processors) are reported. For a further comparison, the time involved in the advancement of a single time-step is also presented.

For the FEM approach it is employed the mini element with SUPG stabilization. The system of equations is solved monolithically with a direct parallel algebraic LU solver for the TEPEM approach and an iterative GMRES method for the FEM. Finally, a total of 160 processors were employed to run the FEM simulations while 36 processors were considered for the TEPEM.

5.3.1 Vascular region obtained from OCT

The first example is devoted to the blood flow simulation in a LAD region obtained with OCT. The vascular region, a rectified coronary artery, is outlined in Figure 5.8 together with a comparison between the discrete mesh employed in the FEM simulation and the reconstructed pipe-type structure employed for the TEPEM simulations. The geometrical pipeline, proposed in the beginning of the chapter, was successfully employed for the pipe discretization of the vascular region, providing a topological structure very close to the one use in the FEM.

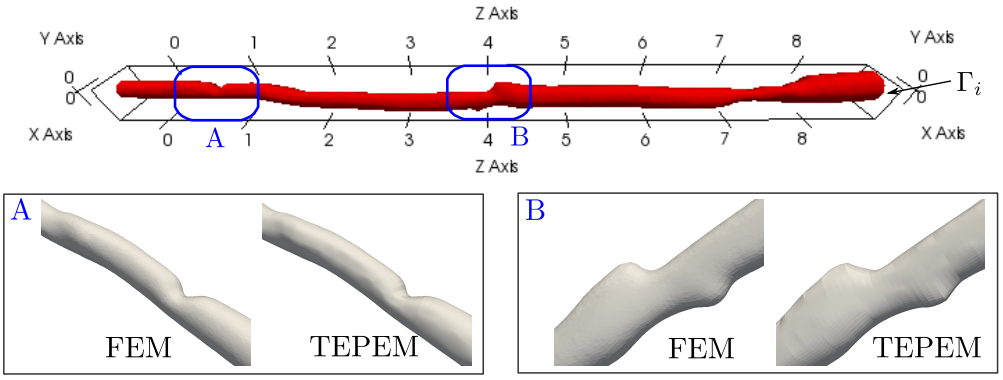

Figure 5.8: Vascular region obtained from OCT. Top row: Geometrical description with dimensions in centimeters. Bottom row: Comparison between FEM discrete mesh (left) and TEPEM mesh (right) in two regions.

For the TEPEM approach, the number of pipe elements in which the geometry is divided is 105 and the transversal order p is considered varying in the range $\mathsf{p} \in \{4, 6, 8\}$. A FEM simulation is also performed to obtain a reference solution. For the FEM simulation, the mesh is composed by 1 975 700 tetrahedral elements. A detailed comparison between the computational effort of FEM and TEPEM simulations is addressed in Table 5.1, where the total number of degrees of freedom in each approach is presented, as well as the average time needed for one single time-step iteration. While the relative reduction in the problem size is superior to the 90% the TEPEM proves to be faster than the FEM in a range from 10 to 150 times.

Table 5.1: Comparison of the computational burden in the FEM and TEPEM approaches. The cost is evaluated through the wall-clock time, the average computational time to perform a single time-step iteration and also through the relative reduction in the problem size, measured with the degrees of freedom in each implementation.

		FEM	TEPEM		
			$\mathsf{p}=4$	$\mathsf{p}=6$	$\mathsf{p}=8$
Elements		1 975 700		105	
DoFs	Total number	1 301 868	6 714	17 687	33 986
	Relative reduction	-	99.48%	98.64%	97.38%
Wall-clock time		440 min	13 min	97 min	240 min
Single time-step	Average time	43.9 min	0.3 min	2.2 min	5.4 min
	Relative reduction	-	99.31%	94.98%	87.69%

As a first comparison to evaluate the capabilities of the proposed approach, Figure 5.9 presents a detail of the blood flow structure for a selected region in the OCT geometry (region A in Figure 5.8) and at four different time instants, $t \in \{0.8, 1.0, 1.2, 1.4\}$ seconds.

For each time, the velocity profile provided by the TEPEM, with different transversal order, is compared with the one obtained with the FEM. The velocity field delivered by the proposed method is very close to the reference one and, as before, the higher the order of the polynomial approximation for the physical fields, the better the TEPEM solution.

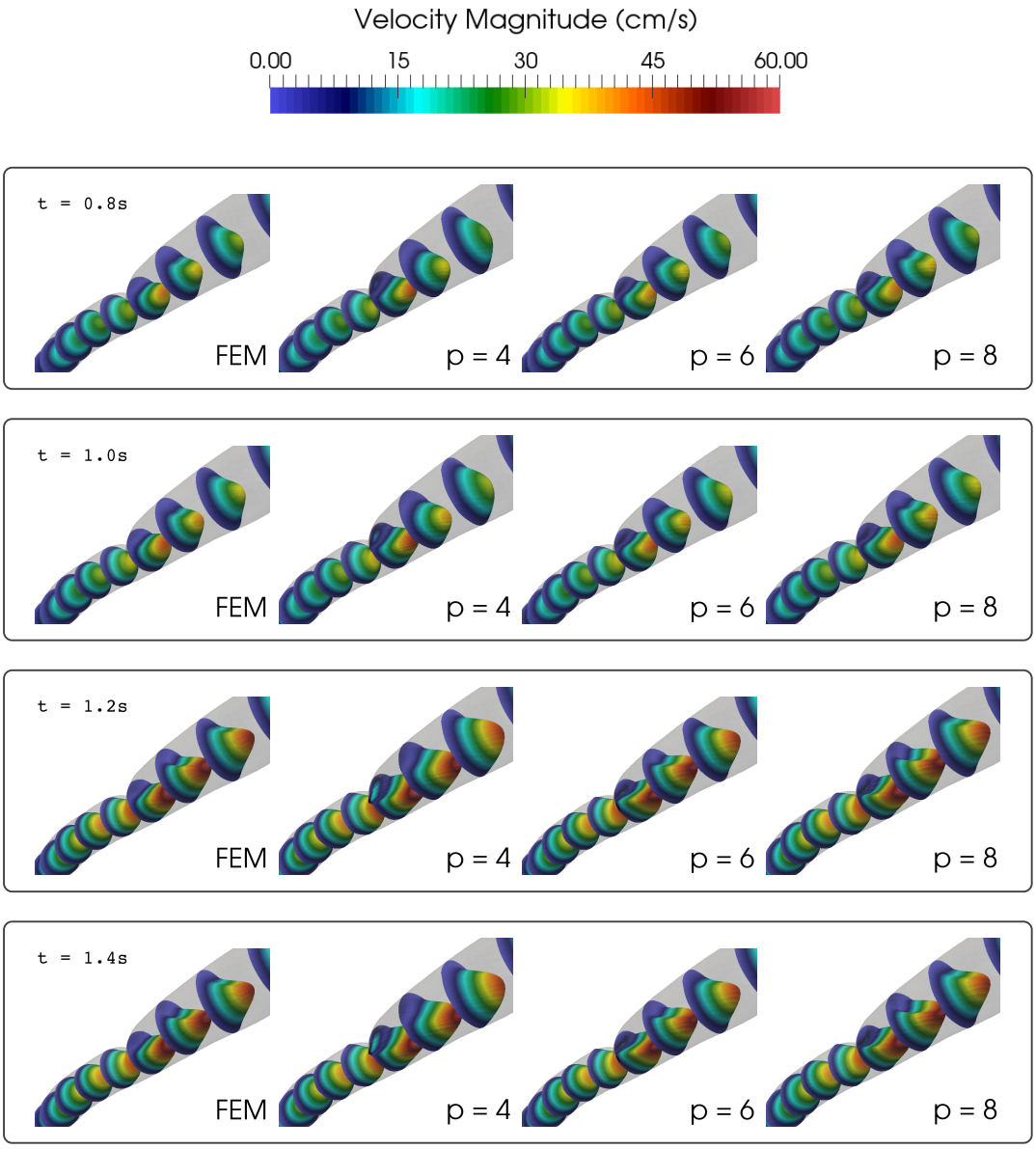

Figure 5.9: Comparison of velocity profiles for different transversal orders for the TEPEM and FEM at selected time instants and region A in Figure 5.8.

Moreover, at the selected region, the formation of a vortex is observed (Figure 5.10). This recirculation structure is accurately approximate by the TEPEM, even for the lowest transversal order considered ($\mathsf{p} = 4$). The precise (and cheap) identification of these zones is fundamental for potential clinical use of this class of simulations.

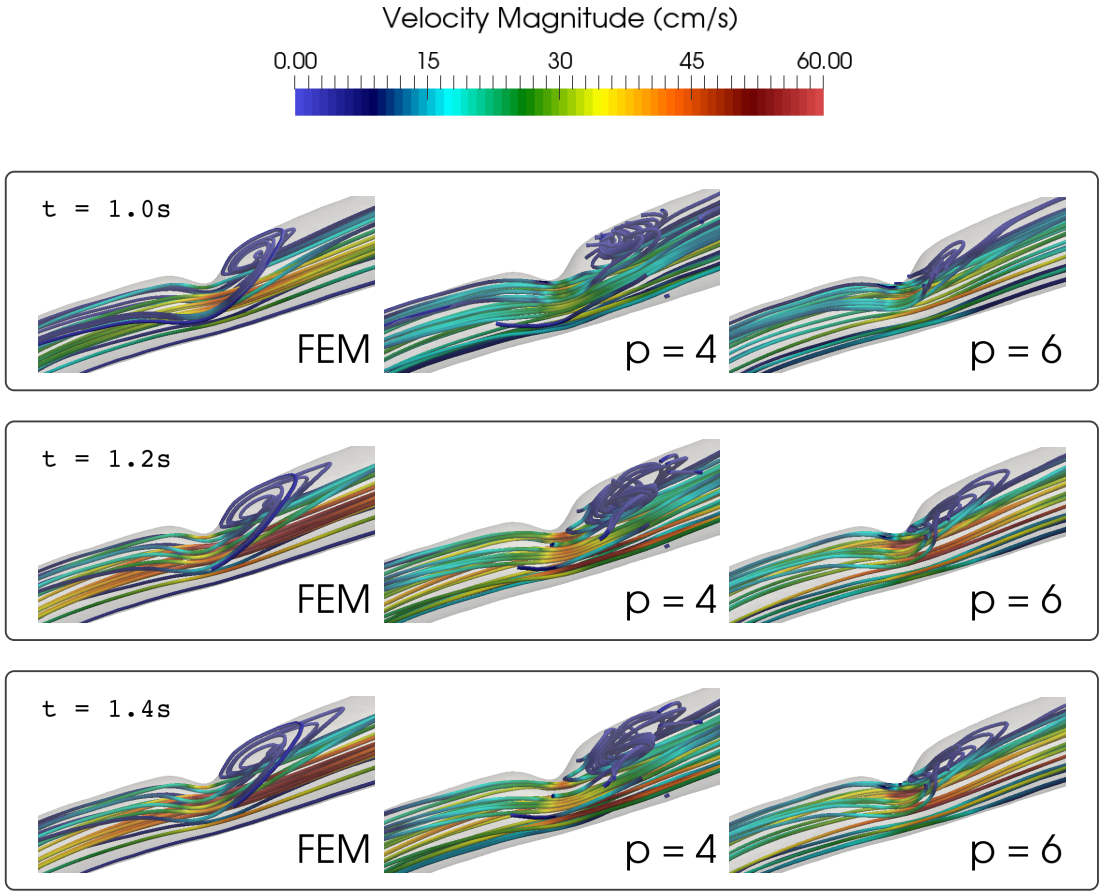

Figure 5.10: Detail of a recirculation region in the blood flow developed in the OCT geometry and TEPEM approximation with different transversal orders.

Together with the identification of recirculation zones, it is fundamental to analyze the wall shear stress produced by the blood flow over the endothelial wall. In Figure 5.11, a comparison between the wall shear stress provided by the FEM and the TEPEM with different transversal orders is addressed, highlighting the ability to provide an accurate spatial description of the field that agrees with the FEM at the selected times. A further comparison is addressed by considering the wall shear stress averaged over the cardiac cycle (AWSS). In Figure 5.12 the spatial distribution of the WSS and the cross-sectional average through the vessel intrinsic coordinate, denoted by s, are presented. Even the lowest order approximation ($\mathsf{p} = 4$) delivers a high-fidelity solution in terms of AWSS, which can be improved as p is increased.

It may be worth noting that no 1D model, basically relying on approximating the axial component of the motion, could be able of capturing vortexes at the velocity and neither describe the heterogeneities in the wall shear stress. On the other hand, with TEPEM, these characteristics are captured with computational costs that are really lower than a full 3D model.

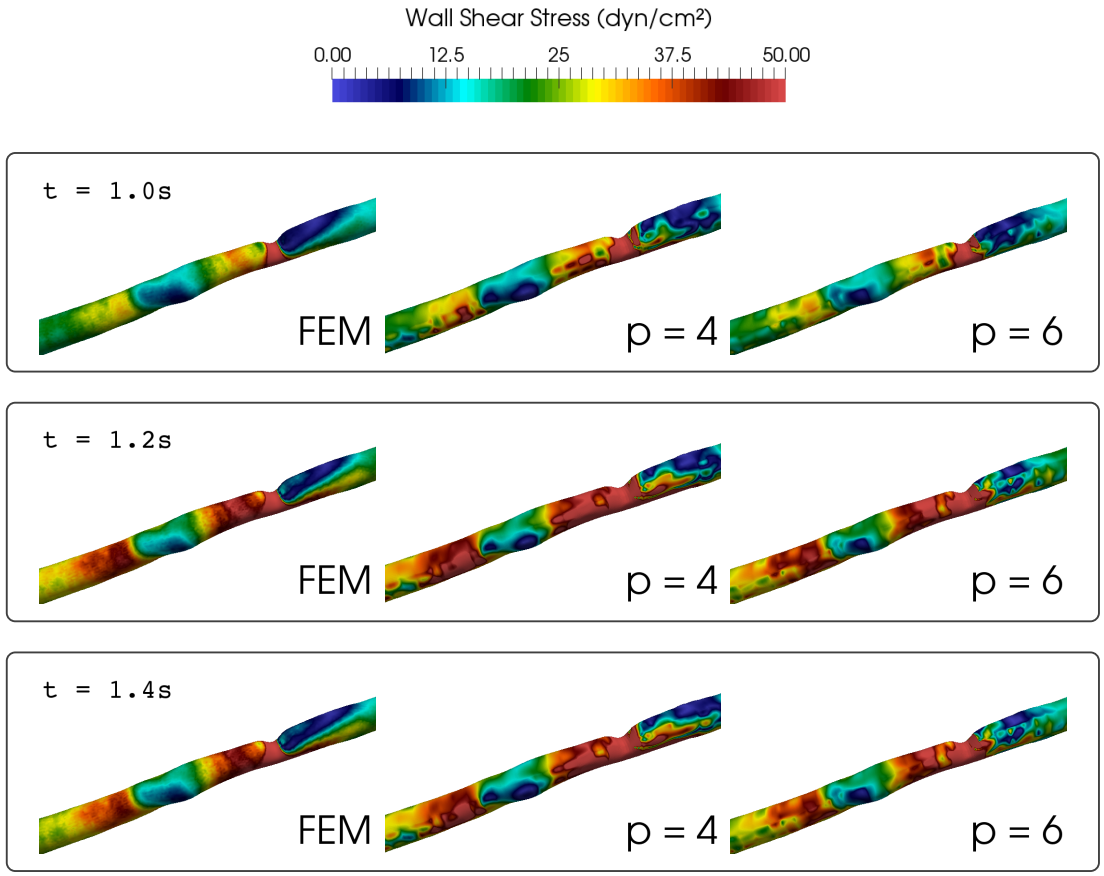

Figure 5.11: Comparison of WSS between FEM and different transversal orders of TEPEM at three selected time instants.

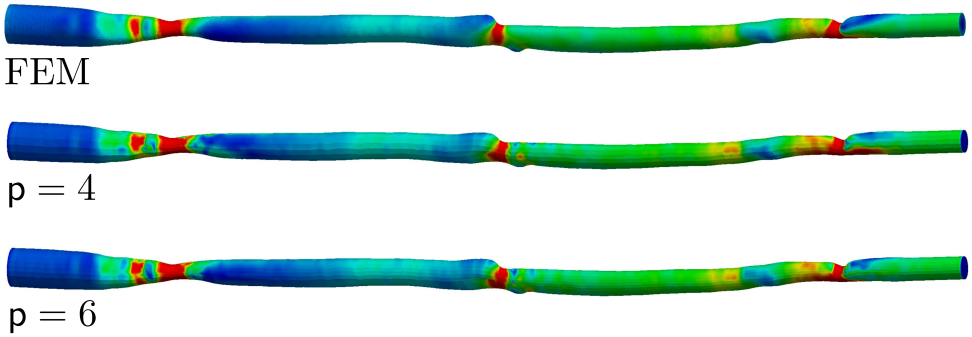

(a) Spatial distribution of the AWSS

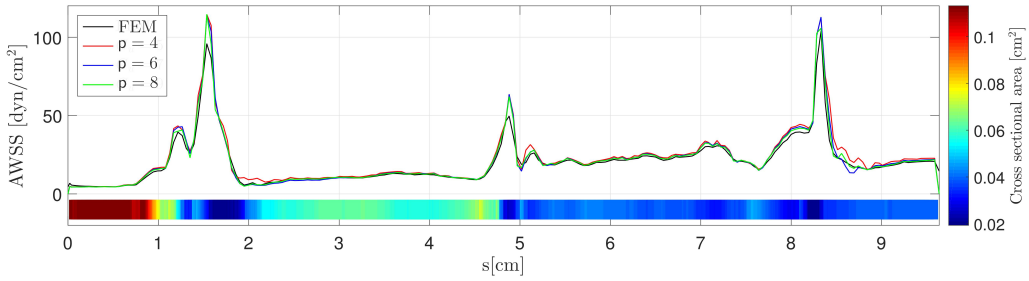

(b) Cross-sectional average of AWSS as a function of the longitudinal coordinate

Figure 5.12: Comparison of the average wall shear stress (AWSS) between FEM and different orders p of the TEPEM.

5.3.2 Vascular region obtained from CCTA

For this example, the vascular region, a tortuous tapered vessel, is obtained from CCTA and is outlined in Figure 5.13. As before, in the same figure two selected areas are highlighted to compare the geometry employed in the FEM (a tetrahedral mesh) and in the TEPEM (a pipe mesh). This comparison reinforces the potentialities in the geometrical pipeline proposed to perform a pipe discretization of arterial regions with variable radius.

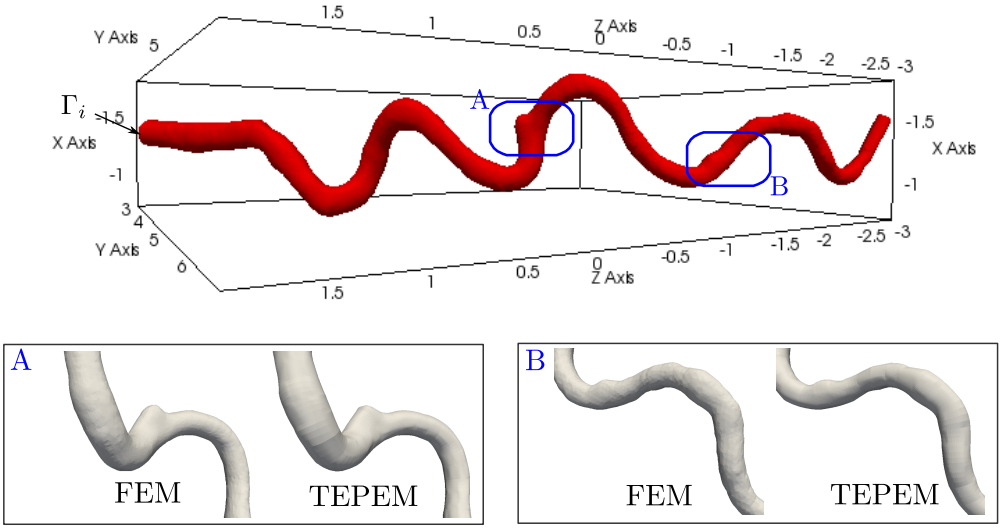

Figure 5.13: Vascular region obtained from CCTA. Top row: Geometrical description with dimensions in centimeters. Bottom row: Comparison between FEM discrete mesh and TEPEM mesh in two regions.

The number of elements employed in the domain discretization for FEM and TEPEM approaches, as well as the degrees of freedom, are detailed in Table 5.2. The reduction in the problem size is measured through the relative reduction in the degrees of freedom which reach an economy superior to 98%. Concerning the reduction in the computational time, the time (in minutes) to perform a single time-step iteration is also presented in the referred table. A direct comparison of the average time for both approaches reveals the TEPEM as being remarkably faster than then FEM, in a range from 15 to 700 times.

Table 5.2: Comparison of the computational burden in the FEM and TEPEM approaches. The cost is evaluated through the wall-clock time, the average time to perform a single time-step iteration and also through the relative reduction in the problem size.

		FEM	TEPEM		
			p = 4	p = 6	p = 8
Elements		2 444 708		90	
DoFs	Total number	1 611 428	5 769	15 197	29 201
	Relative reduction	-	99.64%	99.05%	98.18%
Wall-clock time		670 min	4 min	52 min	217 min
Single time-step	Average time	69.4 min	0.1 min	1.2 min	4.9 min
	Relative reduction	-	99.85%	98.27%	92.93%

For comparison purposes, in Figure 5.16 the velocity profile provided for FEM and TEPEM (with $\mathsf{p} = 6$) are presented in two regions and at some time instants. At these regions, the same regions selected to compare the accuracy in the geometrical pipeline, it is evident the accuracy of the TEPEM approach when compared with the FEM as reference solution. A further comparison in the velocity approximation is outlined in Figure 5.17 where a comparison of the streamlines provided by FEM and TEPEM is addressed.

For the wall shear stress, the cross-sectional average of the AWSS was computed throughout the vessel intrinsic coordinate denoted by s, which is presented in Figure 5.14. The increase and large variability of the AWSS is caused by the combined effects of tortuosity and tapering in the vessel. Even the lowest approximation given by $\mathsf{p} = 4$ delivers a high-fidelity solution in terms of AWSS, which can be improved as p is increased. This is complemented by a node-wise comparison of the AWSS given by the FEM approximation and the one given by the TEPEM approach using scatter plots as displayed in Figure 5.15. The theoretical line at 45° is shown as well as the correlation coefficient (ρ). It is seen that the correlation is extremely high, and, as expected, it improves as p is increased.

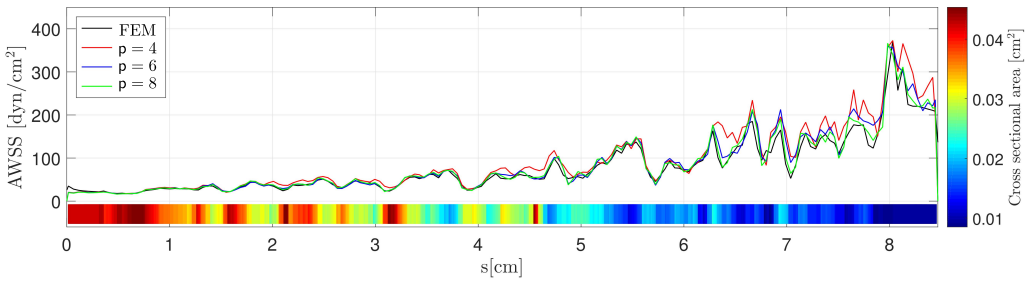

Figure 5.14: Cross-sectional average of AWSS as a function of the longitudinal coordinate.

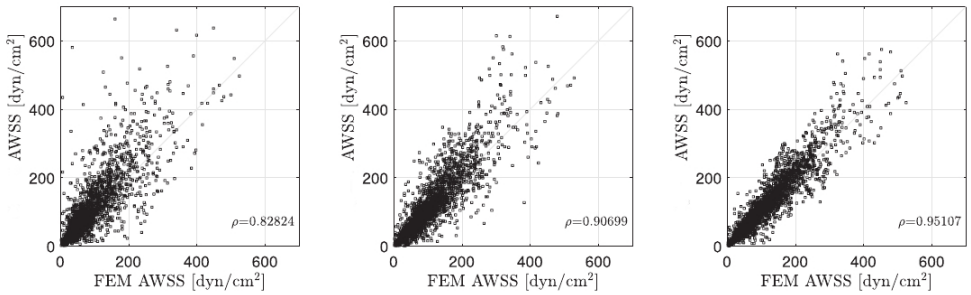

Figure 5.15: Correlation between AWSS obtained with the TEPEM and that obtained using the FEM. From left to right, the TEPEM approach is performed with $\mathsf{p} = 4$, $\mathsf{p} = 6$ and $\mathsf{p} = 8$.

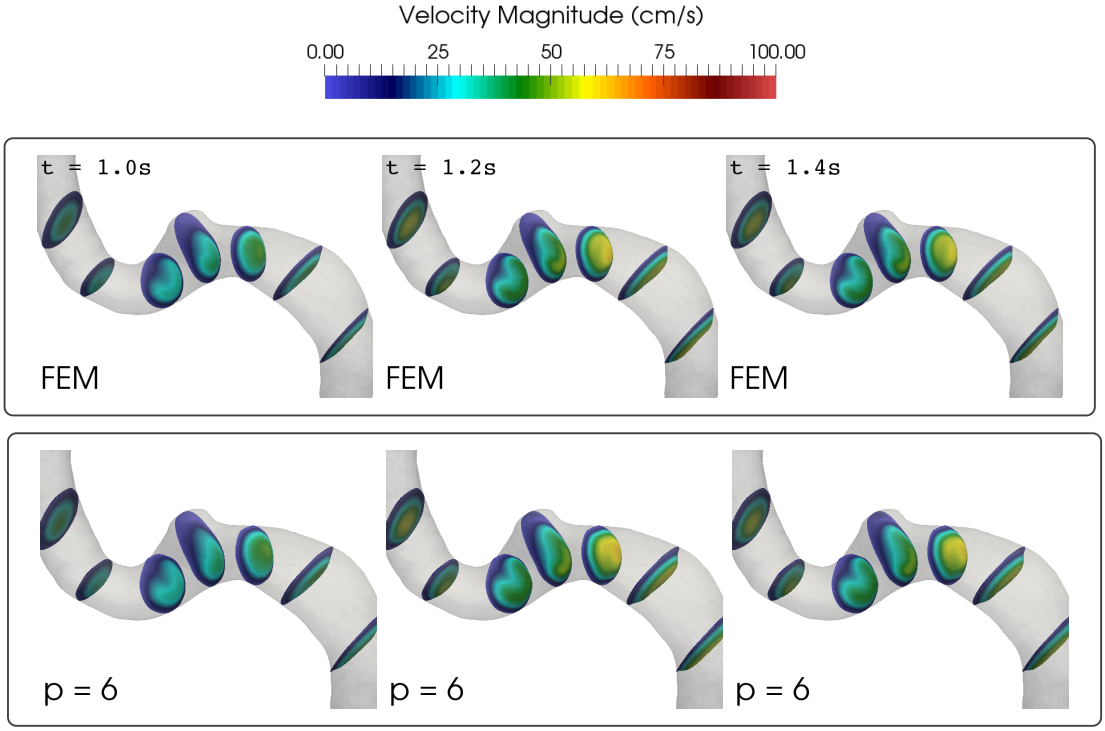

(a) Comparison of velocity profiles in region A

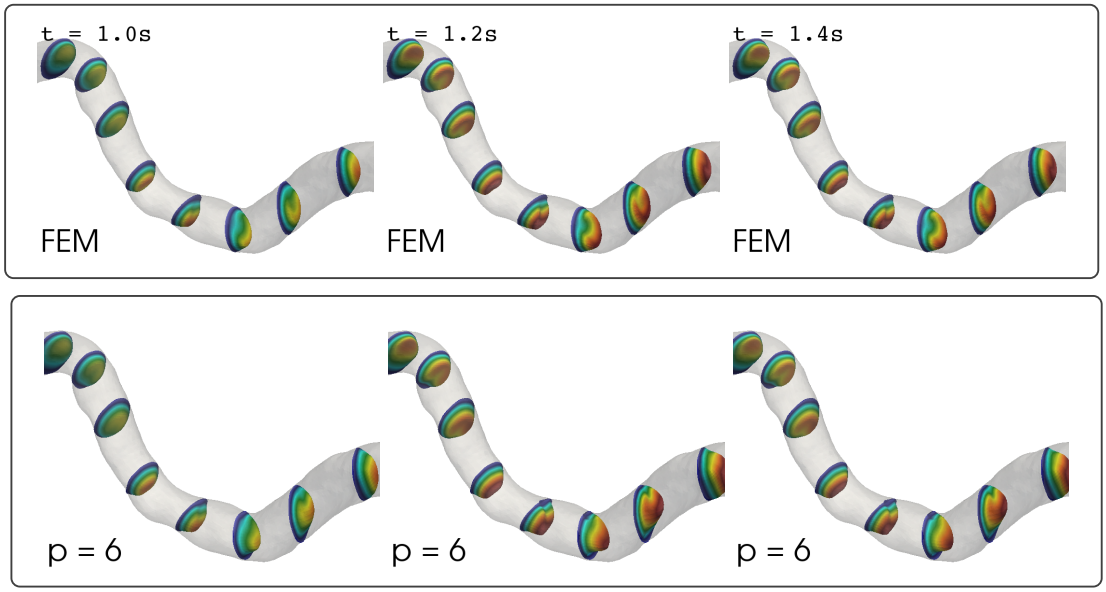

(b) Comparison of velocity profiles in region B

Figure 5.16: Comparison of velocity profiles delivered by TEPEM ($\mathsf{p} = 6$) and FEM at selected time instants.

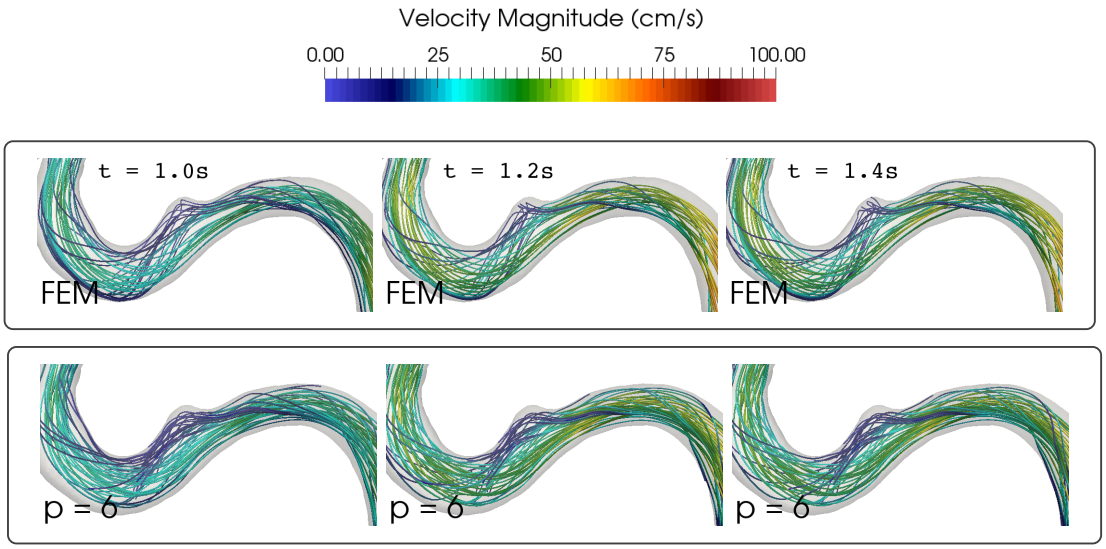

(a) Comparison of velocity streamlines in region A

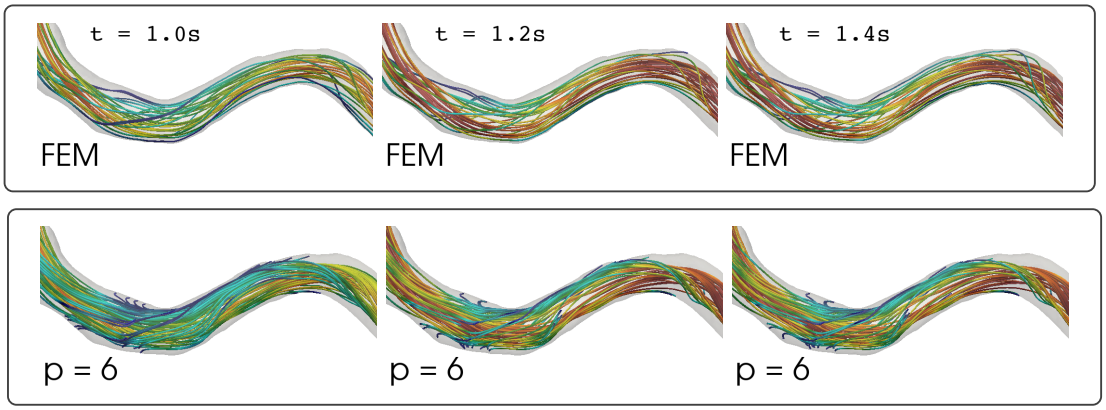

(b) Comparison of velocity streamlines in region B

Figure 5.17: Comparison of the streamlines delivered by FEM and TEPEM at different time instants.

5.3.3 Phantom geometry based in centerline information

For the last example, the vessel geometry is reconstructed based on the centerline and radii information of a patient-specific arterial segment. The geometry, presented in Figure 5.18, is composed by circular transversal sections of variable radius, and is partitioned in pipe elements (143 elements) following the geometric pipeline described before. In the same figure, a comparison between the pipe-mesh structure and a FEM mesh (generated based in the same centerline/radii information) is performed.

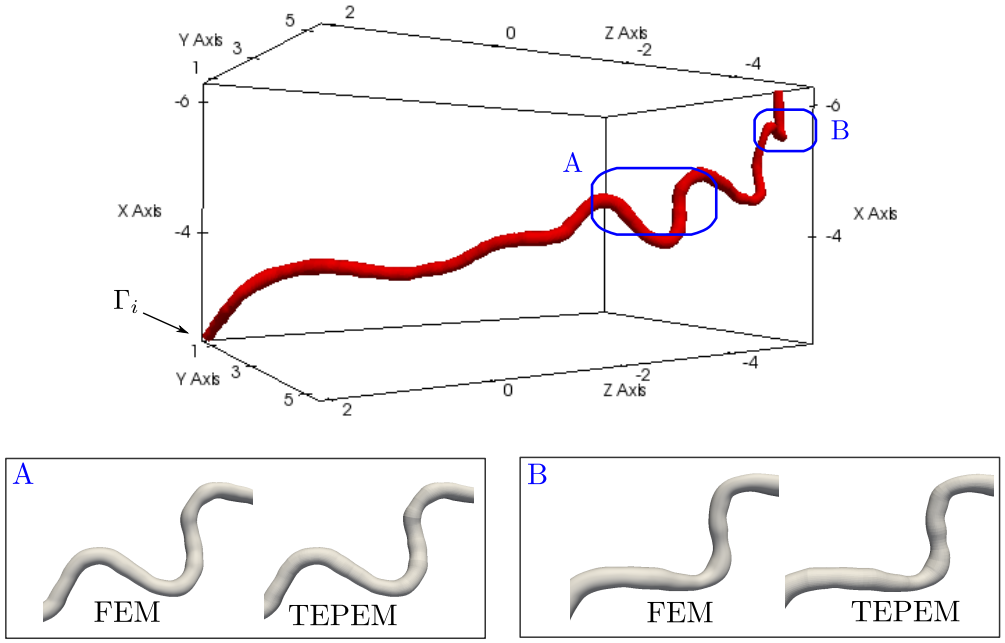

Figure 5.18: Vascular region provided by phantom. Top row: Geometrical description with dimensions in centimeters. Bottom row: Comparison between FEM discrete mesh and TEPEM mesh in two regions.

For this example, a comparison within the TEPEM scope, for different transversal enrichment orders for the approximation of velocity/pressure fields, is addressed. The computational burden in the TEPEM is presented in Table 5.3 where the time (in minutes) for a single time-step and the wall-clock time are compared for three different values of p. Recalling that, for each case, it was employed 36 processors (NP = 36), the average time (NP $\times$ wall-clock time) is also reported.

Table 5.3: Comparison of the computational time in terms of the transversal order in the TEPEM. The time to perform a single time-step iteration, the wall-clock time and the average time are given for different enrichment orders.

	DoFs	Time (min)		
		Time-step	Wall-clock time	Average time
$\mathsf{p}=4$	24 100	0.01	10.31	371.16
$\mathsf{p}=6$	44 494	0.12	89.80	3 232.8
$\mathsf{p}=8$	73 342	0.24	404.05	14 545.8

In Figure 5.19-5.21 the velocity profile, the wall shear stress and the pressure field provided by different transversal orders in the TEPEM, and at six time instants selected at the second cardiac cycle, are displayed. The comparison reveals a small variation between the approximated fields provided with $\mathsf{p} = 6$ and $\mathsf{p} = 8$, which can be understood as a convergence regarding the transversal order, and also as the ability to predict the heterogeneities in the wall shear stress field with a low computational cost.

Note that the TEPEM approach retains predictive capabilities from 3D models, which are naturally far beyond those possessed by one-dimensional approaches. This implies that the TEPEM is able to provide information about the heterogeneities and accurate spatial description of the velocity, pressure and also the wall shear stress, which is of utmost importance in the biomedical engineering applications. At the same time, the TEPEM is able to considerably reduce the computational burden when compared with full 3D models.

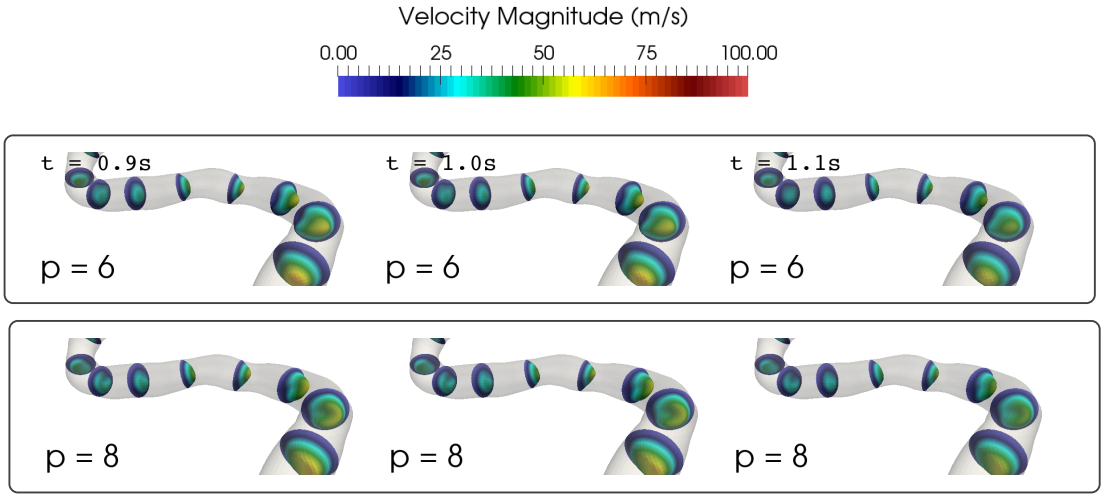

(a) Comparison of velocity profiles in region A

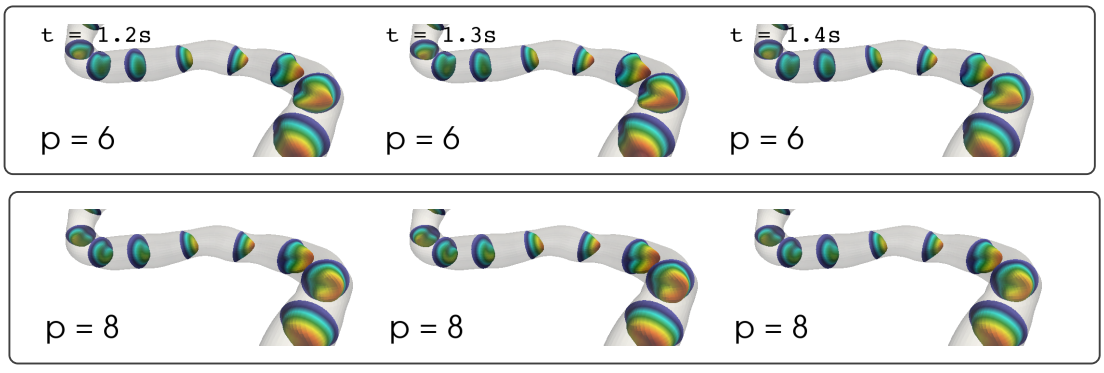

(b) Comparison of velocity profiles in region A

Figure 5.19: Comparison of velocity profiles (left column) and spatial distribution of the wall shear stress (right column) for TEPEM with $\mathsf{p} = 6$ and $\mathsf{p} = 8$ at several time instants.

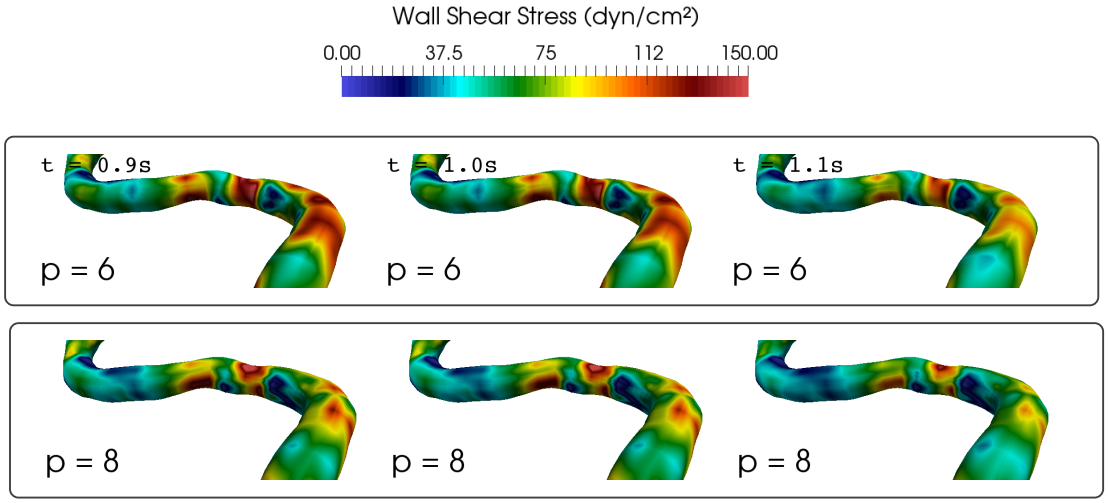

(a) Comparison of velocity profiles in region A

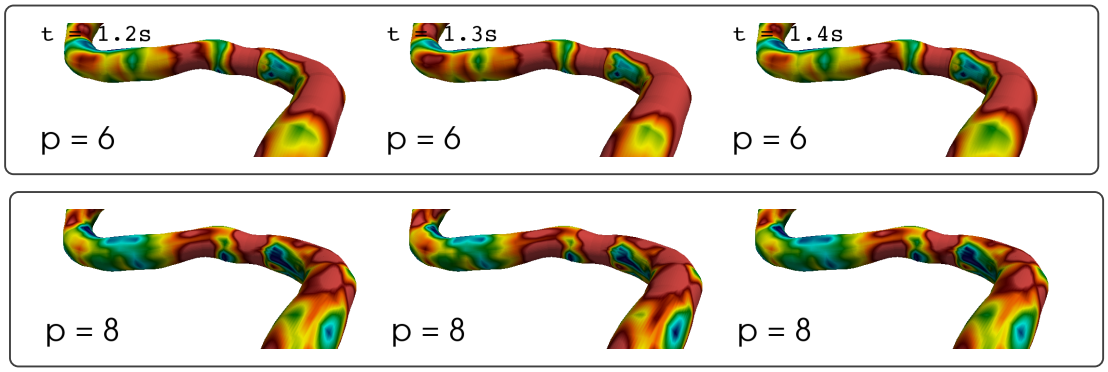

(b) Comparison of velocity profiles in region A

Figure 5.20: Comparison of velocity profiles (left column) and spatial distribution of the wall shear stress (right column) for TEPEM with $\mathsf{p} = 6$ and $\mathsf{p} = 8$ at several time instants.

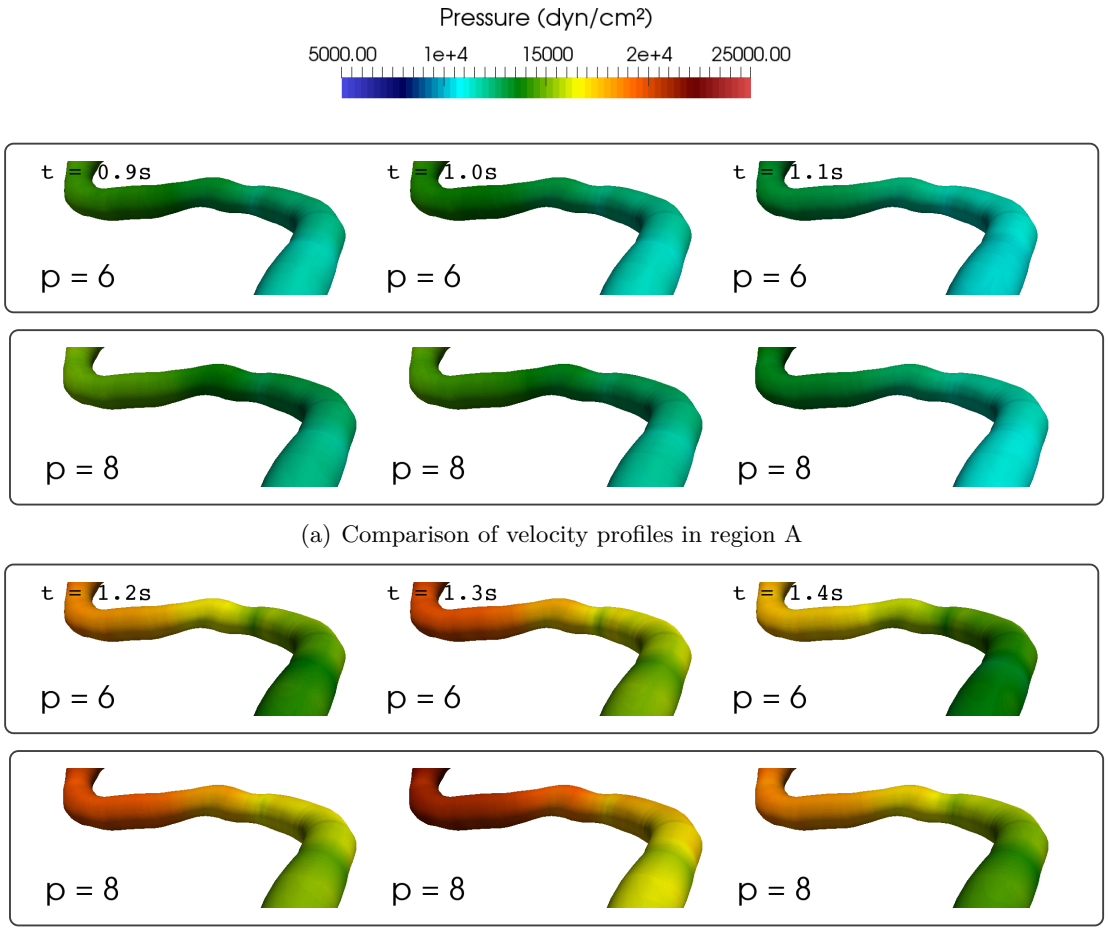

(a) Comparison of velocity profiles in region A

(b) Comparison of velocity profiles in region A

Figure 5.21: Comparison of velocity profiles (left column) and spatial distribution of the wall shear stress (right column) for TEPEM with $\mathtt{p} = 6$ and $\mathtt{p} = 8$ at several time instants.

5.4 Blood flow in a coronary arterial tree

The TEPEM capabilities are now tested in a more complex geometries in this section. Specifically, we are interested in the simulation of the blood flow in two patient-specific geometries corresponding to the left and right coronary trees obtained from a CCTA image. These geometrical domains are the presented in Figure 5.22.

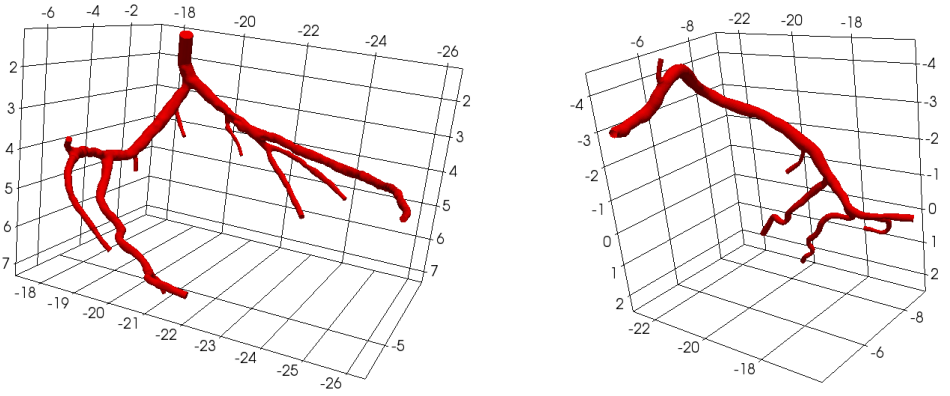

(a) Left coronary arterial tree

(b) Right coronary arterial tree

Figure 5.22: Geometrical outline for the left and right coronary arterial trees.

For the left coronary arterial tree, a steady-state regime is simulated to compare the TEPEM solution, with different transversal orders, with respect to a reference FEM solution. As in the previous section, the comparison will be performed by contrasting the size of the discrete problem, the computational time and the resources needed by each numerical scheme. Similar to the previous section, a distributed computing paradigm is employed for both TEPEM and FEM, employing a total of 10 processors for the TEPEM (NP = 10) and 50 for the FEM (NP = 50). Moreover, the scalability of the TEPEM as a function of the transversal order is also studied.

For the right coronary arterial tree geometry a transient flow is studied using the TEPEM and different transversal enrichment orders. For this case, a flow waveform is prescribed at the outlet boundaries. For each transversal order, $\mathsf{p} \in \{4, 6, 8\}$, it was employed a number of processors equal to NP = 36.

For both cases, the fluid density and viscosity are set to $\rho = 1.04$ g/cm^3 and $\mu = 0.04$ P, respectively. As performed in the previous chapter, the discrete system for the TEPEM is solved with a direct parallel algebraic LU solver while an iterative GMRES method, with a restricted additive Schwarz preconditioner, is employed for the FEM. For both strategies, the solver libraries provided in the PETSc are employed.

5.4.1 Left coronary arterial tree

Let us consider the blood flow through a patient-specific geometry of the left coronary tree obtained from computed tomography angiography. At the inlet, denoted by Γ_i in Figure 5.23, a homogeneous Neumann boundary condition is considered for the normal component of the traction. The flow rate is prescribed to be $Q = 2$ cm^3/s, which is distributed among the outlet boundaries following the power law in terms of vessel radii introduced in Section 5.2. The associated Reynolds number results Re = 150, measured at the inlet boundary.

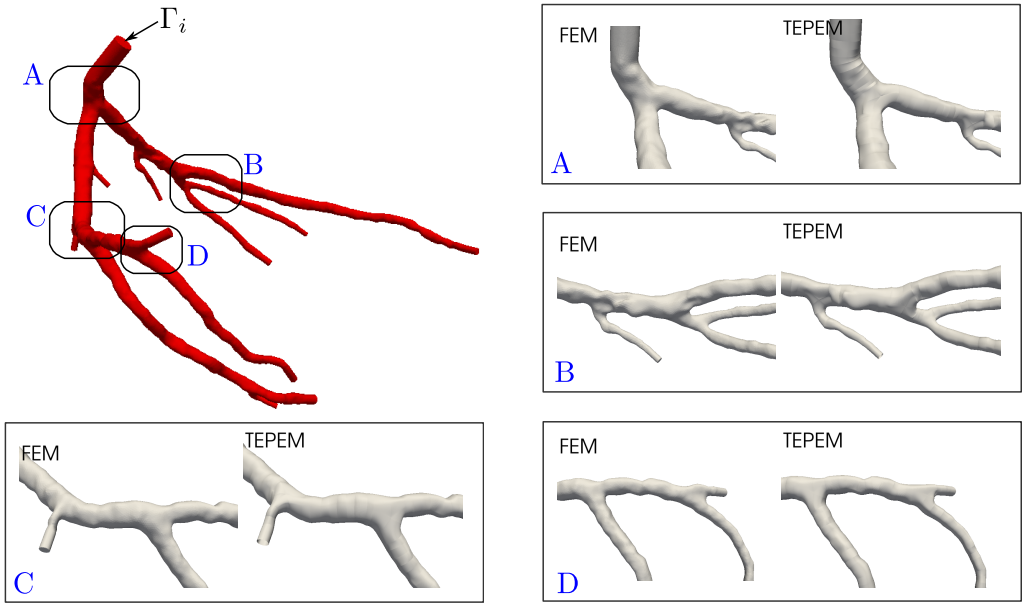

Figure 5.23: Coronary tree geometry obtained via image segmentation. Detailed comparison between the mesh employed in FEM simulations and the pipe-element geometry for the TEPEM at four specific locations.

The geometrical pipeline described in this chapter was employed to discretize the geometrical domain into a pipe-mesh, employing transition pipe elements to deal with a correct discretization of the bifurcation regions. Figure 5.23 shows several details of the FEM mesh and of the TEPEM mesh. As it can be seen, the pipe-element mesh for the TEPEM yields a rather accurate geometric approximation to the reference geometry processed from the medical images and which is the basis for FEM simulations.

The characteristics of both FEM and TEPEM meshes are summarized in Table 5.4. As usual, the size of the discrete problem provided by the TEPEM is remarkably reduced if compared with the FEM, reaching a relative reduction over 85%, for $\mathsf{p} = 10$. The average time for FEM and TEPEM are also compared and the results reported in Table 5.4. A direct comparison between the average time reveals the TEPEM as being clearly faster than the FEM, speeding up the computation in a range from 190 times (for $\mathsf{p} = 4$) to 1.5 times (for $\mathsf{p} = 10$).

Another interest comparison is concerned with the wall-clock time employed by each strategy, FEM and TEPEM, to solve the steady-state flow problem. This time, as a function of the number of processors (NP) employed in the parallel implementation, was computed and the results are presented in Table 5.5. These results, besides evidencing the strong scalability of the proposed approach, reveal the aceleration in the simulation time when moving from FEM to TEPEM.

Table 5.4: Comparison of the computational burden in the FEM and TEPEM approaches. The cost is evaluated through the average computational time (in minutes), obtained by multiplying the number of processors and the wall-clock time at each simulation, and also through the relative reduction in the number of degrees of freedom.

		FEM	TEPEM			
			$\mathsf{p}=4$	$\mathsf{p}=6$	$\mathsf{p}=8$	$\mathsf{p}=10$
Elements		4 094 885	476			
DoFs	Total number	2 814 015	78 226	153 469	253 866	379 417
	Relative reduction	-	97.22%	94.54%	90.97%	86.51%
Total time	Average (min)	1 558.85	8.16	74.03	324.82	1 003.05
	Relative reduction	-	99.47%	95.25%	79.16%	35.65%

Table 5.5: Comparison of wall-clock time (in minutes) for the simulation of the steady-state blood flow in the patient-specific coronary arterial tree for different number of processors (NP) using TEPEM and FEM approaches.

	Number of processors				
	NP = 2	NP = 5	NP = 10	NP = 20	NP = 40
$\mathsf{p}=4$	2.13	1.05	0.82	0.4	0.24
$\mathsf{p}=6$	16.13	9.08	7.40	4.06	1.73
$\mathsf{p}=8$	90.54	46.36	32.40	16.70	8.90
$\mathsf{p}=10$	296.36	144.07	100.30	47.12	37.30

	Number of processors				
	NP = 12	NP = 25	NP = 50	NP = 75	NP = 100
FEM	134.21	61.12	31.16	30.40	31.60

In order to put in evidence the high-fidelity delivered by the TEPEM approximation, a comparison between pressure and velocity fields is now given, paying attention to the regions A, B and C (introduced in Figure 5.23). In Figure 5.24, it is presented a comparison of the pressure field provided by the FEM and the TEPEM for transversal polynomial orders $\mathsf{p} \in \{4, 6, 8\}$. Clearly, a very good agreement is observed even for low degree of transversal interpolation.

In Figures 5.25-5.26 a comparison of the velocity streamlines and profiles (at the three regions A, B and C) between the TEPEM solution for different transversal orders, and the FEM reference solution is given. From these figures, we readily conclude that the velocity profile rendered by the TEPEM is in good agreement with the reference solution.

Concerning the approximation of the wall shear stress, in Figure 5.27 it is addressed a detailed comparison between the spatial description of the WSS provided by the TEPEM and by the FEM. Unfolding the WSS along the longitudinal axes enables us a complete scrutiny of the capabilities of the TEPEM to predict the heterogeneities of the field over all the arterial surface. It is worthwhile to remark that the solution provided with the lowest transversal order considered ($\mathsf{p} = 4$), considering that it reduces in a 97% the number of degrees of freedom and is 190 times faster than the FEM approach, is able to accurately identify the regions of high and low wall shear stress in excellent agreement with the reference solution.

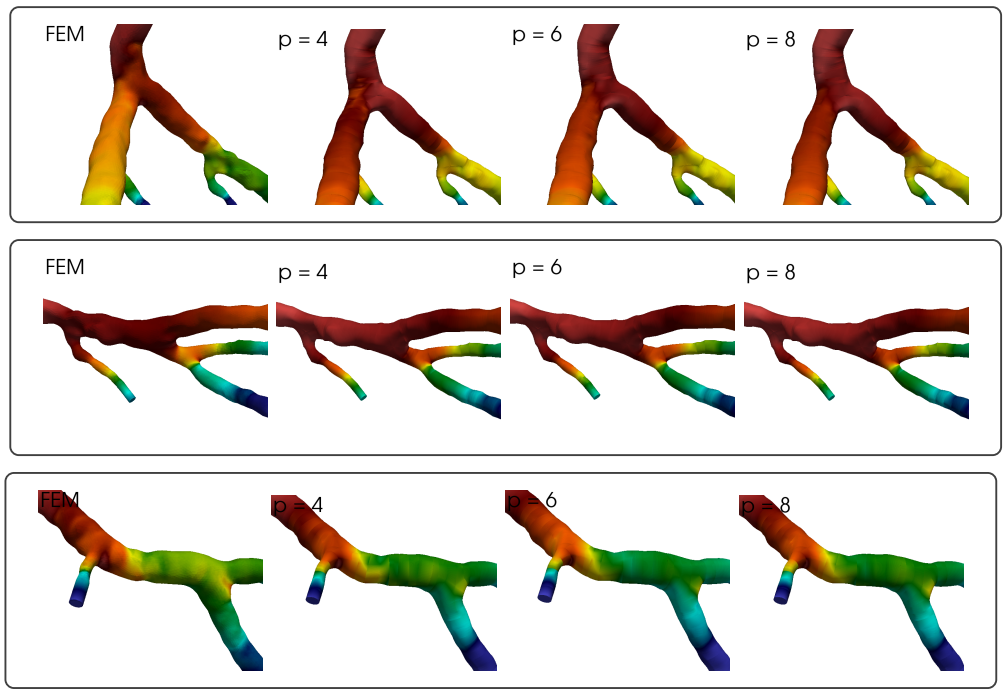

Figure 5.24: Detail of the pressure approximation provided by the FEM and the TEPEM in the regions A (top row), B (middle row) and C (bottom row). Scale for pressure are conveniently adjusted at each region to better visualize pressure gradients.

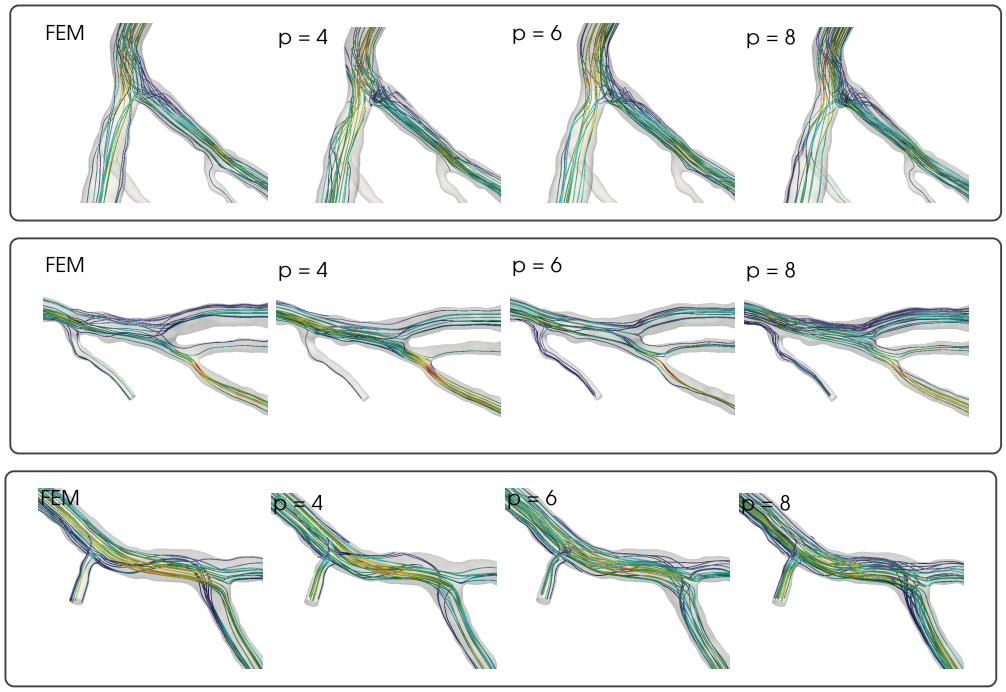

Figure 5.25: Streamlines given by FEM and TEPEM, for different transversal order p, in regions A (top row), B (middle row) and C (bottom row).

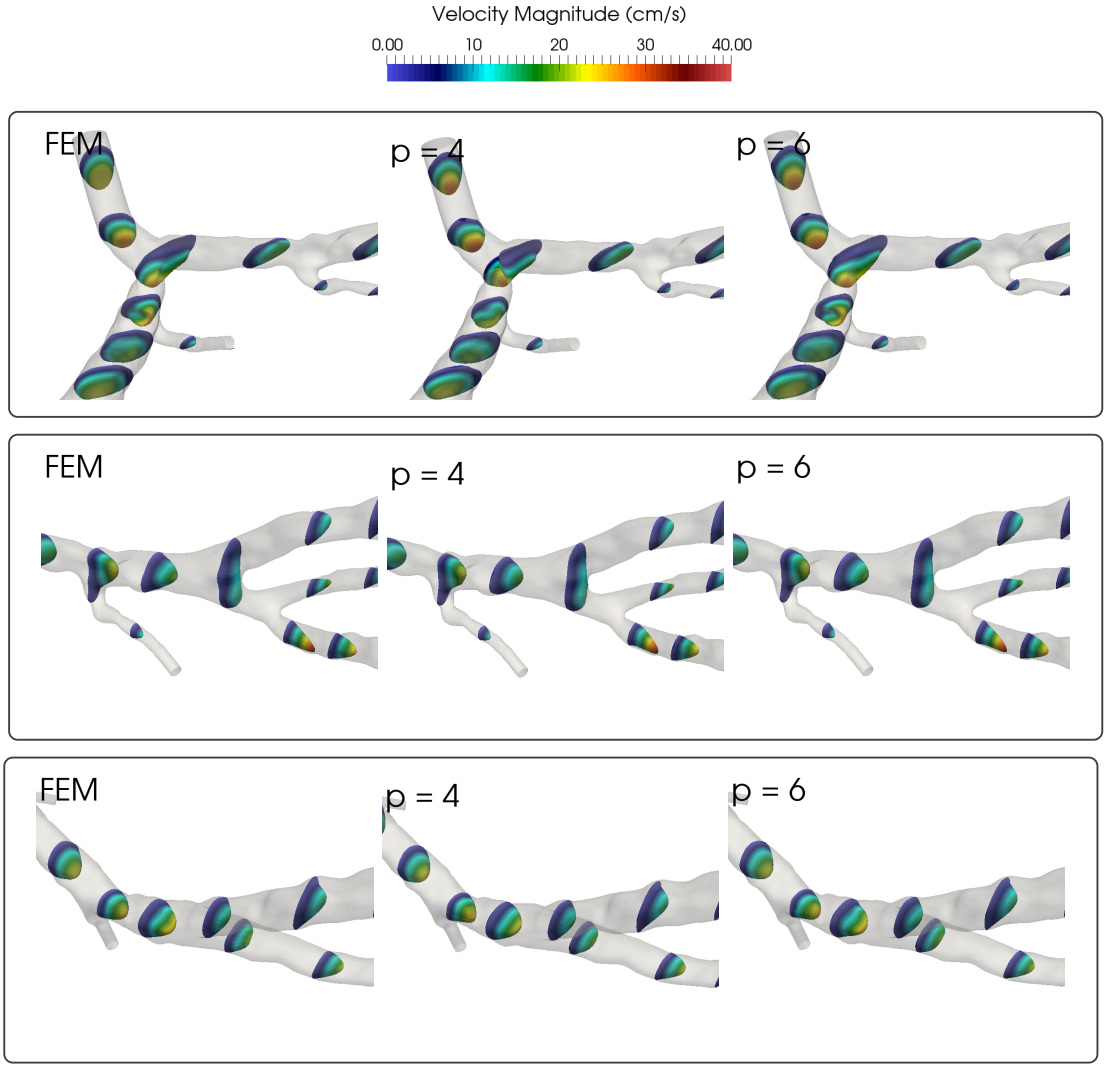

Figure 5.26: Velocity profiles given by FEM and TEPEM, for different transversal order p, in regions A (top row), B (middle row) and C (bottom row).

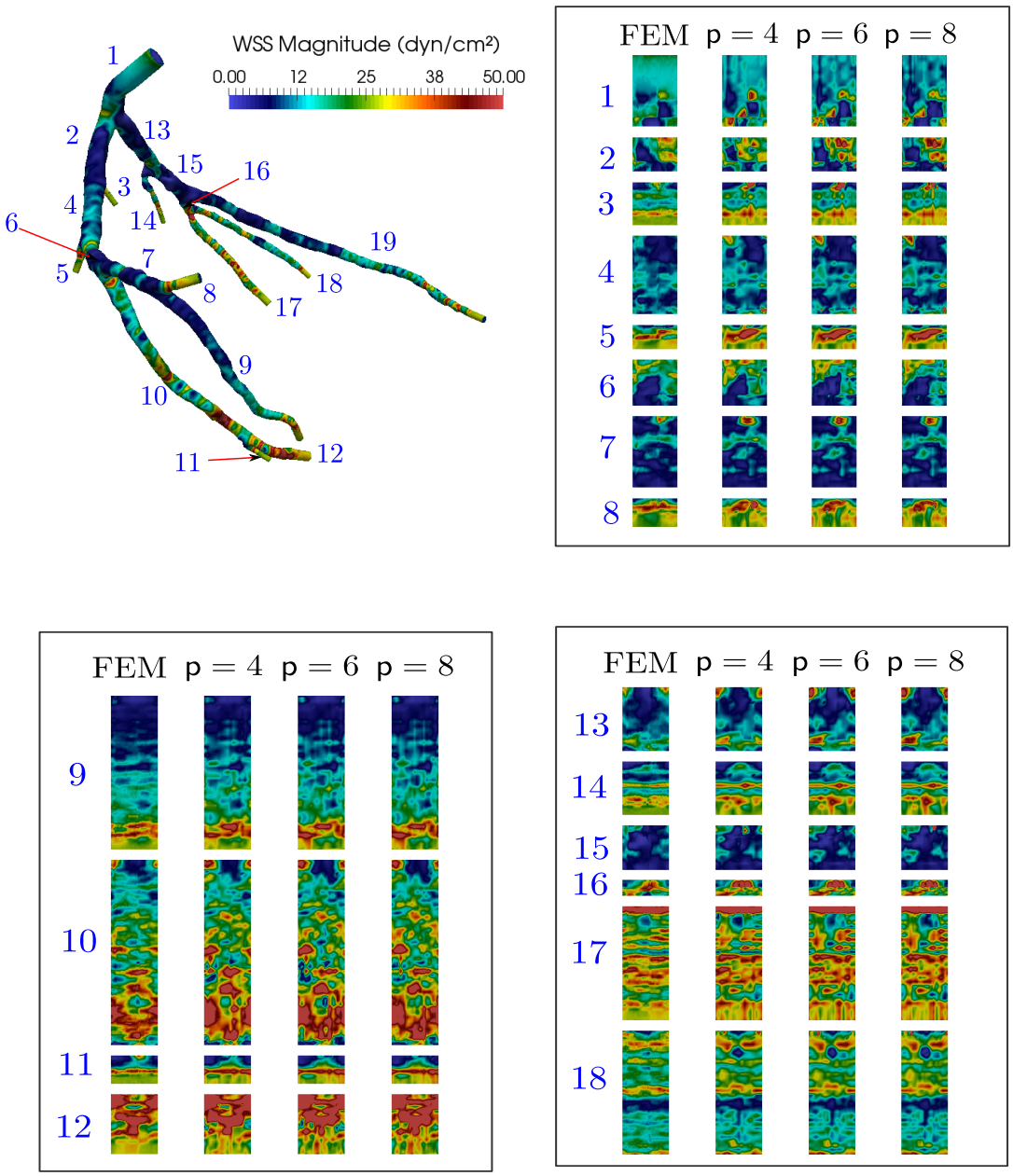

Figure 5.27: Unfolded view of spatial distribution of WSS over the vessel surface obtained with FEM and with TEPEM for different transversal orders.

5.4.2 Right coronary arterial tree

The transient blood flow through a patient-specific right coronary arterial tree, reconstructed based in the centerline/radii information, is addressed here. The centerline, computed from a domain obtained from computed tomography angiography, defines the geometry presented in Figure 5.28.

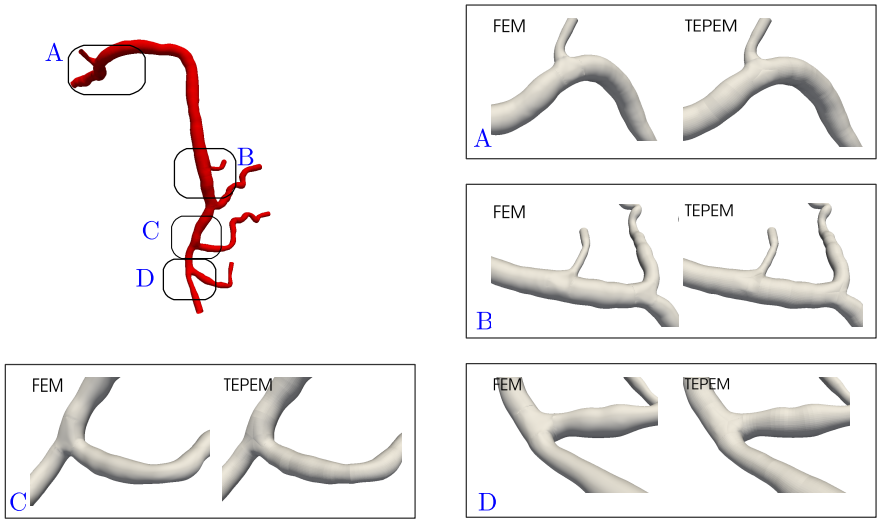

Figure 5.28: Coronary tree geometry reconstructed based in centerline/radii information. Detailed comparison between the mesh employed in FEM simulations and the pipe-element geometry for the TEPEM at four specific locations.

At the inlet, leftmost axial boundary in region A, it is imposed a transient flow rate defined through the signature seen in Figure 5.29 with period $T = 0.8$ seconds, and a resistance-type boundary condition is imposed distributing a total resistance $R = 6 \cdot 10^3$ dyn·s·cm^{-5} among the outlet boundaries. The inlet flow is imposed through a Lagrange multiplier as explained in Section 5.2. Finally, over the wall boundary a no-slip boundary condition is considered. For the time/spatial discretization, time step is chosen as $\Delta t = 1 \cdot 10^{-3}$ s and the geometry is discretized employing a pipe-mesh composed by 290 elements.

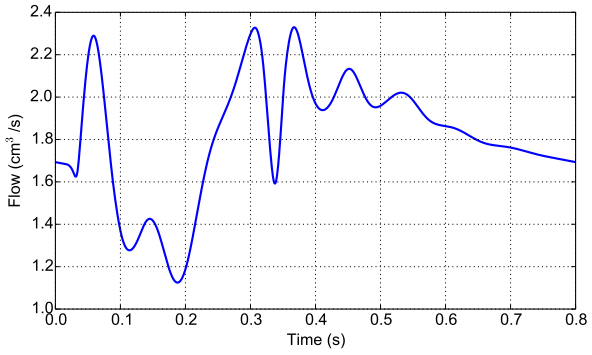

Figure 5.29: Flow signature imposed at the inlet of the right coronary arterial tree.

For the right coronary artery, we will focus our study into exposing the high predictive capabilities of the TEPEM, as a function of the transversal order, together with the sense of convergence reached with respect to this same parameter.

For the transient simulation, 32 processors are employed for the case $\mathsf{p} = 4$, $\mathsf{p} = 6$ and $\mathsf{p} = 8$. The increase in the computational cost when the transversal polynomial order is augmented in the TEPEM is reported in Table 5.6

Table 5.6: Comparison of the computational time with respect to the transversal order in the TEPEM. The cost is compared through the time to perform a single time-step iteration and the wall-clock time of whole simulation. The number of degrees of freedom for each case are also reported.

	Elements	DoFs	Single time-step	Wall-clock time
$\mathsf{p} = 4$		46 023	3.855 s	157.80 min
$\mathsf{p} = 6$	290	90 373	23.359 s	1 078.10 min
$\mathsf{p} = 8$		149 559	100.615 s	3 519.60 min

A comparison between the average velocity (along the second cardiac cycle) is shown in Figure 5.30. Here, a streamline view colored with the magnitude of the velocity is presented for each polynomial order employed in the TEPEM ($\mathsf{p} \in \{4, 6, 8\}$). A more detailed comparison is outlined in Figure 5.31, where it is selected a region of the right coronary arterial tree (see regions C and D in Figure 5.28) to carry out a comparison between the velocity profile provided by the TEPEM, with different transversal orders, at different instants in the cardiac cycle.

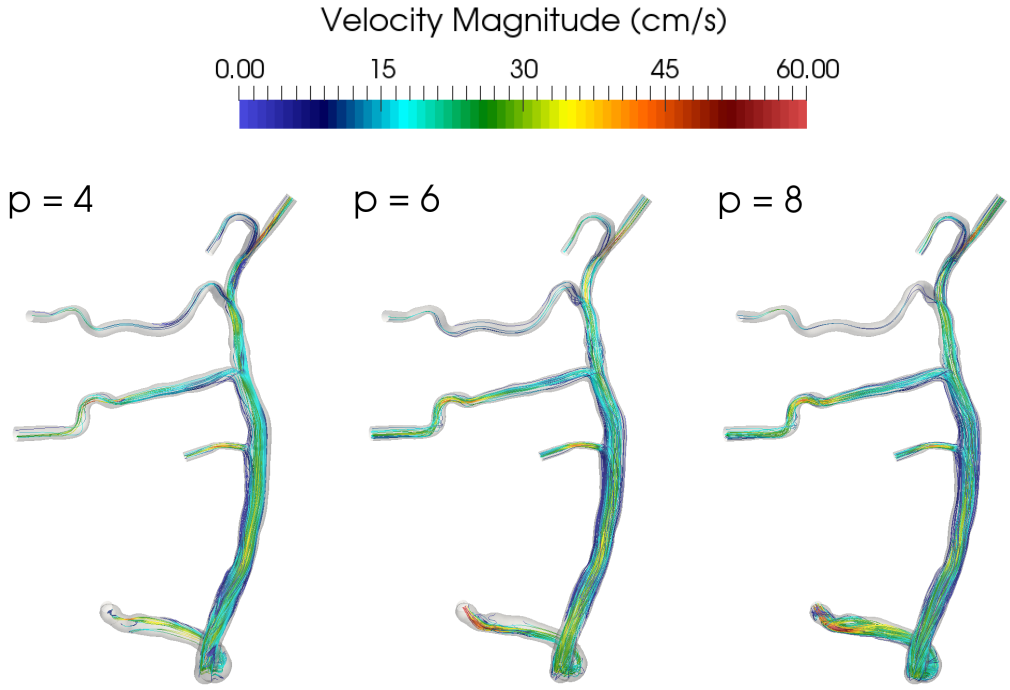

Figure 5.30: Comparison of the streamlines for the mean velocity field in the second cardiac cycle.

The comparison between velocity profiles outlined in Figure 5.31 exhibits the convergence with respect to the parameter p also appreciated in previous examples. Furthermore, in the same figure, streamlines colored by the pressure field allows us to appreciate also the convergence of the TEPEM regarding such field.

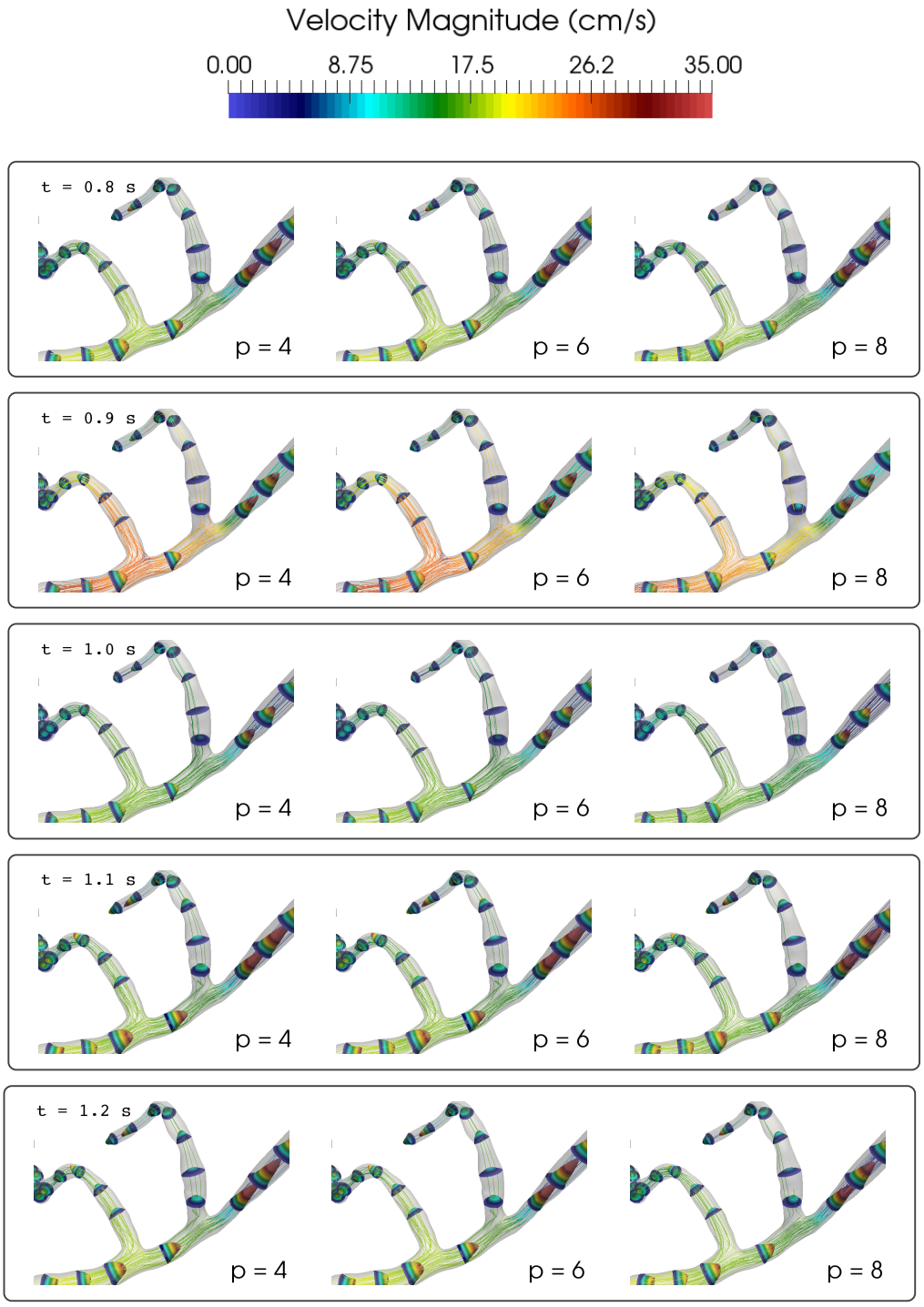

Figure 5.31: Comparison of velocity profiles provided by the TEPEM considering different polynomial orders for the transversal interpolation. Streamlines colored by the pressure field are also presented.

A visualization of the pressure field in the whole domain, and the invariance when increasing the transversal orders in the TEPEM is shown in Figure 5.32.

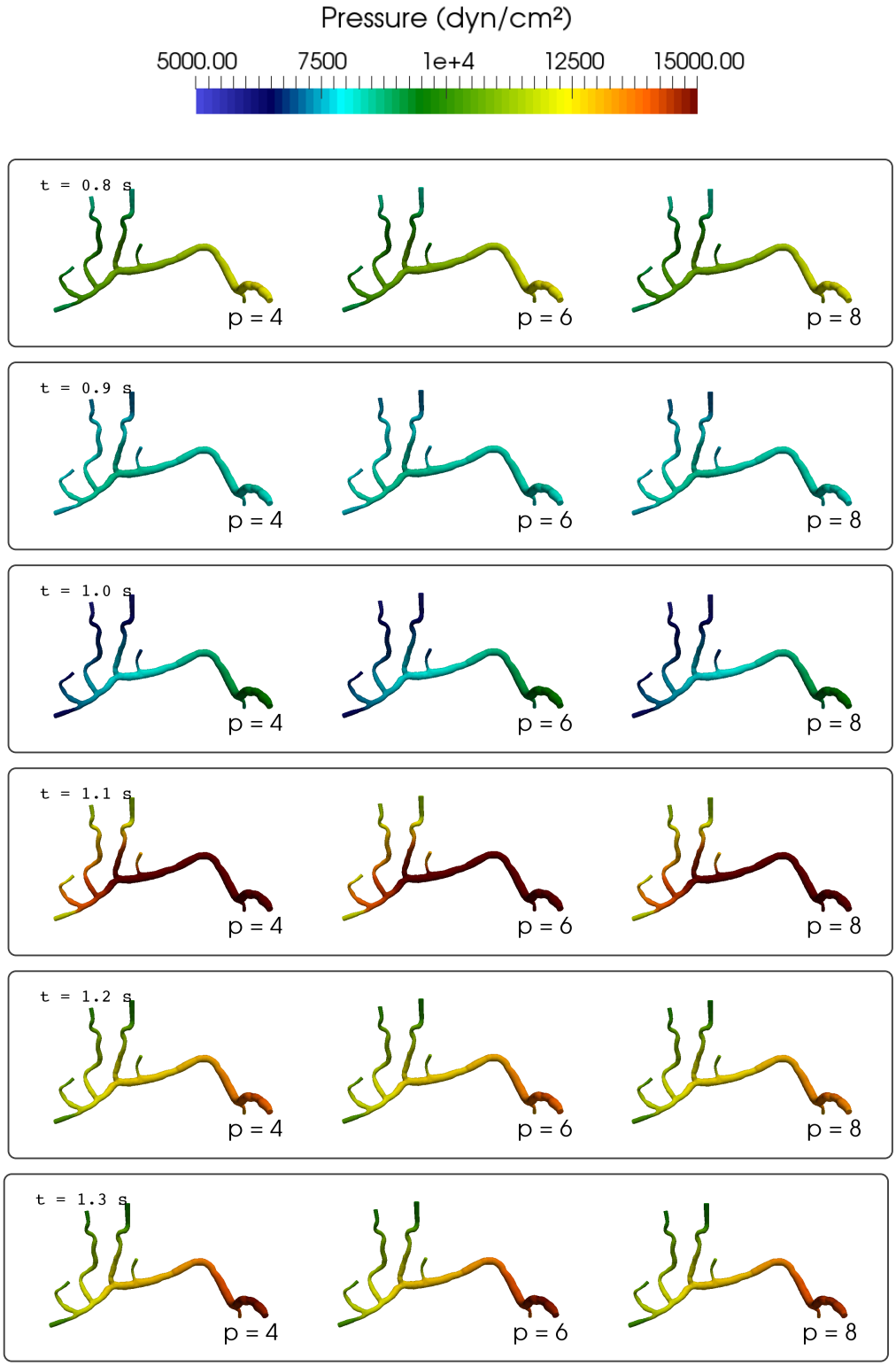

Figure 5.32: Comparison of pressure field along the right coronary artery for different polynomial order for the transversal interpolation in the TEPEM.

5.5 Cerebral blood flow

The demonstrated capabilities of the TEPEM in the accurate description of hemodynamic quantities at a fraction of the computational burden that than employed by standard FEM simulations are analyzed in this section when dealing with a complex and large vascular region in the cardiovascular system. The blood flow through the intracranial arterial tree is simulated here.

For the description of the geometry, the accurate anatomical information provided by the ADAN model ([Blanco et al. 2014b]) is employed here as the basis to reconstruct the three-dimensional geometrical model. The centerline and radii information given by the ADAN model are the input data in the geometrical pipeline proposed for the pipe-type meshing process, resulting in the geometry outlined in Figure 5.33. In the same figure it is also highlighted the reconstruction of the ring-type structure known as the *Circle of Willis*. The geometry, composed by 126 branches and 64 bifurcations, is discretized into a pipe-mesh composed by 3 597 simple pipe elements and 192 transition pipe elements.

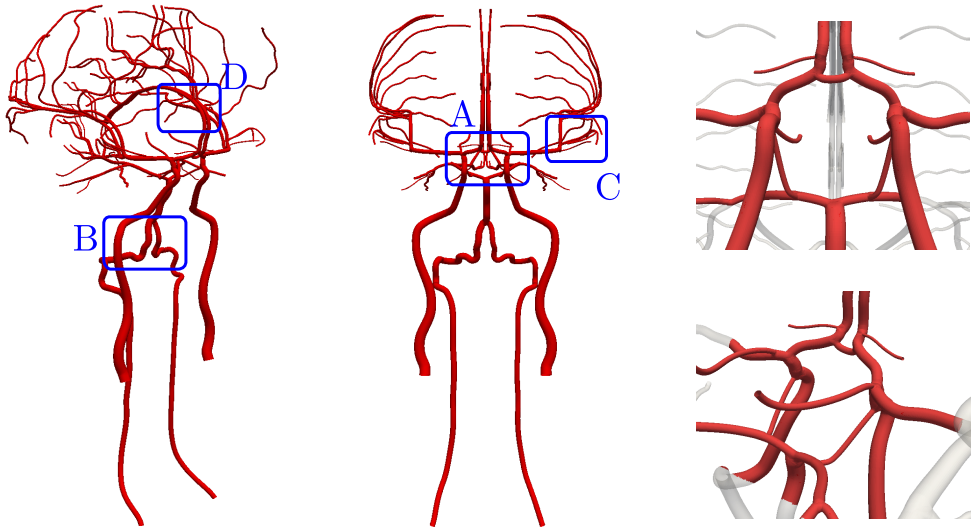

Figure 5.33: Geometry for the 3D intracranial arterial system reconstructed from the 1D ADAN model. Left: Lateral view of the whole system. Center: Frontal view. Right: Detailed view of the Circle of Willis.

To illustrate the application of the TEPEM in this complex vasculature, the blood flow in steady-state regime is simulated. As boundary conditions, a total flow equal to $Q = 5$ cm^3/s is distributed over vertebral and carotid arteries, the four inferior pipe structures in Figure 5.33 and over the outlets a resistance-type condition is imposed considering a total resistance of $R = 6 \cdot 10^3$ $\text{dyn}\cdot\text{s}\cdot\text{cm}^{-5}$, such that the blood pressure is in the normal physiological range. To fully characterize the problem, no-slip boundary conditions are imposed over the lateral surface of the vessel.

The blood flow is simulated employing a number of processors equal to NP = 60 and transversal polynomial order p = 6. Once the high-fidelity in the approximations provided by the TEPEM was stated, no FEM approximation is performed for this problem. The capabilities of the TEPEM to describe the spatial heterogeneities can be appreciated in Figure 5.34 where the approximated pressure and WSS fields are presented.

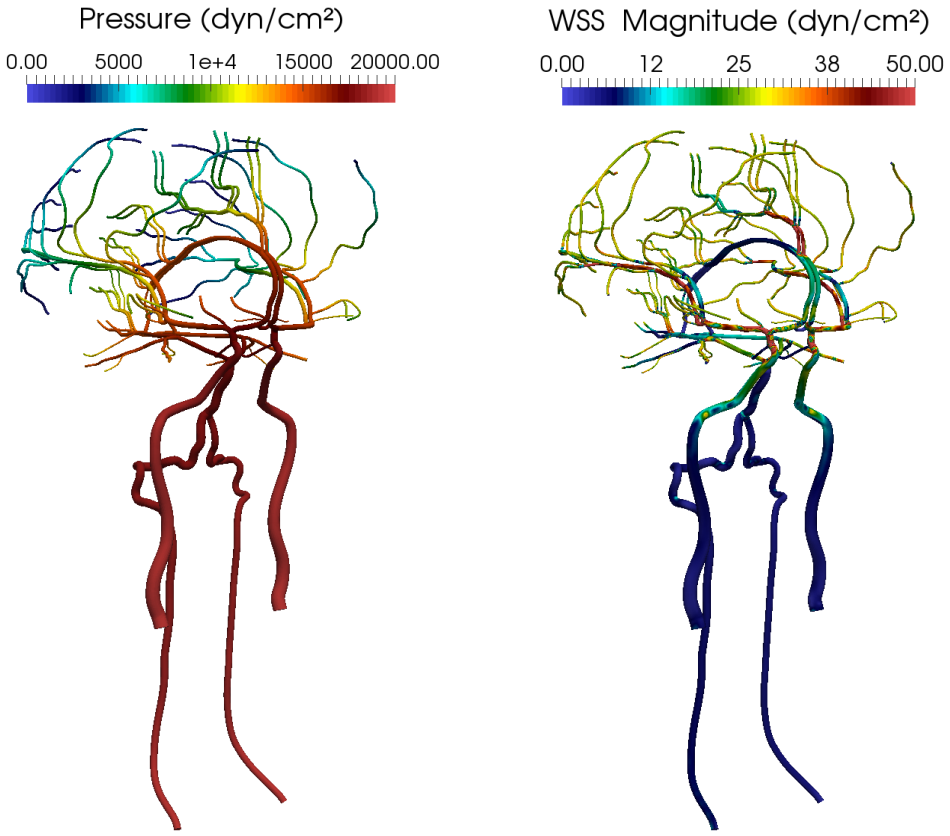

Figure 5.34: Detail of the spatial variation of pressure and WSS fields when the TEPEM is employed to simulate the blood flow through the intracranial arterial system.

Moreover, a detailed view of the physical fields (focused on the regions A, B, C and D described in Figure 5.33) is presented in Figure 5.35. Concerning to the computational time employed in this simulation, the time to perform a single Picard iteration was 36 seconds, while the total wall-clock time until reaching the steady state solution was around 12 minutes. Clearly. this is a small amount of time in view of the level of information provided by the proposed approach.

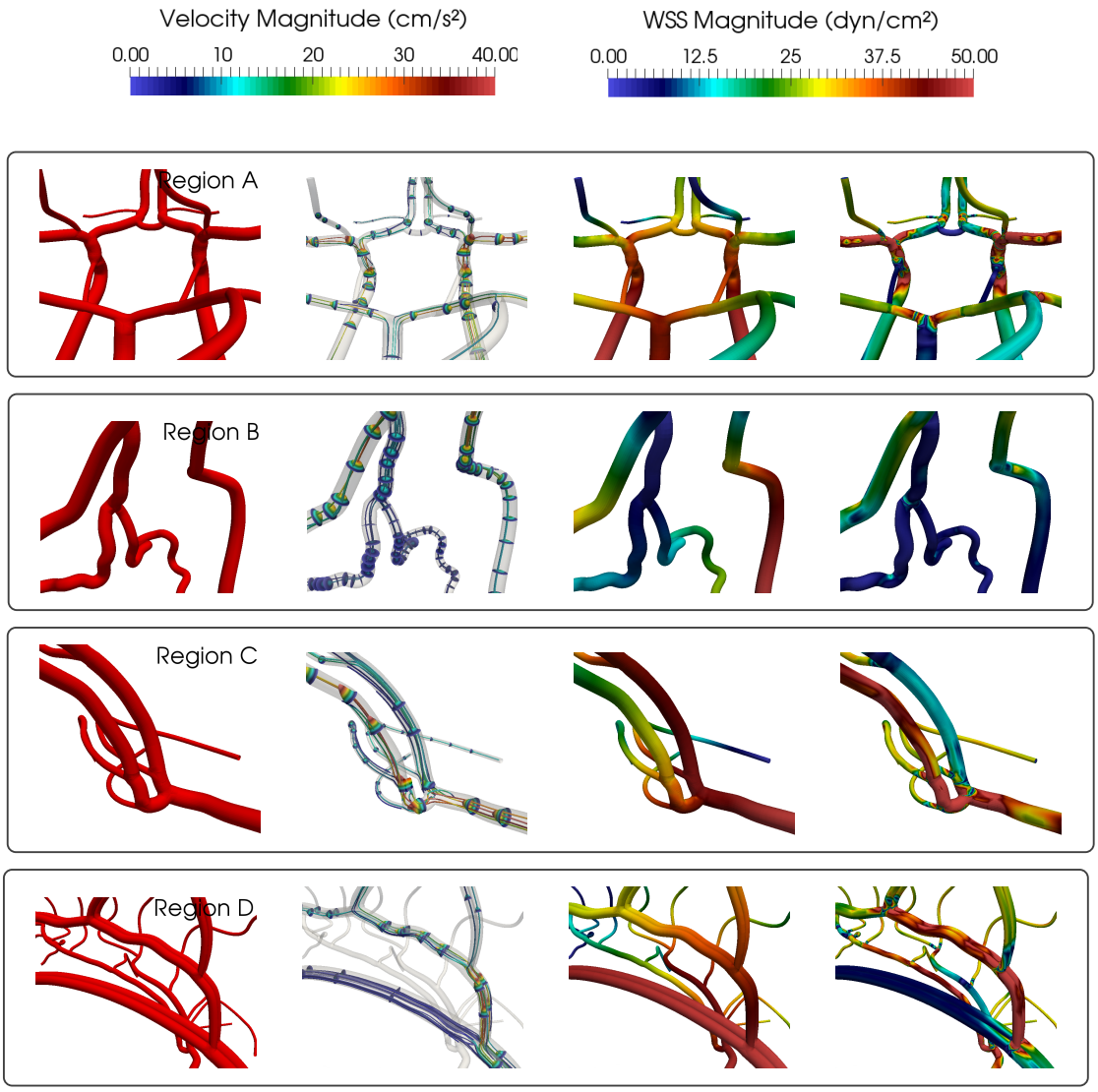

Figure 5.35: Detail of the velocity profiles, pressure and WSS fields provided by the TEPEM in the four regions selected in the intracranial vasculature. In each panel, the scale for the pressure field are conveniently adjusted to visualize the pressure gradients.

5.6 Further remarks

The TEPEM was proposed to become an efficient numerical technique, able to provide relevant hemodynamic information and capable of confronting the trade-off between accuracy and computational cost, which imposes a limit of application on the current numerical techniques in large-scale simulations. Once the abilities of the TEPEM were demonstrated in scalar transport and fluid flow problems, in this chapter it was addressed the study of these characteristics in the scope of blood flow in patient-specific geometries.

For the efficient application of the TEPEM in real-life problems, a pipeline was proposed to deal with the pipe-type discretization of any patient-specific geometry. This pipeline, fundamental for a real use of the proposed strategy in medical practice, covers the different stages in the geometrical discretization: from the image segmentation step to the generation of a final pipe-mesh composed by simple and transition elements. The spatial discretization of the vasculature is performed in a very straightforward and simple way, in comparison with the highly time consuming task of meshing in FEM. Even when an optimization of the pipe-mesh generator must be addressed before a detailed comparison, in terms of computational time, between FEM and TEPEM spatial meshing strategies an initial insight can be obtained with the example addressed in Section 5.4.2. Starting with the same surface triangular mesh, the generation of the volume mesh for the FEM consume a time in the order of 3 minutes while the time employed in the pipeline proposed for the TEPEM was approximately 5 seconds.

Concerning the numerical assessment of the TEPEM addressed in this chapter, comparisons of the accuracy and reduction in the computational burden in the TEPEM were performed with respect to FEM solutions. In contrast to the numerical experiments delivered in the previous chapter, in each numerical test the mesh considered to obtain the FEM reference solution was a standard tetrahedral mesh, employed in the academic practice, instead of an extremely fine mesh. This allows us to establish a better comparison for the computational time and problem size associated to each approach.

Along this chapter, the TEPEM has demonstrated its capability to provide accurate information related to the blood dynamics at a fraction of the time employed by a FEM approach. Many comparisons between the velocity and pressure approximations obtained with the FEM and the TEPEM with different orders in the transversal polynomial interpolants provide solid evidence of the gains when making use of the TEPEM in real applications. Special attention deserves the approximation of the wall shear stress because of its importance in medical applications. The TEPEM, even with low order for the transversal polynomials ($\mathsf{p} \in \{4, 6\}$) is able to provide an accurate spatial description of the wall shear stress, pointing out the high heterogeneity of this field with a low computational cost if compared with the FEM alternative.

Finally, the integration of the high predictive capabilities of the TEPEM with the detailed anatomical description provided by the ADAN model was exemplified through the simulation of the blood flow in the cerebral arterial system. The detailed information provided by the TEPEM, in the spatial description of velocity, pressure and wall shear stress fields, opens the room for developing extremely large scale blood flow simulations, enabling us to retrieve information about the entire circulation at an unprecedented level of integration between anatomy and phenomenology.

Chapter 6

Conclusions

6.1 Final remarks

The potentialities of computational hemodynamics on diagnosis, prognosis and their common use in the daily clinical practice continue to be largely demonstrated in the specialized biomedical literature. Nevertheless, at the same time, the massive use of 3D flow models is strongly restricted because of the enormous computational cost demanded for the simulation of large portions of the cardiovascular system. The trade-off between accuracy and computational cost poses serious limits to current numerical alternatives. Simplified 1D models are inexpensive but unable to provide high fidelity spatial description of physical fields, identify recirculation zones as well as point out the heterogeneities in important indexes such as the wall shear stress. In turn, the information provided by full 3D models is richer in details, but achieving these solutions demands for a computational burden which is prohibitive in the daily medical practice.

In this work a novel numerical strategy was proposed, capable of effectively dealing with the almost inevitable trade-off between accuracy and computational burden. Moreover, the proposed methodology is versatile enough to be employed in complex patient-specific geometries and is able to provide high fidelity predictions of important flow-related quantities at a fraction of the time taken by classical Finite Element Method (FEM). The proposed approach, coined as Transversally Enriched Pipe Element Method (TEPEM), was studied along this work and its capabilities were extensively demonstrated through several numerical examples in scalar transport problems, fluid flow in synthetic academic geometries and complex patient-specific hemodynamic simulations.

For scalar transport problems, an extensive numerical assessment was addressed to demonstrate the accuracy obtained with the TEPEM compared to analytical solutions (when available) or reference solutions obtained with the FEM in extremely fine meshes. A similar convergence study was presented for fluid flow problems together with a numerical validation of the suitability of the proposed combination for the discrete spaces of velocity and pressure in order to satisfy the inf-sup condition.

Concerning the application of the proposed strategy in the blood flow modeling through patient-specific geometries, the advantages of the TEPEM against the standard FEM are worthwhile to mentioning. The judicious use of the number of degrees of freedom in the TEPEM allows us to solve with high degree of fidelity the blood dynamics with relatively small discrete problems and with a gain in the computational time ranging between 150 and 600 times for the cases exemplified through the numerical experiments.

6.2 Future perspectives

The promising results obtained by the use of the TEPEM, specially in the simulation of blood flow through complex patient-specific geometries, motivate further research aiming its inclusion in the biomedical research as well as production stages. Some of the future perspectives and points still to be improved are listed below.

1. Regarding the convergence analysis, further investigations are required to provide theoretical convergence rates for the TEPEM. Convergence results in similar methodologies, such as the Hierarchical Modeling, give reasonable insights about the convergence of our approach but the rates of convergence specific for the TEPEM are still under investigation.

2. An analysis of the suitability of the discrete spaces involved in the fluid-flow modeling is required, that is, a theoretical proof of the inf-sup condition of this type of hybrid-order interpolation scheme is still in order.

3. Aiming of simulating the interplay between the arterial wall and the blood flow, we also envision the adaptation of the TEPEM to handle fluid-structure interaction phenomena, which is also of the utmost importance for the application of this methodology into the modeling of propagatory phenomena in the cardiovascular system.

4. Another pending issue consists in exploring the coupling of the TEPEM with reduced order methodologies, such as the 1D models, aiming of further reducing the computational cost of simulating the blood flow in the whole cardiovascular system.

5. Finally, the improvement of the proposed geometrical pipeline could enrich the accuracy of the representation of the vasculature. The use of IsoGeometric Analysis applied to the axial discretization of the arterial regions and alternatives in the bifurcation reconstruction step are under investigation.

Bibliography

Alastruey J., Parker K.H., Peiró J., Byrd S.M. and Sherwin S.J. (2007). Modelling the circle of Willis to assess the effects of anatomical variations and occlusions on cerebral flows. J. Biomech. 40, 1794–1805.

Aletti M., Mansilla Alvarez L.A., Blanco P.J., Guzzetti S., Perotto S., Reali A., Rusconi P. and Veneziani A. (2016). Hierarhical model reduction methods for incompressible fluids: Basics, isogeometric formulation, applications. in 'Proceedings of HOFEIM 2016. High Order Finite Element and Isogeometric Methods, Jerusalem'.

Aletti M., Mansilla Alvarez L.A., Blanco P.J., Perotto S. and Veneziani A. (2014). Hierarchical model (himod) reduction for incompressible fluid dynamics in rigid and deformable pipes. in 'Proceedings of WCCM 2014. World Congress on Computational Mechanics, Barcelona'.

Aletti M., Perotto S. and Veneziani A. (2017). Himod reduction of advection–diffusion–reaction problems with general boundary conditions. J. Sci. Comput. pp. 1–31.

Antiga L., Ene-Iordache B. and Remuzzi A. (2003). Computational geometry for patient-specific reconstruction and meshing of blood vessels from MR and CT angiography. IEEE Trans. Med. Imag. 22(5), 674–684.

Antiga L., Piccinelli M., Botti L., Ene-Iordache B., Remuzzi A. and Steinman D.A. (2008). An image-based modeling framework for patient-specific computational hemodynamics. Medical & biological engineering & computing 46(11), 1097.

Armaly B.F., Durst F., Pereira J.C.F. and Schönung B. (1983). Experimental and theoretical investigation of backward-facing step flow. Journal of fluid Mechanics 127, 473–496.

Arnold D.N. and Awanou G. (2011). The serendipity family of finite elements. Foundations of Computational Mathematics 11(3), 337–344.

Arnold D.N., Brezzi F. and Fortin M. (1984). A stable finite element for the Stokes equations. Calcolo 21(4), 337–344.

Atkinson K. and Han W. (2005). Theoretical numerical analysis. Vol. 39. Springer.

Avolio A.P. (1980). Multi-branched model of the human arterial system. Med Biol Eng Comput 18, 709–718.

Babuška I. (1971). Error-bounds for finite element method. Numerische Mathematik 16(4), 322–333.

Babuska I., Szabo B.A. and Katz I.N. (1981). The p-version of the finite element method. SIAM journal on numerical analysis 18(3), 515–545.

Balay S., Abhyankar S., Adams M.F., Brown J., Brune P., Buschelman K., Dalcin L., Eijkhout V., Gropp W.D., Kaushik D., Knepley M.G., May D.A., McInnes L.C., Rupp K., Smith B.F., Zampini S., Zhang H. and Zhang H. (2017a). PETSc users manual. Technical Report ANL-95/11 - Revision 3.8. Argonne National Laboratory.
URL: *http://www.mcs.anl.gov/petsc*

Balay S., Abhyankar S., Adams M.F., Brown J., Brune P., Buschelman K., Dalcin L., Eijkhout V., Gropp W.D., Kaushik D., Knepley M.G., May D.A., McInnes L.C., Rupp K., Smith B.F., Zampini S., Zhang H. and Zhang H. (2017b). 'PETSc Web page'.
URL: *http://www.mcs.anl.gov/petsc*

Bathe KJ (2001). The inf–sup condition and its evaluation for mixed finite element methods. Computers & structures 79(2), 243–252.

Belhachmi Z., Bernardi C. and Deparis S. (2006). Weighted clément operator and application to the finite element discretization of the axisymmetric stokes problem. Numerische Mathematik 105(2), 217–247.

Benzi M., Golub G.H. and Liesen J. (2005). Numerical solution of saddle point problems. Acta numerica 14, 1–137.

Bernardi C., Dauge M., Maday Y. and Azaïez M. (1999). Spectral methods for axisymmetric domains. Vol. 3. Gauthier-Villars Paris.

Bernardi C. and Maday Y. (1997). Spectral discretizations of the navier-stokes equations. in 'Handbook of Numerical Analysis, Vol. V'. chapter 5, pp. 373–440.

Bharadvaj B.K., Mabon R.F. and Giddens D.P. (1982a). Steady flow in a model of the human carotid bifurcation. part II: laser-doppler anemometer measurements. J. Biomech. 15(5), 363367–365378.

Bharadvaj B.K., Mabon R.F. and Giddens G.P. (1982b). Steady flow in a model of the human carotid bifurcation. part I: flow visualization. J. Biomech. 15(5), 349–362.

Blanco P.J., Mansilla Alvarez L.A. and Feijóo R.A. (2015). Hybrid element-based approximation for the Navier–Stokes equations in pipe-like domains. Comp. Meth. Appl. Mech. Engrg. 283, 971–993.

Blanco P.J., Pivello M.R., Urquiza S.A. and Feijóo R.A. (2009). On the potentialities of 3D–1D coupled models in hemodynamics simulations. J. Biomech. 42, 919–930.

Blanco P.J., Urquiza S.A. and Feijóo R.A. (2010). Assessing the influence of heart rate in local hemodynamics through coupled 3D-1D-0D models. Int. J. Num. Meth. Biomed. Engng. 26, 890–903.

Blanco P.J., Watanabe S.M., Dari E.A., Passos M.A.R.F. and Feijóo R.A. (2014a). Blood flow distribution in an anatomically detailed arterial network model: criteria and algorithm. Biomechecanics and Modeling in Mechanobiology 13, 1303–1330.

Blanco P.J., Watanabe S.M., Passos M.A.R.F., Lemos P.A. and Feijóo R.A. (2014b). An anatomically detailed arterial network model for one-dimensional computational hemodynamics. IEEE Trans. Biomed. Eng. 62(2), 736–753.

Botnar R., Rappitsch G., Scheidegger M.B., Liepsch D., Perktold K. and Boesiger P. (2000). Hemodynamics in the carotid artery bifurcation: a comparison between numerical simulations and in vitro MRI measurements. J. Biomech. 33, 137–144.

Brenner S. and Scott R. (2007). The mathematical theory of finite element methods. Vol. 15. Springer Science & Business Media.

Brezis H. (2010). Functional analysis, Sobolev spaces and partial differential equations. Springer Science & Business Media.

Brezzi F. (1974). On the existence, uniqueness and approximation of saddle-point problems arising from Lagrangian multipliers. Revue française d'automatique, informatique, recherche opérationnelle. Analyse numérique 8(R2), 129–151.

Brooks A.N. and Hughes T.J.R. (1982). Streamline upwind/petrov-galerkin formulations for convection dominated flows with particular emphasis on the incompressible navier-stokes equations. Comp. Meth. Appl. Mech. Engrg. 32(1-3), 199–259.

Bulant C.A. (2017). Computational models for the geometric and functional assessment of the coronary circulation. PhD thesis. Laboratório Nacional de Computação Científica - LNCC, Petrópolis - Brazil.

Bulant C.A., Blanco P.J., Lima T.P., Assunçao A.N., Liberato G., Parga J.R., Ávila L.F.R., Pereira A.C., Feijóo R.A. and Lemos P.A. (2017a). A computational framework to characterize and compare the geometry of coronary networks. Int. J. Num. Meth. Biomed. Engng. 33(3), e02800.
URL: *http://doi.wiley.com/10.1002/cnm.2800*

Bulant C.A., Blanco P.J., Talou G.D. Maso, Bezerra C. Guedes, Lemos P.A. and Feijóo R.A. (2017b). A head-to-head comparison between CT- and IVUS-derived coronary blood flow models. J. Biomech. 51, 65–76.
URL: *http://linkinghub.elsevier.com/retrieve/pii/S002192901631260X*

Canuto C., Hussaini M.Y., Quarteroni A. and Thomas A. Jr. (1988). Spectral methods in fluid dynamics. Springer Science & Business Media.

Canuto C., Hussaini M.Y., Quarteroni A. and Zang T.A. (2010). Spectral methods: Fundamentals in single domains. Springer.

Canuto C., Maday Y. and Quarteroni A. (1982). Analysis of the combined finite element and fourier interpolation. Numerische Mathematik 39(2), 205–220.

Carapau F. and Sequeira A. (2006). 1d models for blood flow in small vessels using the cosserat theory. WSEAS Transactions on Mathematics 5(1), 54.

Caro C.G., Fitz-Gerald J.M. and Schroter R.C. (1971). Atheroma and arterial wall shear observation, correlation and proposal of a shear dependent mass transfer mechanism for atherogenesis. Proceedings of the Royal Society of London B: Biological Sciences 177(1046), 109–133.

Caro C.G., Lewis C.T. and Weinbaum S. (1975). A mechanism by which mechanical disturbances can increase the uptake of macromolecules by the artery wall. The Journal of physiology 246(2), 71P.

Cebral J.R., Mut F., Weir J. and Putman C.M. (2011). Quantitative characterization of the hemodynamic environment in ruptured and unruptured brain aneurysms. Am. J. Neuroradiol. 32, 145–151.

Cebral J.R., Yim P.J., Lohner R., Soto O. and Choyke P.L. (2002). Blood flow modeling in carotid arteries with computational fluid dynamics and mr imaging.. Acad. Radiol. 9(1), 1286–1299.

Chapelle D. and Bathe K.-J. (1993). The inf-sup test. Comput. Struct. 47(4-5), 537–545.

Ciarlet P. G. (1978). The finite element method for elliptic problems. 1 edn. North-Holland Publishing Company.

Coşkun A., Chen C., Stone P.H. and Feldman C.L. (2006). Computational fluid dynamics tools can be used to predict the progression of coronary artery disease. Physica A: Statistical Mechanics and its Applications 362(1), 182–190.

Courant R. (1943). Variational methods for the solution of problems of equilibrium and vibrations. Bulletin of the American mathematical Society 49(1), 1–23.

DeBlois B.M. (1997). Linearizing convection terms in the navier-stokes equations. Comp. Meth. Appl. Mech. Engrg. 143(3-4), 289–297.

Deparis S. (2004). Numerical analysis of axisymmetric flows and methods for fluid-structure interaction arising in blood flow simulation. PhD thesis. École Polytechnique Fédérale de Lausanne - EPFL, France.

Elman H.C., Silvester D.J. and Wathen A.J. (2014). Finite elements and fast iterative solvers: with applications in incompressible fluid dynamics. Numerical Mathematics & Scientific Computation.

Ern A., Perotto S. and Veneziani A. (2008). Hierarchical model reduction for advection-diffusion-reaction problems. in 'Numerical Mathematics and Advanced Applications, K. Kunisch, G. Of and O. Steinbach eds.'. Springer. pp. 703–710.

Euler L. (1844). Principia pro motu sanguinis per arterias determinando. Opera posthuma mathematica et physica anno pp. 814–823.

Evans L. C. (1997). Partial Differential Equations. American Mathematical Society.

Formaggia L., Gerbeau J.F., Nobile F. and Quarteroni A. (2001). On the coupling of 3d and 1d navier–stokes equations for flow problems in compliant vessels. Comp. Meth. Appl. Mech. Engrg. 191(6), 561–582.

Formaggia L., Gerbeau J.F., Nobile F. and Quarteroni A. (2002). Numerical treatment of defective boundary conditions for the navier–stokes equations. SIAM J. Num. Anal. 40(1), 376–401.

Formaggia L., Lamponi D. and Quarteroni A. (2003). One-dimensional models for blood flow in arteries. J. Engrg. Math. 47(3-4), 251–276(26).

Formaggia L., Quarteroni A. and Veneziani A. (2009). Multiscale models of the vascular system. in 'Cardiovascular Mathematics, Modeling, Simulation and Applications I'. chapter 11, pp. 395–446.

Formaggia L., Quarteroni A. and Veneziani A. (2010). Cardiovascular Mathematics: Modeling and simulation of the circulatory system. Vol. 1. Springer Science & Business Media.

Fried I. (1972). Bounds on the extremal eigenvalues of the finite element stiffness and mass matrices and their spectral condition number. Journal of Sound and Vibration 22(4), 407–418.

Friedman M.H., Deters O.J., Bargeron C.B., Hutchins G.M. and Mark F.F. (1986). Shear-dependent thickening of the human arterial intima. Atherosclerosis 60, 161–171.

Giannoglou G.D., Soulis J.V., Farmakis T.M., Farmakis D.M. and Louridas G.E. (2002). Haemodynamic factors and the important role of local low static pressure in coronary wall thickening. Int. J. Cardiol. 86(1), 27–40.

Gibson C.M., Díaz L., Kandarpa K., Sacks F.M., Pasternak R.C., Sandor T., Feldman C. and Stone P.H. (1993). Relation of vessel wall shear stress to atherosclerosis progression in human coronary arteries.. Arteriosclerosis, Thrombosis, and Vascular Biology 13(2), 310–315.

Giddens D.P., Zarins C.K. and Glagov S. (1993). The role of fluid mechanics in the localization and detection of atherosclerosis. J. Biomech. Engrg. 115, 588–594.

Girault V. and Raviart P. (1986). Finite Element Methods for Navier-Stokes Equations. 1 edn. Springer-Verlag.

Glagov S., Zarins C., Giddens D.P. and Ku D.N. (1988). Hemodynamics and atherosclerosis. Arch. Pathol. Lab. Med. 112(10), 1018–1031.

Green A.E. and Naghdi P.M. (1993). A direct theory of viscous fluid flow in pipes I. Basic general developments. Phil. Trans. R. Soc. Lond. A 342, 525–542.

Green A.E., Naghdi P.M. and Stallard M.J. (1993). A direct theory of viscous fluid flow in pipes II. Flow of incompressible viscous fluids in curved pipes. Phil. Trans. R. Soc. Lond. A 342, 543–572.

Grinberg L., Anor T., Madsen J.R., Yakhot A. and Karniadakis G.E. (2009). Large-scale simulation of the human arterial tree. Clin. Exp. Pharmacol. Physiol. 36, 194–205.

Grinberg L., Cheever E., Anor T., Madsen J.R. and Karniadakis G.E. (2011). Modeling blood flow circulation in intracranial arterial networks: a comparative 3d/1d simulation study. Ann. Biomed. Engng. 39(1), 297–309.

Grinberg L. and Karniadakis G.E. (2008). Outflow boundary conditions for arterial networks with multiple outlets. Ann. Biomed. Engng. 36, 1496–1514.

Gupta A.K. (1978). A finite element for transition from a fine to a coarse grid. Int. J. Num. Meth. Engng. 12(1), 35–45.

Guzzetti S. (2014). Hierarchical model reduction for incompressible flows in cylindrical domains. Master's thesis. Politecnico di Milano.

Hecht F. (2012). New development in freefem++. Journal of numerical mathematics 20(3-4), 251–266.

Hecht F., Pironneau O., Le Hyaric A. and Ohtsuka K. (2005). FreeFem++ manual.

HeMoLab (2015). Hemodynamics Modeling Laboratory (HeMoLab). http://hemolab.lncc.br/.

Huberts W., Bosboom E.M. and van de Vosse F.N. (2009). A lumped model for blood flow and pressure in the systemic arteries based on an approximate velocity profile function.. 6(1), 27–40.

Hughes T.J.R. (1974). A Study of the One-Dimensional Theory of Arterial Pulse Propagation. PhD thesis. University of California, Berkeley.

Hughes T.J.R. and Brooks A.N. (1979). A multi-dimensional upwind scheme with no crosswind diffusion. in 'FEM for convection dominated flows'. ASME. New York.

Hughes T.J.R., Franca L.P. and Mallet M. (1987). A new finite element formulation for computational fluid dynamics: VI. Convergence analisys of the generalized SUPG formulation for linear time-dependent multimensinal advective-diffusive systems. Comp. Meth. Appl. Mech. Engrg. (63), 97–112.

Hughes T.J.R. and Lubliner J. (1973). On the one-dimensional theory of blood flow in the larger vessels. Math. Biosci. 18, 161–170.

Karakashian O.A. (1982). On a Galerkin–Lagrange multiplier method for the stationary Navier–Stokes equations. SIAM Journal on Numerical Analysis 19(5), 909–923.

Karino T. (1985). Microscopic structure of disturbed flows in the arterial and venous systems, and its implication in the localization of vascular diseases.. International angiology: a journal of the International Union of Angiology 5(4), 297–313.

Karino T. and Goldsmith H.L. (1983). Role of blood cell-wall interactions in thrombogenesis and atherogenesis: a microrheological study. Biorheology 21(4), 587–601.

Karniadakis G. and Sherwin S. (2013). Spectral/hp element methods for computational fluid dynamics. Oxford University Press.

Kim J. and Moin P. (1985). Application of a fractional-step method to incompressible navier-stokes equations. Journal of computational physics 59(2), 308–323.

Kraus H. (1967). Thin elastic shells. John Wiley & Sons.

Ku D.N., Giddens D.P., Zarins C.K. and Glagov S. (1985). Pulsatile flow and atherosclerosis in the human carotid bifurcation. Positive correlation between plaque location and low oscillating shear stress. Arteriosclerosis 5, 293–302.

LaBarbera M. (1990). Principles of design of fluid transport systems in zoology. Science 249(4972), 992–1000.

Ladyzhenskaya O.A. (1969). The mathematical theory of viscous incompressible flow. Vol. 12. Gordon & Breach New York.

Lagana K., Dubini G., Migliavacca F., Pietrabissa R., Pennati G., Veneziani A. and Quarteroni A. (2002). Multiscale modelling as a tool to prescribe realistic boundary conditions for the study of surgical procedures. Biorheology 39(3), 359–364.

Lee T., Huang K., Hsiao M., Tang S. and Young S. (2004). Electrical lumped model for arterial vessel beds. Comput. Methods Programs Biomed. 73(3), 209–219.

LeVeque R.J. (2002). Finite volume methods for hyperbolic problems. Vol. 31. Cambridge university press.

Liang F. and Liu H. (2005). A closed-loop lumped parameter computational model for human cardiovascular system. JSME International Journal Series C Mechanical Systems, Machine Elements and Manufacturing 48(4), 484–493.

Lorensen W.E. and Cline H.E. (1987). Marching cubes: A high resolution 3d surface construction algorithm. in 'ACM siggraph computer graphics'. Vol. 21. ACM. pp. 163–169.

Lucia D., Beran P. and Silva W. (2004). Reduced-order modeling: new approaches for computational physics.. Prog. Aerosp. Sci. 40(1-2), 51–117.

Maday Y. and Patera A. (1989). Spectral element methods for the incompressible navier-stokes equations. State-of-the-art surveys on computational mechanics 4, 71–143.

Mansilla Alvarez L.A. (2014). Galerkin formulations with hybrid interpolation for incompressible fluid flow in tubular domains (in portuguese). Master's thesis. Laboratório Nacional de Computação Científica - LNCC, Petrópolis - Brazil.

Mansilla Alvarez L.A., Blanco P.J., Bulant C.A., Dari E., Veneziani A. and Feijóo R.A. (2017a). Transversally enriched pipe element method (tepem): An effective numerical approach for blood flow modeling. Int. J. Num. Meth. Biomed. Engng. 33(4).

Mansilla Alvarez L.A., Blanco P.J., Bulant C.A. and Feijóo R.A. (2017b). Fast blood flow simuation in three-dimensional arterial trees. in 'Proceedings of CILAMCE 2017. XXXVIII Ibero-Latin American Congress on Computational Methods in Engineering, Florianópolis'.

Mansilla Alvarez L.A., Blanco P.J., Bulant C.A. and Feijóo R.A. (2018-submitted). Towards fast hemodynamics simulations in large-scale circulatory networks. Comp. Meth. Appl. Mech. Engrg. .

Mansilla Alvarez L.A., Blanco P.J. and Feijóo R.A. (2015). Pipe-oriented finite elements for the three-dimensional blood flow simulations. in 'Proceedings of USNCCM13. US National Congress on Computational Mechanics, San Diego'.

Mansilla Alvarez L.A., Blanco P.J. and Feijóo R.A. (2017c). An effective method for the numerical solution of blood flow in 3d bifurcated regions. in 'Proceedings of CNMAC 2017. XXXVII Congresso nacional de matemática aplicada e computacional, São José dos Campos'.

Mansilla Alvarez L.A., Blanco P.J. and Feijóo R.A. (2017d). Fast patient-specific blood flow simulations: The transversally enriched pipe element method (tepem). in 'Proceedings of EMI 2017. 3rd Engineering Mechanics Institute International Conference, Rio de Janeiro'.

Mansilla Alvarez L.A., Blanco P.J. and Feijóo R.A. (2018). On enhanced reduced models for advection-diffusion problems. in 'Proceedings of EAMC 2018. XI Encontro Acadêmico de Modelagem Computacional, Petrópolis'.

Maurits N.M., Loots G.E. and Veldman A.E.P. (2007). The influence of vessel wall elasticity and peripheral resistance on the carotid artery flow wave form: A CFD model compared to in vivo ultrasound measurements. J. Biomech. 40, 427–436.

McDill J.M., Goldak J.A., Oddy A.S. and Bibby M.J. (1987). Isoparametric quadrilaterals and hexahedrons for mesh-grading algorithms. Int. J. Num. Meth. Biomed. Engng. 3(2), 155–163.

Melenk J.M. (2002). On condition numbers in hp–FEM with Gauss–Lobatto-based shape functions. Journal of Computational and Applied Mathematics 139(1), 21–48.

Morbiducci U., Raffaele R., Grigioni M. and Redaelli A. (2007). Helical flow as fluid dynamic signature for atherogenesis risk in aortocoronary bypass: a numerical study. J. Biomech. 40, 519–534.

Morton D.J., Tyler J.M. and Dorroh J.R. (1995). A new 3d finite element for adaptive h-refinement in 1-irregular meshes. Int. J. Num. Meth. Engng. 38(23), 3989–4008.

Morton K.W. and Mayers D.F. (2005). Numerical Solution of Partial Differential Equations. Cambridge University Press.

Nerem R.M. and Cornhill J.F. (1980). The role of fluid mechanics in atherogenesis. J. Biomech. Engrg. 102, 181–189.

Olufsen M.S. (1999). Structured tree outflow condition for blood flow in larger systemic arteries. Am. J. Physiol. 276, H257–H268.

Olufsen M.S., Peskin C.S., Kim W.Y., Pedersen E.M., Nadim A. and Larsen J. (2000). Numerical simulation and experimental validation of blood flow in arteries with structured-tree outflow conditions. Ann. Biomed. Engng. 28, 1281–1299.

Patera A.T. and Rozza G. (2007). Reduced Basis Approximation and A Posteriori Error Estimation for Parametrized Partial Differential Equations.. MIT.

Peiró J. and Veneziani Alessandro (2009). Reduced models of the cardiovascular system. in 'Cardiovascular Mathematics, Modeling, Simulation and Applications I'. chapter 10, pp. 347–394.

Pena G. (2009). Spectral element approximation of the incompressible Navier-Stokes equations in a moving domain and applications. PhD thesis. École Polytechnique Fédérale de Lausanne.

Perktold K., Resch M. and Peter R.O. (1991). Three-dimensional numerical analysis of pulsatile flow and wall shear stress in the carotid artery bifurcation. J. Biomech. 24(6), 409–420.

Perotto S. (2012). Hierarchical model (hi-mod) reduction in non-rectilinear domains. Technical Report 52/2012. MOX, Dipartamento di Matematica "F.Brioschi". Politecnico di Milano.

Perotto S. (2014). A survey of hierarchical model (Hi-Mod) reduction methods for elliptic problems. in 'Numerical Simulations of Coupled Problems in Engineering, S.R. Idelsohn ed.'. Springer. Berlin. pp. 217–241.

Perotto S., Ern A. and Veneziani A. (2010). Hierarchical local model reduction for elliptic problems: A domain decomposition approach. Multiscale Model. Simul. 2, 1102–1127.

Perotto S. and Veneziani A. (2014). Coupled model and grid adaptivity in hierarchical reduction of elliptic problems. J. Sci. Comput. 60(3), 505–536.

Perotto S. and Zilio A. (2013). Hierarchical model reduction: three different approaches. in 'Numerical Mathematics and Advanced Applications'. Springer. pp. 851–859.

Peyret R. and Taylor T.D. (2012). Computational methods for fluid flow. Springer Science & Business Media.

Pironneau O., Hecht F., Hyaric A.L. and Ohtsuka K. (2006). Freefem. URL: http://www. freefem. org .

Quarteroni A., Ragni S. and Veneziani A. (2001). Coupling between lumped and distributed models for blood flow problems.. Comp. Vis. Science. 4(1), 111–124.

Quarteroni A and Rozza G, eds (2014). Reduced Order Methods for Modeling and Computationtal Reduction. Springer.

Quarteroni A., Tuveri M. and Veneziani A. (2000). Computational vascular fluid dynamics: problems, models and methods. Computing and Visualization in Science 2(4), 163–197.

Quarteroni A. and Valli A. (2008). Numerical approximation of partial differential equations. Vol. 23. Springer Science & Business Media.

Reymond P., Merenda F., Perren F., Rüfenacht D. and Stergiopulos Nikos (2009). Validation of a one-dimensional model of the systemic arterial tree. Am. J. Physiol. Heart Circ. Physiol. 297, H208–H222.

Robertson A.M. and Sequeira A. (2005). A director theory approach for modeling blood flow in the arterial system: an alternative to classical 1d models. Math. Models Methods Appl. Sci. 15(06), 871–906.

Salzar R.S., Thubrikar M.J. and Eppink R.T. (1995). Pressure-induced mechanical stress in the carotid artery bifurcation: a possible correlation to atherosclerosis. Journal of biomechanics 28(11), 1333–1340.

Sohn J.L. (1988). Evaluation of fidap on some classical laminar and turbulent benchmarks. Int. J. Num. Meth. Fluids 8(12), 1469–1490.

Stergiopulos N., Young D.F. and Rogge T.R. (1992). Computer simulation of arterial flow with applications to arterial and aortic stenoses. J. Biomech. 25, 1477–1488.

Stroud A.H. and Secrest D. (1966). Gaussian Quadrature Formulas. 1 edn. Prentice-Hall, Inc.

Tang D., Yang C., Kobayashi S. and Ku D.N. (2001). Generalized finite difference method for 3-d viscous flow in stenotic tubes with large wall deformation and collapse. Applied numerical mathematics 38(1-2), 49–68.

Taylor C.A., Hughes T.J.R. and Zarins C.K. (1998a). Finite element modeling of blood flow in arteries. Comp. Meth. Appl. Mech. Engrg. 158(1-2), 155–196.

Taylor C.A., Hughes T.J.R. and Zarins C.K. (1998b). Finite element modeling of three-dimensional pulsatile flow in the abdominal aorta: relevance to atherosclerosis. Ann. Biomed. Engng. 26(6), 975–987.

Teman R. (1977). Navier-Stokes Equations. Theory and numerical analysis. 1 edn. North-Holland Publishing Company.

Thomas J.W. (2013). Numerical partial differential equations: finite difference methods. Vol. 22. Springer Science & Business Media.

Thubrikar M.J. and Robicsek F. (1995). Pressure-induced arterial wall stress and atherosclerosis. The Annals of Thoracic Surgery 59(6), 1594–1603.

Urquiza S. and Vénere M. (2002). An application framework architecture for fem and other related solvers. in 'Proceedings of MECOM 2002. First South American Congress on Computational Mechanics, Santa Fe, Argentina'.

Urquiza S.A., Blanco P.J., Vénere M.J. and Feijóo R.A. (2006). Multidimensional modeling for the carotid blood flow. Comp. Meth. Appl. Mech. Engrg. 195, 4002–4017.

Versteeg H.K. and Malalasekera W. (2007). An introduction to computational fluid dynamics: the finite volume method. Pearson Education.

Vignon-Clementel I.E., Figueiroa C.A., Jansen K.E. and Taylor C.A. (2006). Outflow boundary conditions for three-dimensional finite element modeling of blood flow and pressure waves in arteries. Comp. Meth. Appl. Mech. Engrg. 195, 3776–3996.

VMTK (2015). The vascular modeling toolkit.
URL: *http://www.vmtk.org*

Watanabe S.M. (2013). ADAN - An anatomically detailed arterial network model for computational hemodynamics (in Portuguese). PhD thesis. Laboratório Nacional de Computação Científica - LNCC, Petrópolis - Brazil.

Watanabe S.M., Blanco P.J. and Feijóo R.A. (2013). Mathematical model of blood flow in an anatomically detailed arterial network of the arm. Math. Model. Numer. Anal. 47, 961–985.

Womersley J.R. (1955). Method for the calculation of velocity, rate of flow and viscous drag in arteries when the pressure gradient is known. The Journal of physiology 127(3), 553–563.

Xiao N., Alastruey J. and Figueroa C. Alberto (2014). A systematic comparison between 1-d and 3-d hemodynamics in compliant arterial models. Int. J. Num. Meth. Biomed. Engng. 30(2), 204–231.

Yoshida Y., Yamaguchi T., Caro C.G., Glagov S. and Nerem R.M. (1988). Role of blood flow in atherogenesis. Springer.

Zarins C.K., Giddens D.P., Bharadvaj B.K., Sottiurai V.S., Mabon R.F. and Glagov S. (1983). Carotid bifurcation atherosclerosis. Quantitative correlation of plaque localization with flow velocity profiles and wall shear stress. Circ. Res. 53, 502–514.

Ziekiewicz O.C. (1971). The finite element method in engineering science. McGrawe Hill, London.

Zienkiewicz O.C. and Taylor R.L. (1977). The finite element method. Vol. 3. McGraw-hill London.